Design and development of hybrid energy harvesters

Xuan Li

Supervisors: Dr Joe Briscoe
Prof. Steve Dunn

Submitted in a partial fulfilment of the requirements of the Degree of Doctor of Philosophy

School of Engineering and Materials Science
Queen Mary, University of London
18th September 2017

Declaration

I, Xuan Li, confirm that the research included within this thesis is my own work or that where it has been carried out in collaboration with, or supported by others, that this is duly acknowledged below and my contribution indicated. Previously published material is also acknowledged below.

I attest that I have exercised reasonable care to ensure that the work is original, and does not to the best of my knowledge break any UK law, infringe and third party's copyright or other Intellectual Property Right, or contain any confidential material. I accept that the College has the right to use plagiarism detection software to check the electronic version of the thesis. I confirm that this thesis has not been previously submitted for the award of a degree by this or any other university.

The copyright of this thesis rests with the author and no quotation from it or information derived it may be published without the prior written consent of the author.

Xuan Li

18th September 2017

Abstract

Hybrid energy harvesters (HEHs) targeting multiple energy forms have been drawing increasing interest in recent years. While large scale photovoltaic power plants are capable of providing energy for domestic usage, research has also been focused on kinetic energy harvester with less power output which can be integrated into self-powered electronics such as implantable device, remote wireless sensor, wearables, etc. A number of successful designs of hybrid energy harvesters have been demonstrated which could scavenge solar and kinetic energy simultaneously. However the structures remain complicated; the majority of the designs involve different types of energy harvesters connected in series, which involves complex fabrication processes.

Here, a simple structure based on a p-n junction piezoelectric nanogenerator (NG) was designed. The utilization of columnar piezoelectric n-type ZnO nanorods coated with light absorber layer enabled the device to harvest both kinetic and solar energy. This was adapted to either form a N719-based dye-sensitized solar cell (N719-HEH), or a perovskite solar cell (PSC-HEH). To allow high processing temperatures while maintaining mechanical flexibility, Corning© Willow™ (CW) glass substrate was used and compared to the more common ITO/PET. CW showed 56% lower charge transfer resistance and a related 4 times fold increase in power conversion efficiency for N719-HEHs.

Oscillation (NG effect) and illumination (PV effect) testing indicated that both N719-HEHS and PSC-HEHs operated as kinetic and solar energy harvesters separately, with the current generated by the photovoltaic orders of magnitude greater than it from mechanical excitation. In addition, under illumination, both N719-HEHs and PSC-HEHs demonstrated further current output enhancement when oscillation was applied. The fact that the current output under NG+PV condition was higher than the summation of current output achieved under NG and PV conditions individually, suggests the piezoelectric potential originated from ZnO affected the charge dynamics within the devices. Thus, HEHs with enhanced output were successfully designed and developed.

To mother and father, Chunyan Zheng and Yaoqing Li: I would not be able to achieve this without your support, encouragement, love and care through my life.

To Shu Wang: In the vastness of space and the immensity of time, it is my joy to share a planet and an epoch with you.

To people who died fighting for your own beliefs instead of just minding your own 'business', RIP.

Acknowledgement

I would like to thank my supervisor, Joe Briscoe, for his consistent guidance and advices throughout my PhD. He has always been patient and supportive. He kept me motivated when I was frustrated and stressed. He helped me to improve my lab skills and achieve my project goals. I feel lucky and forever grateful to be supervised by him.

I would also like to thank Steve Dunn and Haixue Yan, who motivated and supported me to pursue my PhD and helped me to make a firm start during the early stage of my PhD. They offered me their trust and I am pleased to say I did not let them down. I also thank all my friends and colleagues, Yaqiong Wang, Ying Tu, Hui Luo, Mira Butt, Pelin Yilmaz and Armando Lacerda, for making the lab fun and enjoyable. I would also give my special thanks to Theo Saunders who consistently helped me with his diverse skills in the lab and words of wisdom.

The deepest gratitude goes to my family, especially to my parents. They are the reason I am able to be pursuing my dreams and living a meaningful life. They respected and supported all my decisions since day one. They taught me how to be a man with responsibility. I also thank Shu Wang, who accompanied me and helped me through the toughest times.

Finally, I would like to thank China Scholar Council to provide financial support during my PhD.

Publications and Presentations

Journal Publications

Ananthakumar, S., **Li, X.**, Anderson, A.-L., Yilmaz, P., Dunn, S., Babu, S. M., & Briscoe, J. (2016). Photo-enhanced catalytic activity of spray-coated Cu_2SnSe_3 nanoparticle counter electrode for dye-sensitized solar cells. *Physica Status Solidi (RRL) - Rapid Research Letters*, *10*(10), 739–744.

Li, Z., Ma, J., Gao, Z., Viola, G., Koval, V., Mahajan, A., **Li, X.**, … Bell, A. J. (2016). Roome temperature megnetoelectic coupling in intrinsic mltiferroic Aurivillius phase textured ceramics. *Dalton Trans., 45*(36), 14049-14052.

Ying, T, Chen, S., **Li, X.**, Krause, S. and Briscoe, J., (2018). Control of oxygen vacancies in ZnO nanorods by annealing and their influence on ZnO/PEDOT:PSS diode behaviour. *Journal of Materials Chemistry C.*, 2018,6, 1815-1821.

Pace, S., Resmini, A., Tredici, I., Soffientini. A., **Li, X.**, Dunn, S,. Briscoe, J., Tamburini, U. (2018). Optimization of 3D ZnO brush-like nanorods for dye-sensitized solar cells. *RSC Adv.*, 2018,8, 9775-9782.

Xuan, L and Briscoe, J., Hybrid energy harvesters scavenging solar and mechanical energy based on ZnO nanorods. (In preparation)

Xuan, L., Ying, T and Briscoe, J., Investigation of defects in ZnO/TiO_2 core-shell structure. (In preparation)

- **Oral presentations**

Hybrid energy harvesters scavenging solar and mechanical energy based on ZnO nanorods. *Martials Research Symposium*, Boston, November 2017.

Hybrid energy harvesters scavenging solar and mechanical energy based on ZnO nanorods. *CAM-IES symposium*, London, September 2017.

Hybrid energy harvesters scavenging solar and mechanical energy based on ZnO nanorods. *AEM2017*, Surrey, September 2017.

Development of ZnO/TiO_2 core-shell structures on solar devices. *European Materials Research Symposium*, Lille, May 2015.

- **Poster presentations**

Hybrid energy harvesters scavenging solar and mechanical energy based on ZnO nanorods. *European Materials Research Symposium*, Strasburg, May 2017.

Acoustic enhancement of solar systems due to piezoelectric effect. QMUL, 2016.

Acoustic enhancement of solar systems due to piezoelectric effect. QMUL, 2014.

Two step sintering textured multiferroic layer-structured ceramics. QMUL, 2012.

Contents

List of Figures

List of tables

Chapter 1 Introduction

1.1 Background – Energy harvesting

Human society is driven by energy. Sufficient and environmentally friendly methods to generate power are crucial to the modern world. According to the World Energy Resource report 2016[1], world energy consumption has changed dramatically during the past 15 years. Renewable energy has drawn significant attention from academic researchers, revolutionary industries as well as governments and international organizations.

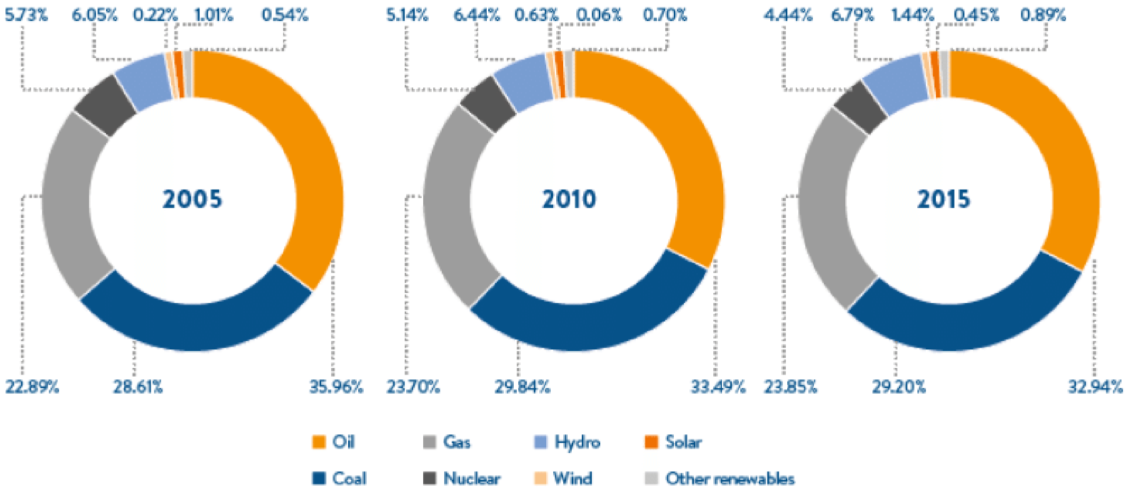

Figure 1-1: Comparative primary energy consumption from 2005 to 2015[1].

It can be seen from Figure 1-1 that, oil (32.94%), coal (29.20%), and gas (23.85%), which are considered the most traditional fossil fuels, still took up 85.99% of the whole world energy consumption in 2015[1]. This heavy reliance on fossil-fuel-based energy production causes severe environmental damage, such as an increase in atmospheric CO_2 level, leading to the greenhouse effect and global warming. On the other hand, known oil reserves will run out by 2052 at this consumption rate even with new reserves being discovered. Therefore, it is critical for us to develop ways to provide sufficient, efficient, secure, affordable, clean, and sustainable energy harvesting technologies[1].

Alternative solutions such as nuclear energy or renewable energy have been proposed and are drawing a great deal of attention. On the nuclear front, the drawbacks include high construction and maintenance cost, potential nuclear radiation, potential high risk of catastrophic accidents, limited fuel availability and radioactive wastes which takes thousands of years to break down. On the contrary, renewable energy generation produces clean energy with no CO_2 emission and requires no input of fuel. Abundant energy forms include solar, wind, tidal, geothermal, biomass, kinetic (such as mechanical vibration and acoustic wave) etc. However, renewable energy technologies do have disadvantages such as low and diffuse energy output (requiring high numbers of installations over large areas) compared to nuclear and traditional fossil fuels, and low reliability of energy supplies due to weather condition limits. Despite this, utilizing renewable energy would be beneficial to provide for long-term, sustainable development of the world. On the middle of the day of 8th of June 2017, it was reported by BBC that real time data showed renewable energy provided for half (50.7%) of UK energy consumption for the first time in history. Benefiting from the sunny and windy weather, photovoltaic power plants and offshore wind farms were working at optimal capacity. For the other parts of the world, Iceland has been running on 100% renewable energy based on geothermal and hydropower. Norway generates 98% of its power using renewable. For Denmark, wind power generates a stunning 140% of the whole country's electricity demand[2]. These show the feasibility and possibility of renewable energy powering large populations. The use of renewable energy has the potential to contribute towards a better future for the world.

1.2 Solar energy harvesting

Among all the renewable energy forms, solar energy is one of the most attractive and has undergone extensive research. The earth receives 120,000 terawatts (TW) of solar irradiation annually whereas the current energy consumption estimates for seven billion people is only about 13 TW[1]. It is then of great interest to utilize solar energy. Thus, the development of inexpensive, non-toxic and environmental friendly solar energy technologies is desired. Currently, limited efficiency, low cost-effectiveness and poor long-term stabilities are the challenges remaining to be solved for solar cell technologies.

A photovoltaic (PV) is a device that can convert incoming sunlight to electricity directly and is the main technology used for solar energy harvesting. According to the International Renewable Energy Agency (IRENA) data in 2016, the global installed capacity for PV electricity has grown exponentially since 2001, reaching around 227 GW. China is the leader in PV installation, taking up 23% of the global installation capacity, followed by USA (14%), Japan (14%), and Germany (13%)[1]. It can be seen here that major solar installations are located in regions with relatively low solar irradiation resource such as Europe and China. High potential still remains in regions such as Africa and the Middle East with rich resource of solar energy. The leading countries have all established relative laws, policies and legislations regarding the promotion of renewable energy technologies such as PV. Feed-in tariff (FiT) is a government scheme designed to encourage the adaption of a range of renewable and low-carbon electricity generation technologies. The first form of this type of scheme was introduced by President Jimmy Carter into the US in 1978. Germany then adopted FiTs in 1990. While the cost of PV was high and this scheme gave insufficient impact on PV installation, it hugely improved the deployment of wind farms in the following 10 years, resulting in Germany taking 1/3 of the global wind energy generating capacity[3]. China was late regarding the FiT scheme (introduced in 2011), but has been trying to increase its renewable energy generations for decades; the huge landscape provides China with rich forms of harvestable renewable energies such as solar, wind, tidal etc. The importance of increasing renewable energy generation and reducing fossil fuel consumption has also raised public concern due to the poor air quality in major cities. Globally, it is expected that more and more countries will join forces to work towards a renewable future. The Paris climate agreement, for example, is the most up to date historical agreement within the United Nations Framework Convention on Climate Change (UNFCCC). The agreement works to tackle the issue of climate change and global warming by cutting greenhouse gas emissions and switching to renewable energy. By June 2017, 195 countries have signed and 148 of which have ratified it. However, disturbing news came as President Donald Trump decides to drop out of the Paris climate agreement even though the US produces 17.89% of the global greenhouse gas emission[4]. With this background, it is imperative to develop more efficient, cost effective energy harvesting technologies.

Martin A, Green characterized photovoltaic solar cells into three major generations depending on material, maximum power conversion efficiency (PCE) obtainable and the capital cost of photovoltaic power[5].

First-generation PVs utilize the purest materials to avoid defects, which hinder the efficiency of a PV. First generation solar cells are mainly based on thick crystalline films (mainly silicon) and utilize either individual form such as monocrystalline silicon, polycrystalline silicon, and amorphous silicon or combined forms such as hybrid silicon. These are considered as the most traditional solar cells and still remain the most efficient types for commercial products. In order to achieve defect-free silicon for higher PCE, purification (removing boron and phosphorus) from metallurgical-grade silicon to solar-grade silicon is crucial. However, due to the large distribution coefficient of boron (B) and phosphorus (P)[6], the traditional directional solidification of molten silicon (m.p. 1414 °C) requires significant amount of energy input. Due to the relatively high labor cost and large amount of input energy required for processing, the associated cost for first-generation PV cells exceed 1 US$/Watt[7].

Second-generation solar cells refers to thin-film solar cells. This is because cells are made from layers of semiconductor materials stacked within micron thickness onto a low-cost backing such as glass, stainless steel or plastic. Second-generation solar cells are mainly based on amorphous silicon, cadmium telluride (CdTe) and copper indium gallium diselenide (CIGS). They have the advantage of reduced cost by eliminating the use of expensive silicon wafers and utilizing mature, cheap and scalable processing technologies such as roll-to-roll processing. The efficiency is limited by the presence of defects within the device (20% PCE). Due to the high cost and complex of production-based establishment, thin-film solar cells are not widely produced (around 17% of all the panels sold globally) compared to silicon-based first-generation solar cells[5]. First solar, which is the number-one producer and seller of CdTe-based solar panels in the world, is currently making solar panels based on CdTe at a price of 0.7 US$/Watt. This is within the range of second generation solar cell capital cost of 0.5 to 1 US$/Watt[7].

Third-generation solar cells refers to cells made from various new materials besides silicon, and have the potential to give higher efficiencies than Shockley-Queisser limit (31% PCE as the maximum efficiency under 1 sun illumination for a PV based on single band gap material[8]). The world record efficiency from a solar cell was reported in 2014. Germany-based Fraunhofer Institute for Solar Energy Systems reported a 46% PCE from a multi-junction photovoltaic cell in the lab[9]. It also includes emerging PV technologies and low-cost PVs including, copper zinc tin sulfide solar cell, organic solar cell, polymer solar cell, quantum dot solar cell, dye-sensitized solar cell and perovskite solar cell. Together with new materials, novel nanostructures and nanotechnologies open up a new promising research area at inexpensive cost of 0.2-0.5 US$/Watt[7].

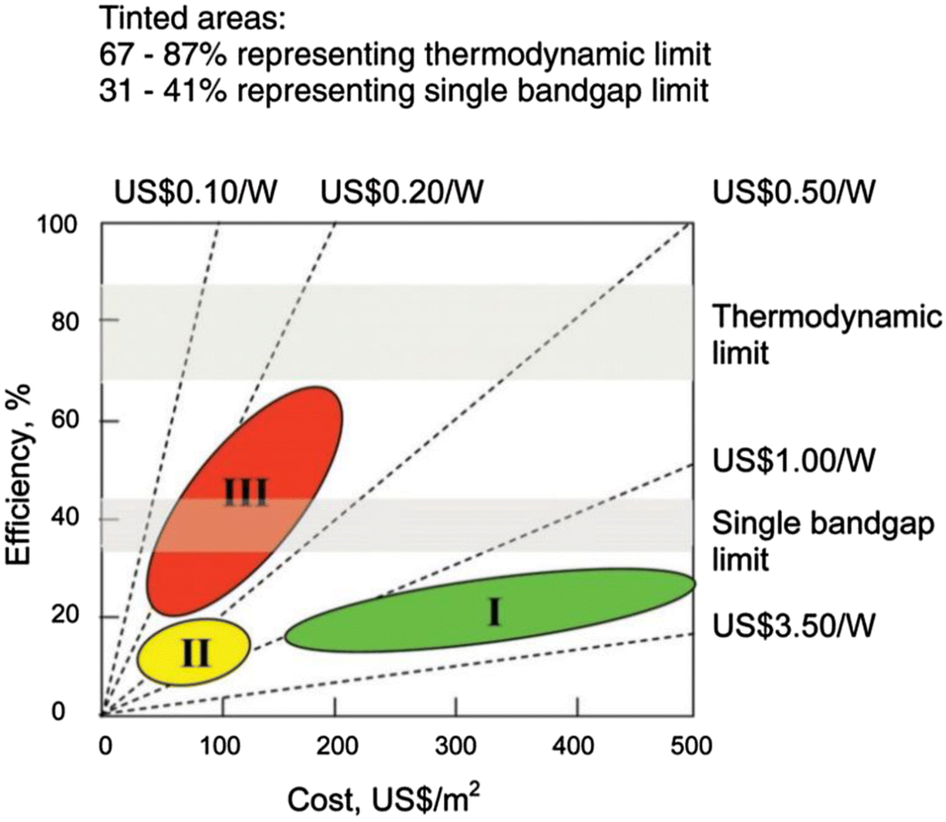

Figure 1-2: Efficiency vs. Cost for generations of solar cells[7].

Figure 1-2 shows the Green Graph, revealing the research efficiency vs. capital cost. First generation remains the main commercialized solar cell technology whereas third generation solar cells are becoming a strong competitor with lower cost and higher efficiency. In the near future, the target is to develop high stability photovoltaic devices and manufacturing process that enable commercial scale up of PV module technology with low lost (<0.2 US$/Watt), high conversion efficiency (>20%), environmentally friendly profile (reducing toxic and harmful materials), long module lifetime (>35 years) and low degradation (<0.3%/year).

1.2.1 Relevant 3rd generation PV technologies

Among the third generation solar cells, dye-sensitized solar cells (DSSC) and perovskite solar cells (PSC) have been attracting a great deal of attention. The DSSC was originally designed using mesoporous TiO_2 nanoparticle film sensitized by an organic dye layer. The nanostructure was sandwiched by two transparent conducting oxide electrodes with confined liquid electrolyte in-between[10]. DSSCs have produced lower efficiency compared to commercialized silicon-based solar cells with a highest record of 13%[11]. It uses inexpensive and nontoxic earth abundant elements such as titanium and zinc in the photo-anode, and relatively simple manufacture processes. It also does not require extremely high quality materials compared to silicon-based solar cells. This means the production process has lower costs due to less required energy input. However, the molecular, liquid-state electrolyte is unstable which reduce the gain from the cheaper production process. Thus, the goal is to design a solar cell using inexpensive raw materials and process techniques, but which also has a long-term stability and efficiency comparable to silicon or thin-film based solar cell. Alternative designs utilize solid-state inorganic hole conductors and p-type semiconductors such as copper iodide (CuI)[12] and copper thiocyanate (CuSCN)[13]. These designs have increased the stability by eliminating volatile liquid-state electrolytes. Other designs have also been demonstrated to increase the PCE for DSSC. Law, Matt *et al.* reported a ZnO/TiO_2 core-shell structure-based DSSC[14]. It was suggested that a thin layer of TiO_2 nanoparticles coating would increase the dye loading by increasing the roughness. The shell would also suppress the charge recombination and improve the open-circuit voltage. An efficiency of 2.25% was reported.

A perovskite solar cell (PSC) utilizes a perovskite-structured compound as light absorber layer. The compound is mostly a hybrid organic-inorganic lead or tin halide-based material. Since the initial report of 3.8% PCE in 2009[15], PSCs have undergone extensive research and surpassed the 20% PCE mark in recent years[16-17]. The advantages of high efficiency and low production costs make PSCs a promising candidate to stand out among 3rd generation PVs. The disadvantages of perovskite solar cells are the poor stability over their operation lifetime and the use of the heavy metal lead in the material processing. Fast degradation has been observed involving water, oxygen and moisture.

In this project, DSSC and PSC are the two types of solar cells investigated, more details regarding these two technologies will be given in Section 2.2 Dye-sensitized solar cells (DSSCs) and Section 2.3 Perovskite solar cells (PSCs).

1.3 Piezoelectric energy harvesting

While large PV power plants could provide significant energy generation on a mega-watt scale, PV technology relies on specific environmental conditions to work; it cannot work properly during the night, in a cloudy weather or at an incorrect angle towards the sun. It also requires high investment and occasional maintenance. Thus, for indoor use and locations where sunlight is insufficient, energy harvesters designed to harvest alternative energy forms are desired. Kinetic energy refers to energy forms such as wind, human motion, transportation and industrial machineries etc. Kinetic energy harvesting aims to convert the kinetic energy into electricity, even though the power output may only be on the micro-to-milli-watt range. It can be used to power small portable electronics, remote wireless sensors, medical bio-implants, micro electro-mechanical systems (MEMS), micro robots etc[18]. Three types of vibration energy harvesting mechanisms have been demonstrated including: electromagnetic induction, electrostatic generation, and piezoelectric[19]. Among the three of them, piezoelectric energy harvesting has been widely investigated. A piezoelectric energy harvester works by using a piezoelectric material that accumulates charge when under stress or strain; this leads to a voltage output. The common piezoelectric materials used are lead zirconate titanate (PZT), polyvinylidene fluoride (PVDF) and ZnO nanostructures. Even with high piezoelectric coefficients of d_{33} (593 pC/N)[20] and d_{31} (-274 pC/N)[20], PZT has limited application due to its brittle nature leading to stress-induced cracking and fracture[21].

PVDF, after being poled, exhibits a -33 pC/N of d_{33} and 18-24 pC/N of d_{31}[20]. For ZnO crystal, the reported strain coefficients d_{33} and d_{31} are 12.4 pC/N and -5.1 pC/N[22]. For piezoelectric application, ZnO has benefits such as low temperature synthesis (<100 °C) and simple process to produce various nanostructures, such as one-dimensional nanorods, nanotubes, nanopropeller, nanocombs, nanorings, nanobows, nanobelts and nanocages etc[23–25]. Wang *et al.* reported a piezoelectric energy harvester (nanogenerator, NG) based on ZnO nanorod arrays in 2006[26]. Since then, extensive research has been done and various designs have been demonstrated[27].

1.4 Hybrid energy harvesting

It has been mentioned above that it is common to have various forms of energy present simultaneously. It is then of great interest to design a device that can harvest multiple energy forms simultaneously. This type of device is referred to as a hybrid energy harvester (HEH). The innovative concept of a hybrid energy harvester aims to harvest multiple types of energy using an integrated structure. Thus the application of the device can be targeted according to its working environment, and can increase the energy harvesting rate.

Light, thermal, mechanical, magnetic, chemical and biological energies are the main forms of renewable energies. Among these, solar and mechanical energies stand out due to wide availability in the environment. However both solar and mechanical energies are time and location-dependent. It would therefore be advantageous to design a HEH that could harvest both solar and mechanical energy. However, in general the structure of devices that could achieve this remains complicated with the majority of designs requiring separate devices connected in series or parallel. This would increase the device size and require more complex processes and assembly techniques.

To sum up, research into energy harvesting has been undergoing for decades. Devices targeting single or multiple energy forms have been demonstrated. It is therefore of great interest to design and develop a simple, integrated structure, which could perform as a hybrid energy harvester.

1.5 Aims and objectives

The aims of this study were to design and develop a nanostructure-based energy harvester with ability to harvest multiple energy forms (solar and kinetic).

The initial motivation of this project was to investigate the acoustic effect upon the performance of ZnO-based solar cells. Through successful device fabrication, the target was to test the device under acoustic environment then evaluate the piezoelectric effect and understand the mechanism.

Later on, it was adapted to utilize a flexible substrate to fabricate the device. Mechanical bending replaced acoustic wave as a potential method for inducing higher degree of strain and extracting a larger amount of energy.

To achieve the above-mentioned aims, the following objectives were outlined:

1) Fabricate ZnO-based solar cells and probe the acoustic effect on the efficiencies of the devices, detailed in Chapter 4.
2) Design, fabricate a dye-based HEH (N719-HEH) and investigate the NG and PV performances of the devices, detailed in Chapter 5.
3) Design, fabricate a perovskite-based HEH (PSC-HEH) and investigate the NG and PV performances of the devices, detailed in Chapter 6.

Chapter 2 Literature review

2.1 Solar cells

2.1.1 Solar cell theory

The sun emits light with a range of wavelengths from ultraviolet (10^{-5} – 400 nm) to the visible (400 – 800 nm) then to the infra-red (800 – 10^6 nm). Ultraviolet is filtered out by ozone and infra-red is mainly absorbed by water vapor and CO_2 in the atmosphere. When the sun is directly overhead, the maximum radiation strikes onto the surface of earth through the shorted path length. This path length is called the air mass (AM) and can be approximated by AM=1/Cos φ, where φ is the angle of elevations of the sun[28]. The standard solar spectrum used for measurements of solar cell is AM 1.5 condition, which is 48.19° of the angle of elevation.

For a traditional semiconductor-based solar cell, the device is assembled around a p-n junction. Without the illumination, the solar cell has the characteristics of a diode equation:

$$J_{dark}(V) = J_0[\exp(\frac{eV}{nk_BT})-1]$$

Equation 2-1

Where J_0 is the reverse saturation current density, e is the charge of an electron, V is the applied bias, n is the diode non-ideality factor, k_B is Boltzmann's constant, and T is the temperature in Kelvin[29]. With illumination, the device produces a short-circuit current when the terminals are connected together. The short-circuit current density is defined by:

$$J_{sc} = e\int b_s(E) \cdot EQE(E) \cdot dE$$

Equation 2-2

Where b_s is the incident spectral flux density, *EQE* is the external quantum efficiency, *E* is the incident photon energy. *EQE* gives the probability that a photon of energy *E* will deliver one electron to the external circuit, therefore also referred as incident photon to current conversion efficiency (IPCE). IPCE is a quantum-yield term for the overall charge separation at the junction and charge collection process through the material[29]. It corresponds to the photocurrent density produced in the external circuit under monochromatic illumination of the cell divided by the photon flux that strikes the cell[28]. Thus it can be calculated from:

$$IPCE = \frac{J_{sc}(\lambda)}{e\Phi(\lambda)} = 1240\frac{J_{sc}(\lambda)[A \cdot cm^{-2}]}{\lambda[nm]P_{in}(\lambda)[W \cdot cm^{-2}]}$$

Equation 2-3

Where *e* is the elementary charge, λ is the wavelength, Φ is the quantum yield. Under illumination, the *J-V* curve of the solar cell is the superposition of the dark current J_{dark} and the short current J_{sc}[29]. In order to plot the *J-V* curve using positive value, J_{dark} is commonly assigned to be negative:

$$\begin{aligned} &J(V) = J_{sc} - J_{dark}(V) \\ &\rightarrow J(V) = J_{sc} - J_0[\exp(\frac{eV}{nk_BT}) - 1] \end{aligned}$$

Equation 2-4

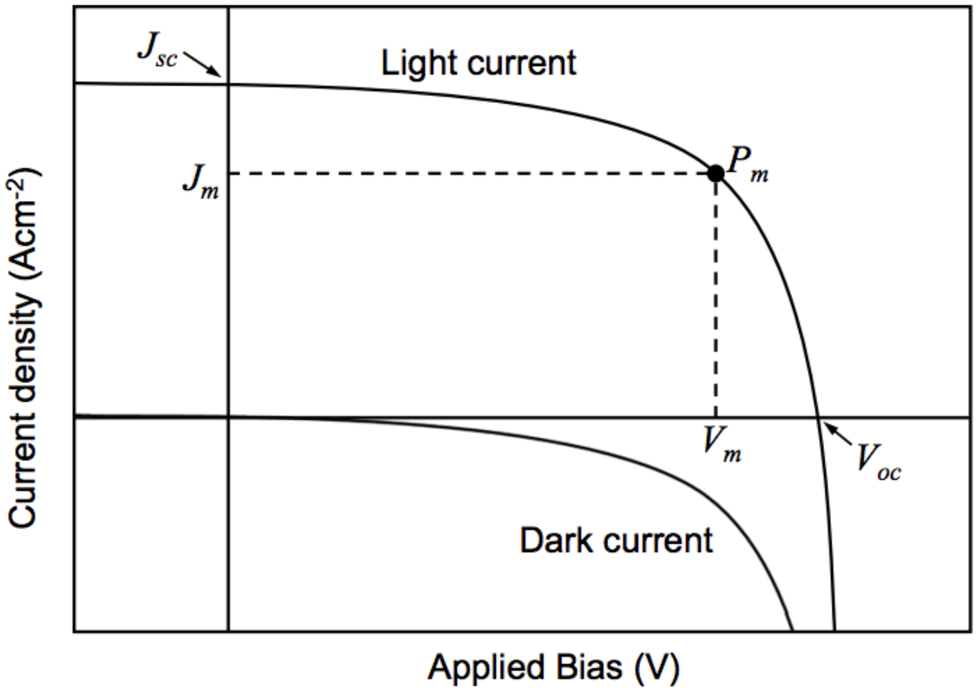

Figure 2-1: Example of *J-V* behaviour of a non-ideal solar cell in the dark and under illumination. At V=0 the current is equal to the short-circuit current density: J_{sc}. At J=0, the cell generates open-circuit voltage, V_{oc}. The maximum power generated, P_m is at current density J_m and voltage V_m. (Courtesy of the graph: Joe Briscoe)

From Figure 2-1, when J reduces to 0, the value of the voltage is defined as open-circuit voltage, V_{oc}. From the range between J_{sc} and V_{oc}, the cell is generating power. At some point, the product of J and V reaches a maximum value (P_m corresponding to current density J_m and voltage V_m in this case). The proportion of this maximum power density to the maximum theoretical power density if operating at J_{sc} and V_{oc} is defined by the fill factor[29]:

$$FF = \frac{J_m V_m}{J_{sc} V_{oc}}$$

Equation 2-5

The power conversion efficiency (PCE) of the cell, η, is defined as the maximum power density as a proportion of the incident light power density, P_{in}.

$$\eta = \frac{J_m V_m}{P_m} = \frac{J_{sc} V_{oc} FF}{P_{in}}$$

Equation 2-6

For standard cell testing, AM=1.5 G, P_{in} =100 mW/cm^2.

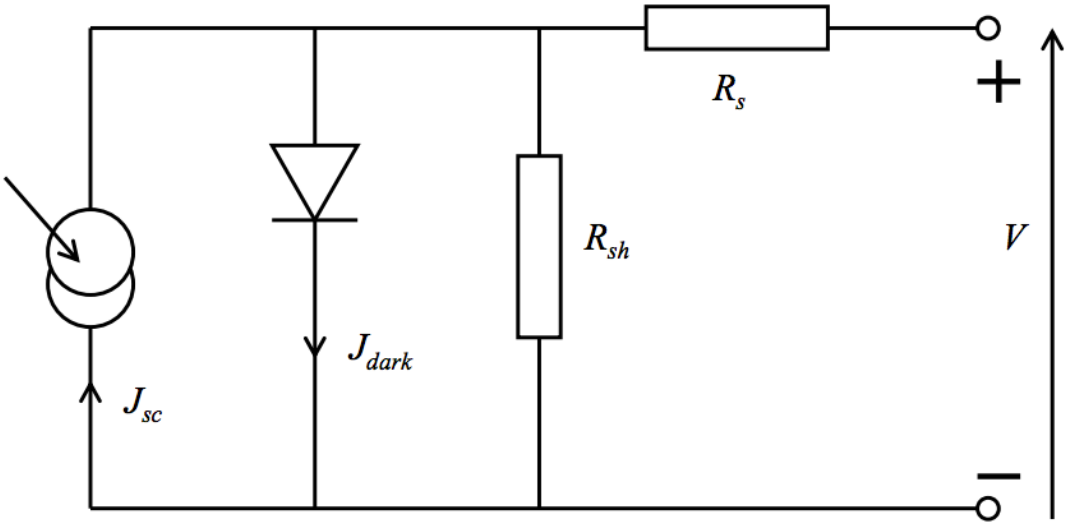

Figure 2-2: Equivalent circuit of a solar cell.

When P_{in} is fixed, η can be improved by improving the J_{sc}, V_{oc} and FF. In a real cell, FF is reduced due to losses in the cell. One example of the losses is the non-ideality of the diode, which is considered as the non-ideality factor n. There are also series resistance R_s and shunt resistance R_{sh}. Series resistance includes resistance to current flow in the materials, resistance at the interface with different contacts and resistance in the contacts, whereas the shunt resistance is reduced by the leakage of the current through and around the cell, such as short-circuits, as well as recombination at interface[29].

2.2 Dye-sensitized solar cells (DSSCs)

In 1991, O'Regan and Grätzel reported the first nanostructured dye-sensitized solar cell[30]. The initial design utilized a 10 μm-thick mesoporous TiO_2 layer with high surface area. Then a thin a layer of organic dye molecules was coated on to the surface of the TiO_2. A redox electrolyte was then used for returning the dye to the ground state. The device exhibited a PCE of 7.9%[30].

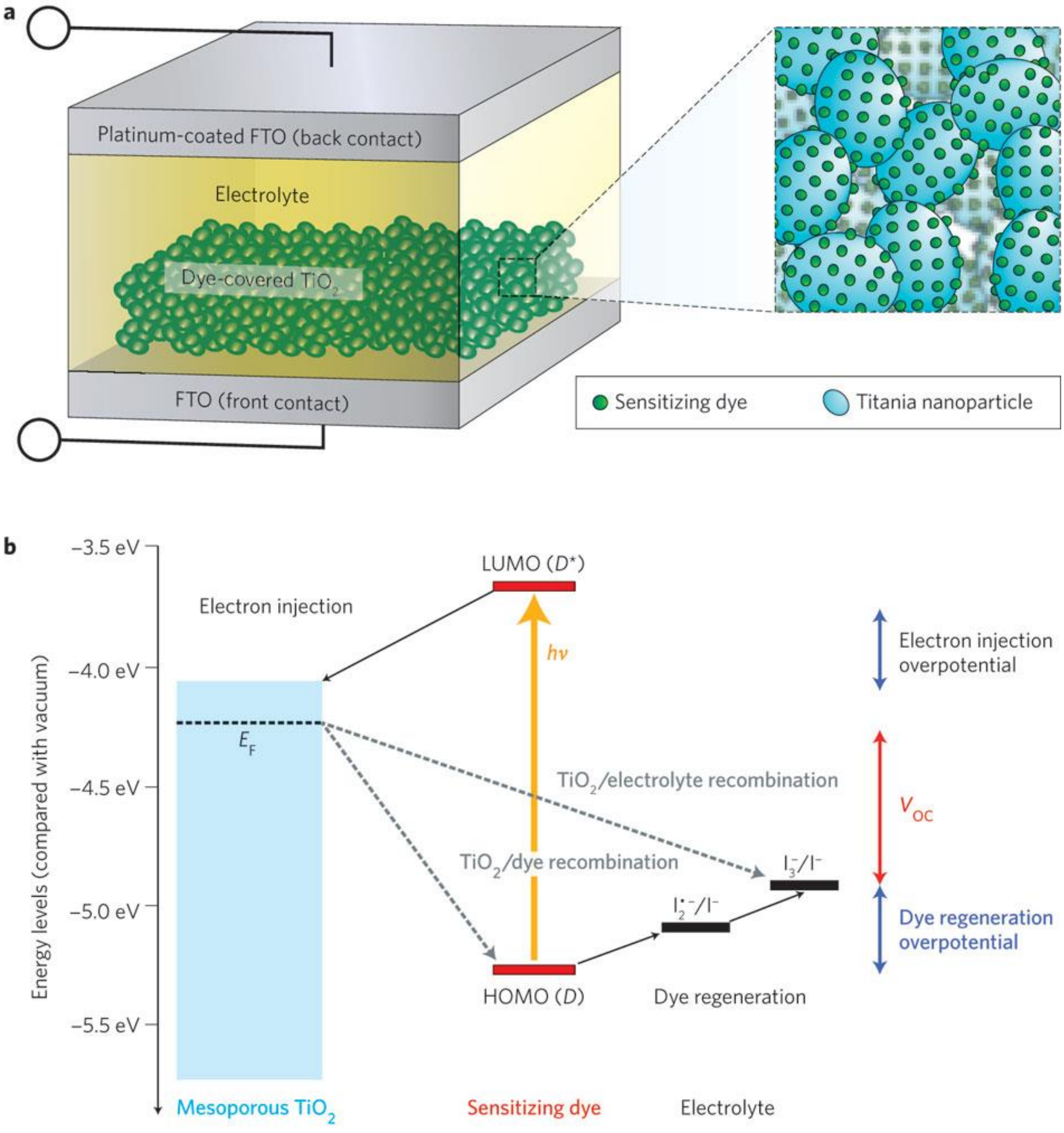

Figure 2-3: Schematic of the principles of a liquid-state DSSC (LSDSSC)[31].

Figure 2-3 demonstrates the device assembly and working principles of the DSSC. From bottom up in Figure 2-3a, the structure of the DDSC is comprised of a transparent conducting oxide (typically fluorine-doped tin oxide) coated glass, a nanostructured photo-anode (TiO_2) covered with a monolayer of sensitizing dye molecule, a hole-transporting electrolyte (typically iodide/triiodide) and finally platinum-coated fluorine doped tin oxide (FTO) glass as counter-electrode.

The energy level graph shown in part b of Figure 2-3 reveals the principles of operation. At the anode surface, a dye molecule (D) absorbs the light and is electrically excited to excited state D^*

$$D + hv = D^* (photoexcitation)$$

Equation 2-7

The molecule in the excited state can decay back to the ground state directly. This process is direct recombination (undesired) of the excited dye, reflected by the excited state lifetime[28]. The desired route is for the molecule to undergo oxidative quenching by injecting electron into the conduction band of semiconductor anode.

$$D^* \rightarrow D + hv'(direct\ recombination)$$

Equation 2-8

$$D^* \rightarrow D^+ + e^-_{cb} (photo\ anode\ charge\ injection)$$

Equation 2-9

The injected electron travels through the photo anode (mesoporous network of TiO_2) and reaches the front working electrode. It will then travel to the counter electrode through the external circuit. The oxidized dye is reduced rapidly to ground state by the donor (iodide) present in the electrolyte:

$$2D^{+} + 3I^{-} \rightarrow 2D + I_3^{-} (regeneration\ of\ D)$$

Equation 2-10

The injected electron could also recombine with the oxidized dye D^{+} in the absence of a redox mediator, I^{-}.

$$D^{+} + e_{cb}^{-} (injected\ electron\ from\ photo\ anode) \rightarrow D(photo\ anode / dye\ recombination)$$

Equation 2-11

There is also photo anode/electrolyte recombination when the injected electron recombines with the oxidized redox couple. These electrons will not travel through the external circuit to generate power and considered as loss.

$$I_3^{-} + e_{cb}^{-} (injected\ electron\ from\ photo\ anode) \rightarrow 3I^{-} (photo\ anode / dye\ recombination)$$

Equation 2-12

For electrons that have travelled through the external circuit and reached the counter electrode, they participate in the regeneration of the charge mediator electrolyte, completing the circuit.

$$I_3^{-} + 2e^{-} \rightarrow 3I^{-} (regeneration\ of\ I^{-})$$

Equation 2-13

The requirements for liquid redox electrolytes are: chemical stability, low viscosity to facilitate charge transport, high solubility for the redox couple components and the ability to coexist with dye molecules and semiconducting photo anodes[28]. However, liquid electrolytes remain difficult to handle, with a high possibility of evaporation, leakage and sealing imperfection issues. In order to solve the stability problem, solid-state p-type semiconductor can be utilized to replace the liquid-state electrolyte, forming a solid-state DSSC.

Tennakone *et al.* reported a solid-state DSSC based on CuI[12]. The device was based on nano-porous n-TiO_2, cyanide dye and p-CuI hole transport material (HTM), which achieved 0.8% PCE. They later reported another HTM: p-type CuSCN[32]. The requirements of p-type HTM are highly restrictive. A high band gap is desired to form a transparent film to allow incident light through to the dye. CuSCN has a direct band gap of 3.6 eV[32]. The valence band of HTM needs to be higher than the conduction band of photo absorber in order to facilitate the hole transport. The PCE of CuSCN based device was around 0.13%, due to the fast charge recombination rate[32]. It is also reported that CuSCN showed improved stability compared to CuI. Also, CuSCN does not decompose to SCN^- or form excessive surface trap sites like CuI[33].

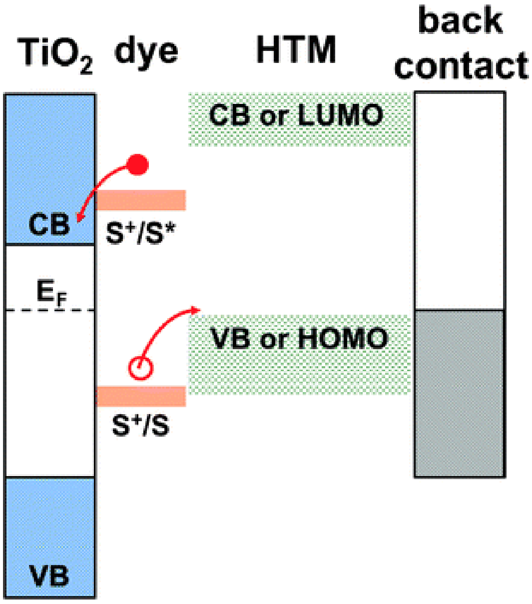

Figure 2-4: Schematic energy level demonstrating the principles of operations of solid-state DSSC[34].

As shown in Figure 2-4, in a solid-state DSSC, when incident photon arrives at the dye molecule, an electron is promoted from the ground state (highest occupied molecular orbital, HOMO) to the exited state (lowest unoccupied molecular orbital, LUMO) with subsequent electron injection into the conduction band of TiO_2, as in a liquid-state cell. A hole transfers and migrates from the ground state of the dye up to the HOMO level of the hole transport material. The whole device is fabricated on FTO glass, which transfers the electrons through the external circuit to the counter electrode.

Although the stability of the cell is improved, the efficiency and open-circuit voltage of solid-state cells (400 – 500mV with PCE <2%) is relatively lower than liquid-state cells (800 mV with PCE >10%). Kron *et al.* investigated the loss of efficiency and voltage with in a solid-state cell[35]. They suggested that the high recombination probability of photo-generated electrons from TiO_2 into the hole conductor, together with the low conductivity of the hole transport material, are the main reasons for lowered performance.

2.3 Perovskite solar cells (PSCs)

In 2009, Akihiro Kojima *et al.* reported organometal halide perovskites used as visible-light sensitizers for photovoltaic cells[15]. Organic – inorganic lead halide perovskite compounds such as $CH_3NH_3PbBr_3$ and $CH_3NH_3PbI_3$ were selected due to unique optical properties, excitonic properties, electrical conductivity[15] as well as large absorption coefficient, high charge carrier mobility and diffusion length[36]. The innovative design is shown in Figure 2-5. The structure comprises (bottom up) FTO glass, compact TiO_2 layer, mesoporous n-type TiO_2 nanoparticle layer acting as photo anode, perovskite light absorber layer, organic electrolyte solution containing lithium halide and halogen as redox couple, finally, a Pt-coated counter electrode[15].

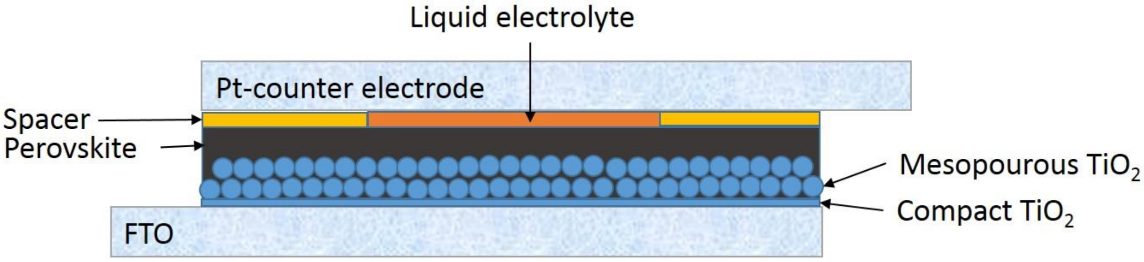

Figure 2-5: Schematic design of perovskite solar cell.

The resulting 3.13% efficiency with 0.96 V open-circuit voltages showed the perovskite compounds to be a promising candidate towards high photo-voltage devices[15]. It can be seen here that the device still resembles a liquid-state DSSC structure, with the perovskite replacing original dye molecules. Since then, the research on perovskite solar cells has accelerated with increasing efficiencies. Saliba *et al.* from EPFL reported the most recent record for perovskite by using a mixture of triple Cesium/Methylammonium/Formamidinium (Cs/MA/FA) cation; they achieved a stabilized 21.1% efficiency[16]. From 3.13% to 21.1%, the fundamental structure remained similar. The 21.1% device kept the FTO, compact TiO_2 and mesoporous TiO_2 layer. It utilized specially engineered perovskite structure, and solid-state hole transport material topped by a Au electrode. The structure actually resembled a solid-state DSSC, with perovskite acting as light absorber and 2,2',7',7'-tetrakis [N,N-di-p-methoxyphonylamine] -9,9'-spirobifluorene (spiro-OMeTAD) used as HTM. Here the hole transporting material is crucial to be compatible with perovskite layer. In the early stage research, the HTMs used were mainly organic compounds, with the most widely used being spiro-OMeTAD[16,37,38], other small molecules such as pyrene arylamine derivatives[17], and conducting polymers[39].

In 2013, J, Christians *et al.* reported that CuI was utilized for HTM in perovskite achieving 6% efficiency[40]. Similar to the research path in solid-state dye-sensitized solar cell, in 2014, it was reported that CuSCN was also utilized for HTM in perovskite, achieving 12.4% efficiency. 20 nm thick CuSCN thin film also exhibits relatively high hole mobility of 0.01-0.1 $cm^2V^{-1}s^{-1}$ (as compared with 4 x 10^{-5} cm^2V^-

$^{1}s^{-1}$ for spiro-OMeTAD)[41].

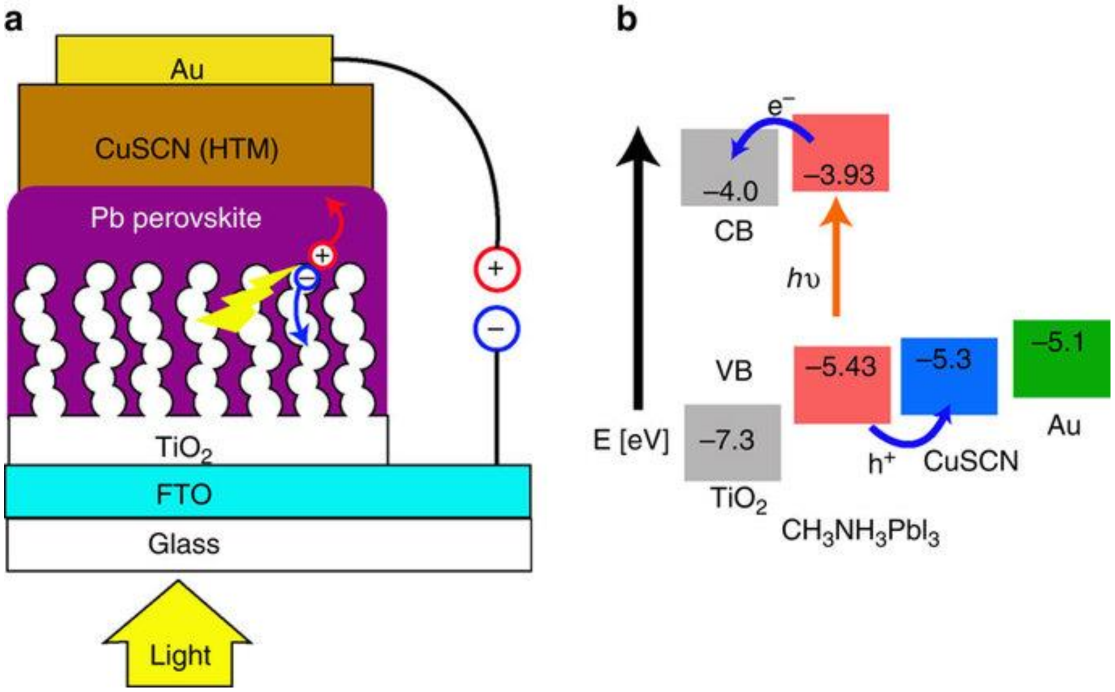

Figure 2-6: Schematic of structure and band level of perovskite solar cells[36].

Figure 2-6 shows an example of the principles of operations of a PSC using CuSCN. Compact TiO_2 (30 nm thickness) and mesoporous TiO_2 were deposited on FTO. The procedure of deposition of perovskite layer was followed by the sequential deposition recipe[37] reported by Burschka *et al.* Lead iodide (PbI_2) was introduced on to the mesoporous TiO_2 by spin coating a 1M solution of PbI_2 in *N*,*N*-dimethylformamide (DMF) kept at 70 °C[37]. The film was then dipped into a solution of CH_3NH_3I in anhydrous 2-propanol (10 mg/ml). The HTM (CuSCN) was then deposited using doctor blade method[36], resulting in a 600 nm capping layer. The final device showed a PCE of 12.4% together with a high short-circuit current density of 19.7 mA/cm^2. The high J_{sc} obtained was attributed to the effective charge extraction between $CH_3NH_3PbI_3$ and CuSCN, followed by fast hole transport through CuSCN layer[36].

2.4 ZnO-based DSSCs and PSCs

The electron transport layer (ETL) plays an important role in DSSCs and PSCs in achieving high-efficiency cells. It needs to be able to transport the electron away before recombination and prevent direct contact between the hole transport layer (HTL) and conductive electrode. It needs to be relatively transparent to allow visible light through to the absorber layer (dye or perovskite), capable of charge collection and transport, and preferably low cost.

The n-type photo anode used during early stage research on DSSCs and PSCs was mainly focused on TiO_2 owing to the wide band gap, non-toxicity, high stability and inexpensive manufacture resources. Later on, ZnO was brought into attention as a substitution for TiO_2. ZnO has the benefit of achieving various nanostructures under low temperature synthesis[25]. The motivations behind this substitution were:

1) Potentially higher active surface are benefited from tuneable nanostructures leading to potentially higher dye loading in DSSCs.
2) Superior charge collection properties from the oriented one-dimensional nanostructure such as nanorods.
3) Higher carrier mobility than TiO_2 (200 cm^2/Vs for ZnO compared to 10 cm^2/Vs for TiO_2[42]).
4) Simpler, low input energy manufacture process.
5) Ease of coating procedures within the structure, as the precursor for the absorber layer can readily reach the entire surface, which opens up innovative design of potential structures[43].
6) Increased optical path through light scattering similarly to mesoporous TiO_2[44].
7) ZnO is piezoelectric which holds the possibility to affect charge transport within the device.

The disadvantage of ZnO is mainly the chemical instability. Dye precipitation was discovered in a ZnO mesoporous structure[45]. Since the Ru complex-based dye was initially engineered for TiO_2 (acidic nature) surface contact[46], dissolution of ZnO by the acidic carboxylic anchoring group of the sensitizer causes insoluble complexes and precipitation in the cores. They will block the contact between incident light and the dye molecules thus reducing the charge injection. They can also act as recombination sites leading to severe recombination.

For the application of DSSC, the adsorption of the dye to photo anode and charge transfer between the dye and the photo anode take place at the interface. It was found that increased active surface area leads to potentially higher degree of dye loading and increase of charge generation[14]. It is also suggested that compared to non-nanostructured crystalline structure electrodes, semiconductor grown in nanotubes or nanorods has higher effective surface area in contact with the dye and electrolyte[33]. However, the surface area of ZnO nanorods or nanowires are still less than mesoporous TiO_2 structure. Lower dye loading causes poor light absorption. In order to achieve a higher degree of dye loading, a number of designs tuning the nanostructures have been demonstrated such as: elongated ZnO nanorods[47], hierarchical structure using secondary growth[48,49] and ZnO/Al_2O_3, ZnO/TiO_2 core-shell structure[14] (details will be discussed in Section 2.6). The best performance of purely ZnO nanorods-based DSSC is 1.5%[47] reported by Law *et al.*. Other structures exceeding this efficiency have also been reported, however they mainly use hierarchical structures such as ZnO nanorods with nanoparticle capping network (1.77%)[50], or ZnO nanorods with nanoflower over layers (2.53%)[51]. For the record efficiency of 1.5%, prolonged nanorods were designed in order to increase surface area and subsequent dye loading. Length and diameter of the nanorods were measured to be 16-17 μm and 130-200 nm, respectively[47].

However for perovskite applications, even though ZnO layer could also acts as the electron transport layer, prolonged length is undesired. The initial research on the optimal ETL thickness was performed on TiO_2 based perovskite[52]. The charge transport and recombination properties of $CH_3NH_3PbI_3$ sensitized cells with varying

TiO_2 thickness were investigated. Recombination in traditional DSSC refers to the process of electrons transfer back to either the oxidized dyes (Equation 2-11) or the oxidized species (Equation 2-12) of the redox couple. Recombination in DSSCs was found to be independent of the ETL film thickness[28,53]. However, in perovskite, electron recombination lifetime (τ) was found to be heavily dependent on the thickness of ETL[52] shown in Figure 2-7.

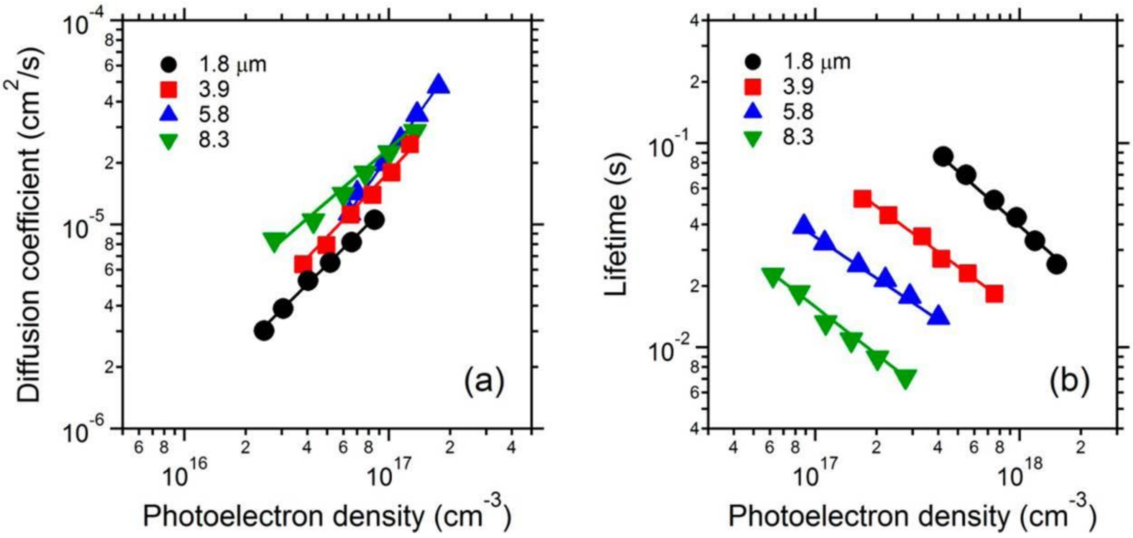

Figure 2-7: Effect of TiO_2 film thickness on the (a) Electron diffusion coefficient and (b) Recombination lifetime of electron-hole pairs[52].

At a specific photoelectron density (eg. 4 x 10^{18} cm^{-3}), the τ decreased from 10^{-1} s down to 6 x 10^{-2} s with increased film thickness (1.8 to 8.3 μm). The diffusion path way was elongated with increased thickness, which led to faster recombination rate. The electron diffusion length L_d was also calculated. A higher diffusion length indicates higher charge collection efficiency. The electrode film thickness in traditional DSSC is commonly designed to be within 1/3 of the L_d to achieve the optimum performance[54]. It was calculated that the L_d decreased monotonically from 16.9 to 11.7 to 8.2 to 5.5 μm when the film thickness increase sequentially from 1.8 to 3.9 to 5.8 to 8.3 μm. The increase of film thickness limits the charge collection process[54] and reduces J_{sc}[52]. V_{oc} and FF were also found to be lower for thicker TiO_2 films due to rapid recombination[55]. Increased V_{oc} in thinner films was attributed to the increased electron density in TiO_2, where the total generated charge is concentrated in a smaller volume of the scaffold. This would increase the electron quasi-Fermi level of TiO_2, hence improving the photo voltage[56]. Therefore, it was concluded that, rapid recombination with thicker ETL limits the cell performance even with increased light absorption due to thicker ETL[52]. The PCE were tested to be 4.58% to 4.43% to 2.57% to 1.92% with increased thickness from 1.8 to 3.9 to 5.8 to 8.3 μm.

Research was needed to further narrow down to the optimal thickness of ETL. It was suggested by Leijtens *et al.* that the different pore filling factor from different thickness has a significant effect on the perovskite solar cell performance[56]. Thicker film with lower pore filling fraction would form an ETL-Perovskite mixture layer with the potential risk of HTM in contact with ETL, or even the conductive substrate. A thinner film has the benefit of forming a perovskite-capping layer, meaning the full ETL film is embedded under perovskite layer. Charges generated would be able to rapidly transfer into TiO_2 due to the high diffusivity of carriers within perovskite material[57]. It was also suggested that thinner film with lower surface area would facilitate a faster charge collection at the conductive substrate. Lower surface area leads to lower amount of possible recombination sites, thinner film means charges would have a higher probability to be collected before recombination[56]. It was found that the efficiency of the perovskite device increased from 11.8% to 15.3% to 16.5% with decreased film thickness from 750 nm to 440 nm to 260 nm, respectively. It was later reported that 400 nm-thickness was around the optimal value for ETL for perovskite[38,58,59].

Similar to the developing pathway in liquid-state DSSCs, ZnO was then selected as a substitute for TiO_2 in PSCs. In 2013, Liu reported a perovskite solar cell based on a ZnO nanoparticle film[60]. The efficiency exceeded 10% on flexible substrates

(ITO/PET) and 15% on rigid substrates (ITO/Glass). In the same year, Dongqin Bi *et al.* reported enhanced light absorption using perovskite upon ZnO nanorods. Nanorods with 1µm length achieved 5.2% using single-step deposited perovskite[61]. In 2014, Son reported 11% efficiency perovskite solar cell based on ZnO nanorods using two-step sequential method[62]. The reported optimal length of nanorods was also 1µm. In 2015, Mahmood reported a ZnO nanorod-based perovskite achieving 16.1% efficiency[63]. The synergistically improved ZnO nanorods, with PEI coated and high aspect ratio (1 µm in length, 85 nm in diameter), were doped with nitrogen. Doping significantly improved electron density, leading to improved current and voltage.

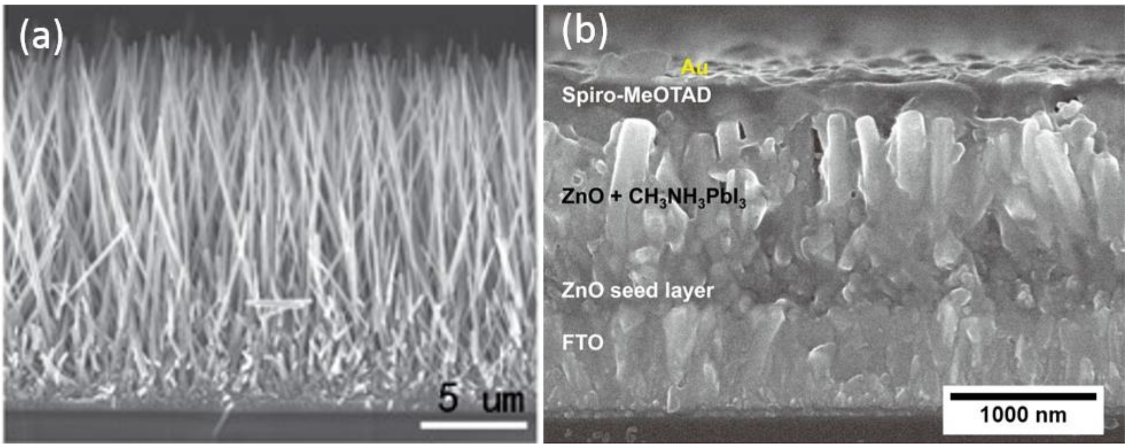

Figure 2-8: (a) ZnO nanorods utilized in record liquid-state DSSC with 16-17 µm lengths[47], and (b) ZnO nanorods utilized in PSC with 1 µm length[62].

Figure 2-8 shows the comparison of structures for ZnO-based LSDSSC and ZnO-based PSC. It can be seen that long rods are utilized for LSDSSC while short rods are utilized for PSC.

2.5 Piezoelectric energy harvester

2.5.1 Piezoelectricity

Jacques Curie and Pierre Curie firstly reported ‘piezoelectricity’ in 1880. They reported electrification under mechanical pressure of certain crystals[64], i.e. certain crystals were subjected to mechanical strain and were able to generate a polarization proportional to the applied strain. The materials reported included tourmaline, quartz, topaz, cane sugar and Rochelle salt. Since then, the term, piezoelectricity is commonly used to describe the ability of materials to develop electric displacement D that is directly proportional to an applied mechanical stress σ (Figure 2-9a)[65]. Following the definition, the electric charge appearing on the electrodes reverses its sign if the stress is changed from tensile to compressive. This has more recently come to be termed the direct piezoelectric effect; when a piezoelectric material is mechanically strained it becomes electrically polarized, producing electric charges on the surface of the material[66]. Lippmann[67] deduced the converse piezoelectric effect, which was later confirmed by the Curie brothers[64]. Converse piezoelectric effect indicates a material deforms under applied electric field. Again, the sign of the strain S (elongation or contraction) follows the change of the direction of electric field E (Figure 2-9b). Shear piezoelectric effect illustrates the relationship between shear mechanical stress and strain with electric charge (Figure 2-9c).

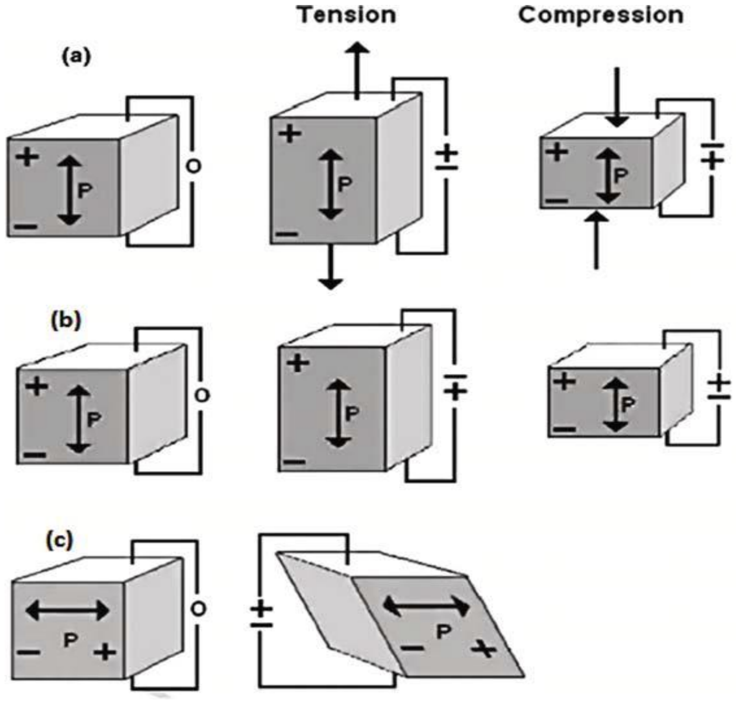

Figure 2-9: Schematic representation[66] of (a) Longitudinal direct (b) Converse (c) Shear piezoelectric effects.

The constitutive equations describing the piezoelectric properties are based on the assumption that the total strain in the material is the sum of mechanical strain induced by the mechanical stress and the controllable actuation strain caused by the applied electric voltage[66].

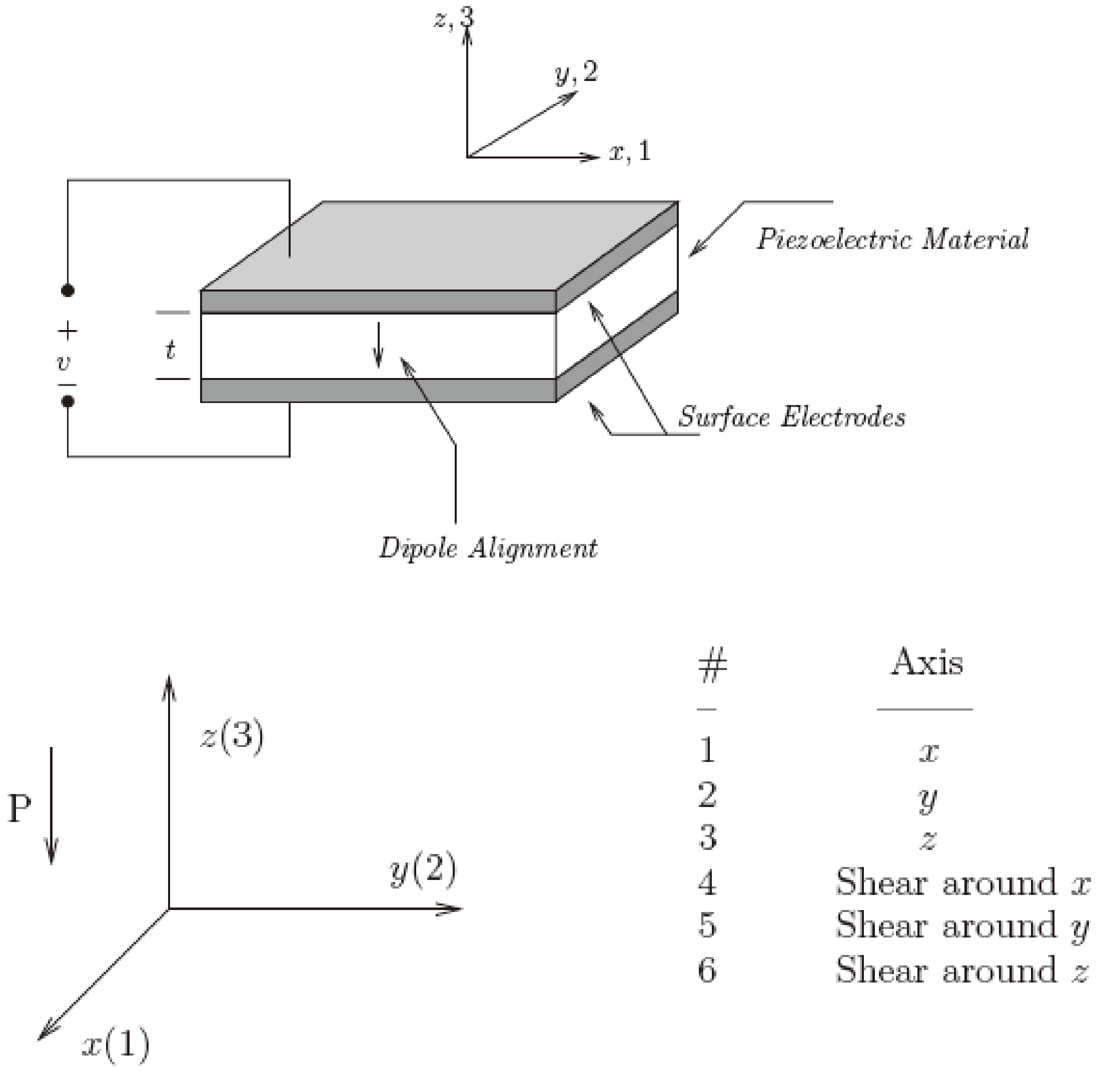

#	Axis
1	x
2	y
3	z
4	Shear around x
5	Shear around y
6	Shear around z

Figure 2-10: Schematic diagram of a piezoelectric transducer and relevant axis nomenclature[66] .

As shown in Figure 2-10, the numbers 1, 2, 3 corresponds to the *x, y,* and *z* axes. Axis 3 is also assigned to the direction of the initial polarization of the material, and axes 1 and 2 lie in the plane perpendicular to axis 3.

The electromechanical equations for a linear piezoelectric materials is:

$$\varepsilon_i = S_{ij}^E \sigma_j + d_{mi} E_m$$

Equation 2-14

$$D_m = d_{mi}\sigma_i + \xi_{ik}^{\sigma} E_k$$

Equation 2-15

Where the indices *i, j* = 1,2,…,6 and *m,k* = 1, 2, 3 refer to different directions within the material coordinate system. According to Figure 2-10, the above equations could be rearranged in the following form, which is more commonly used:

$$\varepsilon_i = S_{ij}^{D}\sigma_j + g_{mi} D_m$$

Equation 2-16

$$E_i = g_{mi}\sigma_i + \beta_{ik}^{\sigma} D_k$$

Equation 2-17

σ … Stress vector (N/m^2)

ε … Strain vector (m/m)

E… Vector of applied electric field (V/m)

ξ … Permittivity (F/m)

d… Matrix of piezoelectric stain constants (m/V)

S… Matrix of compliance coefficients (m^2/N)

D… Vector of electric displacement (C/m^2)

g… Matrix of piezoelectric constants (m^2/C)

β … Impermittivity component (m/F)

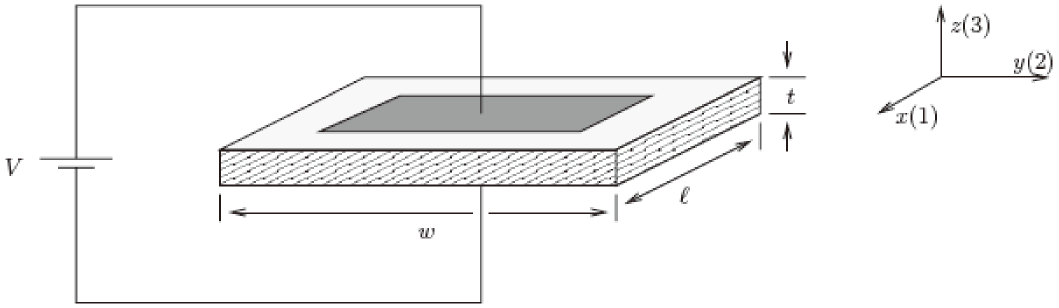

Figure 2-11: Schematic of the arrangement of d_{31} measurement[66].

Piezoelectric constant d_{ij} is defined as the ratio of developed free strain to the applied electric field. The subscripts d_{ij} implies that the electric field is applied or charge is collected in *i*-direction for displacement or force in the *j*-direction.

For example, as shown in Figure 2-11, if a voltage *V* is applied to a piece of piezoelectric material with a dimension of length *w*, width *l* and thickness *t*. The electrical field generated along the direction 3 is:

$$E_3 = \frac{V}{t}$$

Equation 2-18

The strain induced along the direction 1 is:

$$\varepsilon_1 = \frac{\Delta l}{l}$$

Equation 2-19

$$\Delta l = \frac{d_{31} V l}{t}$$

Equation 2-20

Thus, under a fixed given voltage, higher d_{31} indicating a higher strain or *vice versa*. Here d_{31} is normally a negative number. This is due to the fact that the application of a positive electric field will generate a positive strain in direction 3[66].

Alternatively, another interpretation of d_{31} is stated as the ratio of short-circuit charge per unit area flowing between connected electrode perpendicular to the *j*-direction to the stress applied in the *i*-direction.

For the same piece of material in Figure 2-10 but under short-circuit condition, if a force *F* is applied in the direction 3, the stress generated is:

$$\sigma_3 = \frac{F}{lw}$$

Equation 2-21

Which leads to the electric charge flowing through the short circuit:

$$q = d_{33}F$$

Equation 2-22

Similarly, piezoelectric constant g_{ij} signifies the electric field developed along the *i*-axis when the material is stressed along the *j*-axis.

Elastic compliance constant S_{ij}, is the ratio of the strain in *i*-direction to the stress in the *j*-direction, given that no change of stress along the other two directions is applied.

Dielectric coefficient, e_{ij} determines the charge per unit area in the *i*-axis due to an electric filed applied in the *j*-axis.

Piezoelectric coupling coefficient k_{ij} represents the ability of a piezoelectric material to transform electrical energy to mechanical energy and *vice versa*. This transformation of energy between mechanical and electrical domains is the most fundamental principle of operations that employed in both sensor and actuators[66]. The index *ij* indicates that the stress, or strain is in the *j*-direction, and the electrodes are perpendicular to the *i*-axis. For example, if the material is mechanically strained in direction 1, as a result of electrical energy input in direction 3, while the device is under no external stress, then the ratio of stored mechanical energy to the applied electrical energy is denoted as k_{31}^2.

When a piezoelectric element is under open-circuit condition, the application of a force will deflect the element, similar to a spring. This deflection Δ_z, can be measured and mechanical work done by the applied force F can be calculated as below:

$$W_M = \frac{F\Delta_z}{2}$$

Equation 2-23

Due to the piezoelectric effect, electric charges will be accumulated. This amounts to the electrical energy:

$$W_E = \frac{Q^2}{2C_p}$$

Equation 2-24

Which is stored in the piezoelectric capacitor. Therefore,

$$k_{33} = \sqrt{\frac{W_E}{W_M}} = \frac{Q}{\sqrt{F\Delta_z C_p}}$$

Equation 2-25

The coupling coefficient can be written in terms of other piezoelectric constants, in particular:

$$k_{ij}^2 = \frac{d_{ij}^2}{S_{ij}^E e_{ij}^\sigma} = g_{ij} d_{ij} E_p$$

Equation 2-26

Where E_p is the Young's modulus of elasticity of the piezoelectric material.

2.5.2 Piezoelectric ZnO

ZnO is an II-VI compound semiconductor with wurtzite crystal structure shown below.

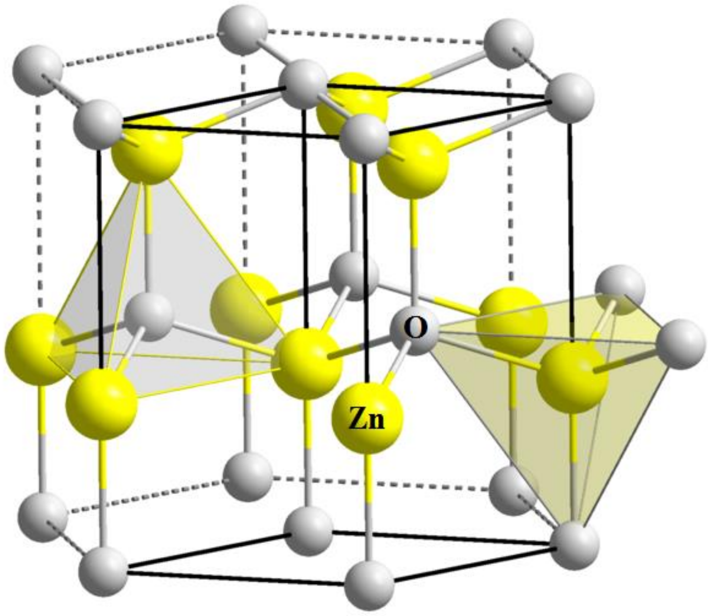

Figure 2-12: Hexagonal wurtzite crystal structure of ZnO, (b) Hexagonal prism of ZnO crystal showing different crystallographic faces[68].

ZnO is asymmetrical and belongs to $P6_3mc$ space group. It can be seen from above figure that alternating planes of *Zn* and *O* ions form tetrahedra coordinated along the z-axis. The convention is that the [0001] axis points from the face of the *O* plane to the *Zn* plane and is the positive *z* direction. Along the z-axis, the lattice of ZnO has distinct atom termination at the alternating surfaces, the (0001) surface is terminated by *Zn* atoms and $(000\bar{1})$ surface is terminated by *O* atoms. Polarization results from strain due to offset of these ions, hence ZnO behaves as a piezoelectric material.

The (0001) surface possesses the highest surface energy when compared to other non-polar surfaces. Thus, ZnO crystals tend to grow along the z-axis and exhibits columnar/pillar structure called nanorods[25].

The Young's modulus of 1 µm length ZnO nanorods has been reported up to 100 GPa[69]. It was also reported that Young's modulus decreases when the diameter of the nanorod increases[70].

2.5.3 ZnO-based piezoelectric energy harvesters

Early measurement on the piezoelectric effect of ZnO nanorods was presented and discussed by Wang and Song[26]. The design of the experiment is shown in Figure 2-13.

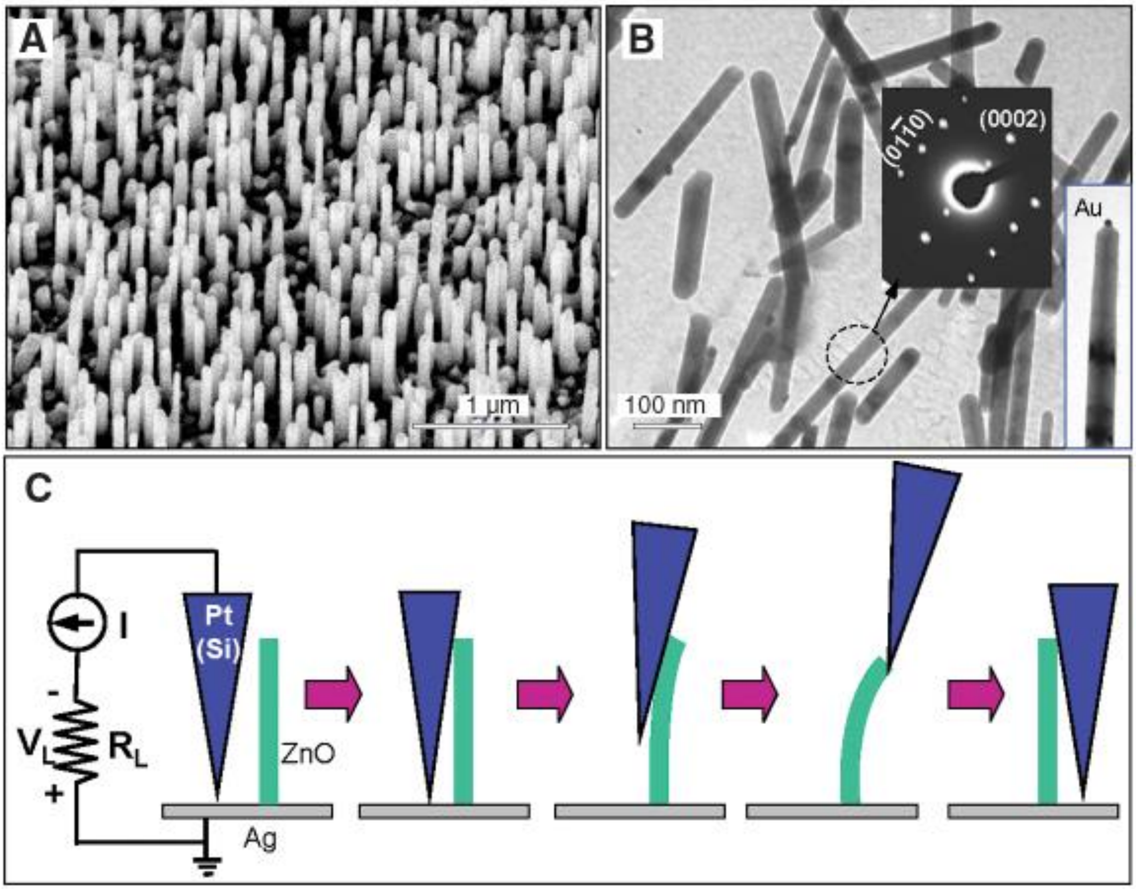

Figure 2-13: Experimental design for converting nanoscale mechanical energy into electrical energy by a vertical piezoelectric ZnO nanorod. (A) Scanning electron microscopy images of the aligned ZnO nanorods. (B) Transmission electron microscopy images of ZnO nanorods. (C) Experimental setup and procedures for generating electricity by deforming a

nanorod with a conductive AFM tip. The base of the nanowire is grounded and an external load of R_L (500 megohm) is applied, which is much larger than the resistance of the nanowire[26].

Nanorods were grown on GaN/sapphire substrate via gold catalysed vapour-liquid-solid method with length of 1 µm and an aspect ratio of 10. The bending of the nanorod was induced by an AFM Si-tip coated with Pt film. In AFM contact mode, a constant normal force of 5 nN was maintained between the tip and sample surface. The output voltage across an outside load of R_L was continuously monitored as the tip scanned over the nanorods.

During the experiment, both the topography of the ZnO nanorods surface and the corresponding output voltage images across the load were recorded simultaneously, thus both images can be used to compare and identify whether the output signal was location-based (ZnO sites). Ideally, the output signal would be generated exactly where there was a ZnO nanorod.

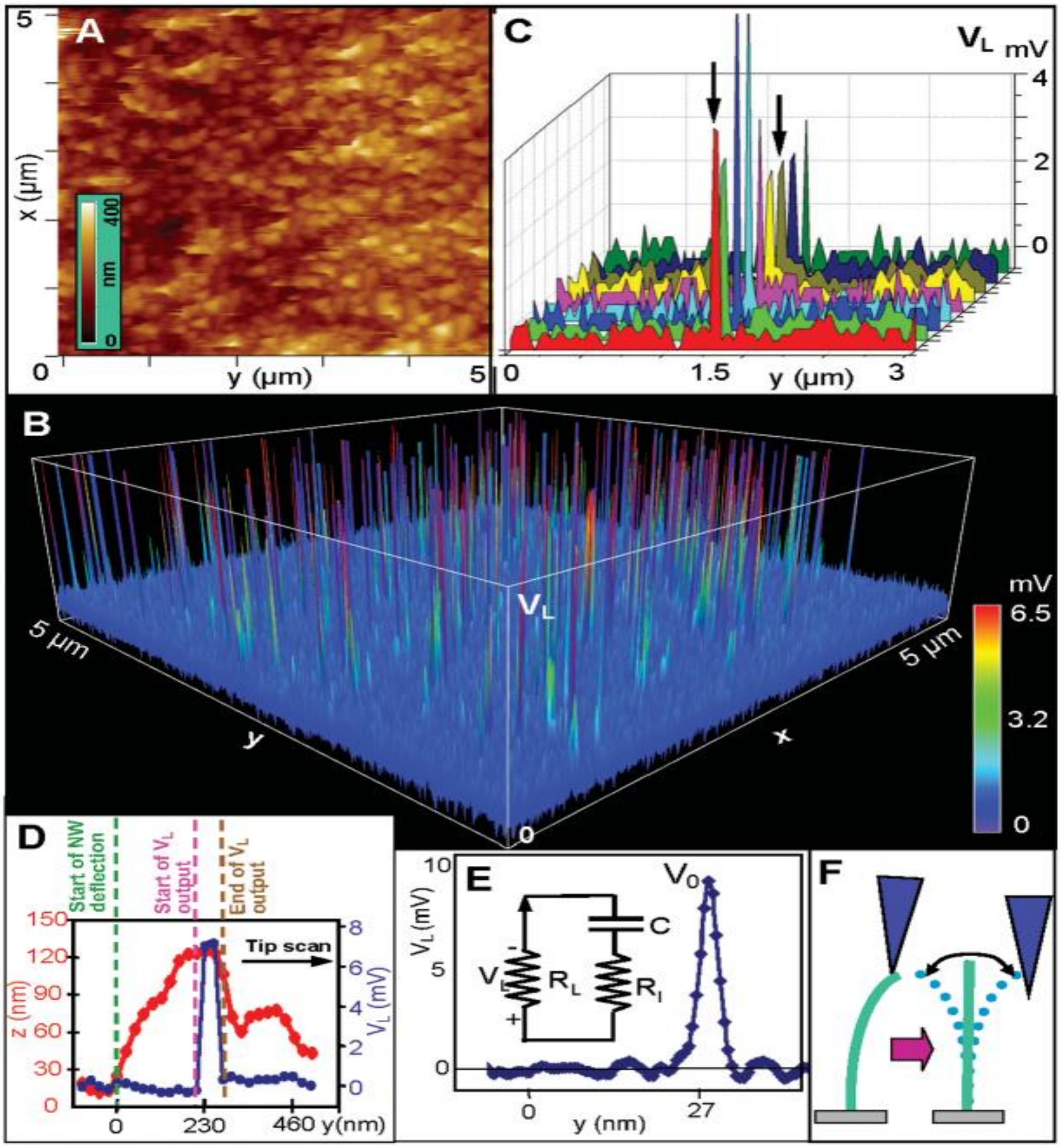

Figure 2-14: Electromechanically coupled discharging process of aligned piezoelectric ZnO nanorods observed in contact mode. (A) Topography (B) Corresponding output voltage image of the nanorods arrays. (C) A series of line profiles of the voltage output signal when the AFM tip scanned across a vertical nanorods at a time interval of 1 min. (D) Line profiles from the topography (red) and output voltage (blue) images across a nanorod. (E) Line profile of the voltage output signal when the AFM tip scans across one specific vertical nanorod. (F) The resonance vibration of a nanorod after being released by the AFM tip, showing that the stored elastic energy is transferred mainly into vibrational energy after creating the piezoelectric discharge[26].

Comparing (A) and (C) in Figure 2-14, the location of the voltage peak was found to be exactly at the site of the nanorod, indicating the physical origin of the output signal. Also, a delay was observed for the voltage output signal as shown in (D). No output signal was received when the tip first touched the nanorod and pushed the nanorod (green dash line in D). The peak of the voltage output corresponded approximately to the maximum deflection (y_m) of the nanorod, indicating that the discharge occurred when the tip passed the stretched side and once was already in contact with the compressed side of the nanorod. When the tip touched the nanorod and induced a strain, piezoelectric charges started to accumulate but no discharge occurred. Discharge only occurred when the deflection reached nearly the maximum[26]. The principle is explained in details below.

For a vertical, straight ZnO nanorod, the deflection of the nanorod by an AFM tip creates a strain field, with the outer surface being stretched (positive strain) and the inner surface compressed (negative strain) (Figure 2-15B). An electric field E_z along the nanorod (z direction) is then created inside the nanorod volume through the piezoelectric effect.

$$E_z = \varepsilon_z / d$$

Equation 2-27

Where d is the piezoelectric coefficient along the nanorod direction that is normally the positive z-axis of ZnO, with the Zn atomic layer being the front terminating layer[26]. The piezoelectric potential is created by the polarization of ions in the crystal, rather than the free-mobile charges. Since the charges associated with the ions are rigid and affixed to the atoms, they cannot freely move[18]. Free carriers in the semiconductor nanorod may screen the piezoelectric charges, but they cannot completely cancel/deplete the charges[18]. The piezoelectric field direction is closely parallel to the z-axis (nanorod direction) at the outer surface and antiparallel to the z-axis at the inner surface.

Across the width of the nanorod at the top end, the electric potential distribution from the compressed to the stretched side surfaces is approximately between V_s^- to V_s^+:

$$V_s^{\mu} = \mu 3T\left|y_m\right|4Ld$$

Equation 2-28

Where *T* is the diameter of the nanorod and y_m is the maximum deflection.

The potential is created by the relative displacement of Zn^{2+} cations with respect to the O^{2-} anions, a result of the piezoelectric effect in the wurtzite crystal structure[26]. The potential difference is maintained as long as the deformation is in place and no foreign free charges are injected.

The contacts at the top and the base of the nanorod are non-symmetric: the bottom contact is ZnO/Ag, resulting in an Ohmic contact. The top contact is the ZnO-Pt contact. The electron affinity (E_a) of ZnO is 4.5 eV and the work function of Pt is 6.1 eV. $\phi_{MS} = \phi_M - \chi_0 = 1.6 > 0$. Thus the ZnO-Pt contact is a Schottky contact. This Schottky barrier is important in producing a measurable voltage output of the whole system. Because the compressed side of the semiconductor ZnO nanorod has negative potential V_s^- and the stretched side has positive potential (V_s^+), two distinct transport processes will occur across the Schottky barrier. When the AFM conductive tip that induces the deformation is in contact with the stretched surface of positive potential V_s^+ (Figure 2-15D and E). The Pt metal tip has a potential of nearly zero, V_m=0, so the metal tip-ZnO interface is negatively biased for $\Delta V = V_m - V_s^+ < 0$. The as-synthesised ZnO nanorods behave as n-type semiconductors, the Pt metal-ZnO semiconductor interface in this case is a reverse-biased Schottky diode, and little current flows across the interface[26].

In the second step, when the AFM tip is in contact with the compressed side of the nanorod (Figure 2-15F), the metal tip-ZnO interface is positively biased for $\Delta V = V_L = V_m - V_s^+ > 0$. The local potential drop leads to the rising of the conduction band near the tip[18]. The metal-semiconductor interface in this case is a positively biased Schottky diode, and it produces a sudden increase in the output electric current. The current is formed from the quick flow of the local accumulated n-type carriers in the nanorod. The discharge process happens at a faster rate than the charge accumulation rate.

The measured voltage pulse is described as:

$$V_L \approx \frac{R_L Q}{\Delta t}$$

Equation 2-29

Even the charge Q from single nanorod is small (1000-10,000 electrons[18]), Δt here (the time interval for the discharge process) is even smaller (0.1-1 ms scale). Hence the value of V_L from the calculation could be measurable.

Electrons from the ZnO will be driven by ΔV and flow via external load. Once the electrons flow back to the tip through the nanorod. They will neutralize the ionic charges within the nanorod and thus reduce the magnitudes of the potential V_s^- and V_s^+. Therefore, V_L starts to decrease back to zero after all the ionic charges in the nanorod are fully neutralized. Due to this mechanism, the discharge curve is nearly symmetric as shown in Figure 2-14D. And the delay can also be explained due to the discharge occurs nearly at the maximum deflection point.

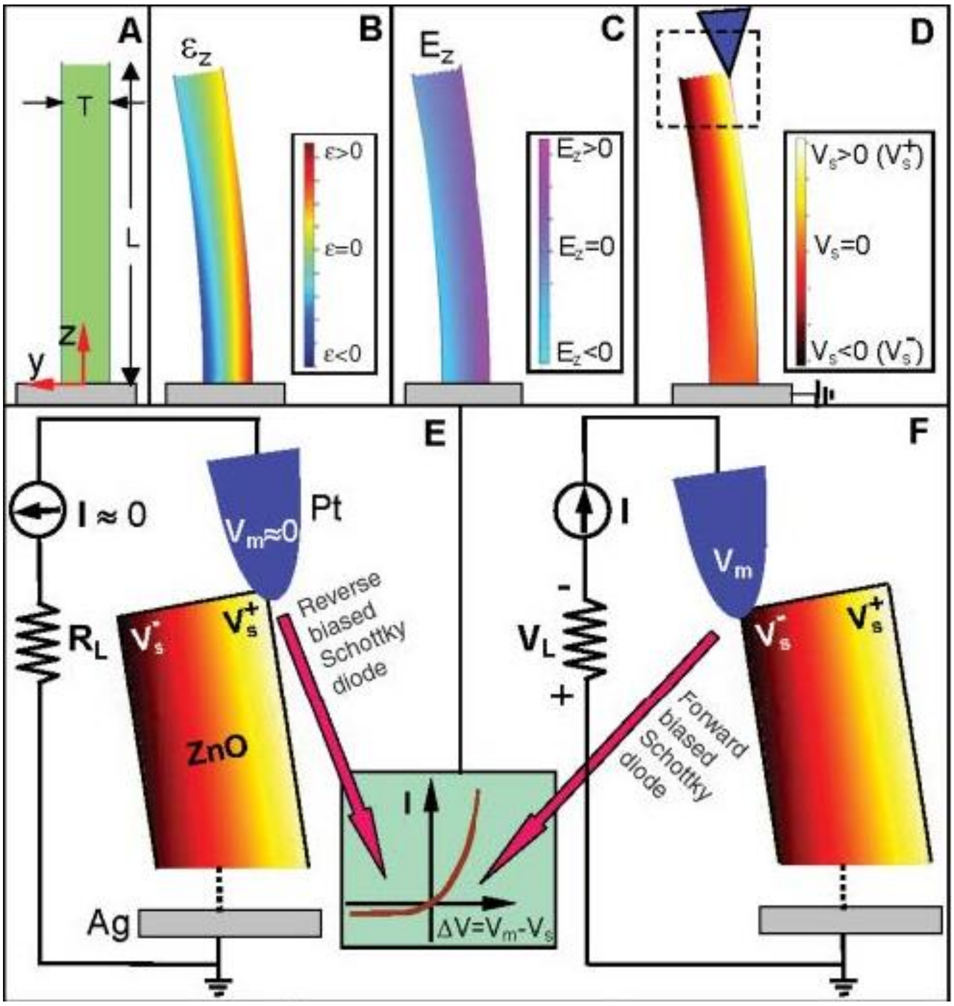

Figure 2-15: Charge transport governed by a metal-semiconductor Schottky barrier for the piezoelectric ZnO nanorod. (A) Schematic definition of a nanorod and the coordination system. (B) Longitudinal strain ε_z distribution in the nanorod after being deflected by an AFM tip from the side. (C) The corresponding longitudinal piezo-induced electric field E_z distribution in the nanorod. (D) Potential distribution in the nanorod as a result of the piezoelectric effect. (E and F) Contacts between the AFM tip and the semiconductor ZnO nanorod at two reversed local contact potentials (positive and negative), showing reverse- and forward-biased Schottky rectifying behaviour respectively[18].

This oppositely biased Schottky barrier across the nanorod preserves the piezoelectric charges and later produces the discharge output. The inset in Figure 2-15 shows a typical current-voltage relation characteristic of a metal-semiconductor (n-type) Schottky barrier. The process in (E) is to separate and maintain the charges as well as build up the potential. The process in (F) is to discharge the potential and generates electric current.

Although measurements of output from single strained ZnO nanorod has proven feasible, for useful applications it is necessary to collect power from an array of nanorods[27]. Wang suggested that by judging from the power conversion efficiency of individual nanorod and the density of nanorods, it is possible to power a single nanorod-based electronic device using a nanorod array with size 10 x 10 μm^2 [26]. Later in 2007, Gao *et al.* demonstrated a nanogenerator design based on an array of ZnO nanorods based on flexible plastic substrate. The weak bonding between the end of ZnO and the flexible substrate was improved by encapsulating a thin layer of spin-coated poly(methyl methacrylate) (PMMA) insulating polymer. AFM was used to confirm the improved stability from the application of PMMA layer as well as demonstrating the arrays of ZnO nanorods grown on flexible plastic substrates can be used to convert mechanical energy into electrical energy[71].

It was also suggested that using ZnO array on polymer substrate has a number of advantages[71]:

1) The nanorod-based nanogenerator can be subjected to extremely large deformations. This opens up the possibility to fabricate flexible power sources.
2) The large degree of deformation from nanorods has higher possibility to generate a larger volume density of power output.
3) ZnO is biocompatible comparing to traditional piezoelectric materials such as PZT.
4) The flexibility of the polymer substrate used makes it feasible to accommodate the flexibility of human muscles thus can be used for wearable technologies.
5) ZnO nanorod-based nanogenerator can directly produce current due to their

enhanced conductivity in the presence of oxygen vacancies.

Early research has demonstrated using AFM that strained ZnO nanorods can convert mechanical energy into electrical energy. In order to incorporate the nanorods into actual working device, other methods need to be designed to induce the mechanical strain in to the nanorods. Typical design morphology, as shown in Figure 2-16, is: ZnO nanorods act as the main part of a two-terminal electronic device; the hexagonal ZnO nanorods grown along c-axis with two ends and short segments adjacent to the ends fully embedded by electrodes; thus external stimuli force would be needed to induce the piezoelectric strain.

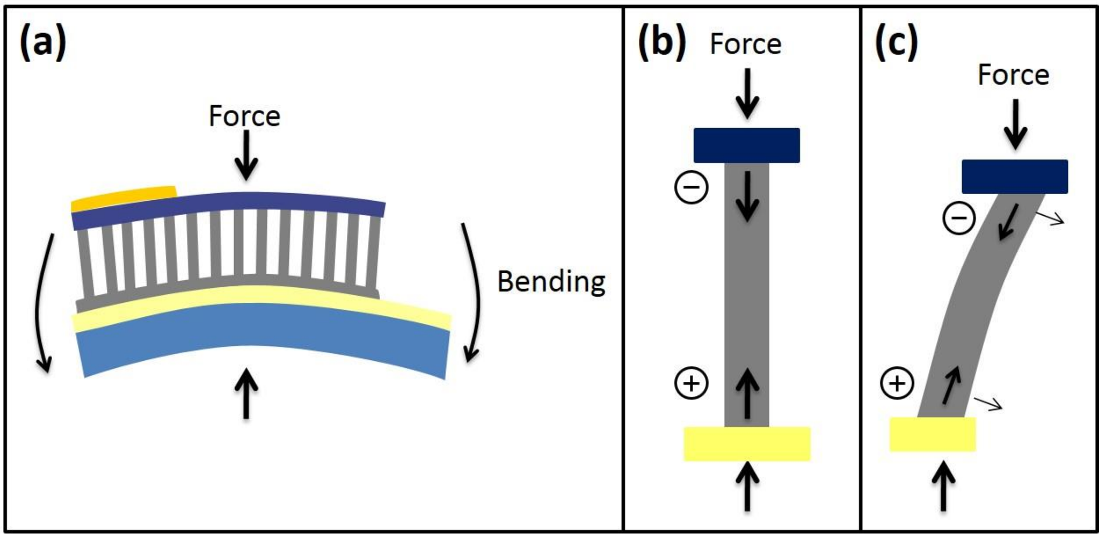

Figure 2-16: Schematic of nanogenerator design upon external force[72].

In 2007, Xudong Wang *et al.* reported a working ZnO-based energy harvester utilizing patterned, platinum-coated silicon top substrate. The ZnO nanorods were grown on rigid GaN substrate. A spacer was used to support a top electrode, which had zigzag shaped pattern in contact with the tips of the ZnO nanorods. The strain was induced by ultrasonic waves. Under the ultrasonic waves, the ZnO nanorods would oscillate while the upper ends would be bent by the sharp tips of the zigzag parts of Pt-coated Si electrode. In this way, similar to be bent by AFM tips, a current output was observed corresponding to the ultrasonic wave[71].

Another design to induce strain to the nanorods was reported by Xianying Wang *et al.*. The nanorods were filled with polymer poly-(vinyl chloride-co-vinyl acetate-co-2-hydroxypropyl acrylate) (PVC)[73]. The rods were almost fully embedded in the polymer matrix. The device was subjected to heating; the thermally expanded polymers were suggested to strain the nanorods, leading a small voltage output of 10 mV[73].

Despite the success of energy harvesting device based on ZnO nanorods on rigid substrates, higher strain was achieved by utilizing flexible substrates. As discussed above, flexible substrates were suggested to be able to subject a higher degree and quicker rate of mechanical bending, thus leading to a stronger local piezoelectric effect.

In 2009, Choi *et al.* reported a working ZnO-based nanogenerator acting as a pressure/force sensor[74]. This was the first design of NG based on a flexible substrate.

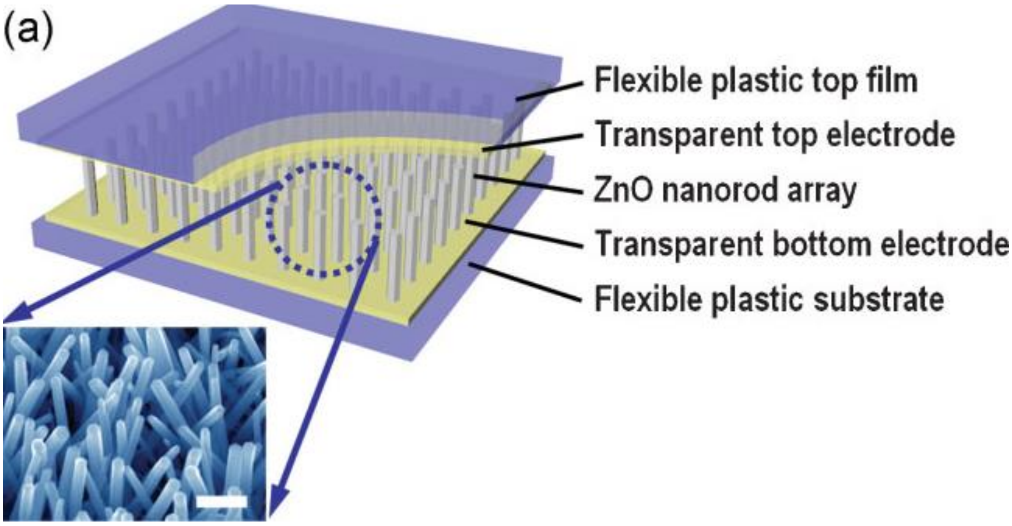

Figure 2-17: Schematic diagram of an integrated flexible nanogenerator and SEM image of ZnO nanorods on a flexible ITO/PES substrate[74]. Scale bar: 300 nm.

Both top and bottom flexible plastic substrates were ITO-coated PES and the top electrode was further decorated with Pd-Au embossed convex arrays. Even though a flexible substrate was utilized, the method to induce strain in this design was applying vertical pressure rather than bending. It was suggested that due to the randomly tilted orientation of the ZnO nanorods. Vertical pressure would be able to bend the rods thus inducing the strain. The device achieved 10 μA/cm^2 when compressed by a force of 0.9 kgf (the force close to a touch or a slight push by human finger)[74].

Minbaek Lee *et al.* reported a nanogenerator harvesting vibration energy[75]. The sandwiched structure was based on flexible Kapton substrate both for the ZnO nanorod array and Au electrode. It was suggested that due to the non-uniformity of the nanorod array synthesised via the hydrothermal method, improved number of contacts can be made when applying vertical pressure. The device achieved around 350 mV of output voltage and 125 nA/cm^2 of current density[75].

Later on, Sangmin Lee *et al.* reported a flexible nanogenerator based on ZnO nanorod and PMMA. The design was using ultra-thin aluminium foil as bottom electrodes. PMMA layer was coated both before and after the ZnO nanorod growth to form an insulating encapsulation on the nanorods. This was believed to reduce short-circuits or electric leakage between the electrodes and the ZnO nanorods due to the semi-conducting properties of ZnO[76].

Although PMMA has been commonly used in a variety of ZnO-based nanogenerator designs, it has been suggested that the insulating property and increased internal impedance of PMMA hinders the performance by lowering the current of the device. Even though it has the benefits of decreasing screening effects (detailed discussion below), increasing the voltage output, reducing short-circuits, and potentially increasing the mechanical stability of the device. The overall power is still limited due to the extremely low current.

In 2012, Briscoe *et al.* reported a p-n junction-based nanogenerator. The structure was based on ITO-coated PET polymer substrate with n-type ZnO nanorods and p-type polymer poly(3,4-ethylenedioxythiophene) poly(styrenesulfonate)

(PEDOT:PSS)[72].

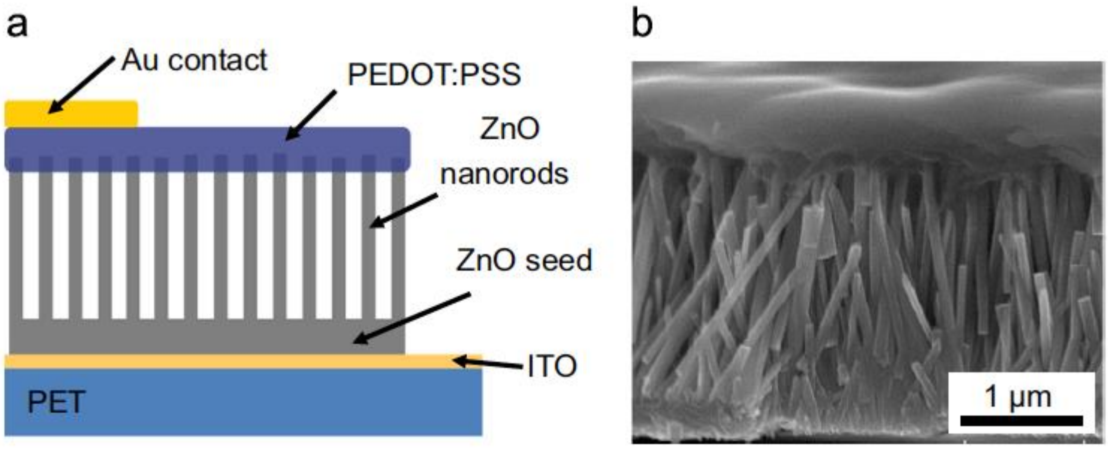

Figure 2-18: (a) Schematic and (b) SEM cross section image of the device design[72].

This design eliminated the PMMA insulating layer. Instead, a conductive p-type hole transport material PEDOT:PSS was deposited. The PEDOT:PSS was acting mainly as a capping layer on the tip of the ZnO as it does not infiltrate down to the bottom of the rods, as shown in Figure 2-18, allowing high freedom of movement of the nanorod array. The flat top surface of the PEDOT:PSS coating also allows a highly conductive coating of Au electrode. This design opened up the possibilities of p-n junction-based energy harvester by achieving a power density of 125.8 nW/cm^2, which was the highest result achieved from single layer ZnO-based devices[72].

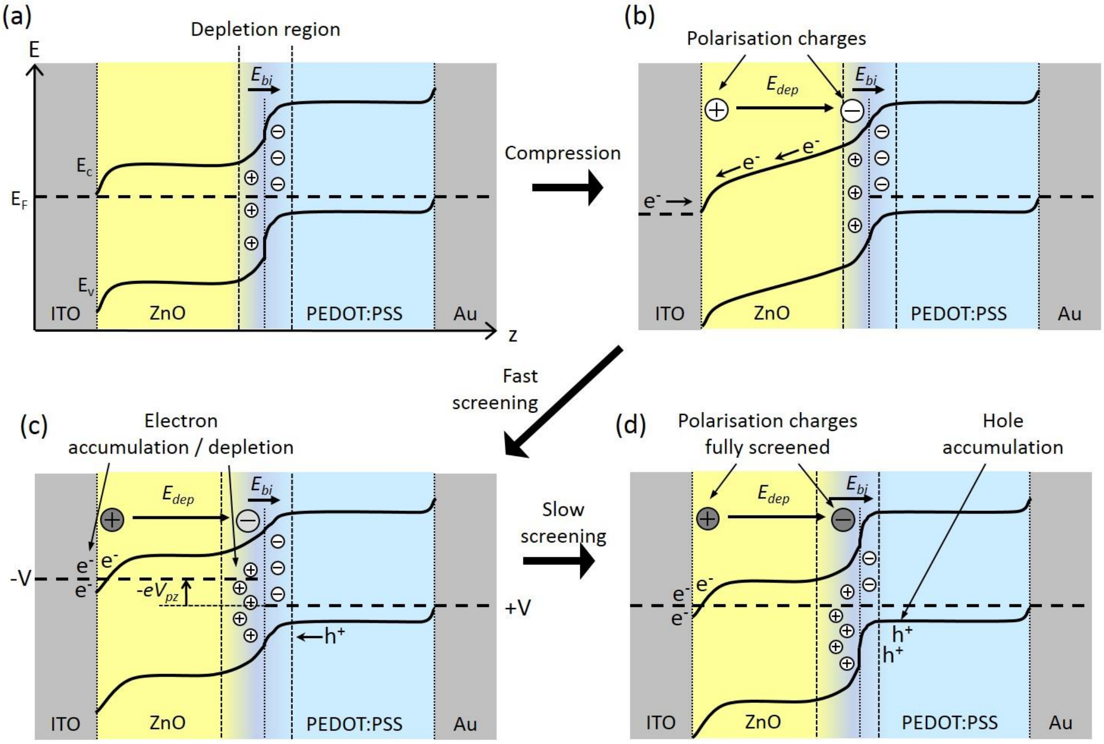

Figure 2-19: Time evolution of the energy band diagrams for a ZnO-PEDOT:PSS junction when under strain. (a) Equilibrium before strain occurs, (b) Band diagram immediately after strain is induced, (c) Full screening of the positive polarization by the metal and partial screening of then negative polarization by internal carriers, (d) Negative polarization is fully screened by hole accumulation in the PEDOT:PSS[72].

The working principle is discussed as follow. When the polarization is induced by strain in ZnO, the depolarization field occurs E_{dep}, which leads to the movement of free carriers within the material (internal screening) or within the external contacts (external screening)[72]. The screening effect would screen the polarization and reduce the E_{dep} field down to zero. As discussed previously, the E_{dep} needs to be preserved long enough to be able to measure.

When strained, polarization charges develop at the surface as in Figure 2-19a. The developed charges accumulate to form the E_{dep}, which acts as the driven force to the movement of the screening charges both internally and externally[72]. At the external ITO contact shown in (b), the positive polarization charges can be screened by the free electrons within the ITO. This process has been suggested to happen in a short time scale due to the abundant and high mobility of carriers at the interface[77]. As discussed before, this is the reason that a Shottky contact is required for the design of nanogenerator, as Ohmic contact would lead to a rapid external screening effect so that E_{dep} does not develop, hence no external voltage can be measured.

The rapid rearrangement of internal carriers would also be induced within the ZnO crystal structure. This confines the band bending to the surfaces shown in (c). The speed of this screening is described using the equation for carrier drift velocity:

$$v_{dr} = \mu E$$

Equation 2-30

Where μ is the carrier mobility and E is the electric field experienced by the carriers[78]. The normal rate of the rearrangement is on an order of hundreds of nanoseconds. This internal screening process is still quicker than the time required to take output measurement. The internal screening also depletes electrons from the negatively polarised surface, partially screening it[72]. The free carriers of low density in the ZnO crystal could not achieve full screening, thus an electric field is still present and can be measured externally.

It has been shown that external screening at the contact and internal screening by free carriers occur extremely rapidly. This leads to the situation in (c), the polarization at the ITO contact are fully screened whereas the polarization with in the ZnO is incompletely screened due to the low carrier concentration in ZnO.

It is suggested that the screening process of polarization by PEDOT:PSS is slower due to lowered density and mobility of carriers. Carrier density in PEDOT:PSS is around 10^{19} cm^{-3} [72] comparing to 1.3 x 10^{17} cm^{-3} in ZnO[79]. Mobility in PEDOT:PSS is however around 3 times lower than ZnO (1.2 $cm^2V^{-1}s^{-1}$), meaning the carrier will take longer to reach the junction[80]. Furthermore, a p-n junction or Schottky contact contains a depletion region with an in-built electric field E_{bi}[78]. Upon the negative polarization at the ZnO/PEDOT:PSS interface, E_{bi} will further reduce the strength of the electric field experienced by the carriers in PEDOT:PSS[72].

This then slows the screening sufficiently (around ns to ms) for a voltage to be generated and measured.

Performance of devices based on this design was further improved by passivation of ZnO nanorods[81,82]. It is well known that ZnO has intrinsic surface donor defects such as oxygen vacancies and zinc interstitials. Externally, interaction with moisture in air would also cause surface hydroxyl OH^- ions which are considered as donor species. These defect states would reduce the piezoelectric voltage by screening the polarization charges[81]. Therefore, surface modification techniques were proposed to suppress the defects. Passivation was achieved by applying a thin layer of copper thiocyanate (CuSCN) coating on the outer side of the rods. It was suggested that surface passivation reduces the parasitic activity of surface defects which causes a decrease in defect-induced carrier density in ZnO[81]. Impedance measurement showed that the passivation improved the internal resistance. Finally the increase in charge storage in the piezoelectric device and decrease in screening rate improved the power output density from 66.80 to 303.39 μWcm^{-2} [81].

2.5.4 Hybrid energy harvesters

As discussed in Section 1.4, a variety of energy harvesting technologies have been developed such as photovoltaic, thermoelectric, and piezoelectric for converting solar, heat, and mechanical energies into electricity. In most environments, multiple forms of energies coexist simultaneously. Thus it has been of great interest to develop hybrid energy harvesters, which can scavenge two or more forms of energy simultaneously using a single device.

Traditionally, photovoltaics have been considered as the dominant renewable energy harvesting technology due to the high efficiency and abundant energy source.

In reality, most solar cells are not operating under full sun illumination due to geographic distributions. Also, the majority of electronic devices operate indoors where sunlight is insufficient. Solar cells cannot achieve the optimal performance indoors. Equivalently, a nanogenerator generates electricity when it is subjected to mechanical vibration, bending or similar stimuli. It will remain dormant in the absence of mechanical energy, the same as photovoltaic in absence of sufficient illumination. Therefore, it has been proposed that a hybrid energy harvester scavenging solar and mechanical energy would be desired. Such device would benefit in areas where both sunlight and mechanical energy coexist simultaneously. Xu *et al.* presented the first concept of hybrid energy harvester in 2009 which was a hybrid cell (HC) based on ZnO nanorods for harvesting solar and mechanical energies[83].

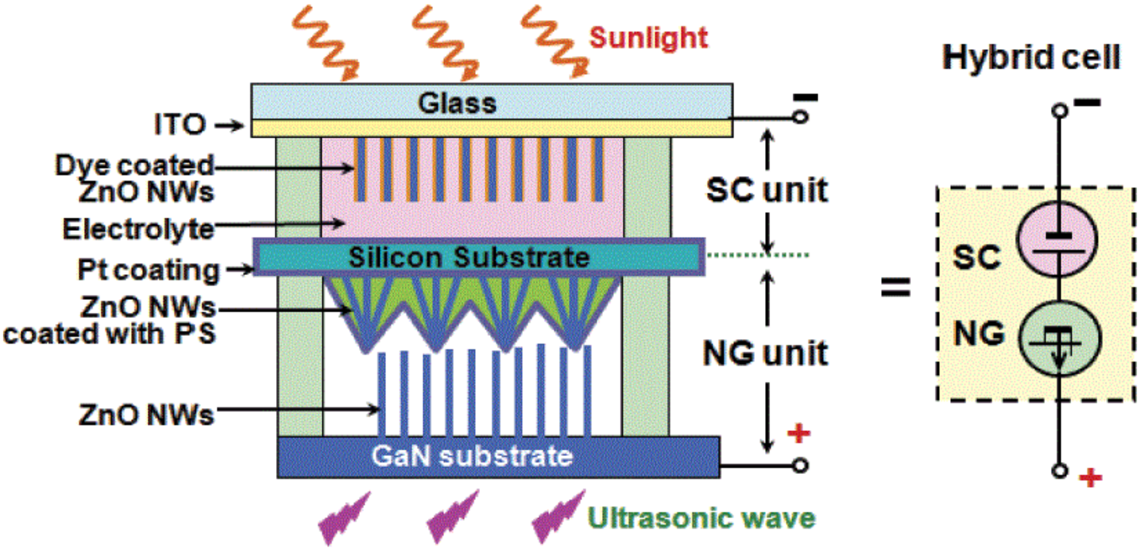

Figure 2-20: The design of HC composed of a serially integrated solar cell and nanogenerator[83].

It can be seen from the schematic of the design shown in Figure 2-20 that the solar cell and nanogenerator share a mutual substrate of silicon. Ultrasonic waves were used here to introduce the piezoelectric effect. It was reported that the output voltage of the device under sunlight differed by 9 mV with or without the application of ultrasonic wave. This indicates the cell was performing as a hybrid energy harvester[83]. However, the liquid-state electrolyte here caused leakage and reduced the stability of the device.

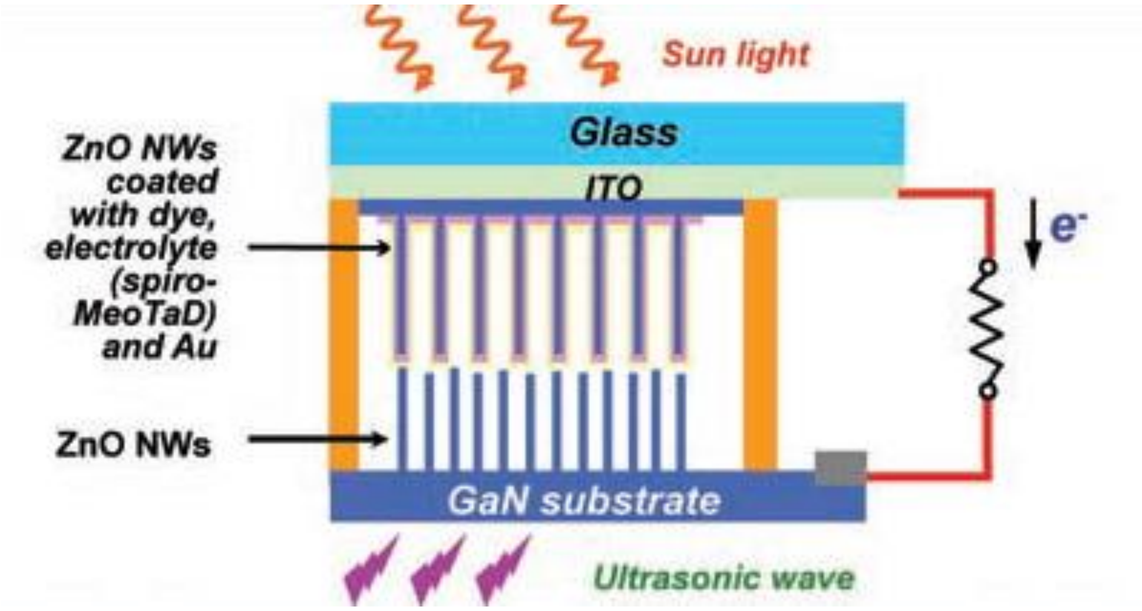

Figure 2-21: Design of HEH based on solid-state solar cell and nanogenerator[84].

Later, Xu *et al.* improved the design by using a solid-state DSSC instead of liquid-state DSSC[84] as shown in Figure 2-21. They reported that a 6% increase was found in optimum power by incorporating the contribution of the nanogenerator. However, this structure was still complicated to fabricate. The SSDSSC and NG had to be fabricated separately on different substrates. Also the two sets of nanorods had to be stacked face-to-face, allowing the gold coated electrode from SSDSSC to mechanically trigger the nanorods located on GaN substrate. The control of distance in-between and the assembly of the whole device require extreme care.

Choi *et al.* presented a design based on a flexible substrate. It could harvest solar energy and act as a touch-sensitive piezoelectric power generator[85]. A ZnO film was utilized to act as both the electron transport layer for the solar cell and the active layer for the formation of a piezoelectric potential. Later they reported another design using ZnO nanorods. The design featured piezoelectric ZnO in conjunction with an organic solar cell. ZnO remained the key factor here due to its intrinsic coupled piezoelectric and semiconducting properties[86]. It is also the first design utilizing intrinsically hybrid structure without additional stacked structures to be connected, shown in Figure 2-22 below.

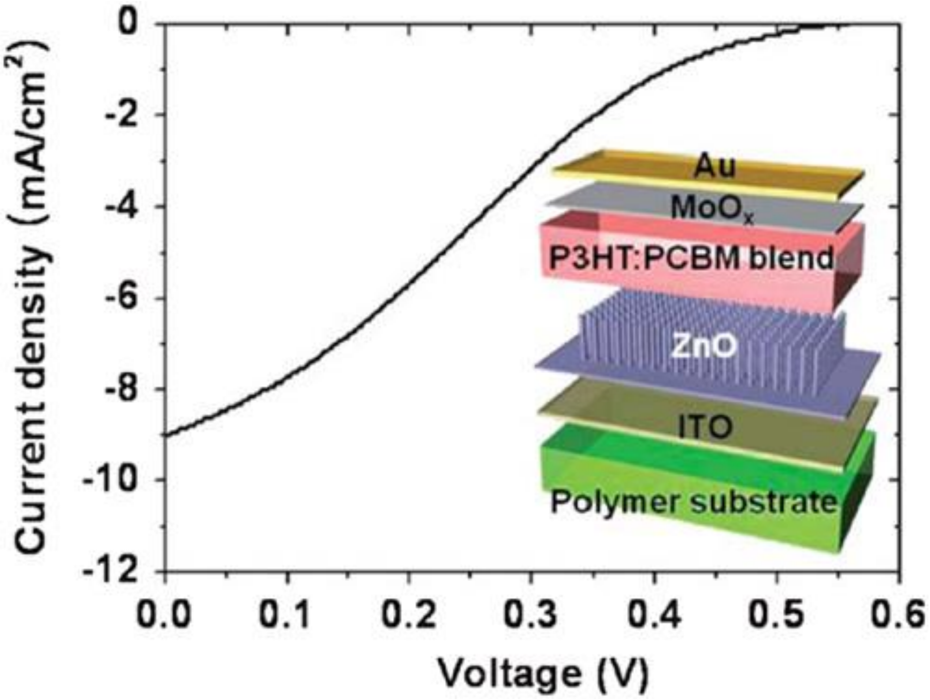

Figure 2-22: Design of naturally hybrid energy harvester. *J-V* curve is taken under AM1.5 illumination[86].

Using the solar cell part, this design achieved 1.5% of efficiency, 0.55 V of V_{oc} and 9.2 mA/cm^2 of J_{sc}. When the device was working normally under illumination, it performed solely as an organic solar cell. When subjected to mechanical strain such as vibration and bending, the piezoelectric output signal was added to the overall output signal, indicating the instantaneous piezoelectric effect within the device, shown in Figure 2-23.

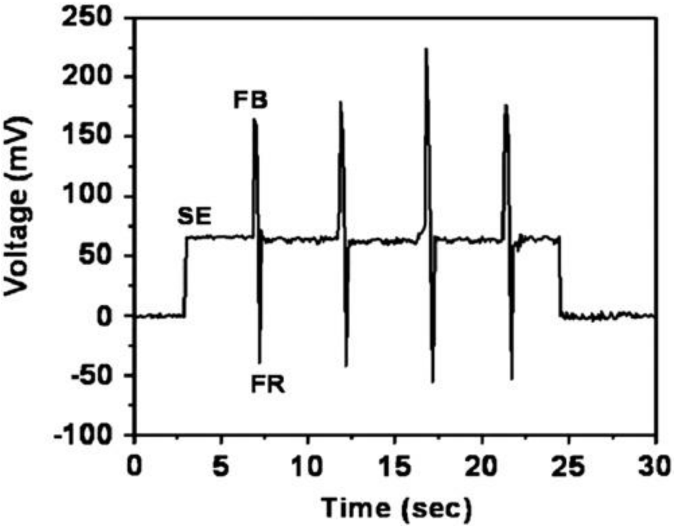

Figure 2-23: The hybrid energy harvesting upon illumination and dynamic mechanical stimuli[86]. SE indicates solar energy harvesting process, FB indicates fast bending process, FR indicates fast release.

It was reported that the piezoelectric response depends on the degree of strain and rate of strain. By varying the strain parameters, the piezoelectric output voltage ranged from several tens of mV up to 150 mV, and the output current was several hundreds of nA, as shown in Figure 2-23. This work is a successful demonstration of a dual-mode scavenging energy generator that harvests both solar and mechanical energies.

In 2013, Shoaee *et al.* reported acoustic enhancement of polymer/ZnO nanorod photovoltaic device performance[87]. It was suggested that the enhancement originates from a reduction in the charge carrier recombination caused by alternating electric field at the surface of ZnO due to its piezoelectric effect[87]. This discovery opened up the potential of applying photovoltaic devices onto the environments with both sunlight and mechanical vibration present, such as air-conditioning units on roofs, top of vehicles and defence applications in order to improve their efficiency, rather than only relying on the separate or simultaneous harvesting of solar and mechanical energy.

The established methodology to harvest solar and mechanical energies such as vibration, wind, body motion etc., opened up the possibility to design a novel hybrid energy harvester that can be integrated into flexible electronics. The potential applications include defence, vehicles, environmental monitoring, remote wireless sensor, wearables etc.[88]. Micro/nano-systems can work under variable environments and conditions, where relying on single type of energy would not meet the demand. It is highly desired to develop hybrid energy harvesters, which can conjunctionally convert multiple types of energy into electricity.

2.6 ZnO, TiO_2 and core-shell structure

2.6.1 ZnO

2.6.1.1 Materials and properties:

The wide range of useful properties exhibited by ZnO has been under research for a long time. Novel applications can be achieved from the unique proprieties. A number of the properties are shown below.

1) Direct, wide band gap. The band gap of ZnO is 3.44 eV at low temperature and 3.37 eV at room temperature[89].
2) Large exciton binding energy of 60 meV enabling application in optical devices[24].
3) High electron mobility. Highest reported room-temperature electron mobility of bulk ZnO single crystal grown by vapour-phase transport method is reported to be 205 $cm^2 V^{-1}s^{-1}$ with a carrier concentration of 6×10^{16} cm^{-3} [90].
4) Large piezoelectric constants. The low symmetry of the wurtzite crystal structure combined with a large electromechanical coupling in ZnO makes ZnO

a promising candidate in piezoelectric and pyroelectric applications[89].

5) Strong luminescence. The n-type conductivity of ZnO makes it interesting for applications such as vacuum fluorescent displays and field emission displays[89].
6) Strong sensitivity of surface conductivity to the presence of adsorbed species. As the conductivity of ZnO thin film changes with the surface state, it is possible to use ZnO as gas sensors[91]. Doped ZnO with altered surface can detect targeted gases such as ethanol[92].
7) Strong non-linear resistance of polycrystalline ZnO. The grain boundaries induced non-linear resistance behaviour makes ZnO a candidate in commercial varistors[93].
8) Large non-linear optical coefficients in the application of integrated optical devices[94].
9) High thermal conductivity makes it useful as additives[89].
10) Availability of various nanostructures as shown in Figure 2-24. One of the most attractive features of ZnO is that ZnO has various nanoscale morphologies including nanowires/rods, nanosheets, nanotubes, nanocombs, nanorings, handsprings, nanobows, nanobelts, nanocages, nanoflowers, nanoneedles, nanocandles, nanodisks, nanonuts, microstars and microballs[24,25,95]. The unique nanostructures demonstrate that ZnO probably has the richest family of nanostructures among all materials both in structures and properties. The variety of nanostructure would lead to novel structure designs and unconventional materials properties.
11) Availability in large single crystals via various synthesis routes, which will be discussed below.

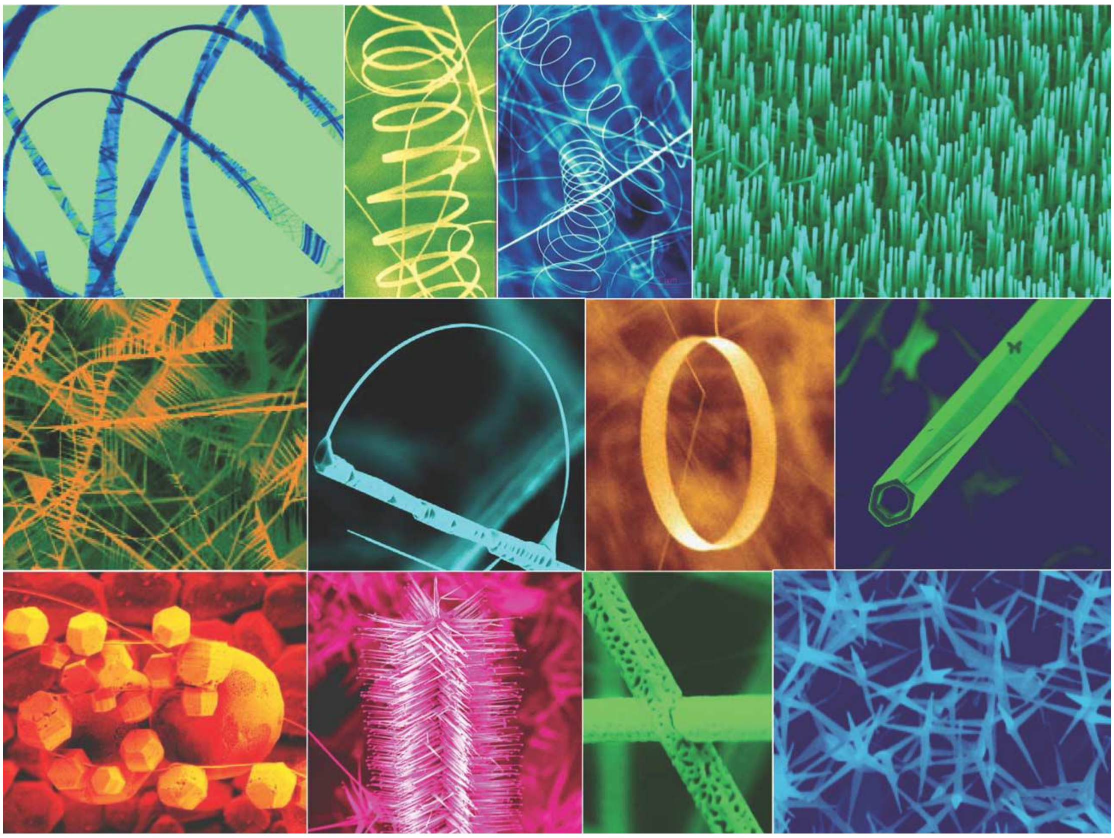

Figure 2-24: A collection of various ZnO nanostructures[25].

As discussed in previous sections on ZnO-based solar cells (Section 2.4) and nanogenerators (Section 2.5.3), the favoured morphology in these two specific applications is 1D nanowire/rod structure arrays as it provides not only larger surface area but also direct pathway for electron transport.

2.6.1.2 Growth methods:

Several methods have been reported to produce ZnO nanostructures. These include: chemical bath deposition (CBD)[96,97], chemical vapour deposition (CVD)[98], sputter deposition[99], thermal evaporation of zinc powders[100], ion beam assisted deposition[101], template-assisted growth[102], etc.

Among all the growth methods, chemical bath deposition method is chosen in this project for the following reasons.

1) The method is well established in the literature and proven to be reliable.
2) It requires low energy input and low cost due to low temperature processing and inexpensive precursors.
3) This method has been used in our laboratory to grow ZnO nanostructure on transparent substrates.
4) Parameters of synthesis can be controlled to tune the resulted morphology of the ZnO nanostructure.

Vayssieres *et al.* first introduced the aqueous solution-based CBD method in 2001[96]. The as-grown ZnO micro-rods were formed from an aqueous solution containing zinc salt at low temperature on different substrates. In this method, substrates such as FTO, silicon wafer and ITO coated polyester were used directly without a seed layer. It was suggested that the weak bonding between ZnO and the substrate makes the structure vulnerable and easy to fall off. In 2002, Tian *et al.* first introduced a seeding method by adding a thin layer of ZnO nanoparticles prior to nanorod growth[103]. Lori E. Greene *et al.* further improved the seeding method and demonstrated improved stability[104]. The seed layer is normally deposited by wetting the substrate with adequate amount of zinc acetate/ethanol solution. The substrate is then rinsed with additional ethanol to facilitate an even coverage then dried using N_2 flow. This process is normally repeated and the substrate is then subjected to thermal annealing at 350 °C in air. The thermal decomposition process produces a thin layer of ZnO nanoparticles acting as a seed layer in the following growth of ZnO nanorods. The substrate is then placed face-down and suspended in a glass jar with growth solutions. The solution consists of an equimolar aqueous solution of zinc nitrate ($Zn(NO_3)_2 \bullet 4H_2O$) and hexamethylenetetramine (HMT). The jar is then placed in a regular oven and kept at 75-95 °C for a fixed period time from 2.5-24 h. Prolonged time leads to elongated nanorods. Upon heating, both homogenous (in the solution) and heterogeneous (on the surface of the substrate) precipitation of ZnO occurs and ceases at a stage (depleted) depending on the initial concentration of the solution and reaction time. For a 0.025 M equimolar solution, the reaction was reported to cease after 2.5h at 90 °C[47].

The possible growth mechanism of ZnO is explained by the controlled precipitation of ZnO from Zn precursor via hydrolysis[105]. The main role of HMT here is to provide a controlled supply of hydroxide ions (OH^-). HMT gradually decomposes to form ammonia and formaldehyde upon heating. The ammonia forms NH_4^+ and OH^- through hydrolysis. Then the Zn^{2+} from zinc nitrate solution will react with OH^- to form ZnO along with ammonia and water. The suggested reaction scheme is shown as follows[23]:

$$(CH_2)_6N_4 + 6H_2O \leftrightarrow 6HCHO + 4NH_3$$

Equation 2-31

$$NH_3 + H_2O \leftrightarrow NH_4^+ + OH^-$$

Equation 2-32

$$2OH^- + Zn^{2+} \rightarrow ZnO(s) + H_2O$$

Equation 2-33

The growth of the ZnO nanorods is influenced by:

1) Seed layer as the layers determine the direction and alignment of the arrays as well as the dimensions of the nanorods[104]. It is suggested that a denser film with aligned crystal orientation leads to dense and well-aligned nanorod arrays. This is ideal to increase the surface area and improve electron transport process. The morphology of ZnO nanorods is strongly influenced by the thickness of the seed

layer and the corresponding crystal size. A thinner ZnO seed layer provides a higher surface area of ZnO nanorods because of the smaller crystal size of the seed layer. The orientation of the ZnO seed layer significantly affects the crystal structure of the rods[106].

2) Initial concentration of the precursors. After the depleted stage is reached, further growth can be obtained by placing the substrate into a new jar with fresh solutions. It is suggested that the width of ZnO rods can be reduced from 1000-2000 nm down to 100-200 nm by lowering the overall concentration of the precursors while keeping the ratio of Zn^{2+} to amine constant at 1:1[96].
3) Temperature of heating. When the growth temperature is decreased from 95 to 60 °C, the average diameter of the ZnO nanorods decreased from 65 to 30 nm, correspondingly[107]. Also the length can increase from 240 to 850, 1100 and 1900 nm when the temperature increased from 40 to 60, 80 and 95 °C[107]. This implies that the growth rate along [001] direction is sensitive to the temperature.
4) Other parameters including pre-treating and annealing methods on the substrate, sealing of the jar, pre-treatment on the precursor solution etc.[108].

In summary, the growth of the ZnO nanorods is extremely sensitive and is affected by a variety of parameters. In order to achieve a reliable ZnO film, care must be taken during each step of the synthesis.

2.6.2 TiO_2

TiO_2 has undergone extensive research and remains the most dominant candidate for the n-type light-harvesting electrode in the applications of solar cells since the pioneering work of Fujishima and Honda in 1972[60].

TiO_2 has a wide band gap, high stability and inexpensive manufacture resources. It has three widely known polymorphs: tetragonal rutile, anatase and orthorhombic brookite. Among these, anatase is preferred structure for the use of dye-sensitized solar cells due to the large band gap (3.2 eV)[28]. Various nanostructures of TiO_2 have been achieved such as nanoparticles, nanorods, nanowires, nanobowls, nanosheets and nanotubes[28].

A number of synthesis routes have been reported for TiO_2 such as sol-gel, micelle and inverse micelle, hydrothermal, solvothermal, sonochemical, microwave deposition techniques, direct oxidation, chemical vapour deposition, physical vapour deposition and electrodeposition[28]. The most common technique for preparing TiO_2 nanoparticles is the hydrolysis of a titanium precursor such as titanium (IV) alkoxide with excess water catalysed by acid or base, followed by hydrothermal growth and crystallization[28]. The proposed reaction is shown below:

$$Ti(OR)_4 + 2H_2O \rightarrow TiO_2 + 4ROH$$

Equation 2-34

Where R is an alkyl, typically an ethyl, butyl or isopropyl group.

Benefiting from the high collection efficiencies for photo injected electrons and an impressively long electron diffusion length on the order of 100 μm, relatively thick TiO_2 films can be prepared leading to improved light-harvesting efficiency[109]. Thus, with new materials such as ZnO being investigated as promising substitutions for TiO_2, combination of materials with heterojunction designs was also proposed to design and fabricate photo anode in solar cell applications.

2.6.3 Core-shell structure

Traditionally, TiO_2 mainly act as the mesoporous electron transport layer in DSSCs. In 1991, Kavan *et al.* firstly demonstrated an extra anatase TiO_2 film deposited on existing P-25 mesoporous layer using anodic oxidative hydrolysis of $TiCl_4$ [60].

The resulting improved dye loading and photocurrents were attributed to the roughened surface with increased surface area[60]. This was the first successful demonstration of modification on photo anode and can actually be considered as TiO_2/TiO_2 core-shell structure, as shown in Figure 2-25.

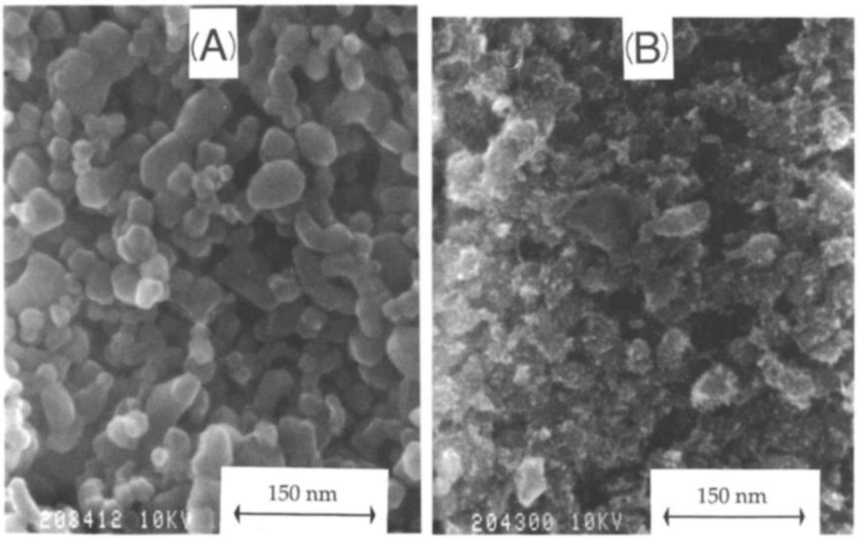

Figure 2-25: SEM images of (A) Naked P-25 film, and (B) After electrodeposition of extra TiO_2 film [60].

In 2005, O'Regan *et al.* demonstrated an Al_2O_3 barrier layer coating on a TiO_2/dye/CuSCN solid-state solar cell[110]. It was reported that Al_2O_3 treated cells show improved open-circuit voltages and fill factors but lower short-circuit currents. The Al_2O_3 layer was considered to act as a tunnel barrier, suppressing the recombination rate hence improving the photo voltage[110]. This was a further demonstration that the possible novel design methodology such as decorating the n-type photo anode by applying outer shell structure.

In 2006, Law *et al.* reported enhanced DSSCs based on ZnO/Al_2O_3 and ZnO/TiO_2 core-shell structures. The as-grown ZnO nanowires had a length of 15 μm and 150 nm in diameter. Atomic layer deposition was used to deposit a thin shell of amorphous Al_2O_3 and anatase TiO_2. It was reported that the insulating Al_2O_3 shell increased the open-circuit voltage, but decreased the short-circuit current[14]. For

TiO_2 shells, an optimal 10-25 nm in thickness increased both photo voltage and fill factor, enhancing the performance up to 2.25%[14] (compared to the record PCE of 1.5% of pure ZnO-based DSSC[47]). It was suggested that the application of shell would decrease the recombination rate possibly due to the passivation of surface recombination sites and build-up of a radial energy barrier that repels electrons from the nanowire to recombine[14]. Lori E. Greene *et al.* reported a solid-state DSSC based on ZnO/TiO_2 core-shell nanorod/P3HT[111]. Short rods were used (150-225 nm in length and 15-25 nm in diameter). Again, atomic layer deposition was used to deposit the TiO_2; the resulting device achieved 0.29% efficiency[111].

So far the deposition method for the extra shell layer has mainly been atomic layer deposition (ALD). Although the ALD method provides precise control of the thickness and quality of the film, it is time consuming and uneconomical.

In 2011, Qiu *et al.* reported a facile route to synthesis aligned TiO_2 nanotube arrays for dye-sensitized solar cells[112]. The original design was applying a thin outer shell layer on the template ZnO nanorods to form the ZnO/TiO_2 core-shell structure. The inner core was later removed by selective wet chemical etching in a dilute aqueous solution of HCl (1%) or $TiCl_4$ (15 mM) for 2h[112]. Thus, it provided a simple method of applying the core-shell structure.

2.7 Summary

To sum up, facing the energy crisis, a number of technologies have been developed to harvest renewable energy. Among them, solar cells and piezoelectric energy harvesters (such as nanogenerators), targeting solar and mechanical energy have been demonstrated. For solar cells, the working principle is generating and separating excited carriers upon the illumination of incident light; lack of sunlight would render the devices dormant. Similarly for nanogenerators, lack of mechanical stimuli would also result no energy harvesting effect. Under most situations, light and mechanical energies coexist simultaneously, thus, it would be beneficial to use a hybrid approach to design a hybrid energy harvester that could scavenge both solar and mechanical energy simultaneously. A number of successful designs have been demonstrated. However the structures remain complex.

For solar energy harvesting techniques, in traditional crystalline silicon solar cells, typical p-n junction was used. For amorphous silicon solar cells, the structure is based on p-i-n junction. Whereas '*i*' stand for intrinsic semiconductor, which separates two heavily doped *p* and *n* regions near the contacts. The intermediate layer acts as light absorber and generates electron and hole pairs. To be more precise, the structure design could be adapted as p-a-n layers where '*a'* stands for light absorber layer. This approach was then adapted in the following solar cell designs. For the original design of dye-sensitized solar cell by Grätzel in 1991, mesoporous TiO_2 layer was used as n-type electron transport layer and dye molecules were used as the '*a*' layer for the light absorption. A redox electrolyte was used as hole transport medium. Later dye molecules were replaced using inorganic narrow band gap semiconductors such as nanoparticles or quantum dots (CdS, CdTe, CdTS etc.). Also to the more recent promising perovskite solar cells, where perovskite structure was selected to act as light absorber layer. The classic p-a-n junction design was still utilized here. The n-type materials such as TiO_2 and ZnO, p-type materials such as CuSCN, PEDOT:PSS and spiro-OMETAD have all been demonstrated in perovskite solar cells.

For mechanical energy harvesting techniques such as nanogenerators, materials such as barium titanate ($BaTiO_3$), aluminium nitride (AIN) and PZT have been demonstrated for piezoelectric energy harvesting. Since Wang's report[26] on ZnO-based piezoelectric nanogenerator in 2006, ZnO has been gaining wide attention due to the unique properties. The initial design was based on rigid substrates such as TCO and silicon wafer. Acoustic waves and vibration were used to induce strain on the rods. Later, flexible substrates based on polymer were utilized. The device can be bent to introduce larger degree of deformation and strain onto the ZnO nanorods. The material used for initial designs was mainly focused on ZnO acting as electron transport layer and origin of the piezoelectric potential. ZnO was then encapsulated with insulating PMMA and Al_2O_3 layers to finish the device. Recently, a p-n junction-based nanogenerator was reported by Briscoe *et al.* This novel design has established a new methodology for mechanical energy harvesting.

So far for designs of both solar cells and nanogenerators, improvements of the performance have been demonstrated via modifying different components within the p-a-n (p-n for NG) junction devices. Different substrates such as rigid TCO glass and flexible polymer PET were used. Different n-type materials such as TiO_2 and ZnO were selected. The morphologies (various nanostructures as well as hierarchical structures of core-shell), optical and electrical properties (passivation by CuSCN coating[81,82]) were tuned to investigate the optimal performance. For absorber layers, different materials with different band gaps have also been used. A number of p-type hole transport materials (HTM) have also been demonstrated such as liquid-state redox electrolyte and solid-state CuSCN. The combinations of each component need to be specifically designed considering principle band gap alignments, practical ease of material manufacture processes and assembly.

Here, after comparison of literature on both p-a-n junction-based solar cells and p-n junction-based nanogenerators, it is noted that both technologies can be fabricated using flexible substrates (ITO/PET), ZnO as n-type ETL and CuSCN as p-type HTL. The only difference would be the ‘a’ layer which exists in solar cell device but not involved in p-n junction nanogenerators. Hence, the question arises that whether the NG device would also work as a solar cell if suitable ‘a’ layer material is inserted between p-n junctions.

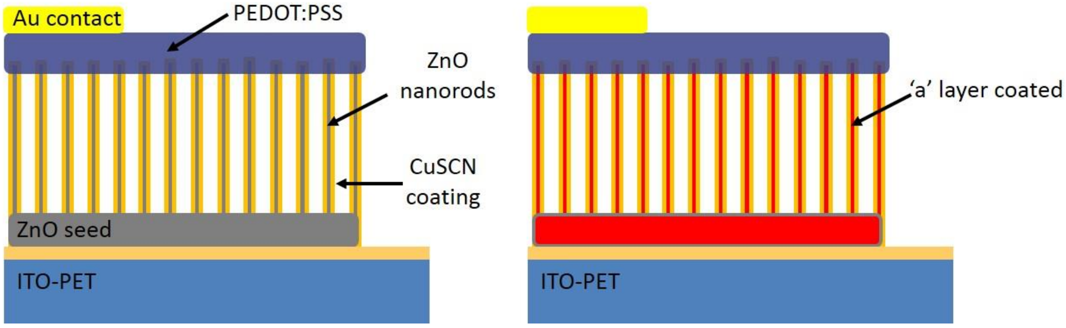

Figure 2-26: Proposed design with 'a' layer inserted between p-n junction of a nanogenerator. Image on the left is the original NG design reported by Jalali *et al.*[82]. The image on the right is proposed design with addition of Di-tetrabutylammonium *cis*-bis(isothiocyanato)bis(2,2′-bipyridyl-4,4′-dicarboxylato)ruthenium(II) (commonly noted as N719) dye coating.

A proposed design is shown in Figure 2-26, here N719 dye is selected as light absorber layer. From the image on the left, the structure is (from bottom): flexible ITO-PET, ZnO seed, ZnO nanorods (piezoelectric potential provider), CuSCN (for passivation), PEDOT:PSS (flexible hole transport layer) and top gold contact. From image on the right, the proposed design is (from bottom): flexible ITO-PET, ZnO seed, ZnO nanorods (piezoelectric potential provider as well as electron transport layer), N719 dye coating (light absorber layer), CuSCN (hole transport layer), PEDOT:PSS (flexible hole transport layer) and top gold contact.

Based on this design approach, detailed structure design, materials and device performance characterization will be discussed in Chapter 5 and Chapter 6.

Chapter 3 Experimental methods

This chapter presents schematic methodologies of fabricating dye-sensitized solar cells, perovskite solar cells, nanogenerators and the corresponding hybrid energy harvester. The p-a-n structure described at the end of the Chapter 2 (where 'a' is the light absorber) is utilized in all the devices; hence the experimental methods will be introduced from bottom-up covering each component, starting from substrate to n-type material, to light absorber material, to p-type material and finally to top contact deposition. The final design of DSSC, PSC, nanogenerator and hybrid energy harvester will be constructed with a cautious selection from choices of each component.

3.1 Substrate engineering

In this project, available substrates are listed below:

Table 3-1: Substrates utilized in this project.

Name	Acronym	Supplier	Flexibility	Resistivity (ohm/sq)	Transmission rate (%)	Notes
Fluorine tin oxide glass	FTO	Solaronix	Rigid	15	80	Use as received
Indium tin oxide coated PET	ITO-PET	Sigma Aldrich	Flexible (120 °C annealing limit)	60	80	Seed layer deposited by spraying or sputtering
Corning® willow™ glass	CW	MTI Corporation	Flexible (800 °C annealing limit)	10	75-80	FTO sputtered by Solaronix

All the substrates here are transparent conducting substrates (CW was received as raw material and a thin layer of FTO was sputtered by Solaronix). All substrates were cleaned by soaking in acetone followed by isopropanol under ultrasonic bath (10 mins each session). As reported by Greene *et al.* [104] and Tian *et al.* [103], a thin layer of ZnO nanoparticles film acting as seed layer is essential for achieving a well-oriented ZnO nanorod array. It was reported that the seed layer plays an important role for the nanorod growth as it affects the diameter, density and orientation[106,108].

In this project, a number of seeding methods have been demonstrated and applied according to the choices of different substrates.

1) Drip seeding method.

   The first and the most traditional seeding method was sol-gel drip seeding method first reported by Greene *et al.* [104]. It involves the decomposition of zinc acetate (Sigma-Aldrich, ≥98%) to form a thin layer of ZnO nanoparticle film. The detail of the method is described as below: First of all, the substrate was cleaned in ultrasonic bath for 10 minutes in the following order (detergent, acetone then isopropanol). Seeding solution (5 mM) consisted of 0.011 g of zinc acetate dissolved in 10 ml absolute ethanol. The substrate was then placed conductive side up onto a clean wipe. The seeding solution was dripped onto the centre of the substrate using a pipette and allowed to wet the whole surface (10 s). The substrate was then 'rinsed' with pure ethanol to remove excess solution and dried with N_2 flow. The wet-rinse-dry step was repeated 5 times then the substrate was annealed at 350 °C for 25 mins. This was considered as one cycle. Three cycles were needed to achieve a uniform coverage of the seed layer.

2) Spray seeding method.

   For polymer-based PET substrate, high temperature annealing is not feasible. Thus, low temperature spray coating was used for the seed layer deposition. The ZnO nanoparticles seeding suspension was made as follows. First of all, stock (A): 2.95 g of zinc acetate was added into 125 ml methanol in a round bottom flask. The flask was then stirred at 65 °C in silicone oil. Stock (B): 1.48 g of potassium hydroxide was dissolved in 65 ml methanol. Add stock (B) into stock (A) drop wise over 15 mins during stirring. The combined stocks were then further stirred for 2.5 h at 65 °C and the suspension turned cloudy. After cooling down, the cloudy suspension was centrifuged in a centrifuge machine (4000 RPM×5 mins×3 times). The remaining solid was then mixed with 70 ml 1-butanol, 5 ml methanol and 5 ml chloroform. The final suspension was sonicated and filtered with 0.45 μm PTFE filter before deposition.

3) Hydrogel spin coating seeding method[113].

   The main process of hydrogel seeding is based on the polymerization of poly(ethylene glycol)dimethacylate (M_n=550). Methanol was used as solvent and 2,2-dimethoxy-2-phenylacetophenone was used as photo initiator. The hydrogel seeding precursor contained 40 wt.% methanol, 40 wt.% of poly(ethylene glycol)dimethacylate, 10 wt.% of 2,2-dimethoxy-2-phenylacetophenone and 10 wt.% zinc nitrate. The viscous metal-loaded organic mixture was spin coated on the conductive side of substrate at 1250 RPM for 45 s. The achieved film was then cured under a UV lamp for 3 h. The resulted polymeric film was annealed at 500 °C for 1 h.

4) Sol gel spin-coat seeding method[114].

   The precursor contained 0.1 M zinc acetate with 0.1 M 2-amino ethanol in 2-methoxyethanol. The solution was stirred for 2h and filtered with 0.45 μm PTFE filter before deposition. The substrate was wet with the precursor the spin coated at 500 RPM for 10 s then 3000 RPM for 30 s. Then it was annealed at 350 °C for 10 mins, cooled down finishing one cycle. Three cycles were required and during the third cycle, final annealing condition was 450 °C for 1 h.

3.2 N-type material deposition

ZnO nanorods and ZnO/TiO_2 core-shell structure were utilized as n-type electron transport materials.

For ZnO nanorods, aqueous chemical growth method was used. Different precursors lead to various structures and morphologies.

1) pH=6 growth method.

   Powders of zinc nitrate hexahydrate (Aldrich, 98%) and hexamethylenetetramine (HMT, Sigma-Aldrich, 99.5%) were dissolved in DI-water at higher concentration (0.25 M) to make the batch solutions. A Kilner® glass jar was filled with 200 ml DI-water. 25 ml of each reactant was measured and added into the jar, making a 250 ml growth solution with 0.025 M of zinc nitrate and HMT. The seeded substrate was taped onto a wired-sample holder using Kapton tape. The substrate was then faced down while being suspended in the middle of the solution (Figure 3-1). By facing down, ZnO nanorods could nucleate heterogeneously on the seed layer with preferential growth direction. Meanwhile the homogeneously nucleated precipitate formed in the solution would be able to settle down to the bottom of the jar without sticking to the surface of the substrate. The jar was then sealed and placed in an oven set at 90 °C. The reaction time was set from 2.5 h to 24 h. Prolonged reaction time led to longer rods. After the reaction, the substrate was then retrieved and rinsed with DI-water to remove the white precipitates. Once taken out of the sample holder, the substrate was placed on a clean wipe with nanorods facing up and dried naturally.

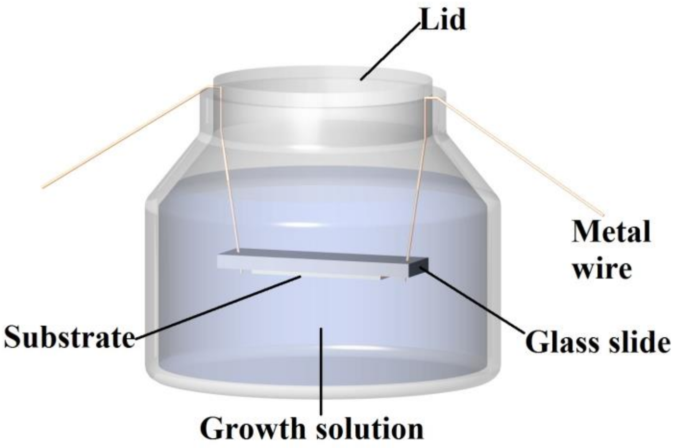

Figure 3-1: Schematic of aqueous growth of ZnO in a jar showing substrate suspended face-down from a glass slide, suspended from PTFE-coated wire.

2) High precursor concentration (0.1 M) for densely packed nanorods synthesis.

By using higher concentration of the precursors and lower temperature of the growth, nanorods with low aspect ratio can be achieved. Lateral growth would result in dense nanorods packed together forming film-like structure. The precursors were 0.1 M zinc nitrate and HMT solution. The growth temperature was 75 °C. The growth set up was same as method 1 shown in Figure 3-1.

3) Ammonia-assisted synthesis.

Homogeneous nucleation could be suppressed with excessive amount of OH^-; hence ammonium solution had been added into the growth solution to accelerate the growth speed[113]. Ammonium hydroxide solution would release extra OH^- into the solution. While homogeneous precipitation was suppressed, heterogeneous precipitation (growth of the nanorods) would be favoured. The growth solution consisted 80 ml mixture in a 100 ml glass bottle with screwed lid. The mixture consisted of: 35 ml of DI-water, 0.833 ml of HMT (2.4 M), 3.5 ml of ammonium hydroxide solution (Sigma Aldrich, 28-30%), 0.493 ml Polyethylenimine from stock (PEI, Sigma Aldrich, Mw ~800 by LS, 1g PEI diluted in 3g DI water in stock), and finally the zinc source: 0.595 g zinc nitrate dissolved in 40 ml DI-water.

Once the solution was ready, four pieces of seeded substrate were then immersed and placed vertically at the bottom of the bottle, as shown in Figure 3-2. Each substrate had the seeded side facing towards the inner wall of the bottle. The growth time was set at 5 h. After 5 h, the bottle appeared to be clean without any white precipitates. This suggested that the homogeneous nucleation was suppressed and longer rods would be achieved.

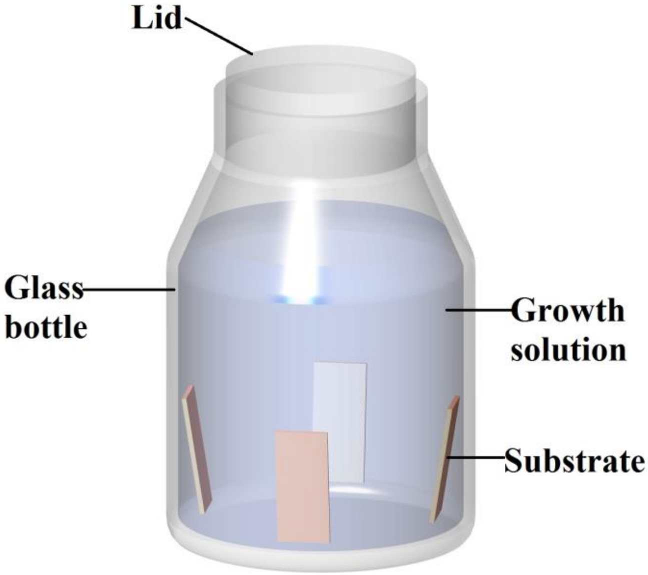

Figure 3-2: Schematic of ammonia-assisted growth set up with substrates leaning against the side of the bottle.

For the core-shell structure, a homemade 3D automatic dip-coating apparatus was designed. A rotating disc held 4 beakers containing solutions in the following sequence, TiO_2 sol, ethanol, DI water and ethanol. The layer-by-layer adsorption reaction (LBL-AR) method for the in-situ coating of TiO_2 was carried out in the following order:

One cycle consists of four steps[112], as shown in Figure 3-3:

1) Adsorption of 'Ti' species by immersing the substrate into TiO_2 sol.
2) Removal of loosely bound species by rinsing in ethanol.
3) Hydrolysis into TiO_2 coating by immersing into deionized water.
4) Dissolving excess water and weakly bound TiO_2 nanoparticles by rinsing in ethanol.

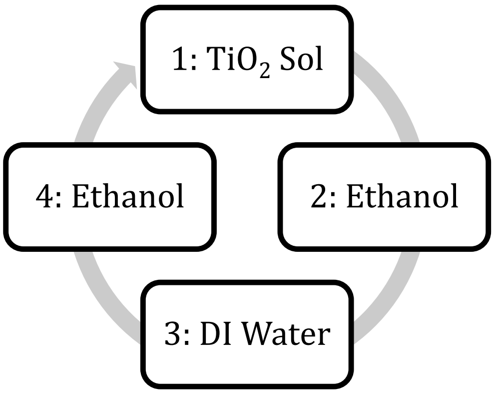

Figure 3-3: Schematic of one cycle of LBL-AR deposition of TiO_2.

The TiO_2 sol consisted of 0.5 M tetrabutyltitanate (TBT, Sigma Aldrich) and 0.5 M acetylacetone (Sigma Aldrich) in absolute ethanol. The hydroxyls were provided by DI water. Acetylacetone was used as modifying agent to inhibit unfavourable homogeneous precipitation during hydrolysis reaction and improve the stability of TiO_2 sol[112]. The achieved ZnO/TiO_2 core-shell structure was annealed at 550 °C.

3.3 Light absorber layer deposition

For the light absorber layer, two materials were selected.

1) Di-tetrabutylammonium cis-bis(isothiocyanato)bis(2,2′-bipyridyl-4,4′-dicarboxylato)ruthenium(II), commonly known as N719, was purchased from Sigma-Aldrich. 3×10^{-4} M concentration was chosen. The solvent was a mixed solution of 1:1/v:v acetonitrile (Sigma-Aldrich, anhydrous, 99.8%) and tert-butanol (Sigma-Aldrich, ≥99%).
2) Methylammonium Lead Iodide (MAPI) Perovskite. Different perovskite recipes were tested on ZnO nanorods.

   2-step sequential method: 0.462 g PbI_2 was dissolved in 1 ml of solvent containing 70% dimethylformamide (DMF, Sigma Aldrich, 99.8%) and 30% dimethyl sulfoxide (DMSO, Alfa Aesar, 99+%). In order to achieve a high quality PbI_2 solution, the PbI_2 powder was measured in a small glass vial then put inside an oven at 120 °C for 10 mins to remove moisture. The vial was then sealed and heated at 70 °C in silicon oil bath and stirred for 2 h. During this time, 0.1 g methylammonium iodide (MAI, Solaronix) was dissolved in 10 ml anhydrous isopropanol (Sigma-Aldrich, 99.5%) for further use. For the deposition, the substrate was preheated at 100 °C. PbI_2 was dripped onto the substrate using a micropipette. The spin coating recipe was 3000 RPM for 30 s. The resulted PbI_2 film was then annealed at 100 °C for 5 mins. Then the cooled substrate was wet with MAI solution and spun at 3000 RPM for 30 s. The film was finally annealed at 100 °C for 1 min.

2-step additive sequential method: in this method, 2-(Dibutylamino)ethanol (Sigma-Aldrich, 99%) was added into the precursor solution. The precursor solution consisted of 0.464 g PbI_2, 0.1 g MAI and 0.04 g additive in 1 g DMF solvent. The mixture was stirred for 10 mins at 70 °C. The substrate was preheated then was wet with the precursor. The spin coating recipe was 3000 RPM for 30 s. The resulted film was then annealed at 100 °C for 45 s. MAI solution (0.1 g MAI in 10 ml anhydrous isopropanol) was dripped on to the surface of the substrate. It was then further spun at 3000 RPM for 30 s. The achieved perovskite film was then annealed at 100 °C for 30 s.

3.4 P-type material deposition

In this project, p-type hole transport materials were selected as follows:

1) Copper(I) thiocyanate (CuSCN) (99%) was purchased from Sigma-Aldrich. It was deposited from a di-n-propyl sulfide (Alfa Aesar, 98+%) solution. 1.8246 g CuSCN powder was dissolved in 100 ml di-n-propyl sulfide, leading to a 0.15 M concentration of the solution. The solution was stirred for at least 72 h then settled for 7 days. During this time, undissolved material would settle down to the bottom of the bottle. Clean solution from the top was retrieved and filtered

with 0.45 μm PTFE filter before use.

The deposition method selected was spray coating. The substrate was taped on to the surface of a hot plate using Kapton tape. The hot plate was set at 100 °C and tilted by 45 degrees, as shown in Figure 3-4. The filtered CuSCN solution was filled in a spray gun reservoir and the spraying was performed in a scanning motion towards the surface of the substrate at approximately 15 cm distance. An appropriate amount (according to the length of the rods) of solution was sprayed (calculated by ml/cm^2). Once the spraying coating was complete. The substrate was then replaced in an oven at vacuum at 70 °C and kept overnight. This step was designed to quickly evaporate the residue solvent within the film.

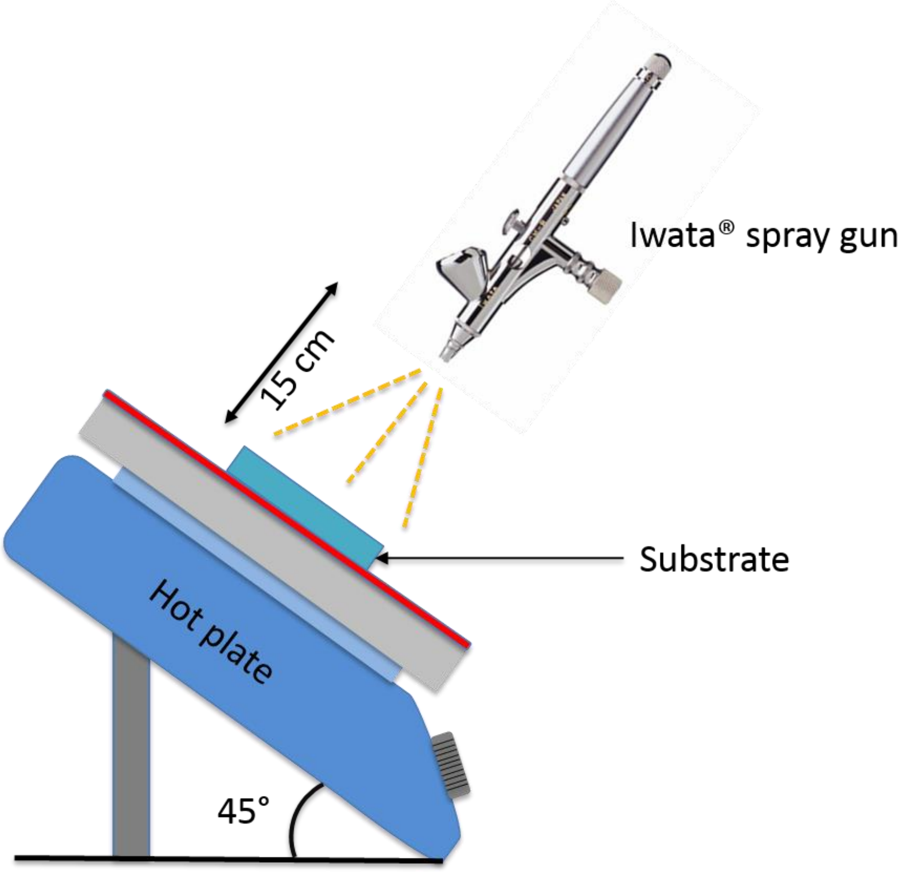

Figure 3-4: Schematic of spray coating CuSCN and PEDOT:PSS.

2) Aqueous Poly(3,4-ethylenedioxythiophene)-poly(styrenesulfonate) solution (PEDOT:PSS) was purchased from Sigma-Aldrich. Spray coating was used to

deposit aqueous PEDOT:PSS. PEDOT:PSS solution was mixed with ethyl glycol (EG) to improve the conductivity[115]. The final solution contains 5% EG. The setup of spraying coating was the same with CuSCN deposition shown in Figure 3-4.

3) Toluene-based PEDOT:PSS (Heraeus Clevios™ HTL Solar 3, 1.5-2.5 wt%) was purchased from Ossila. Spin coating was used to deposit toluene-based PEDOT:PSS. The solution was used as received. The substrate was placed onto the spin coater and wet with the toluene-based PEDOT:PSS. The spinning step was set at 3000 RPM for 30 s. The resulted film was dried at 60 °C for 60 s.

3.5 Top contact deposition

At early stage the top electrode of gold was deposited using Agar auto sputter coater. The substrate was masked and put inside of the sputter. Six run of coating was performed at 0.1 mBar pressure on the defined electrode area.

Later, high vacuum thermal evaporator was used to deposit the gold. 100 nm thicknesses gold was slowly deposited onto the surface of the substrate, resulting a controllable film with better quality.

3.6 Fabrication process for devices

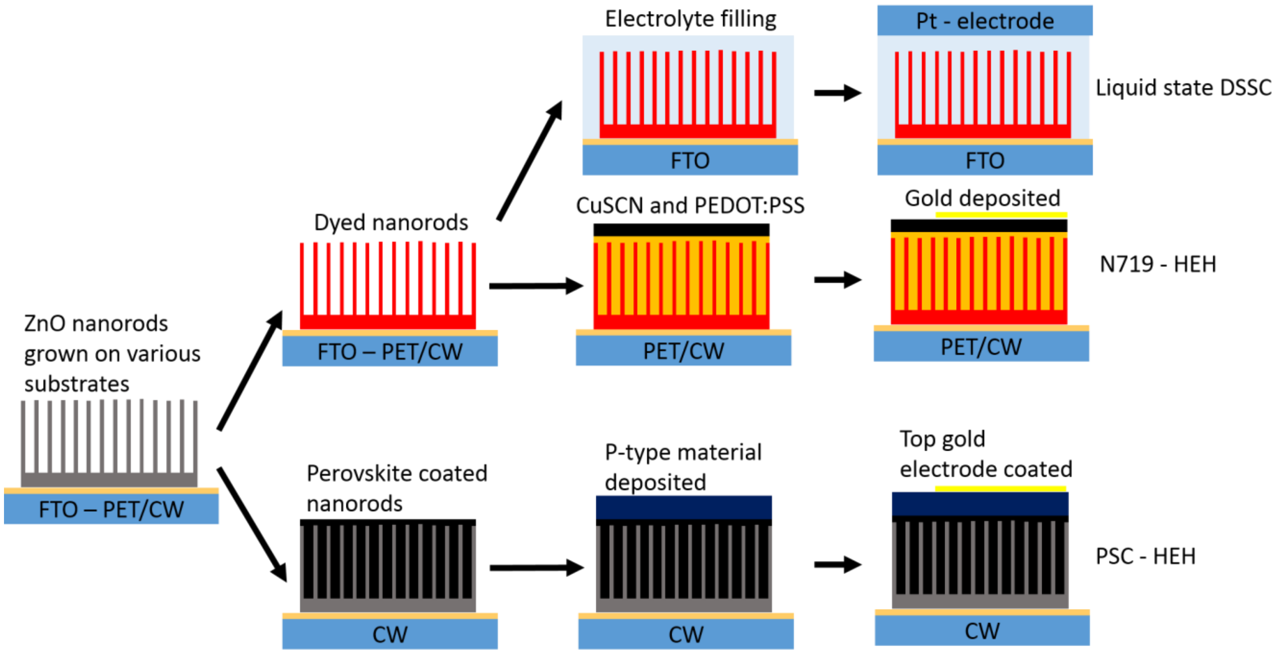

Figure 3-5: Step by step processes in fabrication of devices

In Figure 3-5, the fabrication process for different devices are shown. At first, the nanorods were grown on various substrates. Different morphologies of nanorods were designed depending on the device type, long rods for N719 based devices and short rods for PSC based devices. For N719 based devices, N719 was used as light absorbing layer. In the first case, liquid electrolyte was injected followed by Pt-counter electrode application, leading to liquid state dye sensitized solar cell device. Alternatively, CuSCN and PEDOT:PSS can be used as p-type hole transporting material followed by gold deposition, leading to N719 based hybrid energy harvester device. In the last case, perovskite Methyl Ammonium Lead Iodide can be used as light absorber layer. In this case, toluene-based PEDOT:PSS was used as p-type hole transporting material, leading to PSC based hybrid energy harvester device.

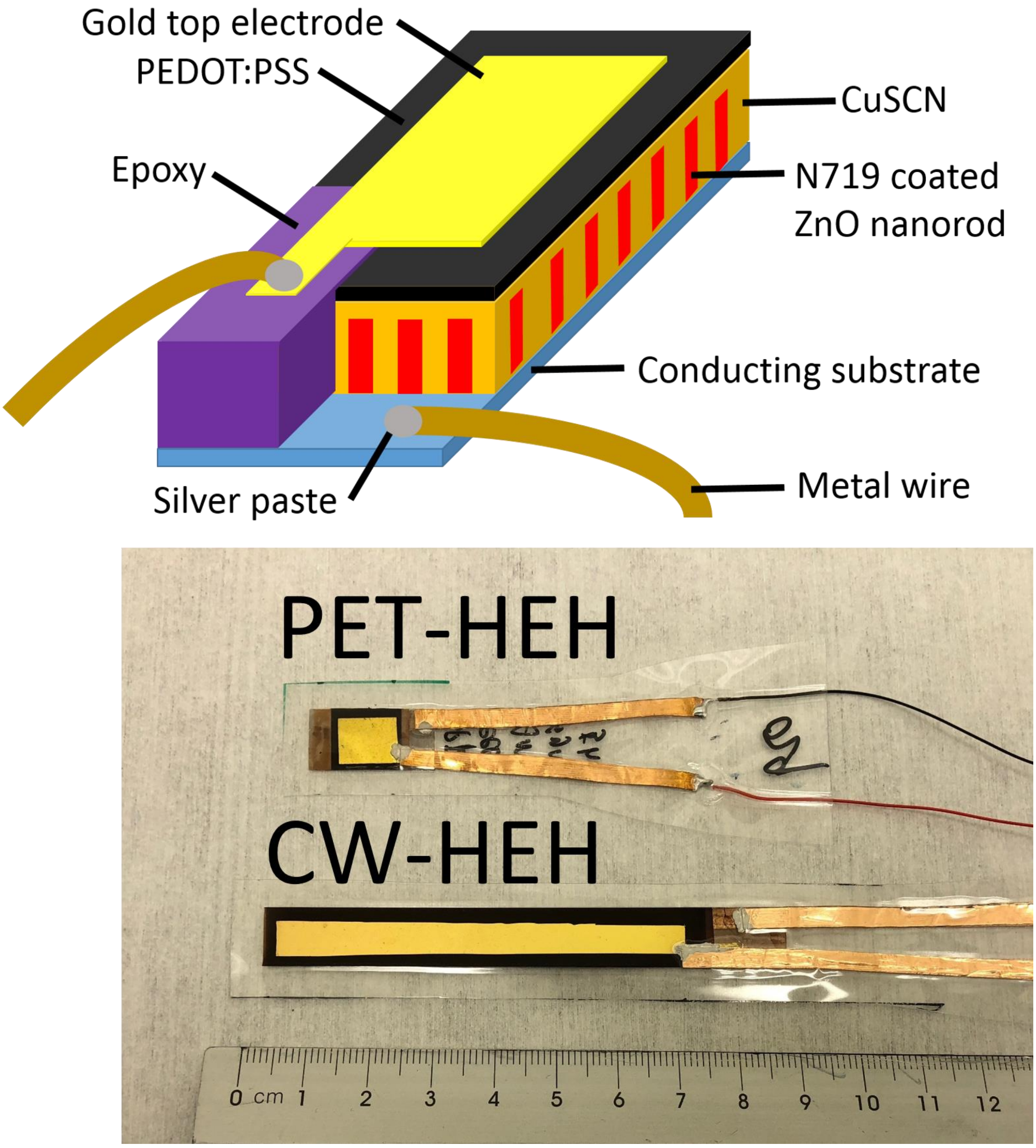

Figure 3-6: Schematic of N719 based hybrid energy harvester device.

Figure 3-6 demonstrates the schematic of the N719 based hybrid energy harvester. Device fabricated on PET is 2 cm long while device fabricated on Corning willow glass is 10 cm long, excluding extended copper tape and metal wires. For PSC-HEH, simply replace the N719 and CuSCN with a thin layer of perovskite layer.

3.7 Measurement and analysis

Scanning-electron microscopy (FEI Inspect F) and transmission-electron microscopy (JOEL 2010F) were used. X-ray diffraction (Siemens D5005 diffractometer) measurement was performed. Scans were performed from 5-90° using $Cu\ K_\alpha$ radiation. Crystal peaks were identified using the International Centre for Diffraction Data (ICDD) database. UV-Vis absorption spectra were measured using a Perkin-Elmer Lambda 950 spectrophotometer. Electrical and photovoltaic measurements were performed using a Kiethley 2400 SMU with LabVIEW 8.0 software. Impedance analysis was performed from 0.01 Hz to 106 Hz using Gamry Interface 1010 Potentiostat. Cells were tested under 1 sun (100 mWcm^{-2}) provided by a Newport solar simulator apparatus (SOL1A class ABB). The simulator was calibrated using Newport reference solar cell and meter 91150V.

For the nanogenerator performance characterization, device was fixed on a permanent magnetic shaker (Brüel & Kjær, LDS V406). The voltage output of the device was recorded using data acquisition module National Instruments NI PXI-4461 on the NIPXI-1062Q chassis, which was operated through LabVIEW program. The terminals of the device were connected in parallel to a resistive decade box, Meatest M602 programmable decade box, which was connected with the PXI-4461 module for data acquisition.

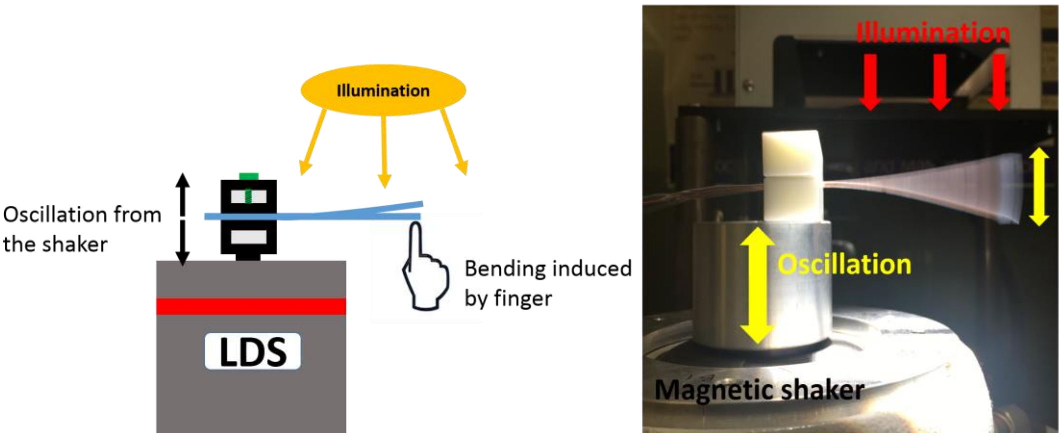

Figure 3-7: Schematic of hybrid energy testing set up.

The testing schematic is shown in Figure 3-7. Bending of the substrate can be induced by finger or the oscillation from the shaker.

Chapter 4 Optimization of ZnO-based DSSCs and effect of acoustic vibration

Based on the acoustic enhancement[87] reported by Shoaee *et al*., the first stage of this project was to produce ZnO-based DSSCs and test the effect of acoustic vibration on the performance of the cells. In order to eliminate the interferences from non-acoustic factors, a stable power conversion efficiency (PCE) of the device was required. This chapter describes the development of the growth of the nanorods suitable for different cells, ZnO/TiO_2 core-shell structures and a high efficiency (compared to literature record 1.5%[47]) DSSC with stable performances. Finally, acoustic vibration was provided onto the stabilized cell to probe the effect on PCE of DSSCs.

4.1 ZnO nanorod growth

4.1.1 Effect of seed layer

As introduced and described in details in Section 3.2, a seed layer of ZnO nanoparticle film is required to grow ZnO nanorods on FTO glass substrates. This section compares the effects of different seed layers on the morphologies of the as grown nanorods. Seed layers were prepared via three methods: (1): drip coating zinc acetate solution in absolute ethanol followed by thermal decomposition, denoted as drip seeding; (2): spin coating of zinc acetate in 2-amino ethanol and 2-methoxyethanol solution followed by thermal decomposition, denoted as sol-gel spin seeding; (3): spin coating of hydrogel precursor containing zinc nitrate and additives in methanol, denoted as hydrogel spin seeding.

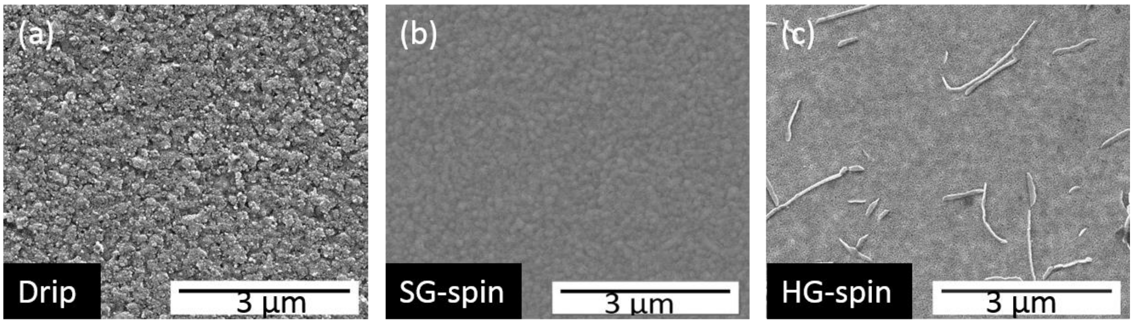

Figure 4-1: Top view of different ZnO nanoparticle seed layer via different seeding methods. (a) Drip seeding method, (b) Sol-gel spin seeding method, (c) Hydrogel spin seeding method.

As discussed in Section 2.6.1, seed layer strongly affects the resulting ZnO nanorod structures. SEM analysis indicated different morphologies of the seed layers. Drip seeding results a rough film while sol-gel spin seeding results a flat and smooth film. It was confirmed in XRD results that sol-gel spin coated seed layer has a strong (0 0 2) peak, indicating good crystallinity. The film produced using a hydrogel precursor does not have a flat surface. Hydrogel spin seeding results a film with impurities (Figure 4-1c). During the hydrogel spinning process, due to the nature of the viscous solution, it attracts dusts in the air. Once the dust is attached on to the surface, the local seed layer structure would be contaminated.

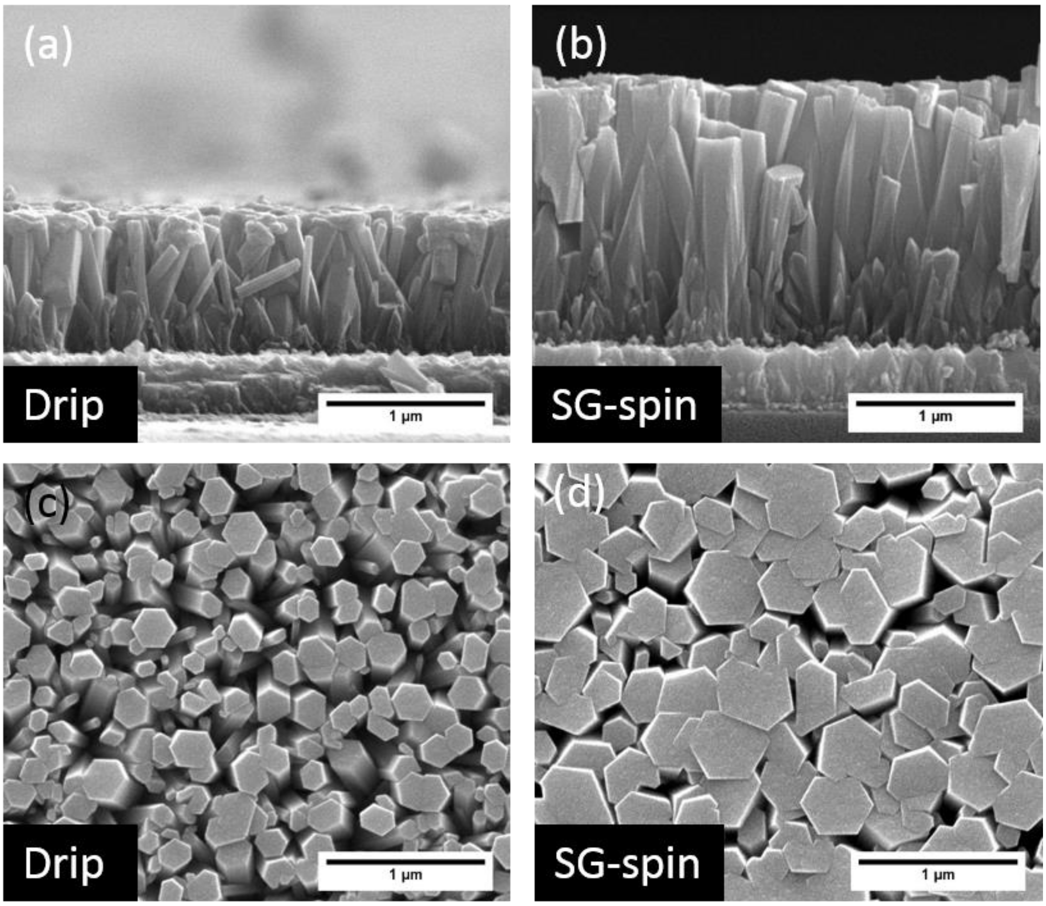

Figure 4-2: Effect of seed layers on the morphology of ZnO nanorods. Growth condition was set to be: 0.1 M equimolar zinc nitrate and HMT at 75°C for 3 h. (a) and (c) show the cross section and top view of nanorods grown on a drip-seeded substrate, respectively; (b) and (d) show the cross section and top view of nanorods grown on a sol-gel spin seeded substrate, respectively.

It can be seen from Figure 4-2 that, for nanorods synthesised via 0.1 M precursor solution at 75 °C for 3 h, the diameter and length of ZnO are 400 nm, 1.65 μm on spin seeded substrate comparing to 200 nm, 0.8 μm on drip seeded substrate. It is clear that sol-gel spin seeding leads to more densely packed film. The diameter of the nanorods is determined by the lateral growth rate of the rods, while the growth rate is affected by both the growth temperature and rods density[116]. Based on the observation from the SEM images in Figure 4-2, at the same temperature during the initial stage of the growth, the randomly oriented drip seed layer would be at lower supersaturation than flat sol-gel seeded layer[116]. For nanorods grown on sol-gel seed layer, initial growth is preferred towards the same vertical direction, during the late stage of the growth, rods are fused together, and hence less hexagonal top surfaces are found. For nanorods grown on randomly oriented drip seed layer, during the initial stage, growth of the rods are competing towards different directions, this can be seen from the cross section image (Figure 4-2a). With low crystal preferential growth direction, rods grew separately from each other rather than fusing together. Hence comparing to the nanorods from sol-gel seed layer, nanorods from drip seed layer has a shorter length, higher density with small diameter, and rough top surface.

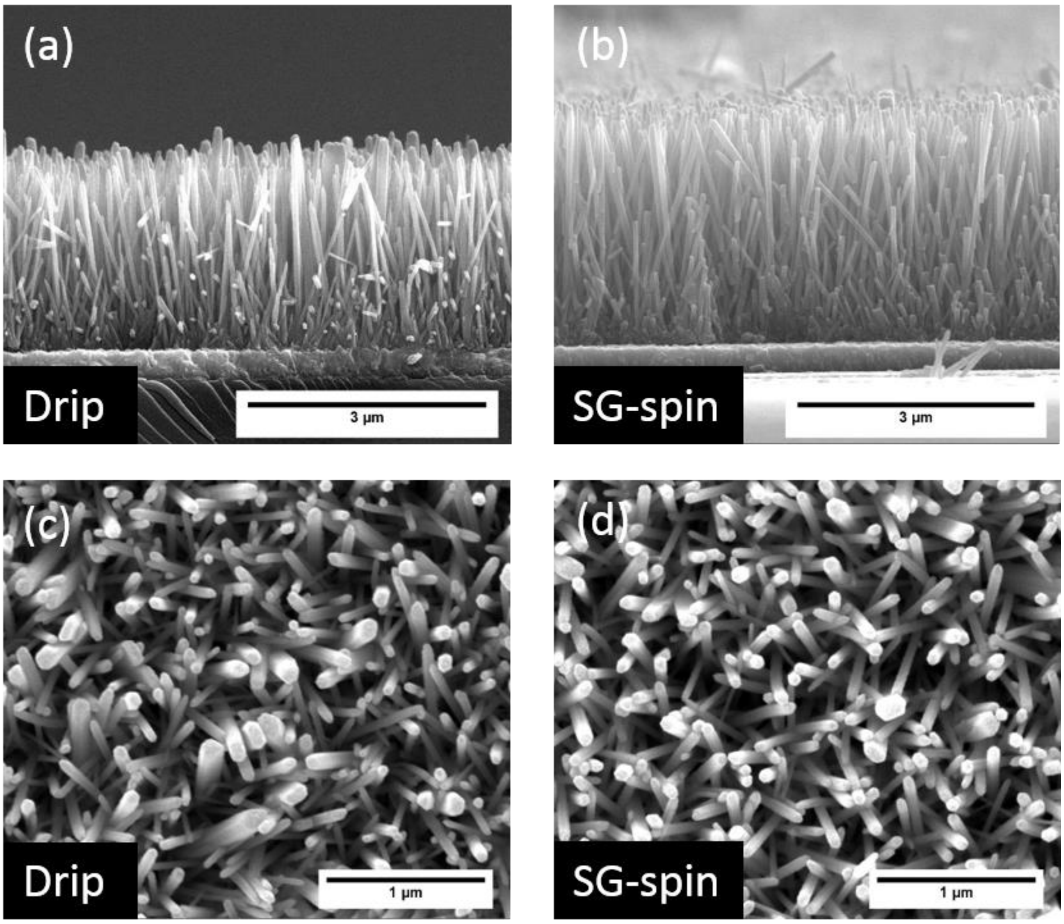

Figure 4-3: Effect of seed layer on the morphology of ZnO nanorods. Growth condition was set to be: 0.025 M equimolar zinc nitrate and HMT at 90 °C for 24 h (pH=6 method). (a) and (c) show the cross section and top view of nanorods grown on drip seeded substrate;

(b) and (d) show the cross section and top view of nanorods grown on sol-gel spin seeded substrate.

It is shown in Figure 4-3 that, for nanorods grown via pH=6 method, although the top view of the nanorods appears to be the same in density and orientation, cross section image reveals that ZnO nanorods grown on sol-gel seeded substrate has a length of 3.5 µm comparing to 2.5 µm of rods grown on drip seeded substrate. For the application in DSSC, longer rods are desired due to improved light scattering and potentially higher dye loading, therefore, sol-gel spin seeding is preferred.

4.1.2 Effect of growth time and ZnO growth method

The length of the ZnO nanorods is time-dependent. For the ZnO synthesised on sol-gel seeded substrate, the initial stages of growth are shown in Figure 4-4:

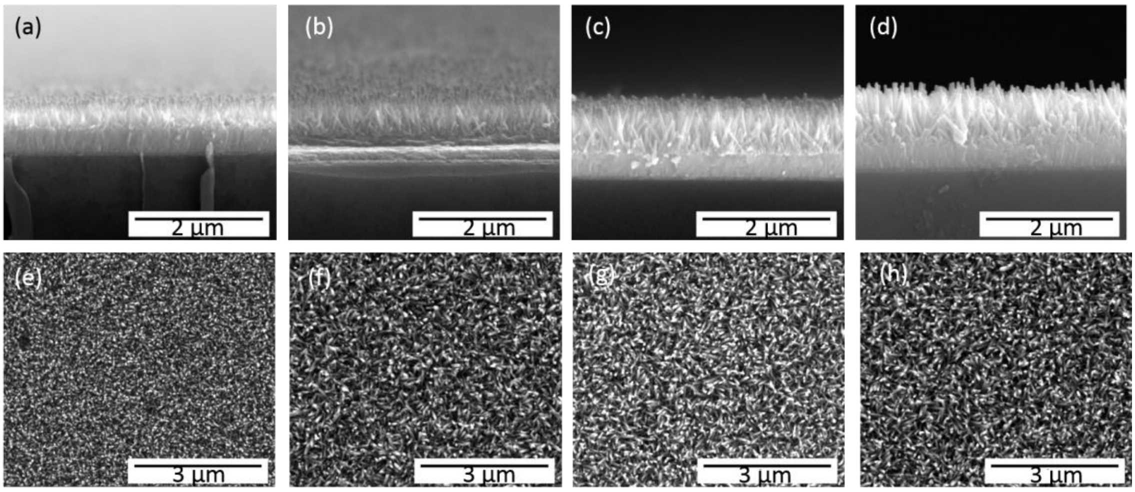

Figure 4-4: Cross section and top view of (a) and (e) 2.5h, (b) and (f) 3h, (c) and (g) 3.5h, (d) and (h) 4h. Growth condition: 0.025 equimolar zinc nitrate and HMT, 90 °C, 24 h.

For nanorods synthesised via pH=6 method on sol-gel spin seeded substrates, the lengths of the ZnO nanorods from 2.5, 3, 3.5 and 4 h are 350, 600, 700 and 900 nm respectively. These shorter rods are ideal for electron transport layers for perovskite solar cells as discussed in Section 2.4.

Other than 0.025 M equimolar synthesis, ammonia-assisted high aspect ratio rods were also synthesised on hydro-gel seeded substrates. Ammonium hydroxide and polyethylenimine (PEI) were added to achieve high aspect ratio rods (details of the growth condition in Section 3.2).

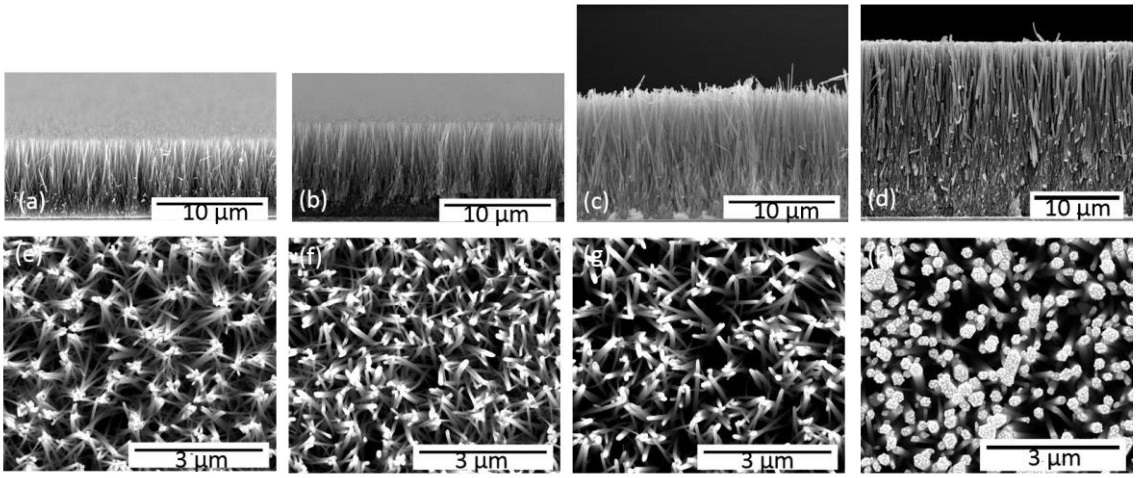

Figure 4-5: Cross section and top view of ZnO nanorods grown via ammonia-assisted growth via different growth times. FTO from each cross section images have been aligned to show the differences of lengths (a) and (e) 5 h, (b) and (f) 7 h, (c) and (g) 14 h, (d) and (h) 24 h.

The lengths of the rods from 5, 7, 14, 24 h are 6, 8, 12 and 20 µm, respectively. On 14 h and 24 h synthesised samples, the bottom part of the rods fuse together. The lower part at the bottom of the nanorods tend to grow wider due to reduced limitation of mass transfer reactants[116]. It is not desired to have a thick ZnO fusion layer as it acts as charge blocking layer and contains a large amount of recombination sites[116].

Table 4-1: Aspect ratios and relative surface areas of two different synthesis methods. The densities of the rods are calculated from SEM images, approximately 45 rods/1 μm² for pH=6 growth and 30 rods/1 μm² for ammonia-assisted growth. Surface area factor is defined as the ratio between the surface area of all nanorods within 1 μm² and the area of the substrate (1 μm²).

ZnO nanorods via pH=6 0.025M equimolar growth				
Growth time (h)	Length (nm)	Diameter (nm)	Aspect ratio	Surface area factor (μm² / Per 1 μm²)
2.5	350	70±10	5	70
3	600	90±10	6.7	190
3.5	700	90±10	7.8	220
4	900	90±20	10	280
8	2000	125±10	16	1180
16	2500	130±20	19.2	1490
24	4000	150±20	27	3370
ZnO nanorods via ammonia-assisted growth				
5	6000	75±15	80	850
7	8000	85±20	94	1450
14	12000	130±20	92.3	5100
24	20000	250±30	80	31800

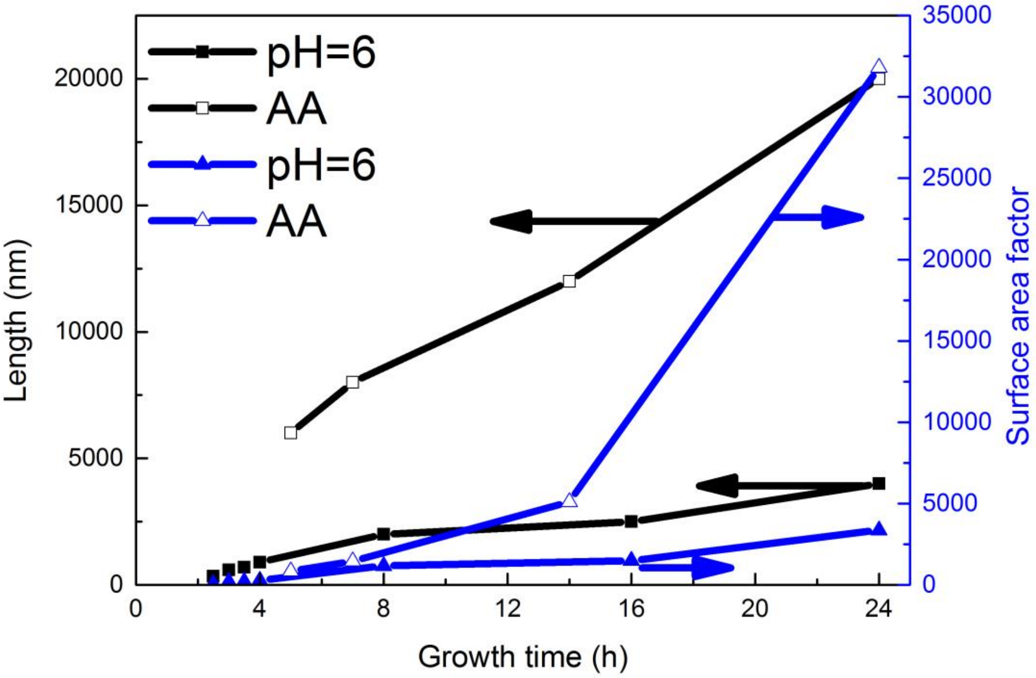

Figure 4-6: Lengths and relative surface areas of the nanorods grown from both pH=6 growth and ammonia-assisted (AA) growth. Surface areas are calculated for rods within 1 μm^2.

It can be seen from Figure 4-6 and Table 4-1 that, both length and surface area increase along growth time. Ammonia-assisted growth has faster growth rate which resulted to longer rods comparing to pH=6 growth. As a result, ZnO film grown from ammonia-assisted growth has higher surface area, which would be beneficial for the dye loading in DSSCs.

The growth mechanism has been discussed in Section 2.6.1. The slow decomposition of HMT provides controlled supply of ammonia, which can form ammonium hydroxide and offer OH^-. Zn^{2+} can complex with OH^- to form several monomeric hydroxyl species, including $Zn(OH)^+$ (aq), $Zn(OH)^2$ (s), $Zn(OH)_3^-$, and $Zn(OH)_4^{2-}$ (aq)[117]. Then solid nuclei are formed by the dehydration of these hydroxyl species at the surface of ZnO seed layer. Without external source of ammonia, growth speed is relatively slow, most of the nutrient would be depleted by homogeneous nucleation to form white precipitates. When ammonium hydroxide is added, length and aspect ratio of the rods would increase. It is suggested that the introduction of ammonia into the reaction suppressed the homogenous nucleation effectively. The suppression effect is due to the coordination of ammonia to Zn^{2+} and the low concentration of free Zn^{2+}. Then the complexes would serve as a buffer for Zn^{2+} and provides continuously Zn^{2+} while lowering the supersaturation degree of the reaction system[117]. Thus, with suppressed homogeneous nucleation, precipitates in the solution would be reduced.

For PEI, protonized form of liner PEI molecules would be adsorbed on the non-polar lateral planes of nanorod and inhibit the lateral growth[118]. Here it is noticed that the top view of the ZnO structures changed along the growth time (see Figure 4-5). On 5 h synthesised substrate, the tips of the ZnO fuse together. With prolonged growth time, the number of fused sites reduces. On the 24 h synthesised sample, all the rods are able to stand vertically and separately from each other. This is also supported by the increasing diameter shown in Table 4-1. The reason is suggested as follow: during the initial stage, lateral growth of ZnO is suppressed by sufficient amount of PEI, with the presence of excessive ammonia, the rods exhibits fast growth rate. Towards the final stage of growth, the amount of PEI is depleted and insufficient to cover all the side surfaces. Hence the lateral growth stops to be suppressed and the diameter would increase to reach an even surface on the sides. As the reason of the fusing during initial stage, it is suggested that: at the fast growth rate due to excessive ammonia, the long aspect ratio rods are not physically stable (higher flexibility at thin diameter stage). The growth direction is random, the rods tend to fuse together to physically support each other. This fusing action could also reduce surface area of the rods, this is caused by surface tension. During the final stages of the growth (approaching to 24 h), lateral growth is not suppressed by PEI any more, hence the diameter increases. The rods would be able to stand vertically free from contact with each other.

XRD analysis was performed to identify the phase of the ZnO crystals.

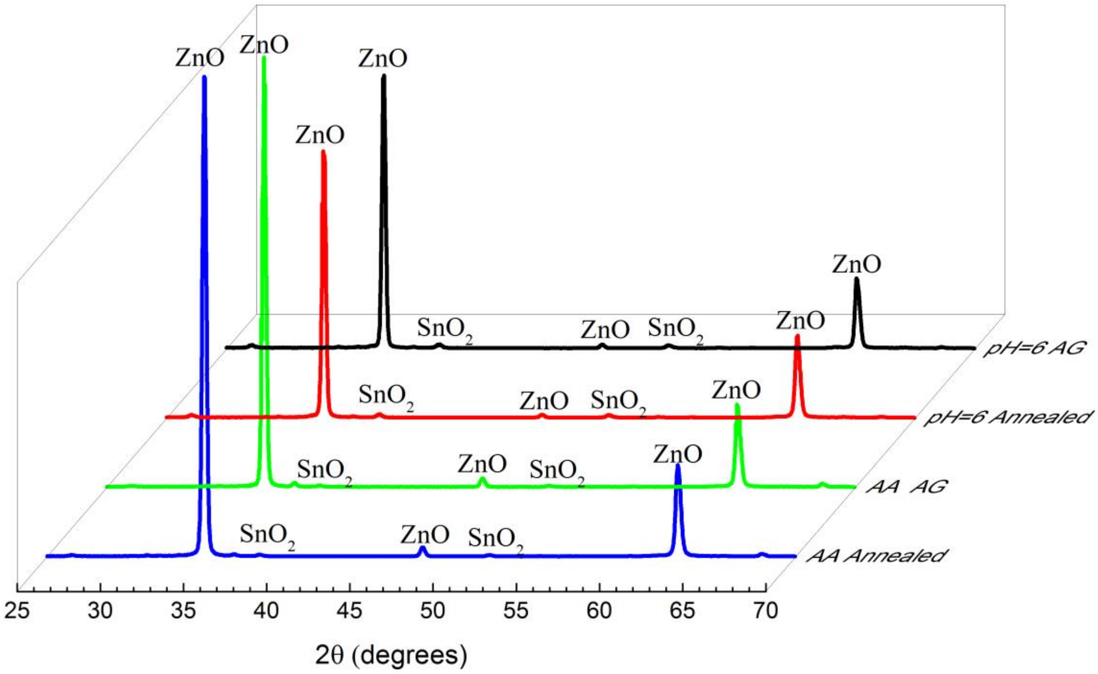

Figure 4-7: XRD results of ZnO from different synthesis route and annealing effects, including pH=6 and ammonia-assisted growth (AA). AG: as grown.

It can be seen from Figure 4-7 that the peak positions do not change within the precision of the measurement as effects of different synthesis routes or annealing. This indicates that the crystal structure and lattice spacing are not affected. The strong (0 0 2) peak at 34.4° for all four measurements corresponds to ICDD (International Centre for Diffraction Data) PDF-Card: 35-1451 for wurtzite ZnO. This peak confirms the c-axis oriented vertical growth of ZnO nanorods, and corresponds to the SEM images in Figure 4-3 and Figure 4-4. No difference in the crystal structure is found post annealing.

In summary, different morphologies of ZnO nanorods can be synthesised via tuning the growth parameters. Seed layer quality greatly affects the structures of ZnO nanorods. Precursor concentration and additives can be used to change the aspect ratio of the rods. The as-grown rods were annealed at 500 °C in air to remove the impurities and surface defects, thus improving the crystallinity. After annealing, ZnO nanorods can be used as the electron transport layer (ETL) in device applications.

4.2 ZnO/TiO_2 core-shell structure

As described in Section 2.6, TiO_2 shell coating has the potential to further improve the surface area of the photo anode[14], as well as reducing the recombination by passivating the surface of ZnO nanorods. However, the reported atomic layer deposition method was time consuming and uneconomical[14]. In this section, a facile route of producing ZnO/TiO_2 core-shell structure via layer-by-layer absorption method was investigated. Morphologies, crystallinity and optical properties were measured and discussed.

The fabrication process has been discussed in detail in Section 3.2. ZnO substrate was coated with TiO_2 shell via four step dip coating process, the sample was dipped in the following order: (1) TiO_2 sol consisting 0.5 M tetrabutyltitanate and 0.5 M acetylacetone in absolute ethanol; (2) ethanol; (3) deionized water; (4) ethanol.

4.2.1 Scanning electron microscopy analysis

SEM analysis was performed first to investigate the effect of TiO_2 on morphologies of the nanorods.

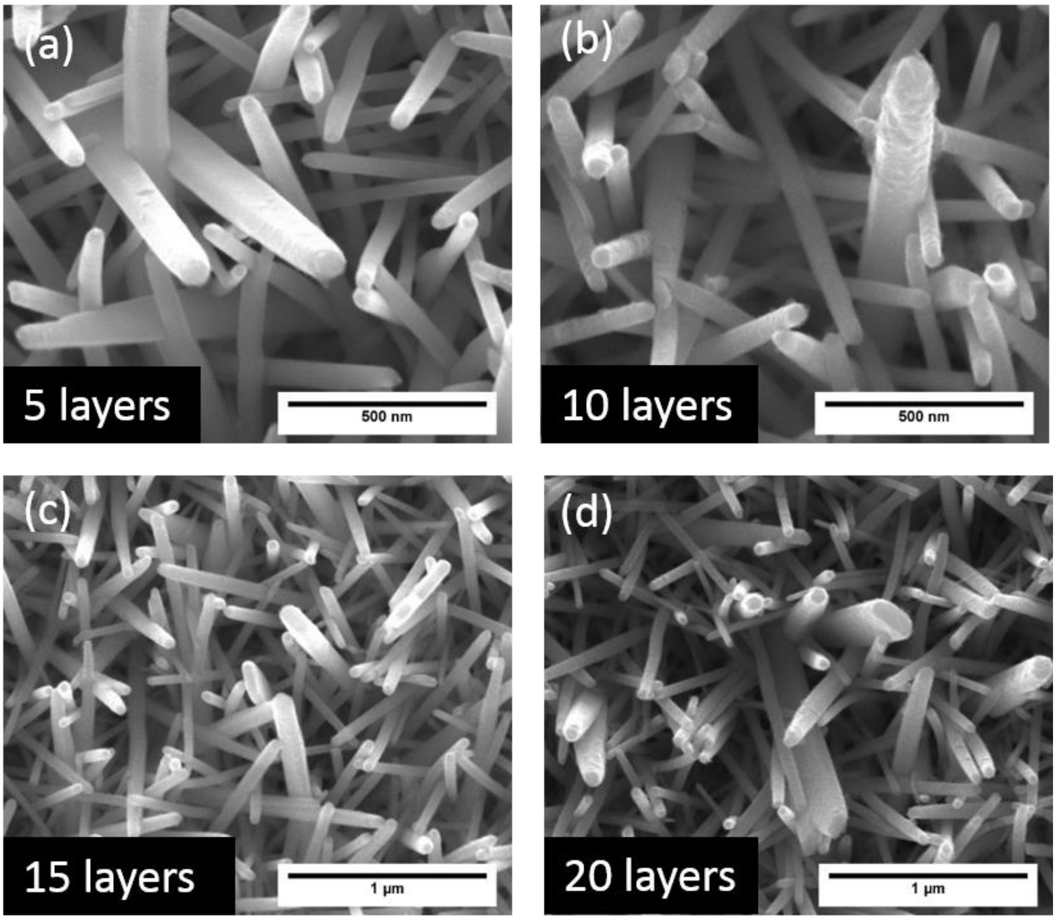

Figure 4-8: Top view of various layers of TiO_2 coated on ZnO grown via pH=6 method. (a) 5 layers, (b) 10 layers, (c) 15 layers, (d) 20 layers.

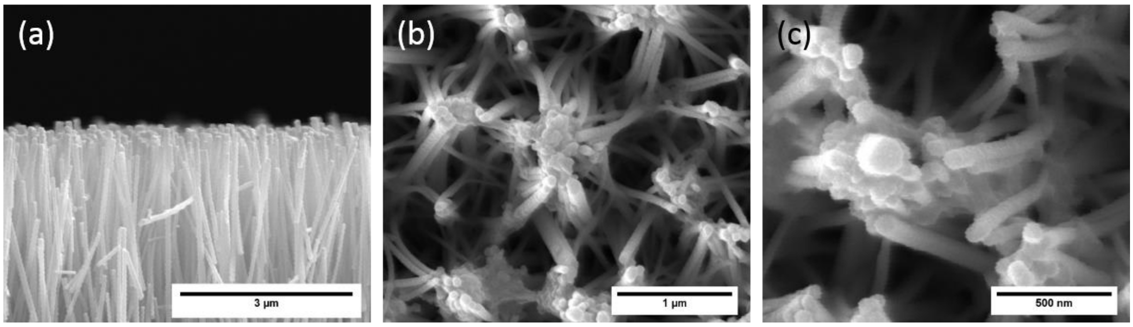

Figure 4-9: Images of 5 layers of TiO_2 coated ZnO grown via ammonia-assisted method. (a) Cross section, (b) Top view, (c) Magnified top view.

Before coating, the surface of the rods is smooth (see Figure 4-3). After 5 layers coating, roughened surface could be observed. After more layers of coating, SEM images could not identify further change due to the resolution limit. It was suggested that the thickness of the TiO_2 shell would be below 10 nm[14], which would be difficult to identify under SEM.

For ammonia-assisted growth, due to the presence of fused tips, TiO_2 nanoparticles form agglomerates at the fusion sites (shown in Figure 4-9c). This phenomenon become more obvious after 15 layers TiO_2 coating shown in Figure 4-10 below:

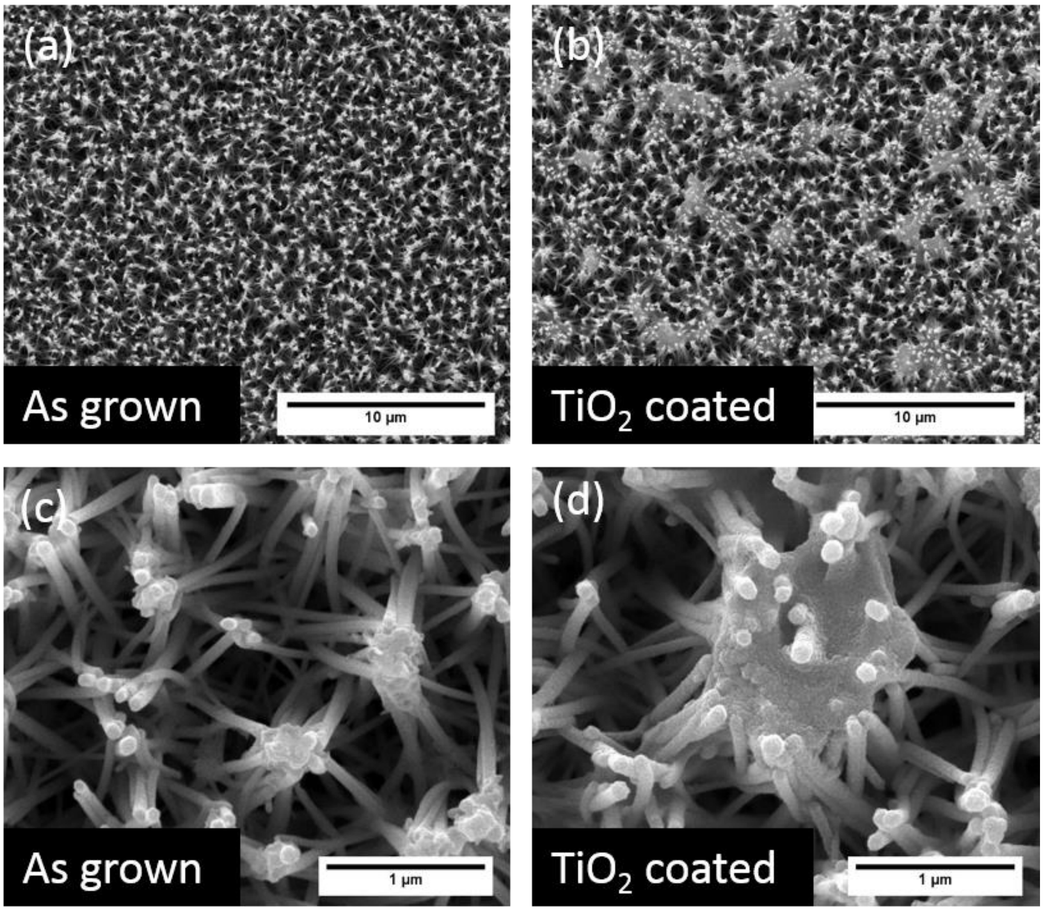

Figure 4-10: Top view of SEM images of effect of TiO_2 coating on rods via ammonia-assisted method. As grown rods are shown in (a) Low mag and (c) High mag. 15 layers TiO_2-coated rods are shown in (b) Low mag and (d): High mag.

It can been seen clearly from Figure 4-10, as the number of TiO_2 layers increased, agglomerates of TiO_2 form at the tips of the nanorods. During the dip coating process, the substrate was withdrawn at a fixed speed (1 cm/s) under room temperature and ambient atmosphere. Capillary force may have led to excessive solution being deposited at the fused region at the tips of nanorods. During each step of the coating, the fused region with excessive TiO_2 sol would develop into large agglomerates, as seen in Figure 4-10.

4.2.2 X-Ray differential analysis

To ascertain whether the coating of TiO_2 had any effect on the crystal structure of the rods, and the phase of the deposited TiO_2, XRD analysis was performed.

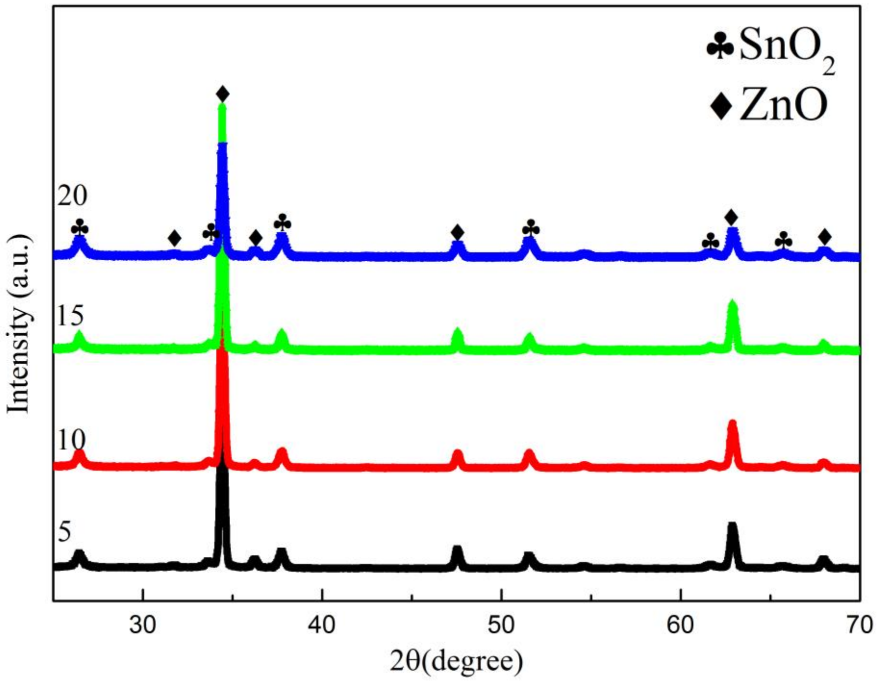

Figure 4-11: XRD results of various layers of TiO_2 coating on ZnO grown via pH=6 method. From bottom to top: 5, 10, 15 and 20 layers, all annealed at 500 °C for 1 h.

From Figure 4-11, SnO_2 exhibits diffraction peaks at 26.5° (110), 37.8° (200), and 51.5° (211) (ICDD PDF-Card: 01-77-0452). In addition, XRD peaks at 2θ = 31.8° (110), 34.4° (002), 47.5° (102), 62.8° (103) and 67.9° (112) occur, representing a wurtzite structure of ZnO (ICDD PDF-Card: 36-1451). The strongest peak of ZnO at

34.4° indicates the (0 0 2) direction is the most preferential crystal plane for the aligned ZnO arrays. ZnO nanorods grow along c-axis, which is perpendicular to the surface of the FTO substrate. As discussed in Section 2.6., anatase phase TiO_2 is commonly produced through hydrolysis of a titanium precursor and conversion of anatase to rutile occurs in the temperature range of 700-1000 °C[28]. The annealing condition for coated TiO_2 was 500 °C for 1 h, which was not high enough to cause the phase transition. Hence anatase TiO_2 standard XRD pattern is chosen to compare with the results here. However, no distinct TiO_2 peak can be identified, which corresponds to the report from Law that XRD is not capable of detecting a thin layer of shell. Law *et al.* suggest that TiO_2 films thinner than about 5 nm are completely amorphous[14].

4.2.3 Transmission electron microscopy analysis

In order to further identify the TiO_2 shell, TEM analysis was performed.

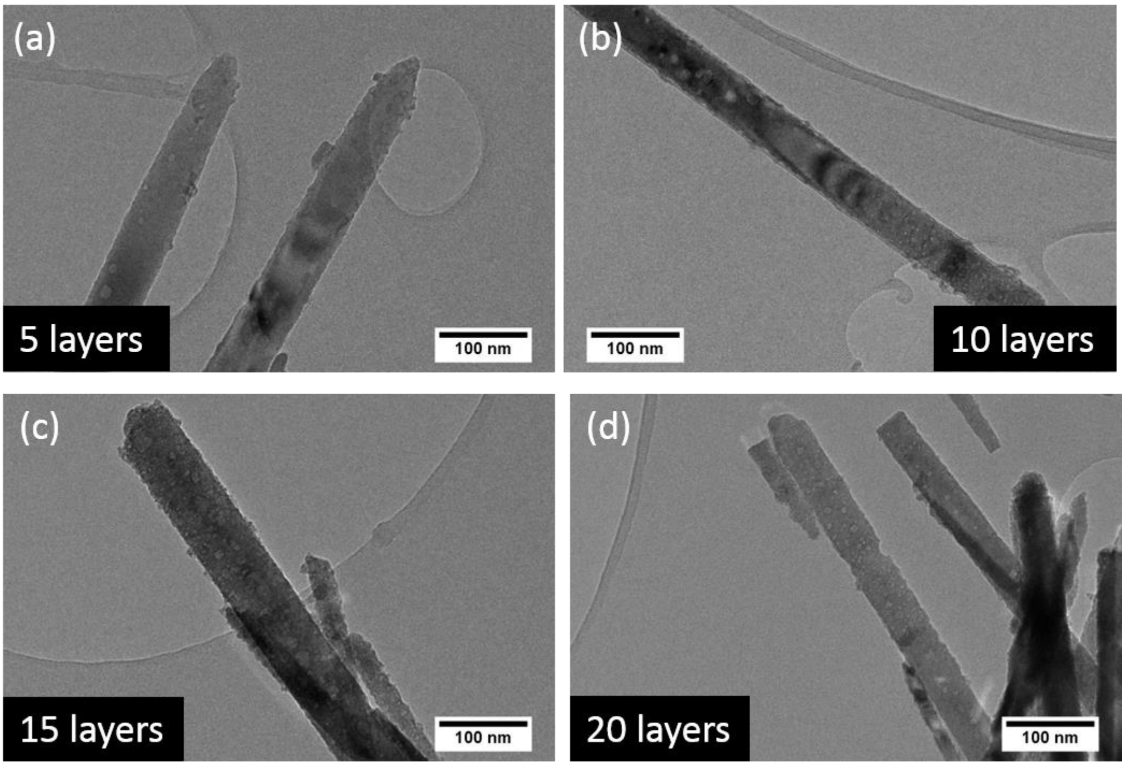

Figure 4-12: TEM images of various layers of TiO_2 coated on ZnO grown via pH=6 growth. (a) 5 layers, (b) 10 layers, (c) 15 layers, (d) 20 layers.

The rough surface of outer shell could be confirmed by TEM. The shell structure fully cover the entire nanorods. However no distinct difference can be identified from different layers of TiO_2 coating. In order to further confirm the phase of TiO_2, HRTEM was performed.

High-resolution Transmission electron microscopy analysis images are shown in Figure 4-13.

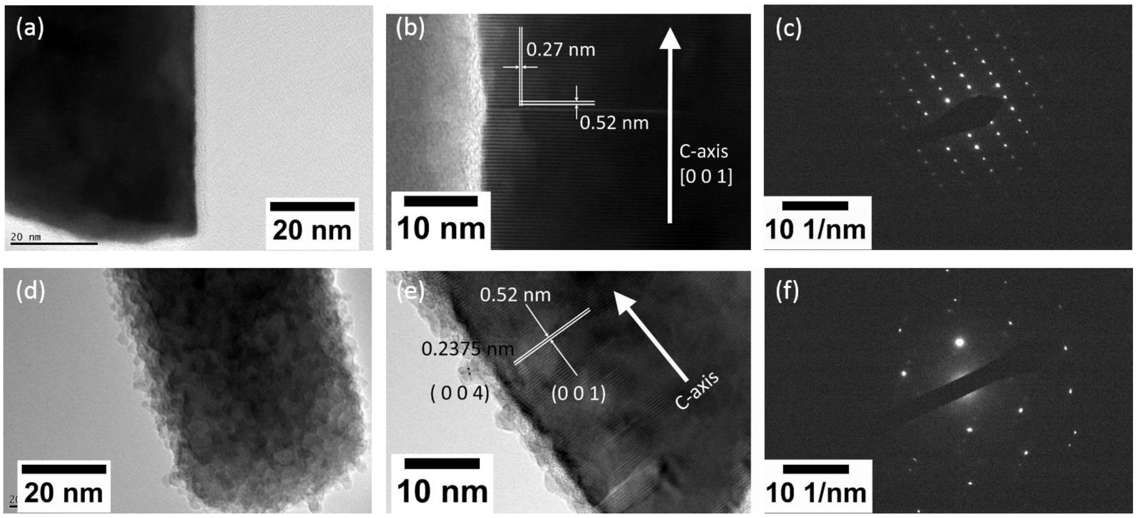

Figure 4-13: HRTEM and Selected area electron diffraction (SAED) patterns. (a), (b) and (c) as grown ZnO; (d), (e) and (f) 5 layers TiO_2 coated ZnO. ZnO were grown via pH=6 method.

Comparing images (a) and (d), it can be seen that the shell coating is successful, leading to a clear increase in the surface roughness of the nanorod. Image (b) indicates the annealed ZnO is highly crystalline with a wurtzite crystal structure and the growth direction is along the c-axis, which is in good agreement with XRD results. The clear lattice spacings of 0.52 nm and 0.27 nm correspond to the interplanar spacings of the wurtzite ZnO (0001) and $\{10\bar{1}0\}$ planes, respectively, which also indicates that the preferred growth direction is along the c-axis. From Image (c): the shortest spacing d_1 = 2.84 å corresponds to (2 0 0) plane of ICDD PDF-Card: 36-1451. The second shorted spacing d_2 = 5.2 å corresponds to (0 0 2) plane of ICDD PDF-Card: 36-1451. This also suggests the ZnO crystal has high crystallinity. From Image (e): the *d* spacing of 0.2375 nm corresponds to (0 0 4) plane for anatase TiO_2. The clear difference of the crystal orientation between the shell and the ZnO indicates the success of TiO_2 shell coating. From Image (f): the shortest spacing d_1 = 2.65 å corresponds to (0 0 4) plane of ICDD ZnO PDF-Card. The second shorted spacing d_2 = 1.06 å corresponds to (2 1 7) plane of anatase phase TiO_2 of ICDD PDF-Card: 03-065-5714. The detection of multiple diffraction patterns from 5 layer TiO_2 coated sample indicates that new crystalline materials is formed at different orientations to the original crystal, which corresponds to Figure 4-13e.

The thickness of 5 layers of TiO_2 shell deposition is 3.46 nm on average. This suggests approximately 0.7 nm of TiO_2 is deposited per each coating cycle during first 5 layers of deposition. It was suggested by Law's report that TiO_2 shell thickness around 5 nm would be considered as amorphous and could not be detected by XRD[14]. In our results, SAED pattern revealed crystalline structure of TiO_2 on 5 layers coated sample. However the shell structure was found to be polycrystalline with only partial TiO_2 transferred to crystalline after annealing. Thickness of 10 layers coated TiO_2 shell is also calculated and the average thickness is 5.64 nm, indicating decreased overall coating rate, morphologies of the shell remained uneven. Decreased coating rate is attributed to the natural of dip coating. Unlike atomic layer deposition where controllable, precise thickness of the coating is achievable, dip coating limits the amount of Ti species that can be absorbed. It is suggested that, when reached a critical thickness, further dipping would wash off the previously attached Ti species. As a result, the amount of materials could be deposited per each cycle is lowered.

In summary, a shell can be identified due to increased roughness. HRTEM revealed TiO_2 crystal phase within the shell region. Even though the deposited shell is thin and non-uniform, the success of lay-by-layer deposition of core-shell structure provides a new route to modify the ZnO photo anode.

4.2.4 Ultraviolet–visible spectroscopy

Optical properties were measured via UV-Vis to investigate the effect of TiO_2 shell coating and N719 dye loading on the absorbance of ZnO nanorods. The results in Figure 4-14 were achieved on nanorods grown via pH=6 method.

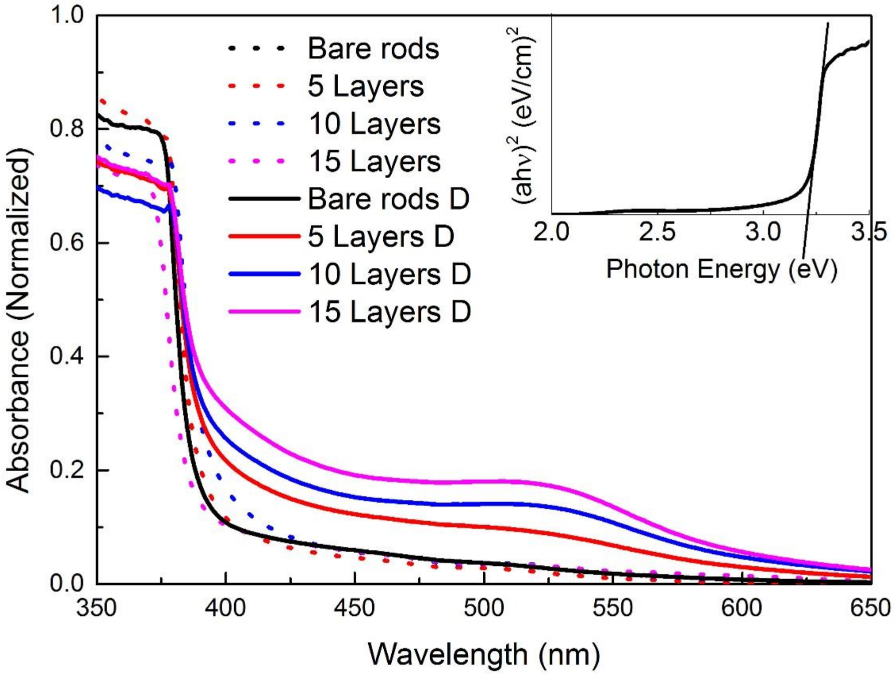

Figure 4-14: UV-Vis plot of ZnO/TiO_2 core-shell structure before and after 6 h of N719 dye loading. 'D' denotes samples after dye loading. Inset shows the Tauc plot of bare ZnO nanorods. Here, nanorods were grown via pH=6 growth method.

For all substrates before N719 dye loading, ZnO nanorods show low absorption within the visible spectrum range (400-700 nm). An absorption edge could be seen at ~380 nm, indicating a band gap of 3.24 eV shown in Figure 4-14 inset (corresponding to the literature value for the band gap of ZnO[24,79]). Comparing the different TiO_2 layers before dye coating, the addition of a TiO_2 shell of any thickness does not affect the absorbance as all of the values are within a similar range. This is as expected as the thin layer of TiO_2 with similar band gap of ZnO would not be able to affect the absorbance of ZnO significantly. After N719 dye loading, it is as expected that absorbance increased within the visible spectrum range. Absorbance is in direct proportion to the coated layers of TiO_2. The more layers of the coating, the higher the absorbance. It is also noted that the dye-related absorbance is negligible on the bare rods, indicating the improvement of absorbance is originated from the coating of TiO_2 shells.

Results in the Figure 4-15 were achieved on rods grown via ammonia-assisted method.

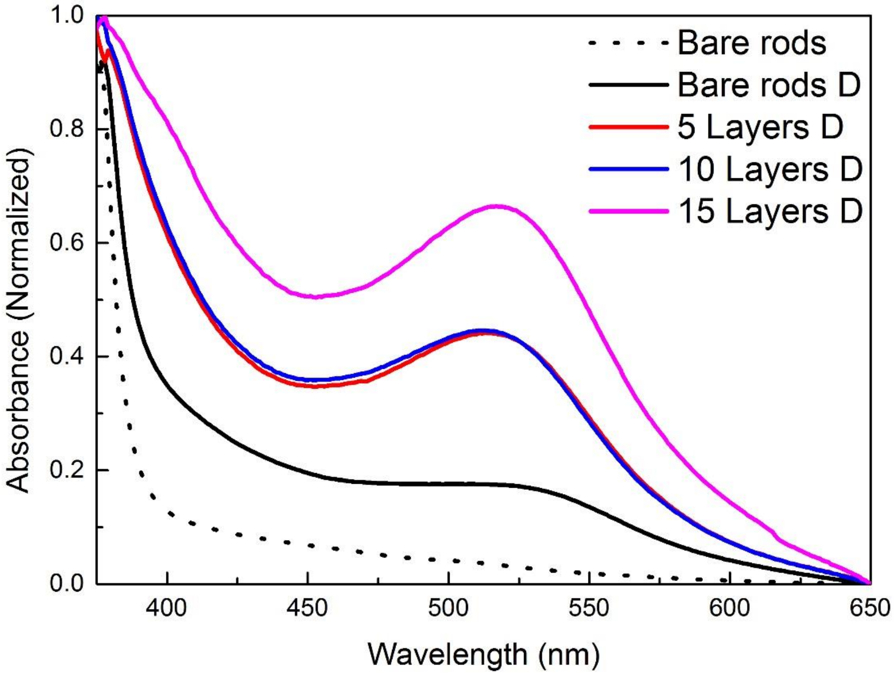

Figure 4-15: UV-Vis plot of ZnO/TiO_2 core-shell structure before and after 6 h of N719 dye loading. 'D' denotes samples after dye loading. Here, nanorods were synthesized via ammonia-assisted growth method.

It can be seen from Figure 4-15 that nanorods grown via ammonia-assisted method has higher absorbance due to enhanced light scattering from longer length (11 μm rods used here). For the TiO_2 coating, 5 layers and 10 layers show similar absorbance except slight increase for 10 layers coated sample around 430-480 nm range. This suggests that due to the natural of dip coating, the thickness of TiO_2 shell was not strictly proportional to the layers of coating, which corresponds to the SEM and HRTEM images that no obvious morphological differences are found between 5-10 layers coated TiO_2 shells. 15 layers coated TiO_2 shell hugely improved the absorbance, considering the SEM images in Figure 4-9, the possible reason is attributed to the formation of TiO_2 agglomerates on the tips of the rods. The agglomerates could be considered as small sized TiO_2 film formed by TiO_2 nanoparticles, which could increase the dye adsorption due to significantly increased surface area. It should be also noted that for ammonia-assisted bare rods, dye absorption greatly increases absorbance across the visible spectrum range.

4.2.5 Photoluminescence spectra of ZnO/TiO_2 core-shell

Photoluminescence (PL) measurement were taken in order to probe the energy transitions within the ZnO/TiO_2 core-shell structure and investigate the defect structures after thermal annealing.

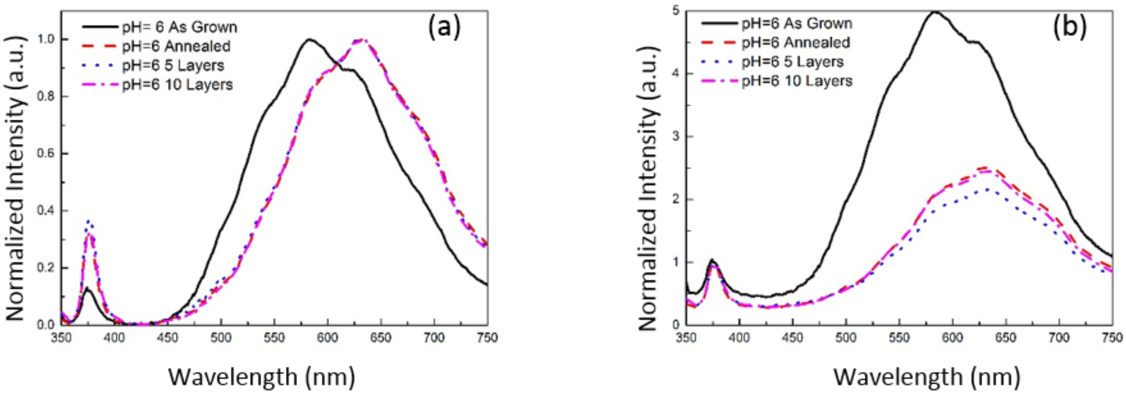

Figure 4-16: Photoluminescence spectra of pH=6 method grown ZnO with TiO_2 deposition. (a) Normalized data, (b) Normalized to the peak intensity of near band edge emission.

Two peaks can be identified from Figure 4-16a and b. The first peak at 376.6 nm is the UV emission peak. It is related to a near band edge emission (NBE) of ZnO, namely, the recombination of the free excitons[119]. According to literature[119], this peak could locate within the range of 375-383 nm (~3.3 eV). It depends on the contribution between the free exciton and the transition between free electrons to acceptor bound holes. The dominant (0 0 2) peak from XRD results and the wurtzite SAED pattern observed in HRTEM indicate high ZnO crystallinity. Consequently, a strong near band edge emission is expected. However in this normalized data (Figure 4-16a), the NBE at 376.6 nm is relatively weak. Here the diminished emission indicates rapid combination of charge carriers in the defect energy states, which would give rise to the deep level emission (DLE) peaks. The second broad and dominant peak is the deep level emission peak that has been attributed to several defects in the crystal structure such as oxygen vacancies, zinc vacancies, O-interstitials, Zn-interstitials and extrinsic impurities[120].

From Figure 4-16a, both near band edge emission and deep level emission are observed in the as-grown, annealed ZnO nanorods and ZnO/TiO_2 core-shell structures. The NBE emission is significantly enhanced and the DLE is shifted for the samples subjected to annealing. The stronger intensity of NBE emission from annealed bare rods (500 °C for 1 h) and TiO_2 shell-coated rods (which also included a post annealing process at 500 °C for 1 h) are in the same range comparing to the weak intensity from as-grown ZnO.

The ratio of relative normalized PL intensity between UV emission and deep level emission is commonly used to characterize the crystallization of the ZnO, as shown in Figure 4-16b. In Figure 4-16b, it can be seen that the ratio of the deep level band to the NBE emissions of the samples subjected to post annealing are much smaller than that of as-grown ZnO. It may also be noted that the ratio of DLE to the NBE emission is almost identical for annealed and 10 layers-coated samples, while 5 layers-coated sample shows slightly weaker DLE. The slightly weaker DLE from 5 layers-coated sample is suggested to be a result variation from the test. In Figure 4-16b, comparing with the DLE of as-grown ZnO, the considerable suppression of

DLE by the post annealing process is attributed to increased intensity of NBE. The increase of NBE is attributed to reduced density of oxygen interstitials at the surface of ZnO core[121] after annealing. The remaining DLE from the core-shell structure may mainly originate from the oxygen interstitials inside the ZnO core.

Alternatively, the enhancement of NBE has also been attributed to the flat-band effect[122]. Negatively charged oxygen ions may adsorb on the surface of as-grown ZnO, resulting in a depletion region near the surface[123]. It has been reported that the width of the depletion region is about 20 nm[124], smaller comparing to the nanorods prepared for ZnO used here (150 nm diameter). This depletion region can be considered as an upward band bending towards the surface of the rods. During PL measurement, photo generated holes are inclined to accumulate near the surface where the photo generated electrons are inclined to reside inside the core. As a result, the probability of radiative recombination is lowered, hence weaker NBE[125]. During thermal annealing process, the oxygen ions adsorbed on the ZnO surface would be eliminated, hence reduce the band bending near the interface[122]. This could enhance the NBE.

The surface of ZnO grown with CBD method is prone to absorb various kinds of functional groups. According to the chemical reaction in the solution (discussed in Section 3.2), these functional groups will be related to elements such as carbon, nitrogen, and hydrogen[120]. These functional groups have a negative influence on the optical properties of ZnO. One small shoulder peak can be identified at the range between 540 nm (2.3 eV) and 544 nm (2.28 eV), which is attributed to surface defects as well as oxygen vacancies (V_o) and oxygen interstitials (O_i), respectively[126]. The strongest peak of yellow DLE at ~570 nm (2.2 eV) is observed which could be linked to $Zn(OH)_2$ on the surface[127] as well as oxygen interstitials[104,119,128]. The second strong peak at ~642 nm (1.93 eV) is linked to naturally charged zinc vacancy V_{Zn}[126]. It has been reported that yellow emission can be suppressed by annealing in vacuum for 2 h at 800 °C or almost entirely suppressed by annealing in 10% H_2/90%

Ar at 500 °C[129]. Thermal annealing could eliminate the unwanted functional groups acting as nonradioactive centres on the surface of ZnO[130]. As a result, the NBE intensity is enhanced (shown Figure 4-16a). On the other hand, the deep level emission has been attributed to the presence of large amounts of defects, particularly V_O and V_{Zn} involved complex defects.

Results shown in Figure 4-17 below were achieved on ZnO nanorods grown via ammonia-assisted method.

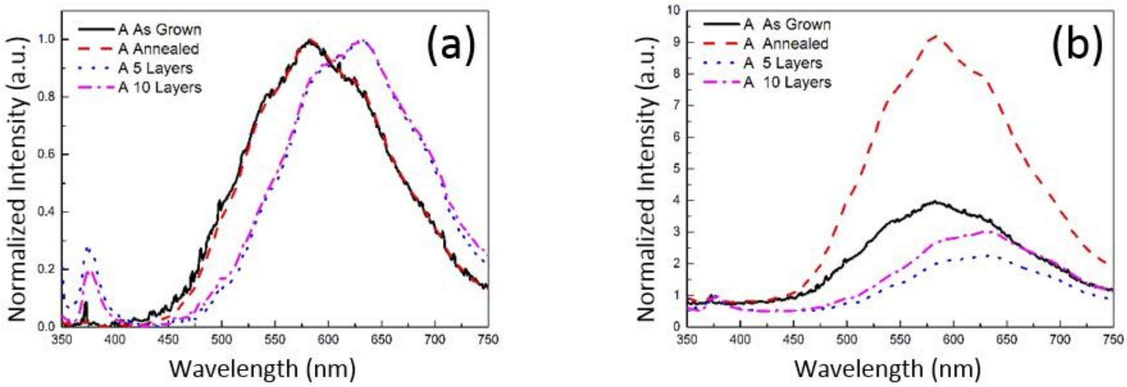

Figure 4-17: Photoluminescence spectra of ammonia-assisted ZnO with TiO_2 deposition. (a) Normalized data, (b) Normalized to the peak intensity of near band edge emission.

Comparing to PL results from ZnO grown via pH=6 method, 5 and 10 layers TiO_2 coated ammonia-assisted ZnO show same increase in NBE and redshift in DLE. Annealed ZnO however shows the weakest NBE, i.e. Strongest DLE. Also to be noted, unlike pH=6 synthesised ZnO which shows a redshift of DLE after annealing, ammonia-assisted ZnO shows no redshift after annealing. This is attributed to the presence of excessive ammonia during the growth of the nanorods.

Due to the presence of ammonium hydroxide, the production of ZnO occurs via the equilibrium reactions[131] is shown in Equation 4-1 and Equation 4-2:

$$Zn\left(OH\right)_4^{2-} \leftrightarrow ZnO + H_2O + 2OH^-$$

Equation 4-1

$$Zn(OH_3)_4^{2+} + 2OH^- \leftrightarrow ZnO + 4NH_3 + H_2O$$

Equation 4-2

This indicates once the Zn-precursors were exhausted, dissolution of ZnO would initiate.

Yellow DLE at ~570 nm (2.2 eV) is observed to be dominant peak for both as-grown and annealed samples, which could be linked to $Zn(OH)_2$ on the surface[127] as well as oxygen interstitials[104,119,128]. It is suggested that excessive ammonium induced large amount of $N\text{-}H_x$ and atmospheric nitrogen species on the surface of the material[131] prior to annealing. These species were oxidized during the air-annealing process to form ZnO. Simultaneously, $N\text{-}H_x$ species trapped in the nanorod bulk would dissociate and form N^- and H^- related species[131]. This led to N-doping of the nanorods, while the liberated H^+ gradually diffused out of the rods[132]. H^+ species acted as hydrogen donor at the surface and are considered to increase the surface recombination sites which reduced intensity for NBE[119].

The high pH synthesis environment arises from the high quantity of available hydroxyl ions, which provides an excess of oxygen for the reaction. It has been reported that the orange PL form oxygen rich films can be obtained by oxidative annealing[133]. Hence, the shift towards orange emission is attributed to oxidative annealing. TiO_2 coating is also suggested to induce large amount of surface trap sites due to incomplete crystallization. It is confirmed in HRTEM images (Figure 4-13) that the shell coating is not uniform and fully crystalline. Also, 5 layers coated sample shows stronger NBE than 10 layers coated sample, consistent with the results from Figure 4-16a.

To summarize, for bare rods without surface modification, it is beneficial to anneal the rods grown via pH=6 method but not beneficial to anneal the rods grown via ammonia-assisted rods. With TiO_2 coating, rods grown via both methods show improved NBE emission which is suggested to reduce charge recombination process for solar cell application.

4.3 Photovoltaic characterizations:

Section 4.1 and Section 4.2 covered the growth of ZnO with various aspect ratios and the fabrication of corresponding ZnO/TiO_2 core-shell structures. This section will present results covering the effects of various photo anode structures, dye adsorption time, electrolyte concentration, and Pt-counter electrodes on the performance of liquid-state photovoltaic performances. The goal was to optimize the parameters using these results, to achieve liquid-state DSSCs with stabilized and relatively high efficiencies (comparing to literature record 1.5%[47]).

4.3.1 Effect of TiO_2 shell coating

This section investigates the effect of TiO_2 shell coating on the performance of LSDSSCs. ZnO nanorods synthesised with different growth methods were used.

4.3.1.1 Core-shell structure based on ZnO via pH=6 synthesis

For results shown in Figure 4-18 below, nanorods were grown via pH=6 synthesis for 6 h. The substrates were annealed at 500 °C for 1 h. N719 dye soaking time was 6 h. Pt counter electrode was thermally deposited onto FTO.

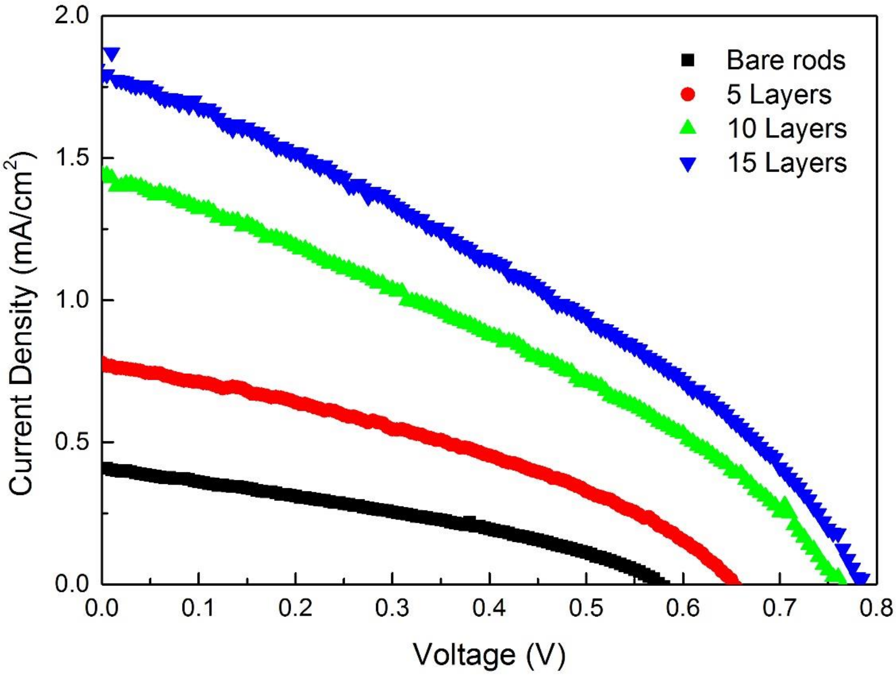

Figure 4-18: *J-V* plot of LSDSSC on ZnO/TiO_2 core-shell structures. ZnO synthesized via pH=6 method. The length and diameter of the rods were 1.63 µm and 46.57 nm, respectively.

Table 4-2: Solar cell parameters of LSDSSC on ZnO/TiO_2 core-shell structures.

Layers	J_{sc} (mA/cm^2)	V_{oc} (V)	P_{max} (mW/cm^2)	*FF*	PCE (%)
0	0.40	0.56	0.08	0.35	0.08
5	0.72	0.63	0.15	0.34	0.15
10	1.41	0.75	0.34	0.33	0.34
15	1.79	0.79	0.47	0.34	0.47

Figure 4-18 and Table 4-2 show the performance increased by applying more layers of TiO_2 coating on nanorods grown via pH=6 method. Enhancement of the performance come from both increase of J_{sc} and V_{oc}. It can be seen that the deposition of the TiO_2 shell increases the J_{sc} and V_{oc} along increased layers of deposition.

Without any TiO_2 shell coating, bare ZnO-based device shows poor performance due to low current. Part of the reasons is due to short rods utilized (1.63 μm), which leads to insufficient surface area. Another reason could be due to the poor chemical stability of ZnO towards acidic N719 dye. As reported, dye precipitation in ZnO structure would cause a decrease in the current and performance[45]. Dissolution of ZnO by the acidic carboxylic anchoring group of the sensitizer caused insoluble complexes and precipitation in the pores (Zn^{2+}/dye complex).

Judging from the HRTEM images from Figure 4-13, TiO_2 coating increases the roughness and surface area. This leads to higher absorbance of the visible light according to UV-vis results obtained from Figure 4-14, which increases the photo current after TiO_2 shell coating.

The current density J_{sc} can be approximated by the expression[134]:

$$J_{sc} = q \cdot \eta_{lh} \cdot \eta_{inj} \cdot \eta_{cc} \cdot I_0$$

Equation 4-3

Where q is the elementary charge, η_{lh} is the light-harvesting efficiency of a cell, η_{inj} is the charge-injection efficiency, η_{cc} is the charge-collection efficiency. Light-harvesting efficiency is determined by the amount of adsorbed dye, which is proportional to the surface area, the light scattering properties of the photo anode, the concentration of the redox species, and other factors[134]. With increased thickness of TiO_2 shell, it is suggested that light harvesting efficiency increases due to higher surface area. It is confirmed from HRTEM images from Figure 4-13 that TiO_2 shell thinner than 5 nm does not fully cover the rods and remain amorphous. With more layers coated, it is believed that gradual crystallization would result in anatase phase polycrystalline TiO_2 phase. The gradual crystallization also improves charge-injection and charge collection efficiency[14] due to reduced bulk and surface trap sites[14]. Additionally, faster electron injection efficiency is also expected for TiO_2

coated ZnO nanorods when compared with bare ZnO nanorods, because the ZnO conduction bands are largely composed of empty *s* and *p* orbitals from Zn^{2+}, while those of TiO_2 consist predominantly of empty *3d* orbitals of Ti^{4+} [135]. As a result, photo current improves with the thickness of TiO_2 shell coating.

As for V_{oc}, it also increases with the coating thickness up to nearly 0.8 V, which is comparable to the state of the art ZnO-based DSSC[135]. The improvement of V_{oc} is mainly attributed to the suppressed interfacial recombination. Recombination not only causes loss of photo-generated electrons leading to a reduced J_{sc}, the presence of a high density of recombination centres also facilitates the rapid recombination of electrons and holes. This affects V_{oc} by decreasing the concentration of electrons in the conduction band of the semiconductor and affects the photo current by decreasing the forward injecting current[136]. The low V_{oc} for the uncoated ZnO nanorods could be the result of high levels of recombination. With increased TiO_2 shell thickness, recombination is gradually suppressed, leading to less recombination and therefore higher V_{oc}.

In general, J_{sc}, V_{oc} and efficiency increase with shell thickness, which is attributed to several reasons: (1) the TiO_2 sol penetrated into the nanorods array interspace during the dip coating and covered the entire surface, this prevents the formation of Zn^{2+}/dye complex; (2) the large amount of defects, which easily trap photo generated electrons on the nanorods were passivated by TiO_2; (3) the electron back transfer from ZnO core to oxidized dye molecules was suppressed[135].

4.3.1.2 Core-shell structure based on ZnO via ammonia-assisted synthesis

ZnO nanorods made via ammonia-assisted method have higher aspect ratio and higher surface area as shown in Figure 4-6. This is considered to improve the dye loading and the photo current of the device. In this section, both 6 μm and 11 μm long rods were tested with various thickness of TiO_2 shell coating.

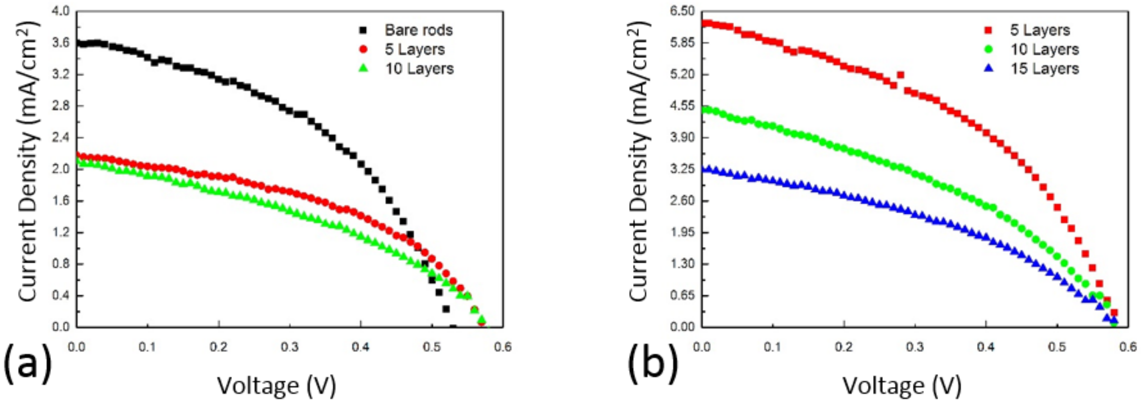

Figure 4-19: *J-V* plots of core-shell devices from ammonia-assisted ZnO. (a) 6 μm long ZnO, (b) 11 μm long ZnO.

Table 4-3: Solar cell parameters of devices from ammonia-assisted ZnO nanorods.

Length	Layers	J_{sc} (mA/cm²)	V_{oc} (V)	P_{max} (mW/cm²)	*FF*	PCE (%)
6 μm	0	3.60±0.18	0.52±0.07	0.86±0.10	0.46±0.05	0.86±0.10
	5	2.18±0.36	0.57±0.02	0.57±0.05	0.46±0.03	0.57±0.05
	10	2.11±0.50	0.57±0.04	0.48±0.06	0.40±0.02	0.48±0.06
11 μm	5	6.25±0.06	0.58±0.06	1.61±0.17	0.44±0.03	1.61±0.17
	10	4.47±0.53	0.58±0.06	1.01±0.16	0.39±0.02	1.01±0.16
	15	3.24±0.25	0.58±0.06	0.74±0.12	0.40±0.06	0.74±0.12

For 6 μm long rods, devices made from bare rods were tested to compare devices made with 5 and 10 layers of TiO_2 shell coated rods. It can be seen from Figure 4-19 and Table 4-3 that, the application of shell reduces photo current from 3.60 mA/cm² for bare rods to 2.18 mA/cm² for 5 layers coated rods and finally down to 2.11 mA/cm² for 10 layers coated rods. On the other hand, V_{oc} is improved from 0.52 V to 0.57 V. In general, efficiency dropped from 0.86% down to 0.48%, which is mainly

caused by the drop of current and *FF*.

For 11 μm long rods, 5, 10 and 15 layers of TiO_2 were coated. The results show consistency comparing to results achieved on 6 μm long rods. J_{sc} drops from 6.25 mA/cm^2 for 5 layers coated sample down to 4.47 mA/cm^2 for 10 layers coated sample and finally 3.24 mA/cm^2 for 15 layers coated sample. V_{oc} remains constant at 0.58 V. PCE drops from 1.61% down to 1.01% down to 0.74%.

When comparing from champion PCE (0.34%) achieved on device made from rods (1.63 μm) grown via pH=6 method, champion PCE (0.86%) for device made from rods (6 μm) grown via ammonia-assisted method shows great improvement. PCE is further improved up to 1.61% using 11 μm long rods grown via ammonia-assisted method. This is attributed to the increased surface area from longer rods, which leads to higher dye loading and light scattering effect. According to Equation 4-3, higher light harvesting efficiency can be obtained on longer rods with higher aspect ratio.

For devices made from ammonia-assisted rods, the drop of photo current is suggested to be caused by the morphological change of the ZnO after TiO_2 shell coating. As seen from SEM analysis (Figure 4-9), ammonia-assisted rods with high aspect ratio tend to fuse at the top. The fused tip however, during the coating process of TiO_2, becomes agglomerate sites for TiO_2 nanoparticles, as seen in Figure 4-10.

Comparing the morphological changes to the UV-Vis absorption results of the dye-loaded ZnO nanorod with various TiO_2 shell thicknesses shown in Figure 4-15, it can be seen that these agglomerates do lead to an increase in dye loading once they reach a certain size after 15 layers. Higher dye loading is expected due to the higher surface volume ratio of TiO_2 nanoparticles than ZnO nanorods, but it is possible, as seen in Figure 4-9, that at lower thicknesses much of the TiO_2 fills between the nanorod tips, and therefore may not significantly increase the available surface area. However, despite the increases of optical absorption, the TiO_2-coated samples produce lower J_{sc}. It is possible that the charge injected into the agglomerates would have a much higher probability of recombining while travelling through the TiO_2 agglomerates than through a thinner TiO_2 layer or bare nanorods; this TiO_2 coating is not optimized for charge transport, only being intended to form a surface coating on the nanorods. Thus, although longer rods improved light absorption and efficiency, extra layers of TiO_2 coating do not improve J_{sc}, despite increasing light absorption. Therefore, it can be concluded that for the TiO_2 coating to be beneficial, the ZnO nanorods need to be synthesised via pH=6 method without additives such as ammonium or PEI to produce well-aligned rods with separated tips, preventing the agglomeration seen here. It is also suggested that the TiO_2 shell may not be fully crystalline. From HRTEM, it is suggested that part of the film is still amorphous, possibility due to limited thickness. This is considered to be insufficient for electron injection. The shell would act as a barrier layer to electrons that move from dye molecules into ZnO core[136].

Despite the drop in current, V_{oc} is improved by TiO_2 shell coating. TiO_2 shell could passivate the surface recombination sites by forming an energy barrier that prevents photo injected electrons from approaching the nanorods surface[14]. The band gaps and band edge energies of ZnO and anatase TiO_2 are equal within ~50 mV[33,79]. It is suggested that TiO_2 and ZnO can form an n-n$^+$ heterojunction free of band discontinuities with a built-in potential, neglecting any difference in density of states[14]:

$$\Phi_{bi} \approx \frac{kT}{q} \ln \frac{N_D^+}{N_D}$$

Equation 4-4

Where N_D^+ and N_D are the donor concentrations in the heavily doped ZnO core and more light doped TiO_2 shell, repectively[137]. It was suggested that the build-in potential could reduce the electron concentration at the surface of the rods by a factor of exp(-Φ_{bi}/kT), which would decrease the rate of recombination and improve the voltage.

4.3.2 Effect of dye adsorption time

4.3.2.1 Optimal dye adsorption on bare nanorods.

In this section, performances of devices made on ZnO nanorods from ammonia-assisted growth were investigated, which were soaked in the dye solution for either 2, 3 or 4h. The length of the rods was 11 μm.

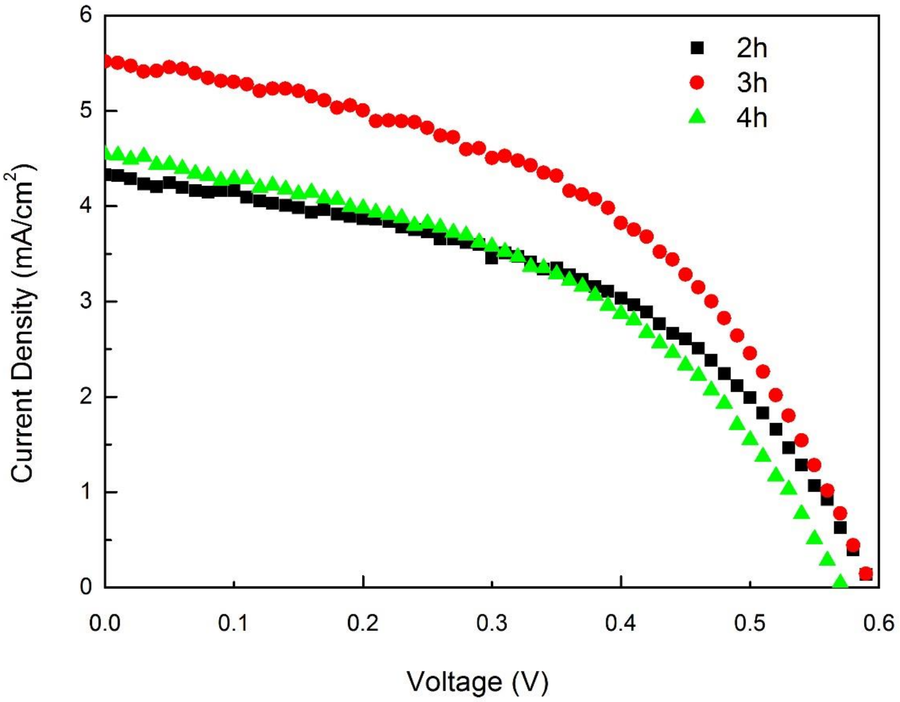

Figure 4-20: *J-V* plot of LSDSSCs on bare nanorods with various dye loading time.

Table 4-4: Solar cell parameters of LSDSSC on bare nanorods with various dye loading time.

Dye loading	J_{sc} (mA/cm^2)	V_{oc} (V)	P_{max} (mW/cm^2)	FF	PCE (%)
2	4.33±0.04	0.59±0.02	1.22±0.20	0.48±0.04	1.22±0.20
3	5.51±0.07	0.59±0.02	1.55±0.08	0.48±0.02	1.55±0.08
4	4.61±0.16	0.56±0.03	1.17±0.02	0.45±0.04	1.17±0.02

It has been reported that for bare ZnO nanorods, 1 h dye soaking is enough to achieve high dye loading without building up Zn^{2+}/dye complex that form from the slow etching of ZnO by the acidic N719 dye[45,138]. It is also reported that prolonged time (up to 12 h[14], 24 h[135,136]) of dye loading could be applied with TiO_2 shell coated rods. This is due to slower rate of dye adsorption on the more acidic TiO_2 surface. From Figure 4-20 and Table 4-4, it is found that for bare rods, 3 h dye loading gives higher efficiency comparing to 2 h and 4 h dye loading time. Samples dyed 3 h exhibits higher photo current. It is suggested that, for ammonia-assisted rods with high surface area, slightly longer dye adsorption time would be required to deposit an optimal dye molecule layer. Less dye loading time (2 h) may result in rods exposed without full N719 coverage and prolonged dye loading time (4 h) may form Zn^{2+}/dye complex which causes recombination. This is also supported by the slight drop in V_{oc} and FF for cells made from 4 h dye adsorption time.

4.3.2.2 Effect of shell coating on the optimal dye adsorption time

It has been reported that the application of shell would prolong the optimal dye adsorption time (up to 12 h[14], 24 h[135,136]). This section investigates the effect of shell coating on optimal dye adsorption time. Bare rods, 5 layers TiO_2 coated rods and 10 layers TiO_2 coated rods were used as photo anodes for device assembly. Each series of devices has undergone 1, 2, 3, 4, 5 and 6 h of dye adsorption time, in order to identify the optimal dye adsorption time for different structures.

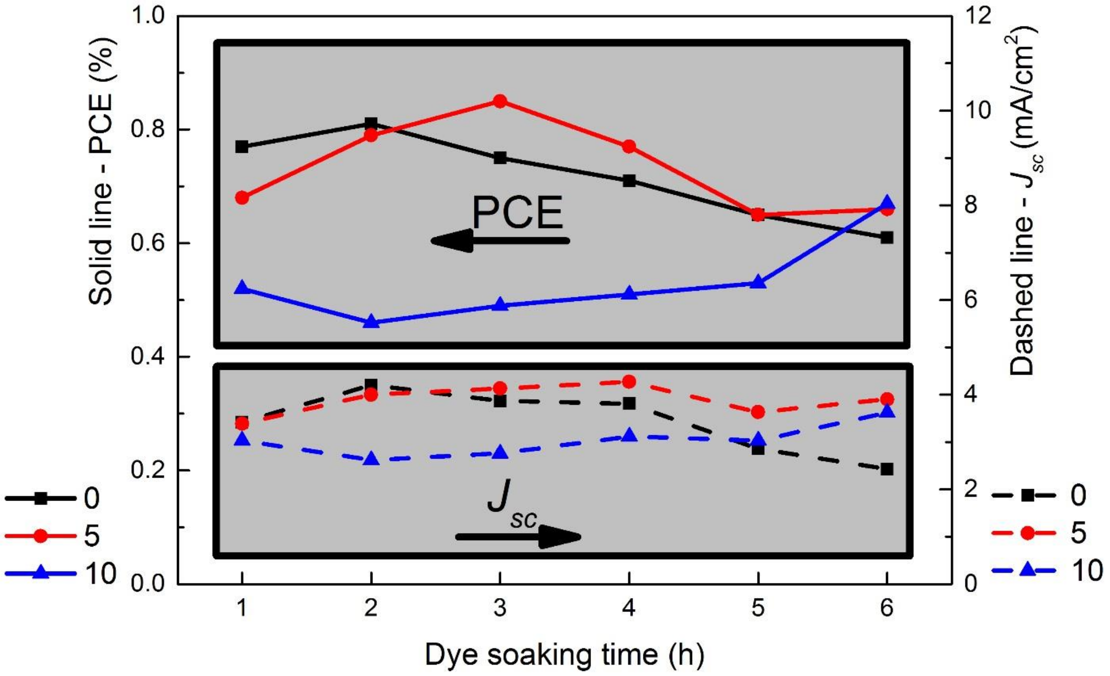

Figure 4-21: Trend of PCE and J_{sc} plot of bare rods and core-shell structures with different dye adsorption time.

Table 4-5: Solar cell parameters of optimal dye adsorption time for bare ZnO and ZnO/TiO_2 core-shell structures. T: Time L: Layers of TiO_2 shell coating. The highest current and efficiency for each structure are marked. The black arrow in the table indicates the trend of optimal dye adsorption time for progressively increased TiO_2 shell coating.

	J_{sc} (mA/cm^2)			V_{oc} (V)			*FF*			PCE (%)		
T/L	0	5	10	0	5	10	0	5	10	0	5	10
1h	3.42	3.39	3.03	0.51	0.55	0.51	0.44	0.37	0.34	0.77	0.68	0.52
2h	4.2	4.00	2.62	0.53	0.54	0.51	0.36	0.37	0.34	0.81	0.79	0.46
3h	3.87	4.13	2.76	0.49	0.57	0.48	0.4	0.36	0.37	0.75	0.85	0.49
4h	3.81	4.27	3.12	0.53	0.54	0.53	0.35	0.33	0.31	0.71	0.77	0.51
5h	2.86	3.63	3.03	0.53	0.55	0.53	0.43	0.33	0.33	0.65	0.65	0.53
6h	2.43	3.90	3.62	0.57	0.56	0.59	0.44	0.3	0.31	0.61	0.66	0.67

From Figure 4-21 and Table 4-5, it can be seen the efficiency follows the trend of J_{sc}, indicating that variation in the photo current is the main variable that changes with dye adsorption time and therefore determines the PCE, as expected. An important finding is that, thicker TiO_2 coating shifted the optimal dye loading time to a longer value, corresponding to the report from Law *et al.*. Comparing bare rods and 5 layer TiO_2-coated rods, optimal dye loading time shifts from 2 h to 3 h and the PCE also increased from 0.81% to 0.85%. For 10 layer-coated ZnO nanorods, the optimal dye loading time further increased to 6 h. However the PCE of 0.67% is lower than the best value achieved from the 5 layer coated sample.

In DSSCs, J_{sc} is a product of efficiencies of light harvesting, electron injection and charge collection[14], as shown in Equation 4-3. Light harvesting efficiency depends directly on the dye loading which is affected by the thickness of TiO_2 coating. Increasing layers of TiO_2 coating increases the surface roughness and therefore increases dye loading. UV-Vis absorbance result confirms improved light harvesting with increased TiO_2 thickness (Figure 4-15). Also, longer dye loading time would also increase the light harvesting until it reached the point where Zn^{2+}/dye complex started to block the election injection process. Hence, for a photo anode with different roughness, optimal dye loading times would be different. The application of a TiO_2 shell not only increases the surface roughness which leads to longer optimal dye loading, but also facilitates the electron injection and collection and prevents the formation of Zn^{2+}/dye complexes. Hence bare rods and 5 layers coated rods show optimal dye loading time of 2 h and 3 h, respectively.

For 10 layers coated device, according to the top view SEM images, TiO_2 agglomerates had already formed at the fusing tips of the rods (Figure 4-10). As discussed in Section 4.2.1, this would improve light harvesting, but lower the charge injection and collection rate due to the limited electron pathways. Therefore it can be concluded that for these ZnO nanorods, 5 layers of TiO_2 with 3h dye soaking gives the optimum efficiency.

4.3.3 Effect of Pt counter electrode and spacers

For DSSCs, the counter electrode also plays an important role. The most common choice for liquid-state iodide/triiodide based cells is platinum-coated transparent conductive oxide (TCO). It is normally prepared by deposition of a thin catalytic layer of platinum onto a conducting glass substrate (FTO). Pt can facilitate the charge collection and transfer processes in FTO, as well as acting as catalysts for reductions of electron acceptors. The iodine reduction at the counter electrodes is several orders of magnitude faster than the recombination rate at the photo anode/electrolyte interface[28]. The regeneration of the oxidized dye occurs in the nanosecond range, which is typically 100 times faster than any recombination reaction and about 108 times faster than the intrinsic lifetime of the oxidized dye[28]. Parameters such as thickness, surface area and morphologies affect the performance of Pt counter electrode.

During the early stage of this project, Pt counter electrode was prepared via thermal deposition of commercial Pt precursor (Platisol T/SP, Solaronix). Later, both commercial Pt electrodes (produced via sputtering, Solaronix) and lab-sputtered (via sputtering using a Pt target) Pt electrodes were tested and compared. Sputtering offers more uniform coating of the platinum than thermal deposition (will be shown in Figure 4-24). For lab-sputtered Pt, lower deposition rate and prolonged sputter time length was used to achieve a rough, uniform Pt layer with high surface area. Sputter plasma current was 10 mA under base pressure of 10^{-2} mBar. A 4 nm/min rate was achieved and 6 times of separate 1 min coating was performed, leading to a theoretical 24 nm thickness of Pt film.

For the spacer between the photo anode (ZnO nanorods) and counter electrode, both Sellotape and Surlyn film were tested. Sellotape has the advantage that it is easy to handle and it does not require heating during deposition. On the other hand, Surlyn film is a hot melt sealing film suitable for laminating photo anode electrodes and closing filling holes. Heat and pressure are required during deposition. Surlyn film easily attracts dust and impurities once the protecting backing foil is removed. It also requires heating at 100 °C under pressure to fully attach to the photo anode, which could potentially degrade the dye molecules.

During the first round of tests, Sellotape was used as spacer, ZnO nanorods were grown via ammonia-assisted method in the same batch. PCE of the devices were tested in sequence with different Pt electrodes on the same ZnO film.

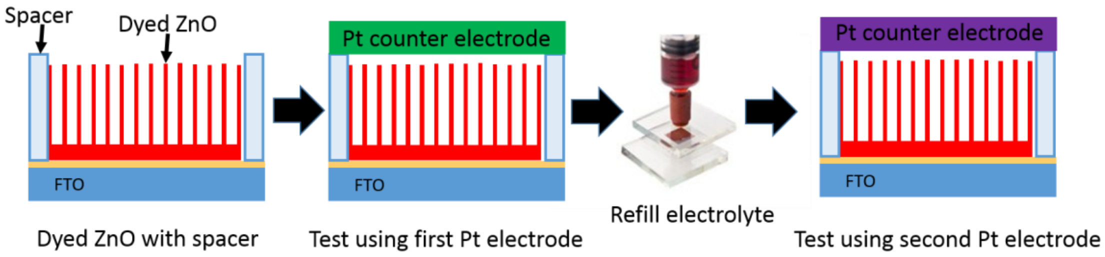

Figure 4-22: Testing sequences to distinguish the performances from different Pt electrodes.

As shown in Figure 4-22, ZnO were made in the same batch and applied same time for dye soaking. After the application of spacer, each sample was selected to test using one Pt electrode. Once the test is finished, the Pt-electrode was removed. Fresh electrolyte was injected, then a different Pt-electrode was applied on the same ZnO. At this stage, the change of the performance could be caused due to electrolyte leakage during the test, which gave out a decreasing performance. By varying the sequence during the testing of two different Pt-electrodes, it would gave a more accurate result.

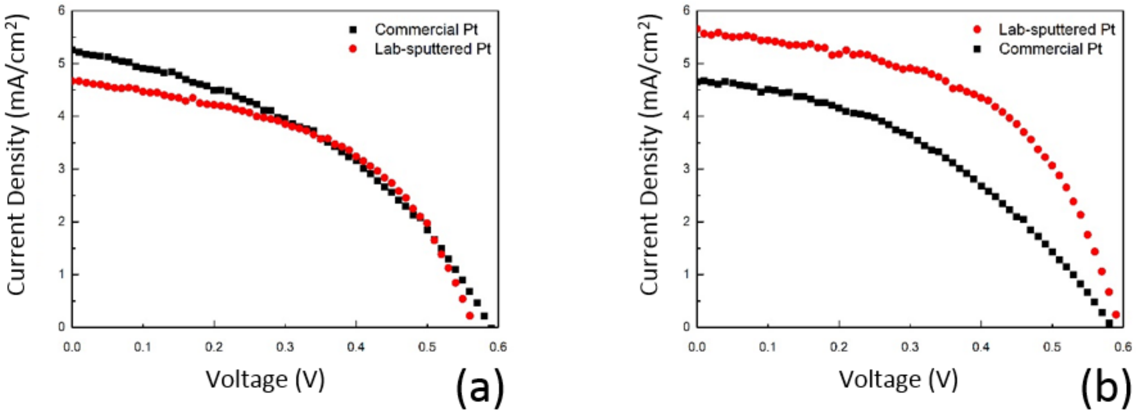

Figure 4-23: *J-V* plots of LSDSSC on different Pt electrode on Sellotape spacer. Both ZnO films were prepared in the same batch and dyed for same time. (a) Commercial Pt electrode was tested first, lab-sputtered Pt electrode was tested second on the very same film. (b) Lab-sputtered Pt electrode was tested first, then commercial Pt electrode was tested second on the very same film.

Table 4-6: Solar cell parameters of LSDSSC on different Pt electrode on Sellotape spacer. C-Pt denotes commercial Pt while L-Pt denotes Lab-sputtered Pt.

	Layers	J_{sc} (mA/cm^2)	V_{oc} (V)	P_{max} (mW/cm^2)	FF	PCE (%)
1	C-Pt	5.26±0.12	0.58±0.02	1.27±0.14	0.42±0.03	1.27±0.14
	L-Pt	4.67±0.10	0.56±0.03	1.31±0.09	0.50±0.02	1.31±0.09
2	L-Pt	5.66±0.07	0.59±0.03	1.76±0.12	0.53±0.00	1.76±0.12
	C-Pt	4.65±0.10	0.58±0.04	1.13±0.06	0.42±0.00	1.13±0.06

Both tests indicate a better performance from lab-sputtered Pt electrodes. Comparing to previous thermally-decomposed Pt, which had a PCE below 1%, both Pt counter electrodes lead to efficiencies higher than 1.1%. Here the voltages for both C-Pt and L-Pt are within the similar range comparing to each other. The improvement of the performance of lab-sputtered Pt is mainly attributed to improved current (4.67 from C-PT to 5.26 mA/cm^2, 4.65 from C-PT to 5.66 mA/cm^2) and *FF* (0.42 from C-PT to 0.50, 0.42 from C-PT to 0.53).

It is reported that 2 nm-thick Pt is sufficient to fully cover the FTO and obtain a reasonable charge transfer resistance[139]. It is also suggested that due to the prolonged sputtering time during lab-sputtered Pt preparation, a porous layer of Pt with high surface area could be achieved. The dependence of J_{sc} on the Pt electrode is attributed to the change of charge transfer resistance, which in this case, is the resistance against electron transfer from the counter electrode to I_3^-. Less charge transfer resistance at the Lab-sputtered Pt/electrolyte interface implies a quicker electron transfer from the counter electrode to I_3^- ions and enhanced J_{sc} for the device[140]. The sheet resistance is also reported to drop by 66% after 25 nm thickness of Pt deposition from that of bare FTO[139]. The fill factor is related to the resistances within the photo anode, electrolyte and counter electrode. The lowered charge transfer and sheet resistance may therefore be the origin of improvement of *FF*. Another factor is that, through visual inspection, lab-made Pt appears a reflective mirror shade after the deposition whereas the commercial Pt is highly transparent. This phenomenon is only reported to happen once the thickness of the Pt reached above 25 nm[139]. The mirror shade is beneficial as it has good light reflecting ability to improve the light harvesting for the dye molecules. Increased light reflectance would reduce the loss of incident light due to transmittance, leading to improvement in J_{sc}.

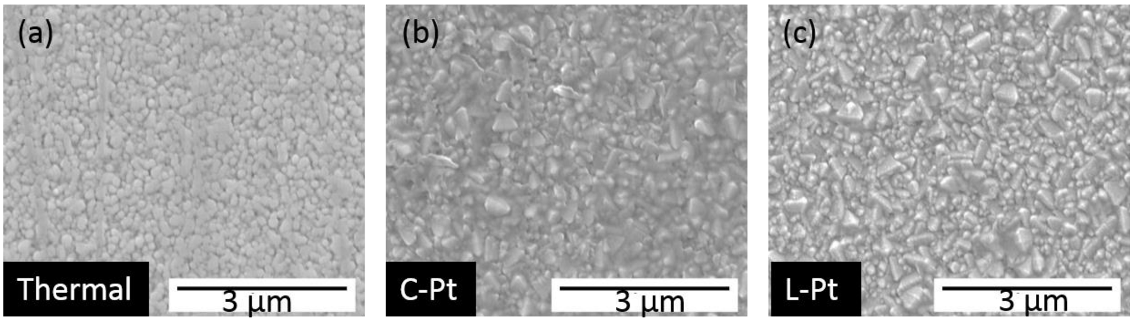

Figure 4-24: SEM images of top view of Pt counter electrode. (a) Thermally deposited Pt, (b) Commercial Pt, (c) Lab-sputtered Pt.

It can be seen from Figure 4-24 that, the morphologies of the Pt via different deposition methods are not same. On thermally deposited Pt, large Pt particles form aggregates with low surface roughness, leading to lower surface area. Commercial Pt and lab-sputtered Pt were both fabricated via sputtering. The thin layer of sputtered Pt could not be identified via SEM due to the resolution limitation. Thus, the morphologies shown in Figure 4-24b and Figure 4-24c are the surface of FTO. However for the commercial Pt, contaminants are visible on the surface. The contaminants covered small areas of Pt, which would block the contact between the electrolyte and Pt, reducing the active surface area. As for the lab-sputtered Pt, no such contaminants are present judging by the obvious morphology of FTO surface. The larger surface area is suggested to reduce the charge transfer resistance onsite and facilitate the electron transport process, leading to a higher current and *FF*.

In the second round of tests, Surlyn film was used as a spacer, and the same testing sequence was utilized to compare:

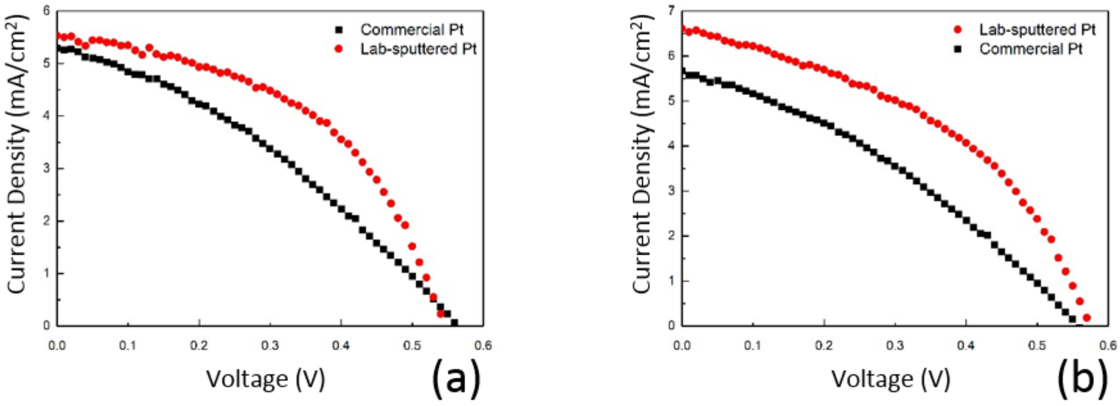

Figure 4-25: *J-V* plots of LSDSSC on different Pt electrode on Surlyn spacer. (a) Commercial Pt electrode was tested first, lab-sputtered Pt electrode was tested second on the very same film. (b) Lab-sputtered Pt electrode was tested first, then commercial Pt electrode was tested second on the very same film.

Table 4-7: Solar cell parameters of LSDSSC on different Pt electrode on Surlyn spacer. C-Pt denotes commercial Pt while L-Pt denotes Lab-sputtered Pt.

	Layers	J_{sc} (mA/cm^2)	V_{oc} (V)	P_{max} (mW/cm^2)	*FF*	PCE (%)
1	C-Pt	5.29±0.00	0.56±0.01	1.02±0.07	0.34±0.01	1.02±0.07
	L-Pt	5.53±0.24	0.54±0.03	1.47±0.10	0.49±0.02	1.47±0.10
2	L-Pt	6.61±0.15	0.57±0.02	1.63±0.04	0.43±0.02	1.63±0.04
	C-Pt	5.67±0.07	0.55±0.05	1.07±0.16	0.34±0.02	1.07±0.16

From the results shown in Figure 4-25 and Table 4-7, the same trend further supports the fact that lab-sputtered Pt leads to higher efficiency. The photo current and *FF* are still the determining factors of PCE for this set of results.

The electrolyte is a key component of a DSSC: it functions to collect electrons at the cathode and transport them back to the dye molecules. Important factors for electrolyte include the concentration and amount of electrolyte. In this project, electrolyte was purchased from Solaronix with no further treatment. The spacer affects the amount of electrolyte due to different thickness. A low amount of electrolyte (indicating lower iodine concentration) is difficult to maintain sufficient charge transfer process. Consequently, low redox reaction rate would deteriorate the photo current. At high iodine concentration, higher electron recombination rate at the photo anode/electrolyte interface also deteriorates the performance of DSSC[141]. Here, the amount of electrolyte in the device is determined by the thickness of the spacer since all the working areas of the devices were fixed at 0.49 cm^2 (0.7×0.7 cm). For Sellotape, the thickness is around 35-50 μm while the thickness for Surlyn film is 60 μm. Mathematically, DSSCs using Surlyn film would have a higher amount of electrolyte contained in the devices. During the application of Surlyn film spacer, heating (100 °C) and pressure were applied on the surface of the ZnO film. Comparing to Surlyn film spacer, Sellotape spacer does not require heating. After the deposition, surface of Surlyn film is sticky and rough comparing to the smooth surface from backing of Sellotape.

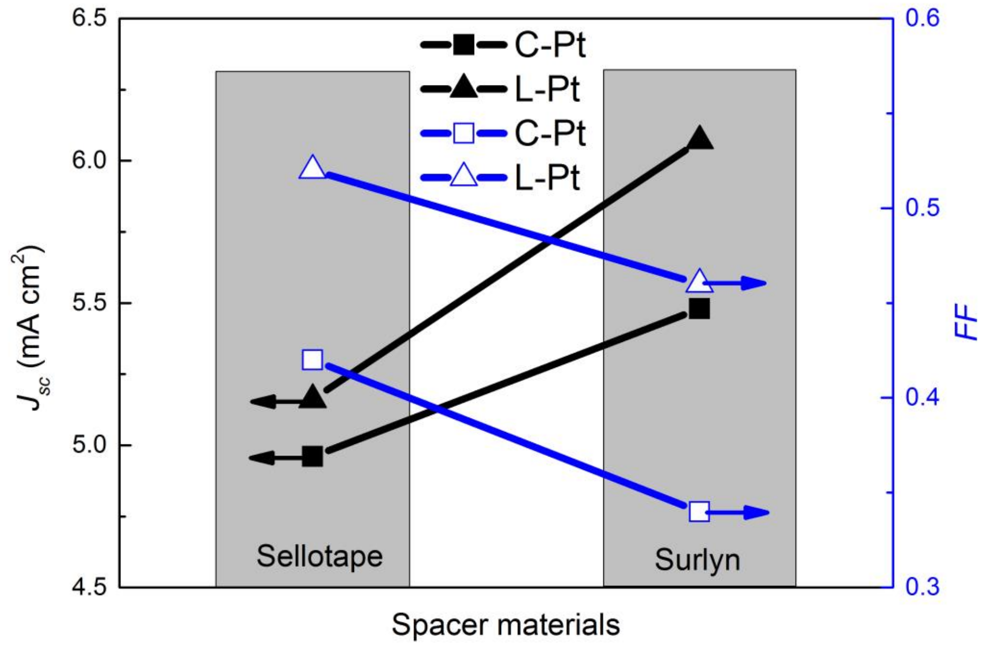

Figure 4-26: Comparison of J_{sc} and *FF* with different counter electrodes and different spacers.

As shown from Figure 4-26, devices using Surlyn spacer have higher current comparing to devices using Sellotape. Average J_{sc} (mA/cm^2) increases from 4.96 to 5.48 for devices used commercial Pt and 5.16 to 6.01 for devices used lab-sputtered Pt. Meanwhile, devices using Sellotape spacer have higher *FF* comparing to devices using Surlyn spacer. Average *FF* increases from 0.34 to 0.42 for devices using commercial Pt and 0.46 to 0.52 for devices using lab-sputtered Pt. While the V_{oc} showed value in same range, 0.58±0.02 V for devices used Sellotape and 0.56±0.02 V for devices used Surlyn film, PCE balanced out to be in the same range. Average PCE for devices using commercial Pt are 1.20% and 1.05% with Sellotape and Surlyn film, respectively. Average PCE for devices using lab-sputtered Pt are 1.54% and 1.55% with Sellotape and Surlyn film, respectively.

Results from Figure 4-26 show the same trend comparing to the literature. It is reported that when the amount/concentration of electrolyte decreased (from Surlyn to Sellotape), the photovoltaic current would decrease, but the fill factor would increase[141]. The reason for the decrease of J_{sc} is attributed to inadequate amount of injected electrolyte causes fewer amount of liberated electrons and fewer amounts of electrons to accumulate at the photo anode[141].

It is suggested that, for limited spacer thickness with inadequate amount of electrolyte, the amount of free electrons is not sufficient to compensate the liberated electrons from the dye molecules; for thicker spacer with higher amount of electrolyte, the liberated electrons from the dye would be compensated, but the increased electron travel path through the electrolyte increased the recombination probability of free electron[142]. The smooth hydrophobic surface of the Sellotape is also considered to accelerate the leakage flow of electrolyte, further reducing the amount of electrolyte in contact with the active working area.

For the *FF*, it is reported that the electron life time constant for the transfer of electron from the electrolyte to photo anode decreased with increasing spacer thickness[141]. Hence the decrease of *FF* in spite of the increase of J_{sc}.

To summarize, devices made on ammonia-assisted rods exhibit higher efficiency which is attributed to the improved surface area. Annealing and TiO_2 coating should not be performed on ammonia-assisted rods. Optimal dye loading for bare ammonia-assisted rods is 3 hours while TiO_2 shell coating further prolonged the optimal dye loading time. Surlyn film is preferred for spacer material due to improved current comparing to Sellotape spacer. Finally, lab-sputtered Pt counter electrodes exhibits the best performance.

4.3.4 Effect of sealing on stability of the device

It has been discussed about the importance of spacer and electrolyte. Another important factor for liquid-state DSSC is the sealing of the device. Due to the volatile nature, electrolyte is easy to flow, spread, leak or even evaporate during testing under heating from incident irradiation. The reduced amount of electrolyte would decrease the photo current and deteriorate the performance of the device. Results shown in Figure 4-27 below were achieved on ZnO nanorods (6 μm) grown via ammonia-assisted method. The experiment was performed prior to the optimisations achieved in above Section 4.3.3. Thus, the results are only used here to compare the sealing effect instead showing an optimal efficiency. Dye loading time was 3 h. Surlyn film was used as spacer and lab-sputtered Pt was used as counter electrodes.

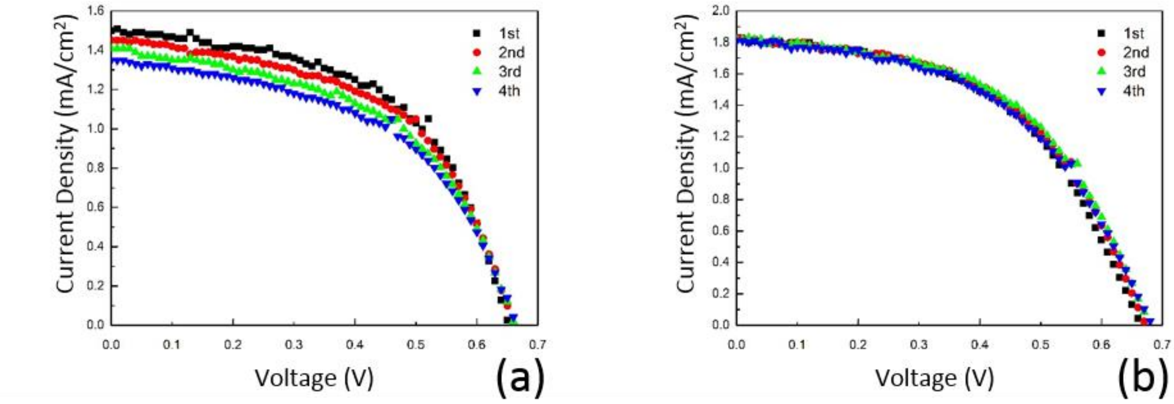

Figure 4-27: *J-V* plots of LSDSSC on the sealing effect in numerical testing order. (a) Without sealing, (b) Sealed. Each test had a 3 minutes' interval.

Table 4-8: Solar cell parameters of LSDSSC on the sealing effect in numerical testing order. Each test had a 3 minutes' interval. The black arrows in the table indicate the trend for the current density and efficiency.

	J_{sc} (mA/cm^2)	V_{oc} (V)	P_{max} (mW/cm^2)	*FF*	PCE (%)
Not sealed	1.50	0.65	0.55	0.56	0.55
	1.45	0.65	0.53	0.56	0.53
	1.41	0.66	0.49	0.53	0.49
	1.35	0.66	0.48	0.54	0.48
Sealed	1.83	0.66	0.62	0.51	0.62
	1.83	0.67	0.63	0.51	0.63
	1.82	0.67	0.64	0.53	0.64
	1.81	0.68	0.62	0.50	0.62

It can be seen from Figure 4-27 and Table 4-8 that, for devices that are not sealed, current decreases along numerical testing order while voltage remains the same. This is attributed to the leakage of the electrolyte. For devices that are sealed, the current remains same and a stabilized PCE (±0.02%) is achieved.

For this set of data, the sealing of the device was achieved by using epoxy to seal the four edges to stop leakage.

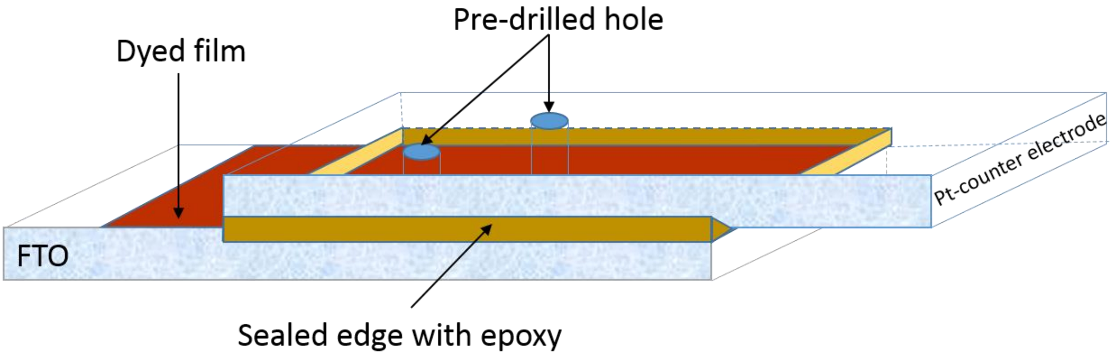

Figure 4-28: Schematic of the sealing of the device using epoxy.

For this design, Surlyn film was used as spacer as the Pt counter electrode needs to fully adhere to the spacer, leaving no route for the leakage. The Pt counter electrode was drilled with two holes for electrolyte inlet and outlet. Once the inside empty chamber was fully filled with electrolyte, another two capping polymer caps were used to seal the holes. The caps were further covered with epoxy. Epoxy was also deposited along the four edges where the dyed film in contact with Pt-coated FTO. The cell was then clamped by clips then settled in the dark to allow the drying of the epoxy. The purpose of this design was to seal the electrolyte within the chamber and block any possible leakage routes.

The resulted structure shows improved stability compared to cells that are not sealed in this way. The major improvement is attributed to the photo current. There is still a slight tendency for the current to decrease. However, the fluctuation is small (±0.02%) and the stability is considered significantly improved comparing to non-sealed cells. The small drop of photocurrent may be caused by the heating of the cell during testing, since each testing had an interval of three minutes. It is also possible that small amount of the electrolyte was evaporated (even being confined within the chamber) during the testing.

Finally, through careful engineering and investigations of the factors of the device fabrication, a stable performance has been achieved.

4.3.5 Effect of acoustic vibration

As reported by Shoaee *et al.*[87], it was shown the solar-to-electric power conversation efficiency of ZnO/P3HT solar cells can be enhanced by the application of modest acoustic vibration. The enhancement has been attributed to reduced charge carrier recombination losses via the piezoelectric effect in the ZnO nanorods[87]. The vibration was applied using a loud speaker at 75 dB, with frequencies in the range of 1-50 kHz[87]. The author suggested the effect may be relevant to other photovoltaic device structures which employ high aspect ratio nanostructures capable of piezoelectric effect. Here in this project, dye sensitized solar cell utilizing high aspect ratio piezoelectric ZnO nanorods were fabricated. To investigate the acoustic effect on the performance of the DSSCs, a stabilized performance was required.

Followed by the previous results achieved in this chapter, the candidate device was fabricated on 11 μm long ZnO via ammonia-assisted growth. No annealing or TiO_2 coating was applied, as this was found to produce the highest efficiencies. 3 h dye loading time was utilized. Surlyn film was used as spacer and lab-sputtered Pt-electrode was firmly bonded with the ZnO film. The edges of the device were sealed using epoxy.

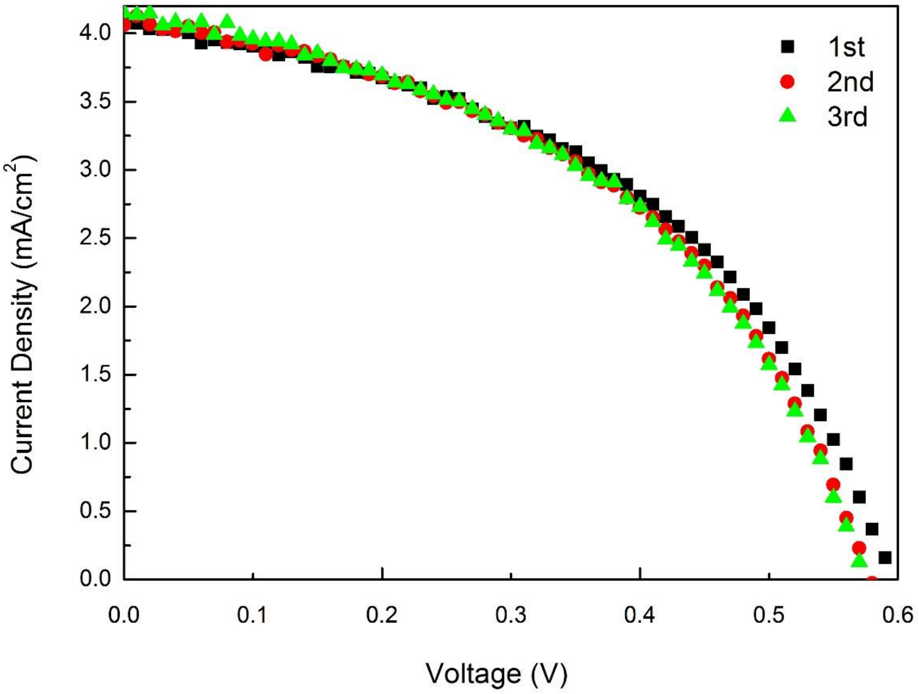

Figure 4-29: *J-V* plot of a stabilized LSDSSC. Each test had a 3 minutes' interval.

Table 4-9: Solar cell parameters of a stabilized LSDSSC. Each test had a 3 minutes' interval.

Test sequence	J_{sc} (mA/cm^2)	V_{oc} (V)	P_{max} (mW/cm^2)	*FF*	PCE (%)
1st	4.10	0.59	1.39	0.47	1.39
2nd	4.06	0.57	1.35	0.47	1.35
3rd	4.15	0.57	1.36	0.47	1.36

It can be seen from Figure 4-29 and Table 4-9 that: a stable efficiency of around 1.37 (±0.02)% is achieved. As discussed above, it is imperative that a stabilized DSSC is achieved. Only by applying acoustic vibration onto a stabilized device, then the change of performance can be attributed to the application of acoustic vibration.

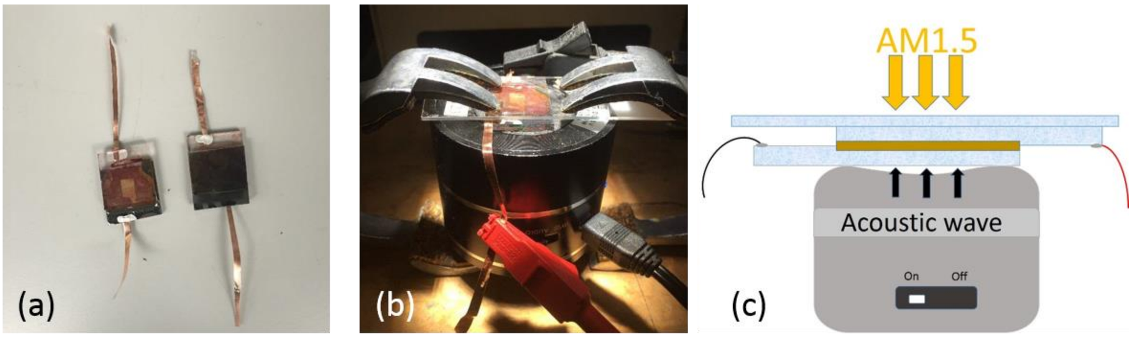

Figure 4-30: (a) Assembled device, (b) Testing set up, (c) Schematic of testing set up.

The apparatus shown in Figure 4-30 was designed to probe the effect of acoustic vibrations on the performance of a ZnO nanorod-based DSSC. As reported by Shoaee *et al.*, acoustic enhancement of polymer/ZnO nanorod photovoltaic device performance was found by simply pointing the speaker towards the device[87]. In our design, the cell was physically attached to a vibration source (speaker) by clamps. The acoustic wave ranged from 5 kHz to 20 kHz. It was suggested by Shoaee that ZnO, as a piezoelectric material, develops a polarization and associated surface charge upon the application of external stress. Acoustic wave would induce vibration upon the nanorods, creating localised strain on ZnO. The resulted alternating polarization would develop across the rods. The associated electric field is then expected to affect the free carriers at the interface. Increased spatial separation of photo-generated electrons and holes thereby would reduce charge carrier recombination and improve the performance of the device[87].

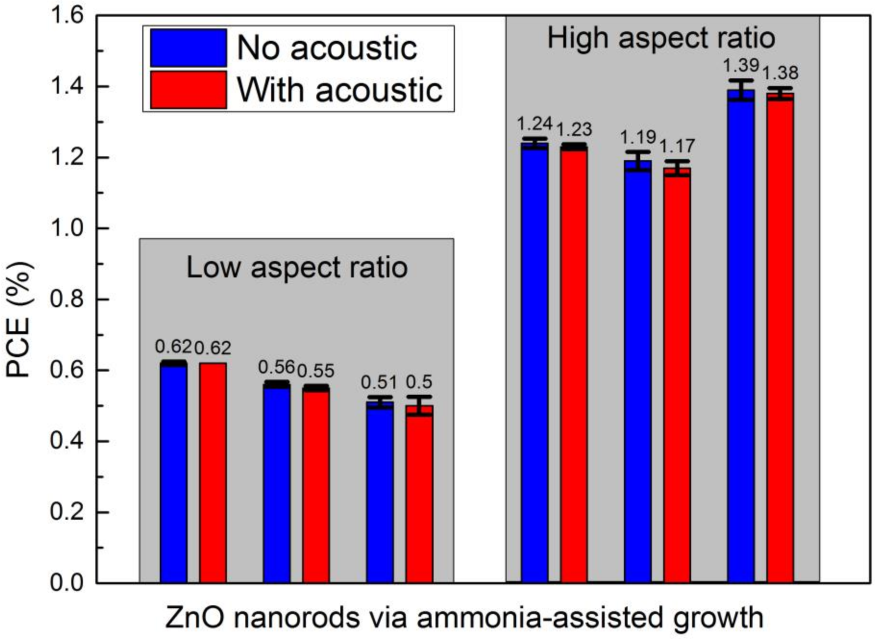

Figure 4-31: Acoustic effect on the average PCEs of liquid-state DSSCs made on low aspect ratio (80, length=6 μm) ZnO and high aspect ratio (92.3, length=11 μm) ZnO. Three cells were tested for both groups.

Figure 4-31 shows the device performances for cells under no acoustic companied to those under acoustic. It can be seen here that acoustic vibration does not affect the performance of the cells. Average PCEs shows a slight decrease for each device, but this is mainly due to prolonged heating during the testing. During the test, even though the cells were sealed. Prolonged heating could still cause boiling and evaporation of the electrolyte, which led to slight decrease in the photo current of the cells, which led to slight decrease in PCE.

To discuss the reasons of this finding, the structure of the device and the testing set up are both considered here. The structure utilized in Shoaee's report was a solid-state hybrid organic-inorganic photovoltaic cell based on ZnO naonrods and poly(3-hexylthiophene) (P3HT). The ITO/ZnO seed layer/ZnO nanorods/P3HT/Au structure was fabricated and tested under acoustic waves produced by a loud speaker (75 dB at 1-50 kHz)[87]. For ZnO-based LSDDSSCs tested here, the proposed effect is shown below:

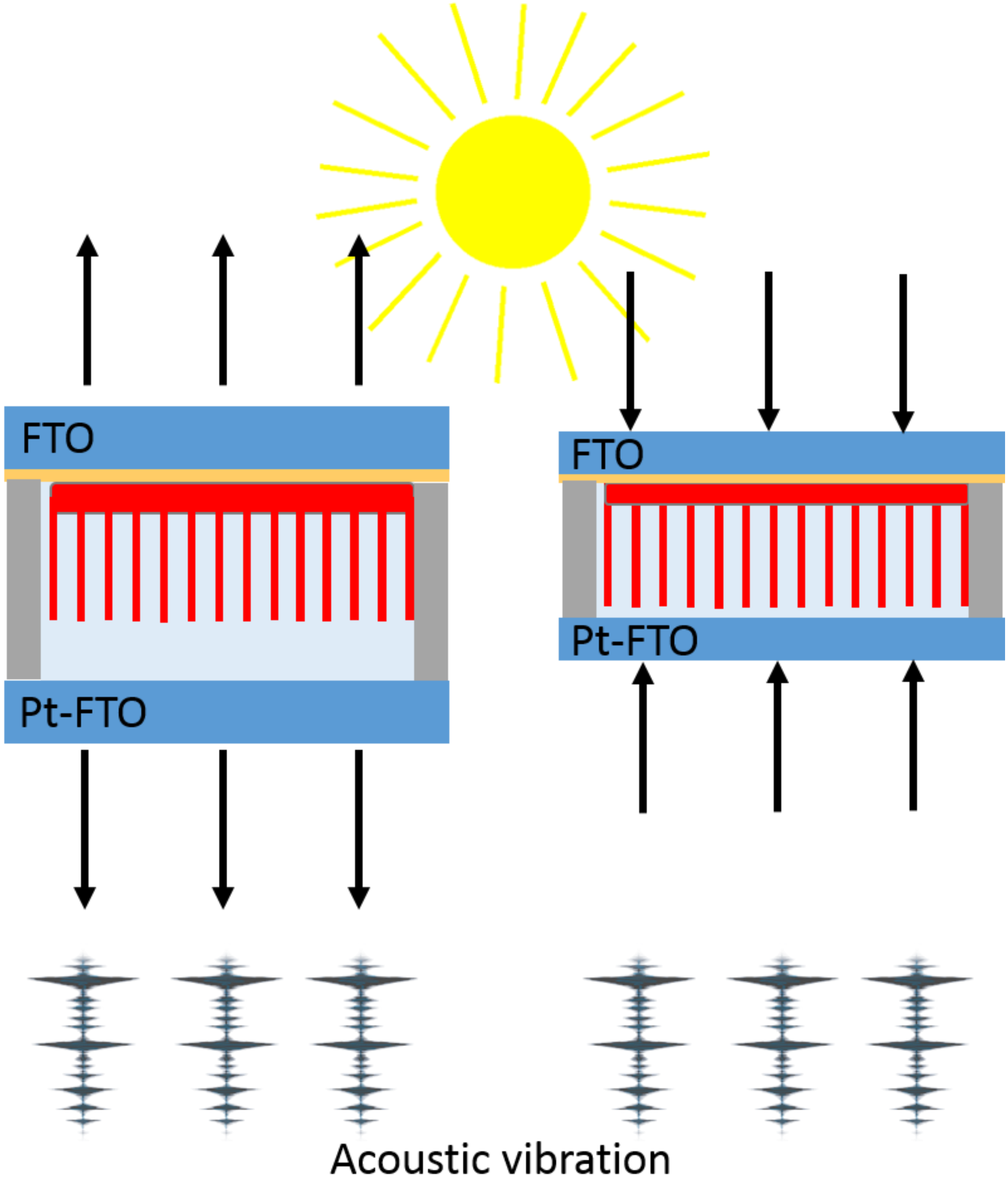

Figure 4-32: Schematic of acoustic application on liquid-state DSSCs. Compression and tension were induced by the transverse acoustic wave.

The substrate of the device is rigid FTO glass. Upon the application of acoustic wave, a small portion of the wave will pass through the Pt-FTO. Acoustic wave would become weaker as a greater number of particles would be involved during travelling. Hard and brittle glass had a tendency of vibrating upon the contact with waves and most of the waves may be refracted. Here acoustic waves can cause localized acoustic vibration, with the nanorods subjected to compression and tension, shown in Figure

4-32. However, it is doubtful that the acoustic wave would be strong enough to cause actual strain on the rods, reason being discussed shortly.

As reported by Z.L. Wang[18], for one ZnO nanorod with diameter 2a and length *l*. The maximum deflection of the nanorod tip $d_{\max}$, can be expressed by:

$$d_{\max} = \frac{f_y l^3}{3EI_{xx}}$$

Equation 4-5

Where f_y is the lateral force, E is the Young's modulus of ZnO, I_{xx} is the cross section area $\frac{\pi}{4}a^2$.

The maximum potential at the surface of the nanorod is:

$$\varphi_{\max} = \pm \frac{3}{4(\kappa_0 + \kappa_\perp)}[e_{33} - 2(1+\nu)e_{15} - 2\nu e_{31}]\frac{a^3}{l^3}d_{\max}$$

Equation 4-6

Where κ_0 is the permittivity in vacuum, $\kappa_\perp$ is the dielectric constant, e_{kp} is the linear piezoelectric coefficient, *v* is the Poisson ratio.

Equation 4-6 suggests that the electrostatic potential is directly related to the aspect ratio of the nanorods. For a nanorod with a fixed aspect ratio, the piezoelectric potential is proportional to the maximum defection at the tip.

For ZnO nanorods surrounded by liquid electrolyte, to induce a piezoelectric potential on the nanorods, the acoustic vibration must induce localized strain. Young's modulus of ZnO nanorods have been reported to be up to 100 GPa[69]. The bulk modulus of liquids are normally within the range of 1-5 GPa[143]. This suggests that nanorods are much stiffer than the liquid. As a result, while the whole device is subject to compression and tension, no strain would occur on the nanorods. Majority of the strain would occur in the liquid. As a result, this small amount of strain would only cause minimum piezoelectric potential, which is not strong enough to greatly affect the charge recombination process. Furthermore, liquid is incompressible. This would further resist the traveling of acoustic wave within the device and reduce the intensity of the acoustic wave that reached the rods. In conclusion, no effect could be observed from acoustic vibration.

In order to compare more closely to Shoaee's device, a series of solid-state DSSC was fabricated and tested. The structure of the device was based on FTO/ZnO seed layer/ZnO nanorods/N719/CuSCN/gold, shown in Figure 4-33. For solid-state DSSC, shorter rods (2 μm) is preferred comparing to long rods. This is due to the poor pore filling of hole transport material comparing to liquid electrolyte. Thus, pH=6 method (8 h growth time) was utilized to grow nanorods on FTO substrates. Dye loading time was 3 h. CuSCN was spray coated as shown in Figure 3-4. A capping layer of

CuSCN was required to provide a flat top surface for gold deposition.

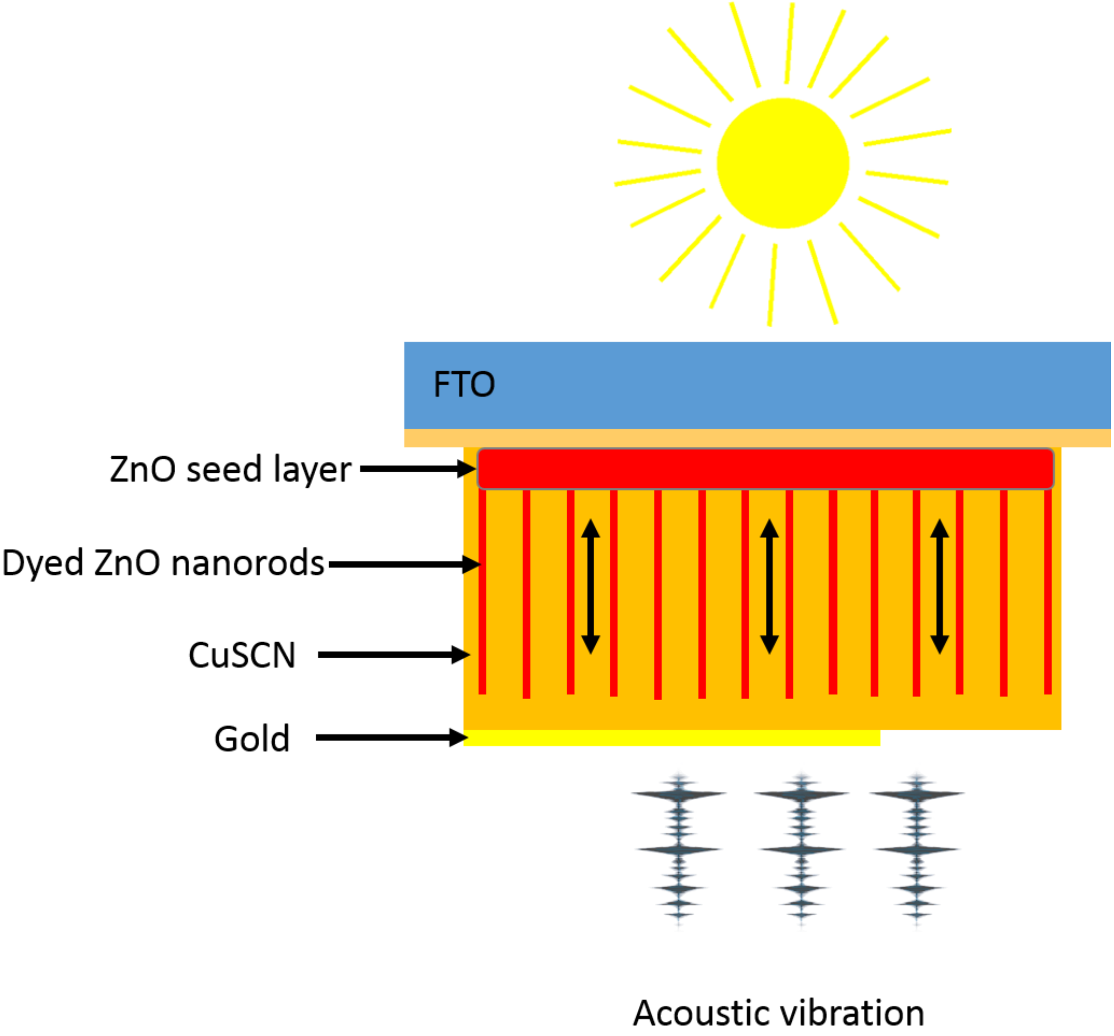

Figure 4-33: Schematic of ZnO-based solid-state DSSC. In order to improve the penetration of CuSCN, short ZnO nanorods grown via pH=6 method were used. Nanorods grown via ammonia-assisted method would lead to poor pore filling due to fused tips and long length.

Compared to liquid-state cells, solid-state cells use CuSCN as hole transport material instead of liquid electrolyte. The thickness of the device is reduced from 60 µm down to approximately 4 µm. Due to the poor conductivity of CuSCN[144] (10^{-4} Scm^{-1}), SSDSSCs are commonly reported to exhibit lower current and lower PCE comparing to LSDSSCs.

The same test was performed on the SSDSSCs. Devices were hold under illumination and multiple *J-V* scans were performed to characterize the PV performance. During the *J-V* scans, acoustic vibration was applied to the device via a loud speaker, numerical tests were performed with speaker turned on and off. The efficiencies with and without the acoustic vibration are shown in Figure 4-34.

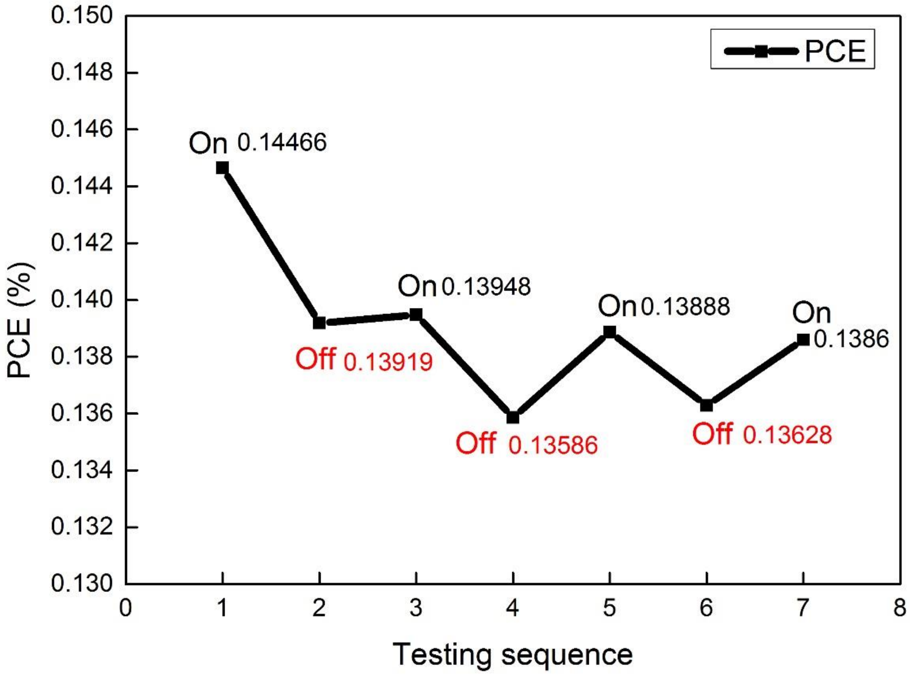

Figure 4-34: PCE of one solid-state DSSC. PCEs were taken in numerical order with 3 mins' interval. 'On' suggests the PCE was taken under acoustic vibration. 'Off' suggests the PCE was taken without acoustic vibration.

Results from Figure 4-34 suggested acoustic vibration could improve the PCE of this device with an average efficiency of 0.1404 (± 0.0043)% with applied vibration, compared to 0.137 (± 0.0021)% without. Therefore, the acoustic vibration demonstrates a small, but statistically significant increase in PCE. This supports the hypothesis that the acoustic vibrations are able to induce the piezoelectric effect in solid-state DSSCs, leading to reduced recombination and therefore increased PCE, similar to the previous report of the ZnO/P3HT system[87], however the effect is not significant nor consistent.

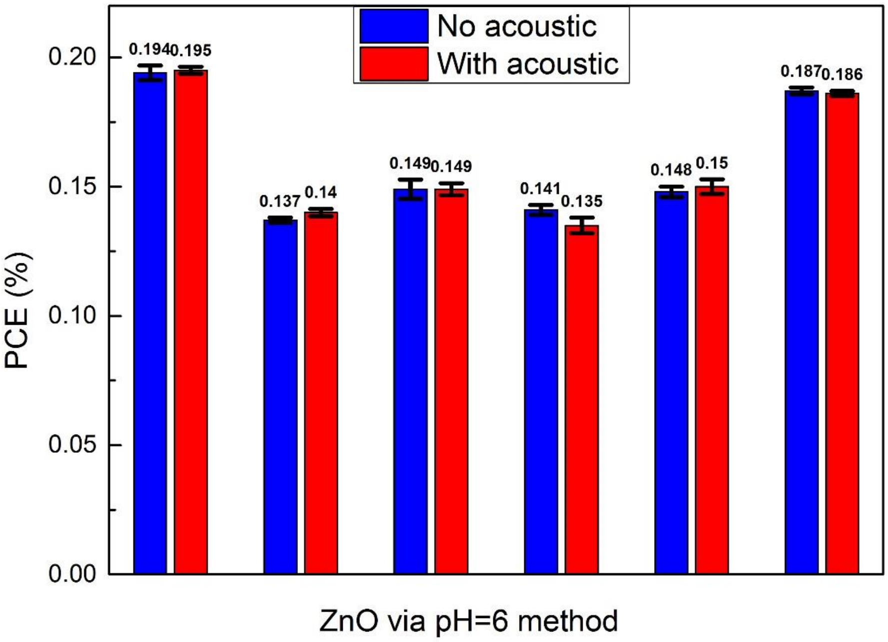

Figure 4-35: Acoustic effect on the average PCEs of solid-state DSSCs made on short ZnO (2 μm). Six cells were tested and average PCEs are shown in the figure. The average PCEs show no conclusive response towards acoustic vibration.

However, acoustic enhancement was not observed in all the devices tested. From Figure 4-35, three cells showed slight increase of average PCE upon acoustic vibration. One cell showed no response and two cells showed decreased average PCE upon acoustic vibration. It is suggested that, the acoustic effect is small and can only cause negligible changes on our solid-state devices, comparing Shoaee's report where 50% increase of PCE was observed upon acoustic vibration[87]. Slight changes in our experiment setup, such as connections and speaker locations, can lead to it not occurring. This is most likely due to a change in the acoustic coupling. Comparing to liquid-state devices which all showed slight decreases in PCE (Figure 4-31), solid-state devices show slightly more promising results. This is mostly attributed to the use of CuSCN instead of liquid electrolyte. In this way, no Pt-FTO is required for counter electrode. The thickness of the device is significantly reduced from 60 µm down to 5 µm. As liquid electrolyte is nearly incompressible and the rigid Pt-FTO would also reduce the penetration of acoustic vibration. A thin device without liquid electrolyte and rigid Pt-FTO has great advantage for the transport of acoustic vibration towards the nanorods. Upon acoustic vibration, higher amount of stress and tension would be able to apply to nanorods, which would lead to a higher degree of strain.

It is also suggested that acoustic vibration utilized in the test set up is not able to induce enough energy to cause enough strain on the rods to affect the charge recombination process. In order to achieve a higher strain, flexible substrates should be considered to replace rigid FTO glass as bottom substrate. In that way, when the substrate is bent to the maximum displacement, highest stress/tension would be applied on the surface of ZnO film. The lateral force f_y applied on the rods would also be maximum, which leads to the maximum deflection $d_{\max}$ according to Equation 4-5. Thus, the highest piezoelectric potential would be generated on the rods according to Equation 4-6, leading to a possible stronger influence on the charge recombination process within the rods.

4.4 Summary

In summary, this chapter has demonstrated the optimization of ZnO-based DSSC and the effect of acoustic vibration upon both liquid-state and solid-state devices. Seed layer, growth time and concentrations of precursor solution were investigated and showed great impact on the morphologies of the ZnO nanorods. ZnO/TiO_2 core-shell structures were fabricated on ZnO with different morphologies. SEM and HRTEM measurements confirmed the success of shell coating. UV-vis confirmed the improved light absorbance with increasing thickness of TiO_2 shells. PL results confirmed the improved near band edge emission after TiO_2 coating which suggests suppressed recombination. Both low aspect ratio ZnO nanorods grown via pH=6 method and high aspect ratio ZnO nanorods grown via ammonia-assisted method were used to fabricate devices. The coating of TiO_2 shell was found to improve the performance on devices made on pH=6 synthesized ZnO and deteriorated the performance on devices made on ammonia-assist synthesized ZnO. This is mainly attributed to the difference of the morphology of the nanorods leading to different core-shell structure. Optimal dye adsorption time was found to be 3 h which was prolonged upon TiO_2 shell coating. The effect of Pt counter electrode and spacer was investigated. It is found that lab-sputtered Pt leads to higher performance due to increased surface area. A proper sealing of the device was achieved via using epoxy. Thus, devices with stabilized PCE were fabricated and tested with acoustic vibration. It is found that: acoustic vibration showed no effect on liquid-state DSSCs, possibility due to the limited amount of energy transferred to the rods due to the higher modulus of ZnO comparing to low bulk modulus of liquid electrolyte. Thus, acoustic vibration could not lead to strain of the rods. However, for solid-state DSSCs which did not use liquid electrolyte or rigid Pt-FTO counter electrode, slight improvements of PCE were found in a number of devices tested. Even though the enhancement is not significant nor consistent across of the devices, this showed a promising design direction of the device. Solid-state devices are suggested to be able to induce higher strains onto the rods. In order to further increase the strain, a flexible substrate would be beneficial. Such design will be discussed in the following chapters for the application of hybrid energy harvesters.

Chapter 5 Hybrid energy harvester based on N719 dye

5.1 Design of the structure of hybrid energy harvester

5.1.1 Kinetic-to-electrical energy conversion

From Chapter 4, it was suggested that a flexible substrate could potentially be able to induce a higher degree of strain on the nanorods which could lead to larger piezoelectric potential. As discussed in Section 2.5, from the report of Briscoe *et al.*, ZnO nanorods grown on a flexible substrate were combined with p-type semiconducting polymer PEDOT:PSS to produce a p-n junction-based device that successfully demonstrated kinetic-to-electrical energy conversion[72]. The voltage and current output of the devices were measured to be in range of 10 mV and 10 µA /cm^2. The maximum possible power density was measured to be 0.4 mW/cm^3. Performance of the device was further improved up to 1.07 V as an instantaneous peak open-circuit voltage giving a maximum calculated 434 µW/cm^2 peak power density, which was achieved by coating the ZnO nanorods using copper thiocyanate (CuSCN)[82]. This was attributed to reduced ZnO surface-state-induced screening.

The improved structure design of the nanogenerator (NG) is shown in Figure 5-1 below:

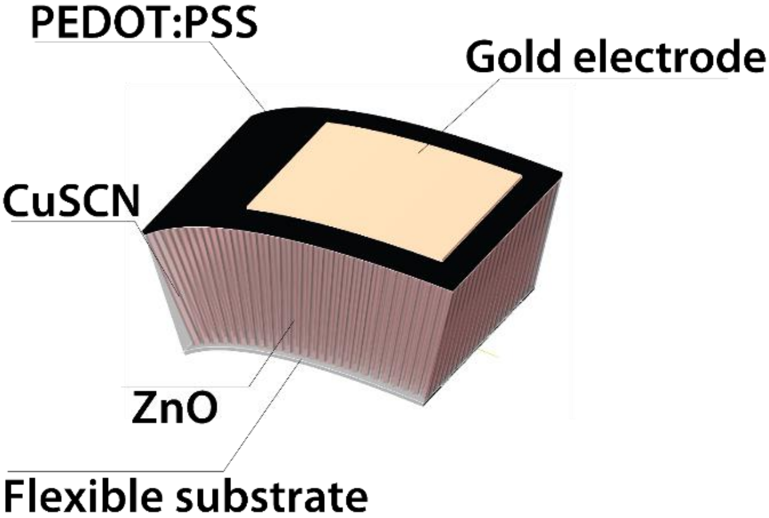

Figure 5-1: Structure of the device designed solely for kinetic-to-electric energy conversion.

As shown in Figure 5-1, ZnO nanorods are grown on flexible substrate (PET). CuSCN coating is applied to passivate the surface of the rods, which is suggested to reduce ZnO surface-state-induced parasitic losses and improve the power density of the ZnO nanorod-based energy harveserter[82]. PEDOT:PSS is then deposited on top, with gold deposited last as the top contact.

The working principle of NG has been discussed in details (see Section 2.5.4). The behaviour is explained by considering the time-dependent changes in band structure resulting from the straining of the piezoelectric ZnO nanorods within the p-n junction. It was suggested that the rate of screening of the depolarization field determines the power output of a piezoelectric energy harvesting device[72].

5.1.2 Solar-to-electric energy conversion

As a p-type semiconductor, CuSCN has also been utilized as hole transporting layer (HTL) in solar cell designs. In the early stages, a TiO_2/light absorber layer/CuSCN structure was investigated and an efficiency of 1.25% was achieved[144]. Alternatively, ZnO nanorods/N719/CuSCN structure was proposed and 1.7%[145] was achieved, with the structure shown in Figure 5-2 below:

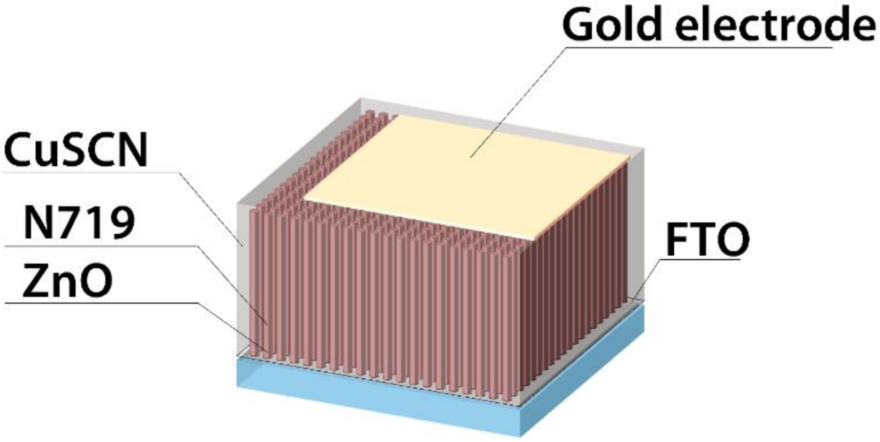

Figure 5-2: Structure of the photovoltaic (PV) designed for solely solar-to-electric energy conversion. ZnO nanorods are grown on rigid substrate (FTO). N719 dye molecules are used as light absorber layer. CuSCN is used as p-type hole transport layer.

In this PV design, unlike in a NG where the CuSCN coating was utilized as a surface modification method, CuSCN is utilized as the hole transport layer. This solid-state DSSC design uses gold as top electrode. To prevent direct contact between gold and ZnO/FTO which would cause short-circuiting, CuSCN would also act as a barrier, meaning the rods would need to be fully embedded. The extra CuSCN film (capping layer) thickness required between the top gold contact and tips of the ZnO to achieve this was suggested to be around 1 μm[145]. Too thick a film would increase the series resistance of the cell due to the low electrical conductivity of CuSCN. It is critical to ensure that the CuSCN layer formed at the top is uniform, yet thin enough for optimum device performance[145].

5.1.3 Design of hybrid energy harvester

Combining the structures in Figure 5-1 and Figure 5-2, the design of a hybrid energy harvester (HEH) is proposed and shown in Figure 5-3 below:

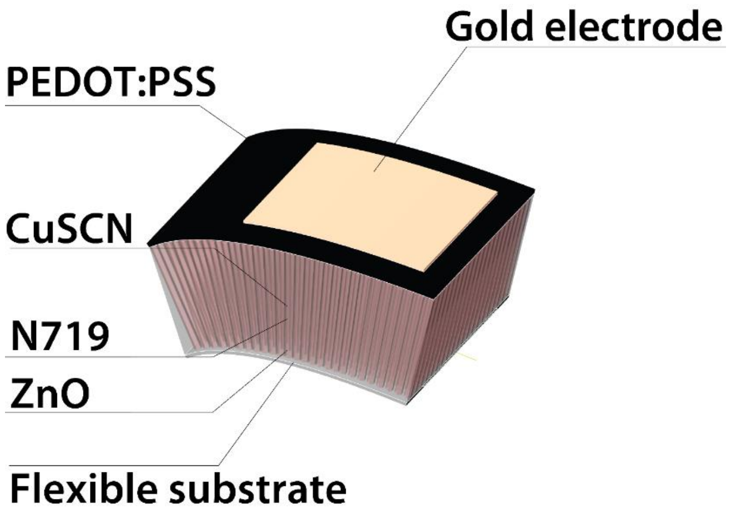

Figure 5-3: Structure of the device designed for hybrid energy harvesting. ZnO nanorods are grown on flexible substrate (typically PET polymer). N719 dye is used as light absorber layer. CuSCN coating is applied to passivate the surface of the rods as well as act as hole transport layer. PEDOT:PSS is then deposited on top, with gold deposited as the top contact.

In this design, a flexible substrate is selected to induce large strain onto the rods. ZnO nanorods are the origin of the piezo potential as well as the electron transport material. The ZnO/N719/CuSCN structure is adapted from the PV design shown in Figure 5-2. Both CuSCN and PEDOT:PSS can act as hole transport materials (HTM). Also to be noted, the CuSCN coating for the initial design is to not fully embed the rods. The thin layer of CuSCN coating is suggested to passivate the surface defects of the rods. This is also to maintain mechanical flexibility and resemble more towards the NG design shown in Figure 5-1. Thus, PEDOT:PSS layer is necessary to ‘cap’ the rods and provide a flat surface for gold deposition.

Compared to the NG design in Figure 5-1, the HEH design simply added an extra layer of N719 dye molecules between the ZnO and CuSCN. The addition of light absorb layer is to improve the light harvesting efficiency of the proposed design.

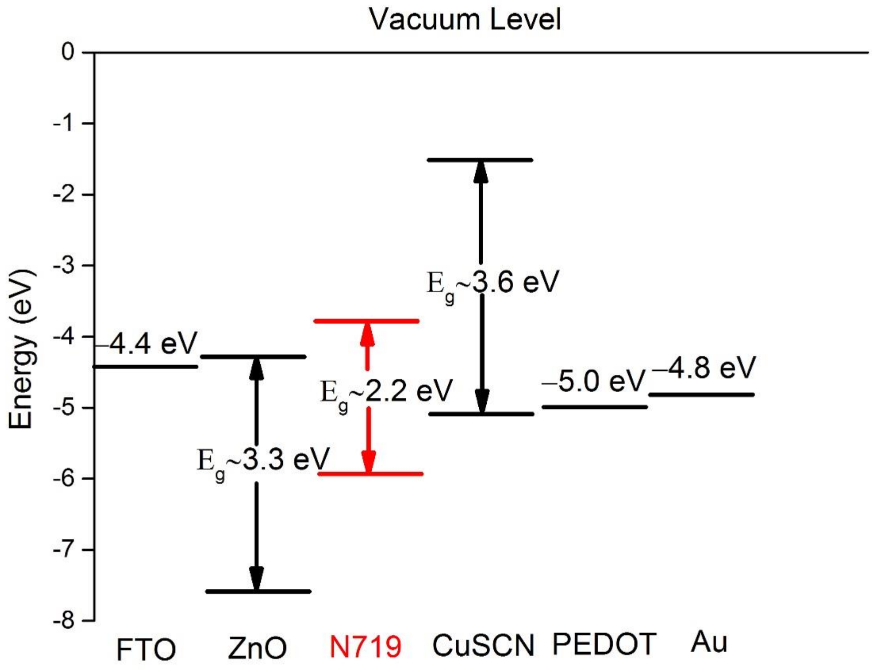

Figure 5-4: Band diagram of the materials used to fabricate the hybrid energy harvester.

Alignment of the band gaps of the materials are shown in Figure 5-4. It is designed that, upon illumination, electron-hole pairs will be separated within N719. Electrons will flow from the conduction band of N719 into ZnO nanorods then onto FTO substrate. Holes will flow from valance band of N719 to CuSCN, PEDOT and then to gold.

For the solid-state DSSC, electrons from the highest occupied molecular orbital (HOMO) of the HTM, instead of the redox couple of the electrolyte from liquid-state DSSC, regenerate the dye molecules. The theoretical open-circuit voltage is the difference between the Fermi level of ZnO (E_F) and the Fermi energy of HTM (E_{homo}). Due to the much larger recombination probability of photo generated electrons from ZnO with holes in the HTM as compared to recombination with the I^- / I_3^- redox couple[35] in liquid-state DSSC, open-circuit voltage, V_{oc}, of solid-state cells is in the range of 400-500 mV (comparing to $V_{oc} \approx 800$ mV for liquid-state cells).

5.1.4 Characterization methods for hybrid energy harvester

In order to demonstrate the device works as a hybrid energy harvester, preliminary tests are required to demonstrate whether it works as a photovoltaic and a nanogenerator separately.

For photovoltaic (PV) devices, electrical characterization is normally investigated using current-voltage scan under illumination. Short-circuit current, open-circuit voltage, fill factor and power conversion efficiency can be calculated to evaluate the performance. For piezoelectric devices (nanogenerator, NG) based on flexible substrates, the strain-induced piezoelectric polarization is studied by bending the device, and simultaneously recording the open-circuit voltage output. One end (the end with the contacts) of the device is normally fixed by a sample holder. The other end of the device is then bent to the maximum displacement of the substrate, followed by a quick release. Bending can be induced manually or by using a cam attached to a motor rotating at a fixed frequency (1-3 Hz) (tip bending). Using a cam has the advantage of maintaining a constant maximum displacement of the device while manual bending can induce larger displacement by bending it further. Another way to induce the bending is oscillating the substrate on a permanent magnetic shaker (oscillating), shown in Figure 5-5. The device is mounted on a spring steel cantilever (optional) then fixed on the moving stage of the shaker. The stage is able to move up and down in controllable frequency and amplitude. By programming the signal generator at various frequency and amplitude, the spring steel would reach its resonance frequency at one point. The device would follow the movement of the spring steel and thus is bent up and down at a constant displacement at a fixed frequency. For both methods, the voltage output can be recorded using a Tektronix TDS2012C oscilloscope in trigger mode.

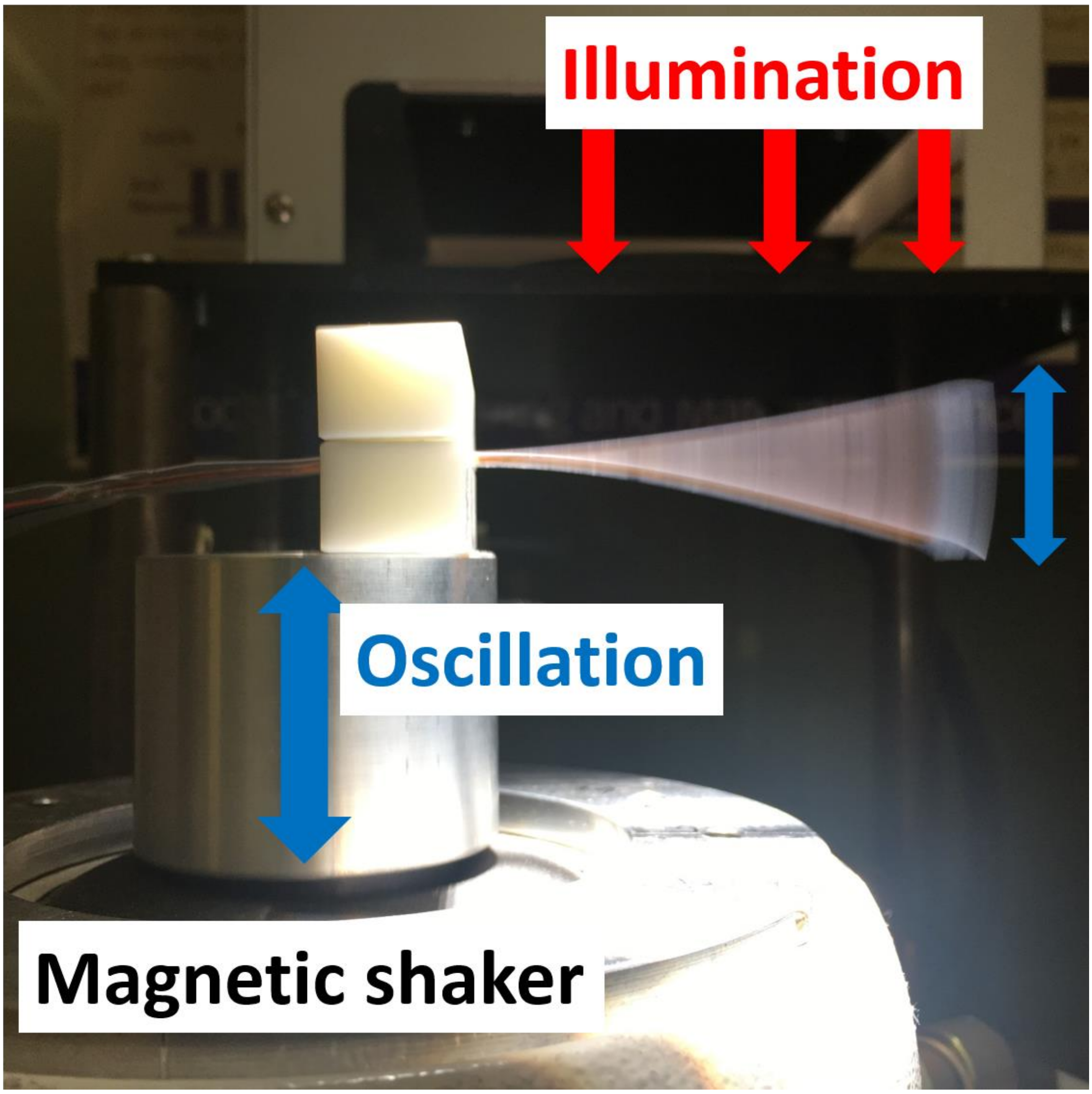

Figure 5-5: Testing setup of HEH device. The long aspect ratio sample under illumination while oscillating.

For the tip bending test, the device would generate an output pulse when it is released from its maximum bending displacement. When released, the strain rate of the device would reach its maximum value and lead to the first and normally strongest peak open-circuit voltage output. A ripple-like oscillating voltage signal is generated due to the mechanical resonance of the plastic base substrate. The device would come to rest when the oscillations are decayed. An example of the signal output plot is shown in Figure 5-6:

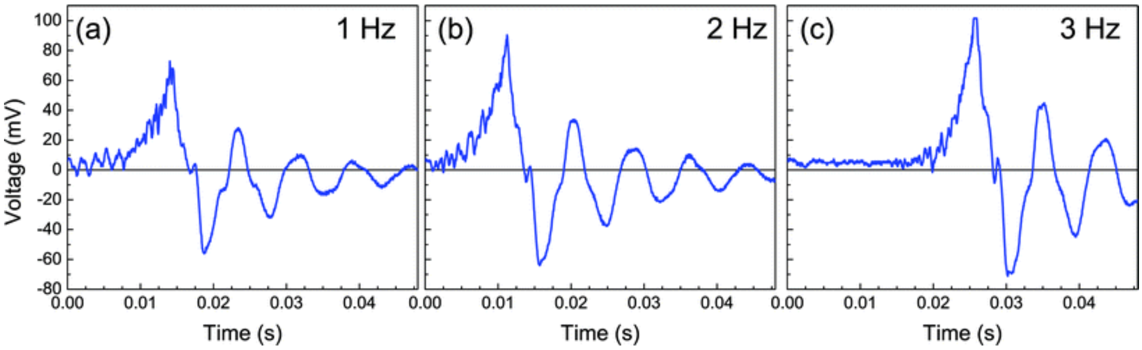

Figure 5-6: Open-circuit voltage output of a ZnO/PEDOT:PSS piezoelectric energy harvesting device. Measurement (a)-(c) were obtained when the cam was set at 1, 2 and 3 Hz. With increase in bending rate, the peak voltage increases from around 80 to 100 mV. This demonstrates that the peak voltage generated by a device can be increased by increasing the strain rate[146].

For hybrid energy harvester (HEH), both tests of *J-V* scan and open-circuit output measurement upon bending are required to demonstrate whether the device works as PV or NG separately.

On the other hand, it is not enough to just measure the open-circuit voltage output of the NG, but to measure the power output of the device, which would make the results comparable to other energy harvesting techniques (such as PVs). To consider the actual working condition, the device is connected to a load. While the most basic test that is common for other energy harvesting techniques is to measure the voltage generated when the device is connected to a range of resistive loads[146], in our case, by measuring the voltage output when connected to a programmable variable resistor, the instantaneous power generated by the device can be calculated approximately using the equation:

$$P = \frac{V^2}{R}$$

Equation 5-1

Where P is the power and V is the peak voltage measured across the load R. Hence, by a sweep of resistances, the peak-voltage V across each resistance R can be used to calculate the peak-power density delivered.

5.2 N719-based HEH using PET

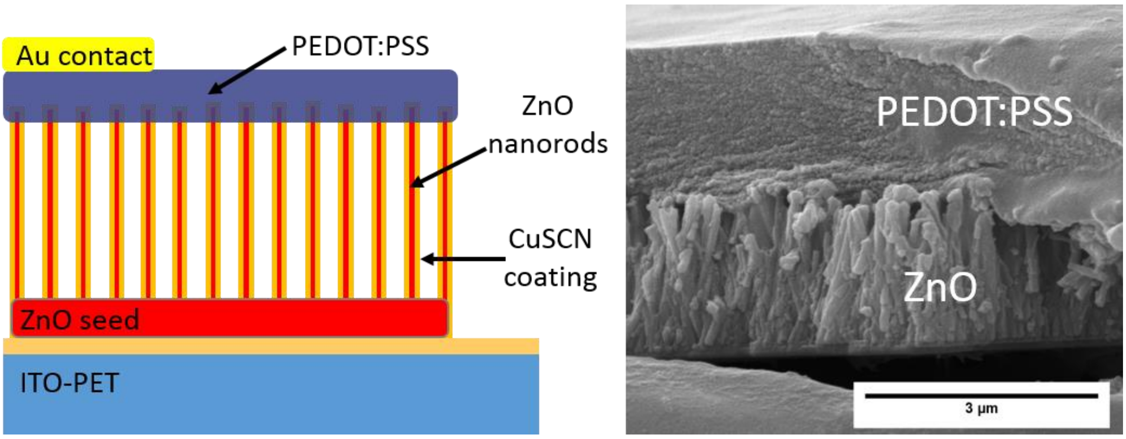

Figure 5-7: HEH design using PET substrate with the corresponding SEM image of the cross section of an actual device.

To demonstrate whether the design would work as a HEH, a batch of NG were first fabricated using the structure shown in Figure 5-1 (NG). As comparison, during the fabrication, 3 samples were dyed using N719 before the CuSCN deposition, leading to the structure shown in Figure 5-7 above (HEH). Thus, by adding a thin layer of N719 dye molecules, the PV and NG performances of the devices can be tested to evaluate the effect of N719 dye coating.

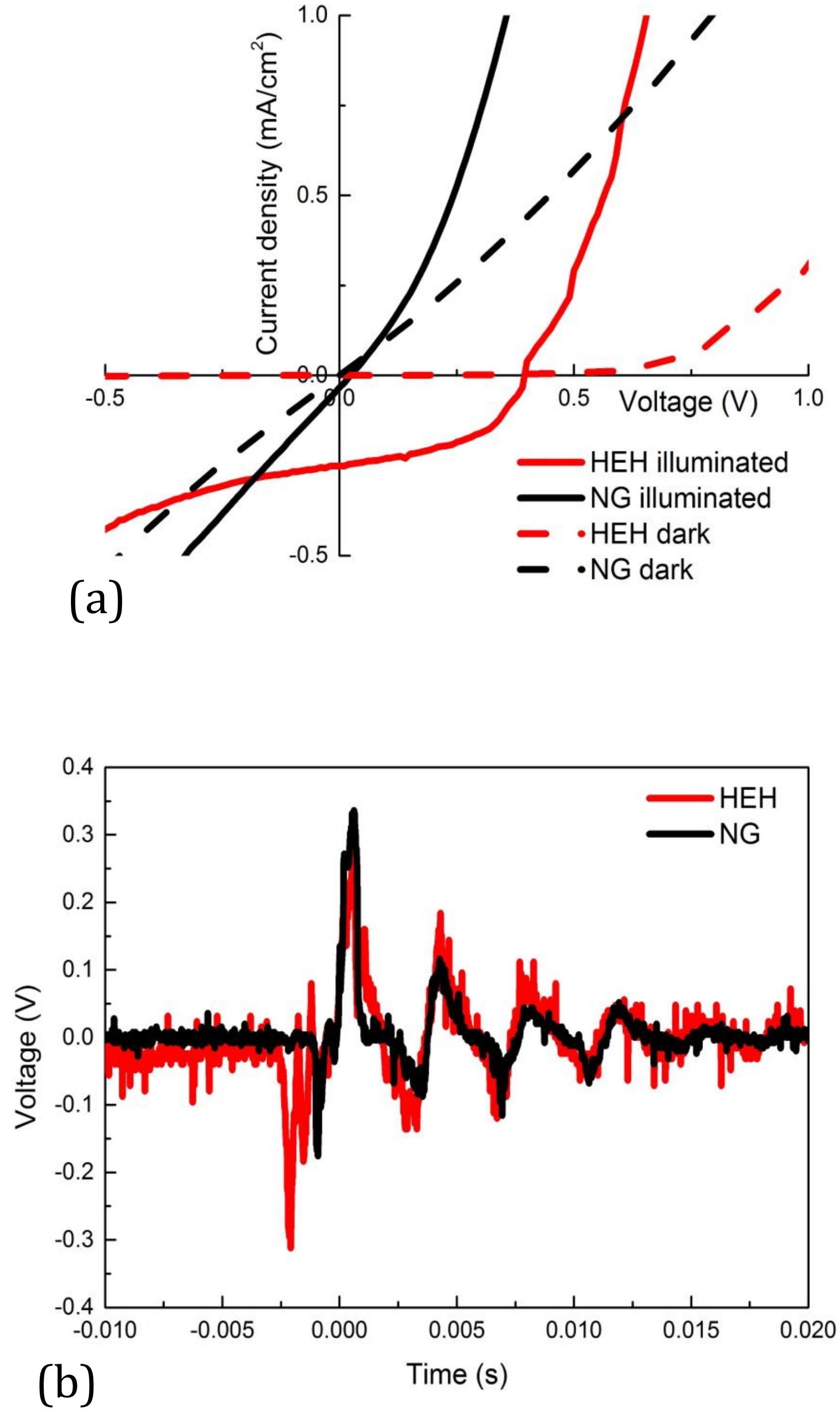

Figure 5-8: (a) Current density-voltage characteristics and (b) Time-dependent open-circuit voltage output of NG and HEH design.

Table 5-1: Solar cell parameters and peak voltage outputs of NG and HEH.

Device structure	J_{sc} (mA/cm^2)	V_{oc} (V)	P_{max} (mW/cm^2)	*FF*	PCE (%)	Peak voltage (V)
NG	0.032	0.02	0.0002	0.31	0.0002	0.336
HEH	0.25	0.39	0.05	0.49	0.05	0.288

It can be seen from Figure 5-8a that, without N719 dye coating, the nanogenerator itself shows poor PV performance, which is mainly attributed to the poor light absorption behaviour without N719. The minimal current and PV response are attributed to the UV photovoltaic effect of the ZnO-CuSCN junction. With an additional N719 layer, the *J-V* plot shifts down and shows relatively stronger PV response. Short-circuit current, open-circuit voltage and *FF* all increased leading to the PCE of 0.05% comparing to 0.0002% without N719. Figure 5-8b shows that the HEH design with N719 still performs as NG. The peak open-circuit voltages are 0.336 V for NG and 0.288 V for NG with N719. However the value is not directly comparable as this bending test was performed manually. The manual error could cause different strain rate which could lead to different peak voltage. This result however is able to confirm the HEH works as PV and NG separately.

Two batches of HEH were fabricated. Four samples were tested: HEH001 and HEH002 from the first batch, HEH003 and HEH004 from the second batch. The structure is based on the design shown in Figure 5-7. PET substrates were sputtered with ZnO thin film. ZnO nanorods were grown using 24 h of pH=6 method. HEH001-002 were fabricated in the first batch with 6 h of N719 dye loading, HEH003-HEH004 were fabricated in the second batch with 4 h of N719 dye loading. CuSCN and PEDOT:PSS were spray coated manually. Finally, 100 nm gold was evaporated on top. The devices were then laminated using a commercial laminator with laminating pouches. The laminating process is designed to improve the durability and stability of the device.

The PV performances of HEH001-004 are shown in Figure 5-9.

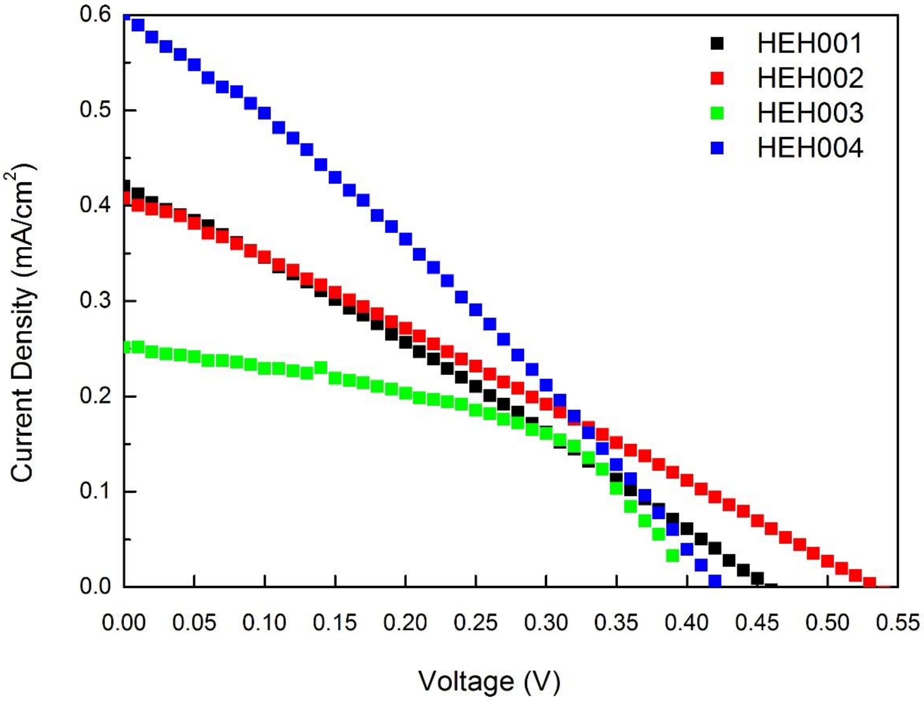

Figure 5-9: *J-V* plots of HEH001-004 under AM1.5 illumination.

Table 5-2: Solar cell parameters of HEH001-004.

Samples	J_{sc} (mA/cm^2)	V_{oc} (V)	P_{max} (mW/cm^2)	*FF*	PCE (%)
HEH001	0.42	0.45	0.05	0.28	0.05
HEH002	0.41	0.53	0.06	0.27	0.06
HEH003	0.25	0.39	0.05	0.49	0.05
HEH004	0.60	0.42	0.07	0.29	0.07

It can be seen from Figure 5-9 and Table 5-2 that, all devices showed PV response upon illumination. All devices show PCE within a similar range, however the short-circuit current, open-circuit voltage and *FF* all vary. This is attributed to device variations originated from the fabrication processes. The whole PET substrate exhibited a small curvature after the sputtering process of ZnO seed layer. During the aqueous growth of ZnO nanorods, the surface of PET would draw small bubbles which formed during the synthesis (this effect was not observed on FTO substrate using the same ZnO synthesis method). The bubbles would leave a small area of pinholes without ZnO growth. As a consequence, the followed CuSCN and PEDOT deposition would make direct contact with the seed layer, which would cause short-circuiting within the device. At this stage, both CuSCN and PEDOT:PSS were deposited via manually spray coating. Not only manually spray coating would lead to device-to-device variation, but also lead to non-uniform coverage of PEDOT:PSS layer on the same substrate which potentially form gaps in the polymer layer and allow underlying nanorods to be exposed to gold contact. As a consequence, the increasing amount of short-circuit would reduce the shunt resistance in the device which leads to low *FF* in device HEH001, 002 and 004. In general, the performance of the PV shows PCEs below 0.1%. Part of the reasons would be the high recombination within the ZnO nanorods. Due to the nature of polymer substrate, the nanorods grown via pH=6 synthesis could not survive high temperature post annealing. As the PL results shown in Section 4.2, as-grown rods show low near-band-edge emission which contributes to a faster recombination rate. The high recombination for the photo injected electrons in ZnO back to CuSCN has also been reported to be the origin of the low V_{oc} and PCE of the device[35,42]. It is also to be noted that the high series resistance in the ITO (60 ohm/square) could also cause the low V_{oc} and PCE.

Impedance analysis of the devices were performed and the results were fitted using ZView software with the equivalent circuit shown in Figure 5-10a. The scanning range was 10^6 Hz down to 0.01 Hz.

Typically for impedance analysis results obtained from DSSC, three semicircles can be observed as the frequency starts from 10^6 Hz down to 0.01 Hz. The high-frequency semicircle (10^3-10^5 Hz) is related to the capacitance (CPE1) and charge transfer resistance between the counter electrode and p-type HTM. The second or middle semicircle is associated with the capacitance (CPE2) and electron diffusion in the photo anode and electron back reaction at the photo anode/HTM interface. This is represented by interfacial charge transfer resistance (R_{ct})[147]. This semicircle is normally the largest. A small R_{ct} indicates a facile charge transfer while a large R_{ct} indicates a sluggish charge transfer and higher probability of recombination[140]. The third or the low-frequency semicircle (in mHz range) corresponds to the Warburg diffusion of electrolyte in liquid-state DSSCs and is commonly merged with the middle semicircle in solid-state DSSCs. The sheet resistance of the electrode substrate and the resistance of the HTM are the main contributor to the Ohmic series resistance R_s.

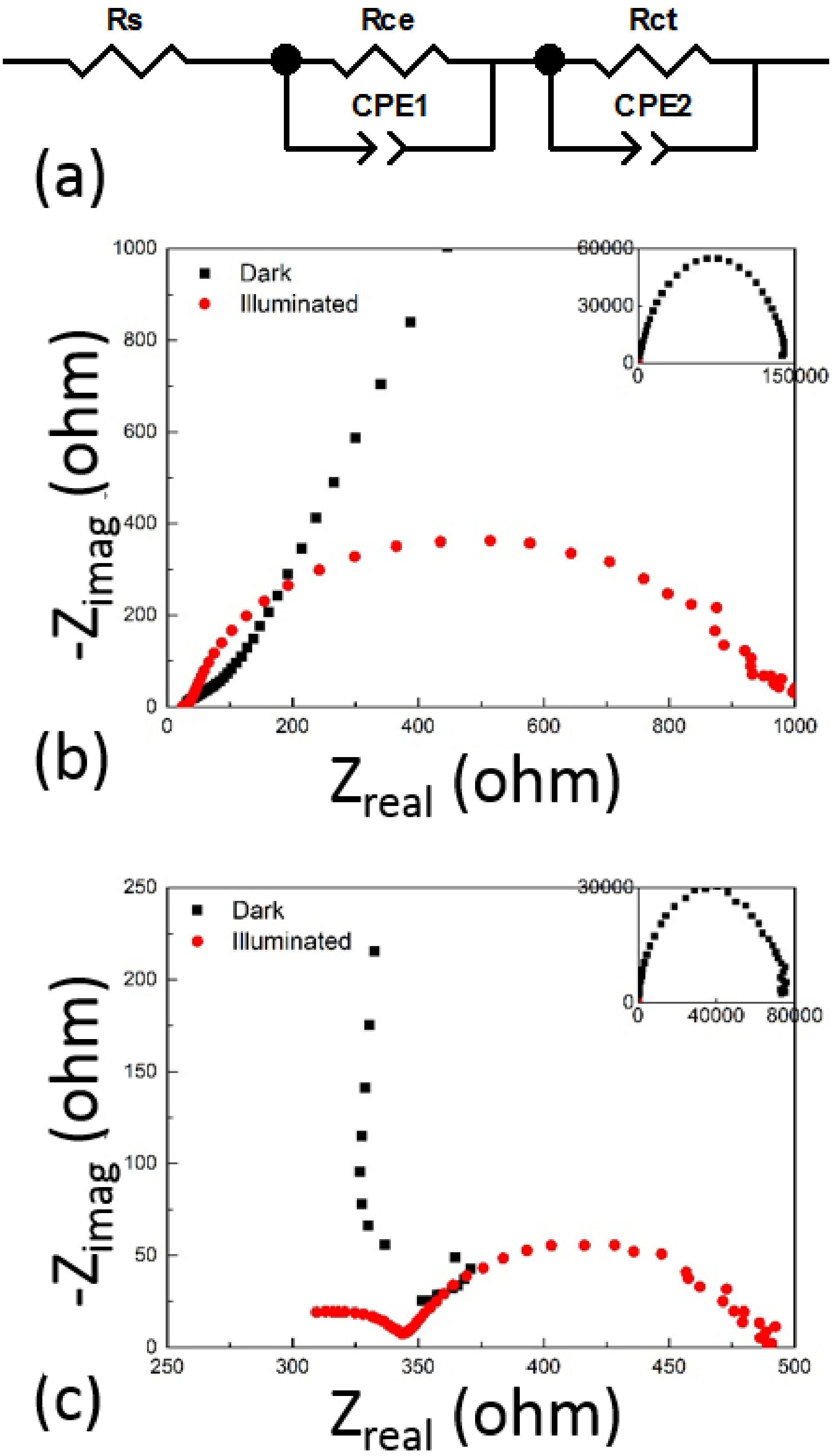

Figure 5-10: Impedance plots of HEHs in the dark and under illumination. (a) Equivalent circuit for impedance fit, (b) HEH003, (c) HEH004. Inset figures have the same units.

Table 5-3: Series resistance R_s, charge transfer resistance R_{ct} derived from impedance analysis.

Test condition	Dark		Illuminated	
Fit results	R_s (kΩ)	R_{ct} (kΩ)	R_s (kΩ)	R_{ct} (kΩ)
HEH003	0.047	140	0.034	0.93
HEH004	0.337	68.3	0.287	0.14

Impedance analysis results suggest significantly reduced charge transfer resistance within the device upon illumination, which is attributed to the difference of electron density[148] under illumination with the presence of N719 light absorber layer. Comparing the charge transfer resistance under illumination, it is suggested that the higher current and PCE for PV performance from HEH004 compared to HEH003 is attributed to the lower charge transfer resistance.

Even though the performances are poor, these results still demonstrate the HEHs perform as PVs. For NG performances of the HEHs, resistive load matching was performed to analyse maximum peak-power densities delivered by the HEHs to their optimum load resistances. The device was fixed on a spring steel cantilever then onto the sample stage of magnetic shaker (see Figure 5-5). The resonance frequency was identified first by tuning the signal generator. For each device, peak-voltage output across a sweep of resistive loads from 100 Ω to 100 kΩ were recorded and power delivered to each load was calculated using Equation 5-1.

The resulted resistive load matching plots are shown below in Figure 5-11 and Figure 5-12.

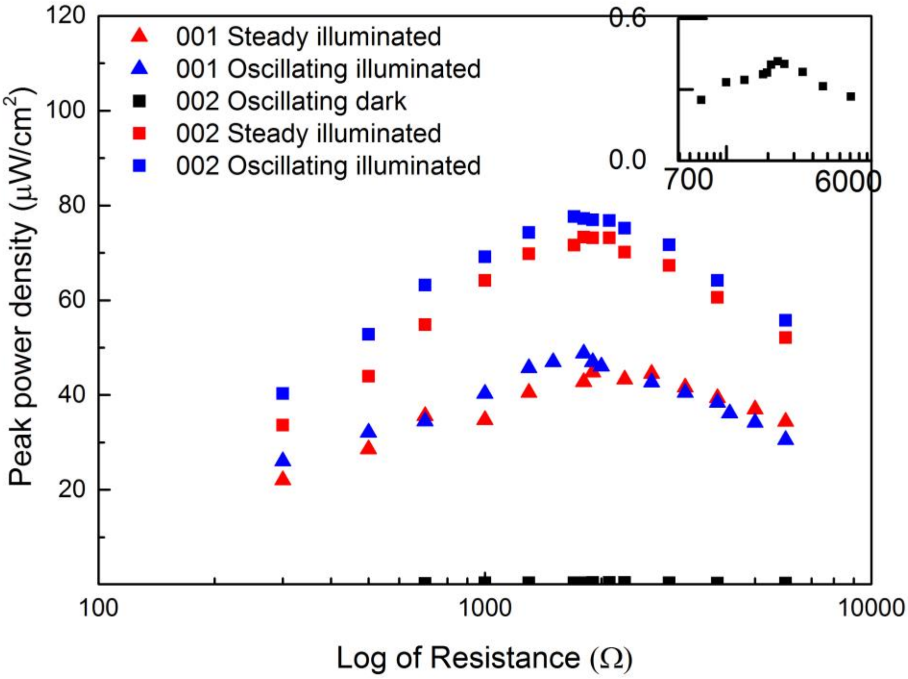

Figure 5-11: Resistive load matching plots for devices (HEH001-002) when either oscillated in the dark, not oscillated (steady) under illumination, or oscillated under illumination.

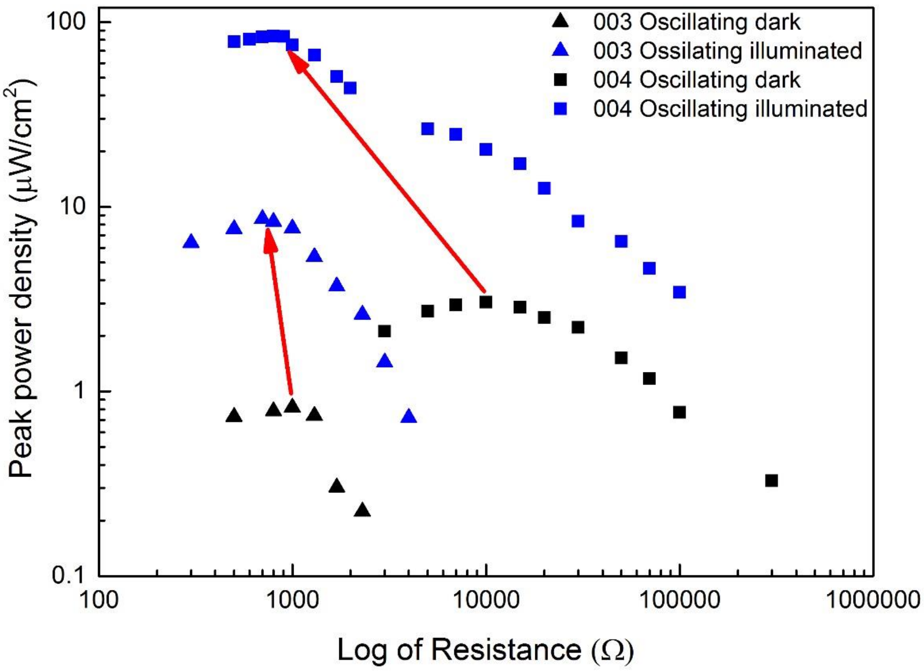

Figure 5-12: Resistive load matching (log scale) plots for devices HEH003 and HEH004. Red arrows indicating the positions of the peak.

Table 5-4: Peak power density, optimum load and resistive impedance of fabricated devices. NA indicates the samples were made in the early stage and could not be measured anymore.

Device name	Peak power density (μW/cm^2)		Optimum load resistance (kΩ)		Resistive internal resistance (kΩ)	
	Dark	Illuminated	Dark	Illuminated	Dark	Illuminated
HEH001	NA	48.81	NA	1.8	NA	NA
HEH002	0.42	77.66	2.1	1.7	NA	NA
HEH003	0.82	8.58	1.0	0.7	140	0.93
HEH004	3.05	83.83	10.0	0.8	69	0.50

From Figure 5-11 and Figure 5-12, it can be seen that upon illumination, peak power densities of all four devices increased significantly comparing to the peak power densities without illumination. Under illumination, HEH001 shows 48.81 μW/cm^2 at 1.8 kΩ; HEH002 shows 77.66 μW/cm^2 at 1.7 kΩ; HEH004 shows 83.51 μW/cm^2 at 0.8 kΩ; HEH003 is much lower and shows 8.58 μW/cm^2 at 0.7 kΩ. This trend is consistent to the PV performances obtained from the *J-V* scans shown in Figure 5-9 and Table 5-2, that the current density (mA/cm^2) for HEH001, HEH002 and HEH004 are 0.42, 0.41 and 0.6, respectively; while the current density for HEH003 shows the lowest at 0.25. Impedance analysis were performed on HEH003 and HEH004 and the Nyquist plots are shown in Figure 5-10 and Table 5-3. The devices' internal resistance can be calculated from the real-axis diameter of these plots[81,146,148]. The resistive internal impedance values of the HEH003 and HEH004 under illumination were found to be close to the device optimum load resistance as shown in Table 5-4. This corresponds to the maximum power transfer theorem[149], which states that the maximum power transfer occurs when the impedance of a connected load is equal to the internal impedance of the source[149].

For HEH001 and HEH002, peak power densities were also measured when kept steady under illumination (see red curves in Figure 5-12) and compared to values obtained under oscillating and illumination. HEH001 shows improvement of peak power density from 44.76 μW/cm^2 at 1.9 kΩ (steady under illumination) to 48.81 μW/cm^2 at 1.8 kΩ (oscillating under illumination). HEH002 shows improvement of peak power density from 73.35 μW/cm^2 at 1.8 kΩ (steady under illumination) to 77.66 μW/cm^2 at 1.7 kΩ (oscillating under illumination). These results indicate oscillating increased the peak power density of the devices under illumination.

The working principles of the HEH devices are discussed below.

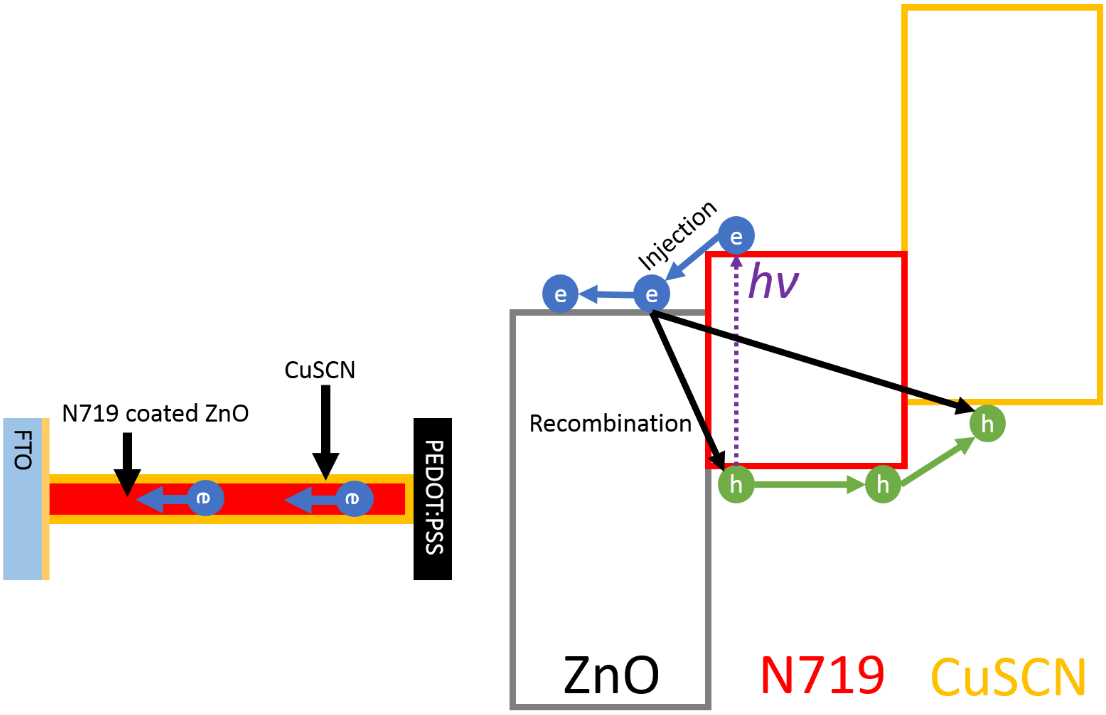

Figure 5-13: Schematic of ZnO/N719/CuSCN system illustrating the photo induced charge carrier dynamics of device working solely as PV. During the travelling process towards FTO electrode, photo injected electrons are prone to recombine with holes and reduce the photo current and the power output.

When the device is exposed to AM1.5 illumination without oscillation (steady illuminated, shown in red curves in Figure 5-11), it performs solely as a solar cell. A photo voltage is generating a photo current through the load. A direct photo current and photo voltage remain constant under illumination. Without oscillation, the power output would be increased with the origin being the device working solely as a solar cell ($P = \frac{V^2}{R}$) comparing no illumination condition. By performing a load matching, the maximum power point could be identified. The maximum power from the *J*-*V* scan measurements (converted to μW/cm²) for HEH001-004 are 0.05, 0.06, 0.05 and 0.07. These values correspond well with the maximum power achieved from load matching (except HEH003), which shows the maximum power (μW/cm²) for HEH001-004 are 0.049, 0.078, 0.009 and 0.08, respectively. The abnormal result of HEH003 may suggest the device is broken or has a bad contact.

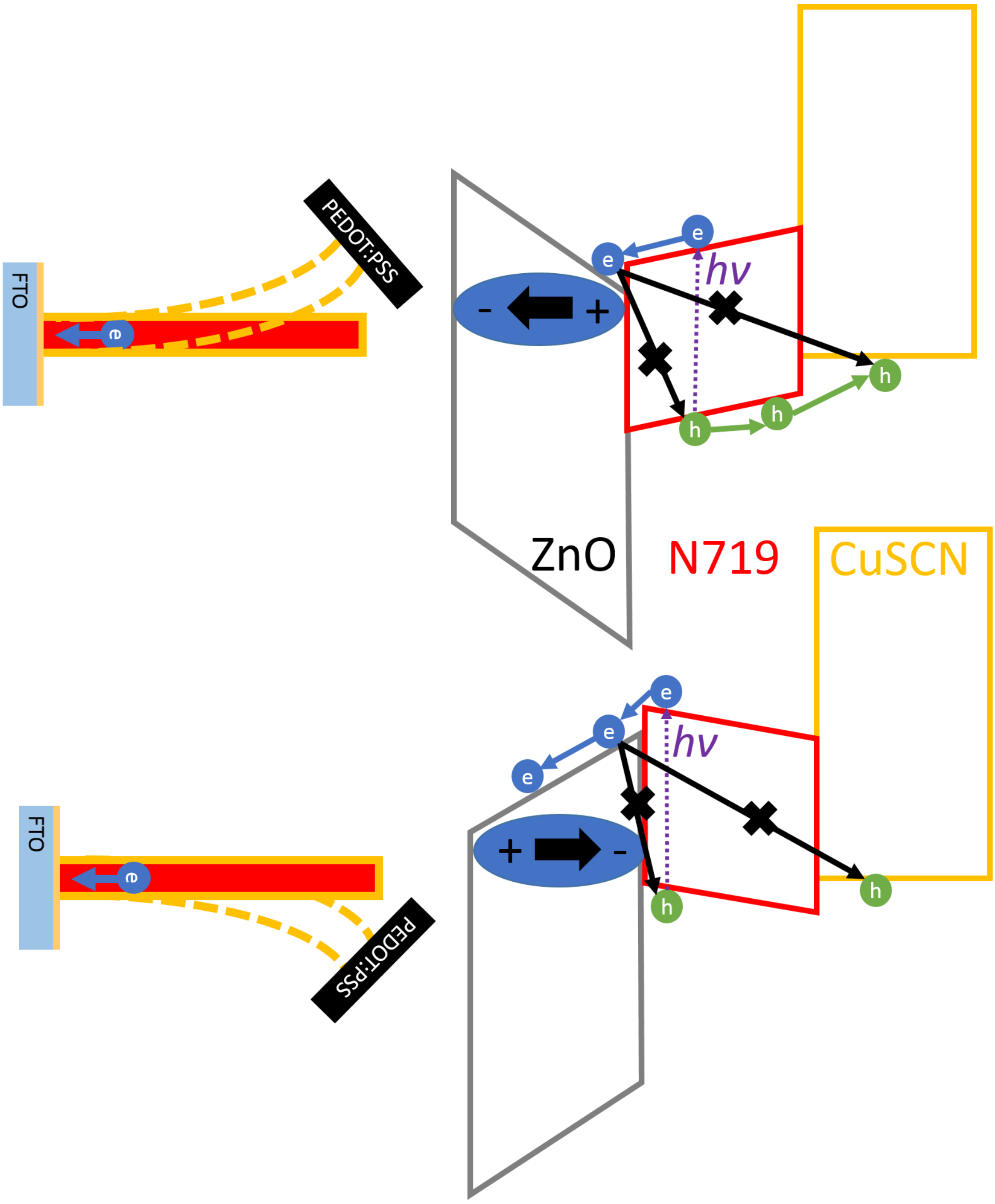

Figure 5-14: Schematic of ZnO/N719/CuSCN system illustrating the potential impact of an oscillating vibration of ZnO nanorod upon photo induced charge carrier dynamics. Illustrated are the dynamics in the presence of oscillation under illumination. The potential impact of strain-induced piezoelectric dipoles upon these charge carriers are shown. The

gradients of the conduction and valence band edges illustrate the impact of the ZnO piezoelectric polarization upon these energy levels. In the upper image in Figure 5-14, the ZnO polarization drives holes away from the interface. With the holes moved away from the junction, electrons are unable to cross it due to the energy barrier. In the lower image in Figure 5-14, the opposite polarization, photo generated electrons are driven from the surface and holes cannot cross the junction. In both cases, the net effect is to increase the spatial separation of electrons and holes, and so to reduce recombination losses.

When the device is oscillating under illumination, the power is slightly further improved comparing to the power tested steadily under illumination as shown in Figure 5-11. With the presence of N719 dye layer, a large amount of electron hole pairs will be excited upon illumination. The followed charge injection process increase the charge carrier density within the ZnO. When the nanorods are subject to oscillation induced strain, an alternating polarization will develop across the nanorods. The electric field associated with this polarization is expected to extend into both ZnO and CuSCN components. As the working principle from NG, this leads to screening of the polarization as the carriers rearrange. As the nanorods vibrate under oscillation, the surface will fluctuate between positive and negative polarizations shown in Figure 5-14 above. These polarization will provide an oscillating modulation of the energetics of exciton separation at the ZnO/N719-CuSCN interface. As this effect should alternate between a positive and negative contribution, and is found to be small compared to the large energy offset driving exciton separation (~1 eV), the oscillation is not considered to enhance separation[87]. After the charge separation, photo excited electrons and holes are separated and are prone to recombine. The recombination would decrease the charge collection efficiency and reduce the photo current. Depending on the polarity of the ZnO polarization relative to the ZnO/N719-CuSCN interface, the resultant electric field will either drive separated electrons in ZnO or positive holes in CuSCN away from the interface. Thus in both case, the oscillation induced polarization would alternate in direction and enhance the charge separation after the electron/hole pair generation. This model is proposed to account for the improvement of power under illumination from the tests without oscillation to tests with both illumination and oscillation. Similar to the mechanism[87] proposed for enhancement of ZnO nanorod/P3HT solar cell, the reduction of charge carrier recombination is suggested to be the origin of improvement.

To summarize, a N719-based hybrid energy harvester was successfully designed and fabricated, which could harvest kinetic and solar energy simultaneously. Furthermore, unlike the HEH devices reported in literature where the output is simply the combined effect from NG and PV, a further enhanced performance is shown benefiting from the dual-functional ZnO nanorods. The ZnO nanorods in our design acts as both origin of piezoelectric potential and electron transport material. The piezoelectric potential further enhanced the charge separation within the device and further improved the power output. As shown in Figure 5-11 and Figure 5-12, the power generated from PV effect is much higher than power generated from NG effect. Thus, to achieve the maximum power, PV performance of the HEH needs to be optimized. To further improve the PV performance, post annealing is suggested to be able to improve the crystallinity of the ZnO and the current output of the DSSCs. Thus, it would be beneficial to utilize a flexible substrate with high thermal stability. Corning© Willow™ (CW) substrate is a promising candidate which was investigated in this project as a substitute for ITO-PET. Results based on CW substrate will be presented in the next section.

5.3 N719-based HEH using Corning© Willow™ glass

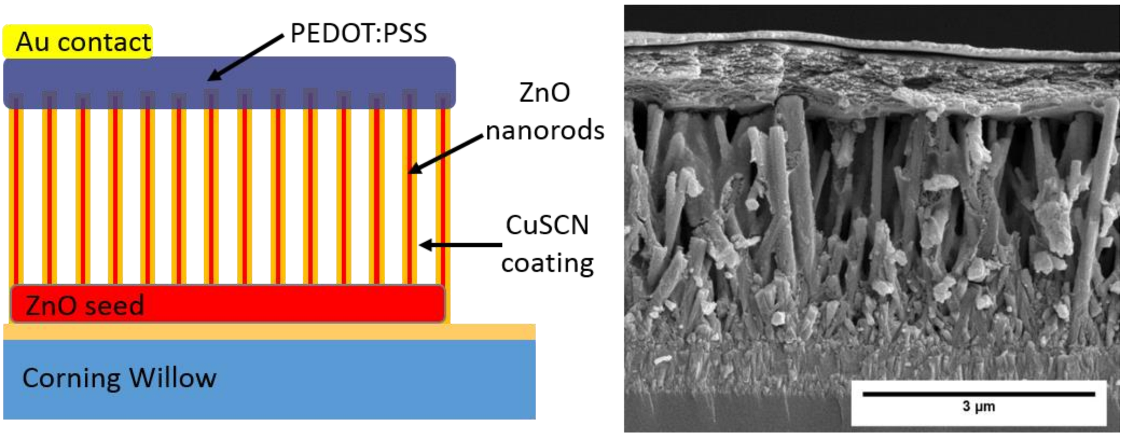

Figure 5-15: HEH design using CW substrate with the corresponding SEM image of the cross section.

Previous studies of ZnO-based solar cells have employed thermal annealing to improve the performance of the device. Thermal annealing is suggested to reduce the native defects and impurities of ZnO nanostructures[120,130,131,150]. However for the original design of NG which was based on polymer PET substrates, high temperature annealing was prohibited due to the substrate limitation. Thus, to potentially improve the performance of PV from HEH and probe the effect of annealing on the performance of NG from HEH. Corning® Willow™ glass was selected as the alternative substrate. CW substrate is ultra-thin (0.2 mm), lightweight and conformable glasses with high transmission (75-80%). It can be annealed up to 800 °C. The glasses were purchased from MTI Corporation, USA. A thin layer of conductive FTO was sputtered onto the CW substrates by Solaronix, Switzerland. Even though CW are flexible to a small degree, they are still delicate and brittle. To improve the flexibility of the whole device, a long aspect ratio 10×1 cm^2 dimension was utilized for the CW substrate. In order to optimize the photovoltaic performance of the HEH design, FTO glass was used first. Once the parameters were optimized, the optimized procedures were then transferred onto CW substrates, followed by kinetic-to-electricity characterization.

5.3.1 Optimization of photovoltaic performance

ZnO nanorods were grown using pH=6 method for 24 h and then annealed at 500 °C for 1 h. For the design of the HEH based on CW glass, morphologies of the n-type ZnO nanorods are fixed. Thus, for p-type HTM, thickness of CuSCN and PEDOT:PSS were considered to be variables and investigated to identify the optimum parameters.

5.3.1.1 CuSCN coverage

The coating of CuSCN layer in the original HEH design is to passivate the surface of the rods (adapted from NG design) as well as acting as hole transport material (adapted from PV design). The amount of CuSCN coating would affect the NG[82] and PV[42] performance of the device. In order to identify the optimal CuSCN coating thickness, various amount of CuSCN was spray coated on a set of substrates based on FTO glasses. Here, the thickness of CuSCN layer was determined by the amount of CuSCN solution coated on to each substrate. Per each substrate (1.5×1.5 cm^2 working area), 1, 2 and 3 ml of CuSCN solution (0.15 M) were spray coated. CuSCN solution was achieved by dissolving 1.8246 g CuSCN powder in 100 ml di-n-propyl sulfide. Resulted coverages were examined under SEM, shown in Figure 5-16:

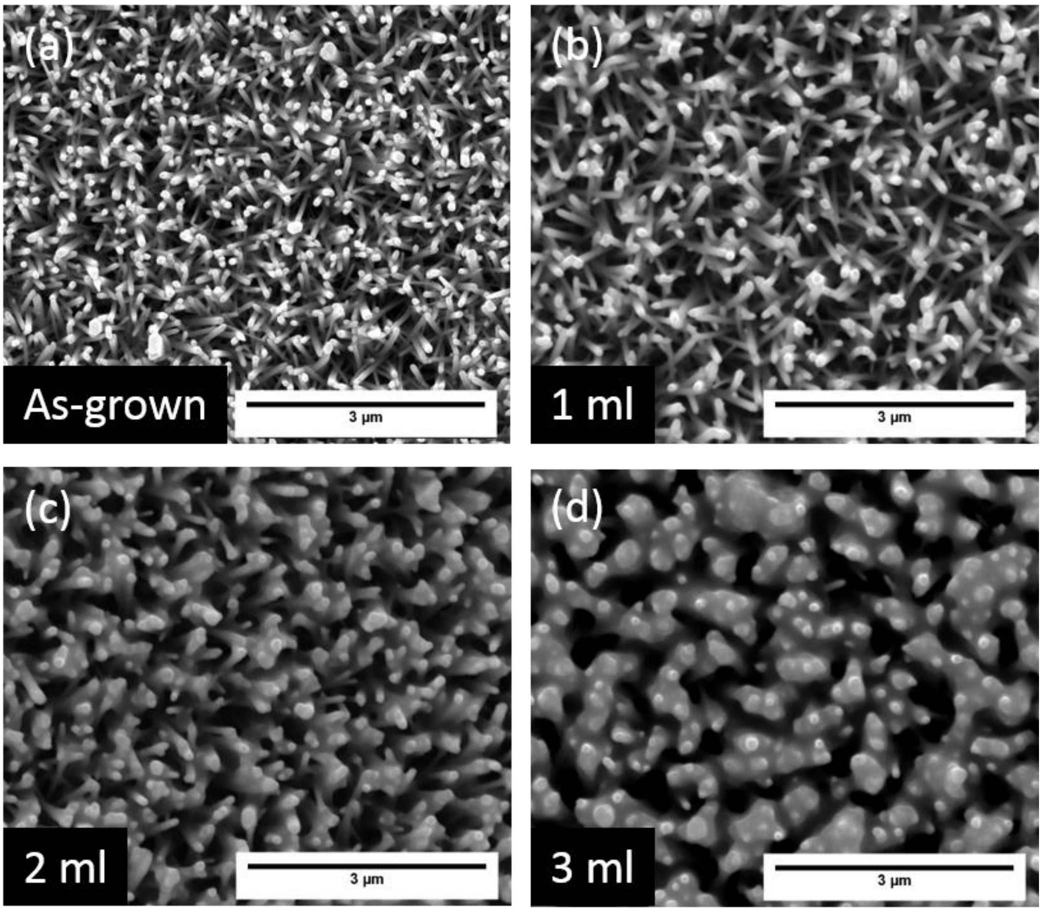

Figure 5-16: CuSCN coverage comparison. (a), (b), (c) and (d) show 0, 1, 2 and 3 ml of CuSCN deposited, respectively.

From Figure 5-16, it can be seen that higher CuSCN coverage can be achieved by gradually increasing the amount of CuSCN solution. 1 ml CuSCN deposition shows the lowest coverage where the gaps remain empty between the rods. 3 ml CuSCN deposition is able to fully cover the side of the nanorods.

After CuSCN deposition, all substrates were spray coated with same amount of PEDOT:PSS then 100 nm of gold contact. *J-V* scans were performed to compare the PCEs from different CuSCN coverage.

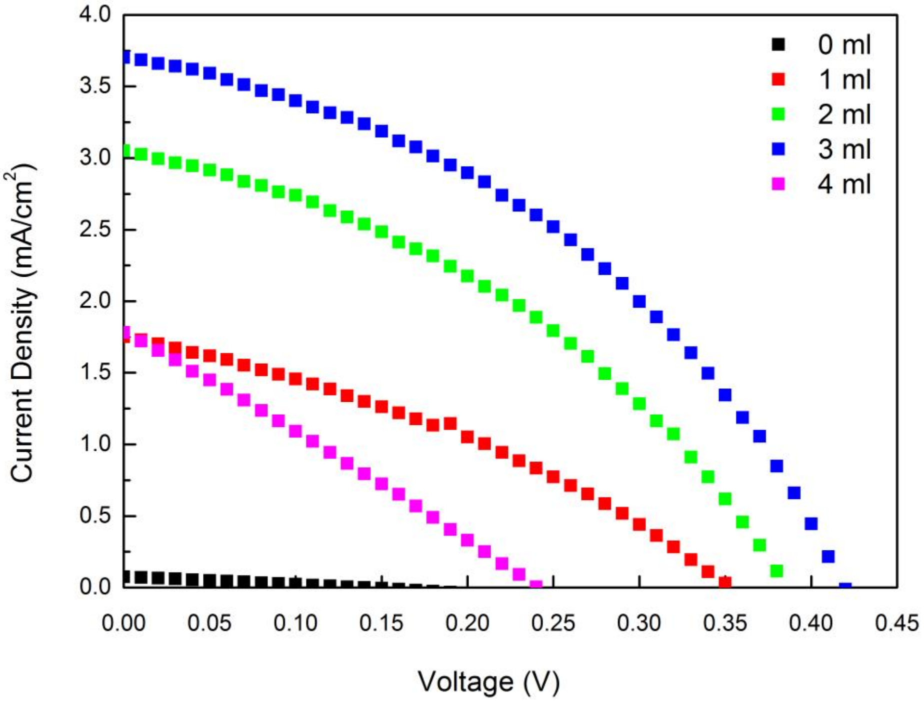

Figure 5-17: *J-V* plot of devices with gradually increased CuSCN coverage.

Table 5-5: Solar cell parameters of SSDSSCs with gradually increased CuSCN coverage.

CuSCN per substrate	J_{sc} (mA/cm^2)	V_{oc} (V)	P_{max} (mW/cm^2)	*FF*	PCE (%)
0	0.075±0.015	0.14±0.01	0.0028±0.0007	0.26±0.02	0.0028±0.0007
1	1.75±0.12	0.35±0.02	0.22±0.02	0.35±0.02	0.22±0.02
2	3.1±0.30	0.38±0.01	0.45±0.04	0.39±0.02	0.45±0.04
3	3.70±0.32	0.41±0.01	0.63±0.06	0.42±0.02	0.63±0.06
4	1.78±0.28	0.24±0.01	0.11±0.02	0.26±0.02	0.11±0.06

From Figure 5-17 and Table 5-5, it can be seen that PV performance of the devices improves with increasing amount of deposited CuSCN. For devices made on pure

ZnO/PEDOT:PSS structure with no CuSCN passivation, short-circuit current, open-circuit voltage and *FF* all show the lowest value, leading to the lowest PCE (0.0028%). With the amount of deposited CuSCN increasing from 1 to 3 ml, all parameters show gradual increase, leading to the best performance of 0.63% with 3 ml CuSCN deposited per substrate. For the device made using 4 ml CuSCN, performance dropped again, possibly due to excessive CuSCN coating. If the CuSCN coating was too thick, it would reduce the electron/hole transport due to limited electron travel length. Thus, 3 ml is considered to be the optimal amount. To investigate the reason of the improvements, impedance analysis was performed and results shown below in Figure 5-18:

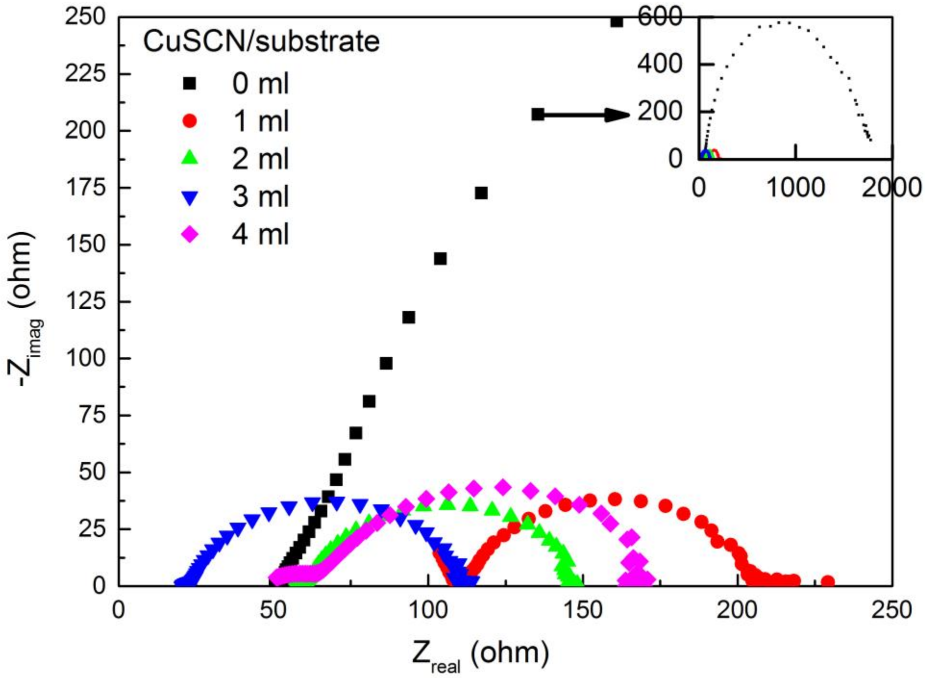

Figure 5-18: Impedance analysis of devices from 0-3 ml deposited CuSCN per substrate under AM1.5 illumination.

Table 5-6: Series resistance R_s and charge transfer resistance R_{ct} derived from EIS results.

Amount of CuSCN deposited	R_s (Ω)	R_{ct} (Ω)
0	48.92	1670
1	109.8	99.63
2	58.65	88.02
3	20.65	87.24
4	44.19	95.62

From Figure 5-18 and Table 5-6, it can be seen that device with no CuSCN coating showed the highest charge transfer resistance, 1670 Ω, which is attributed to the inefficient charge transfer between ZnO/dye and ZnO/PEDOT. Without CuSCN coating, only the tips of the rods are in contact with PEDOT:PSS layer(SEM evidence will be shown in 5.3.1.2). The other part of the rods are coated with N719 and exposed in air. After the separation of photo induced electron/hole pairs, electrons would be injected into ZnO. However holes have to travel long distance to the top tips of the rods to be collected by PEDOT:PSS layer. Thus, the charge recombination process is severe, indicating the high resistance.

Both series resistance and charge transfer resistance decrease with increased amount of CuSCN coating from 1 ml to 3 ml per substrate. The decrease of R_{ct} is attributed to the increased contact area between CuSCN and PEDOT with increased CuSCN coating, which reduced the resistance. The decrease of R_s is attributed to the increased thickness of CuSCN leading to a more complete pathway for hole transport and less resistance. It is suggested that the coating of CuSCN would modify the surface properties of ZnO, reduce the surface defects by passivation and thus reduce the recombination[81]. SEM images from Figure 5-16 confirm that increased amount of CuSCN can increase the surface coverage of ZnO, which increases the suppression of active parasitic surface states.

5.3.1.2 PEDOT:PSS deposition

The concept behind using a semiconducting PEDOT:PSS layer as top electrode in original NG design is suggested to be related to reducing external screening effects of the device[72]. The p-type PEDOT:PSS material in contact with n-type ZnO is reported to form a p-n junction with a depletion region. The formation of depletion region is suggested to reduce the external screening effect by acting as a barrier between p-type (free holes of PEDOT:PSS) and n-type material (free electrons of ZnO), as discussed in Section 2.5. Furthermore, a polymer-type electrode based on PEDOT:PSS would significantly improve the flexibility of the device as the testing setup requires large degree of bending movement from the substrate. Early experiment of a solid-state DSSC fabricated on PET/ZnO nanorods/CuSCN/Au was tested in our lab and the ceramic CuSCN formed cracks after bending test. The cracks were visible by eye inspection. This suggests the structure comprised of double p-type materials is essential in our design as CuSCN would reduce the charge transfer resistance and passivate the surface defects while PEDOT:PSS would improve the flexibility of the substrate. PEDOT:PSS could also provide a planar surface for gold deposition. More importantly, both materials would act as hole transporting materials.

In the device fabrication for N719-based HEH, PEDOT:PSS is dissolved in aqueous solution. Due to the hydrophobic nature of ZnO nanorods[151,152], the wetting of the PEDOT:PSS solution is poor. It has been proposed that spin coating[80] and spray coating[82] are the two common deposition methods. Ideally, spin coating would be able to give a more consistent and repeatable film by eliminating manual error. Thus, both deposition methods were utilized and the PV performance of the HEH was compared.

For spin coated PEDOT:PSS, the coating setup was 3000 RPM for 30 s, followed by 100 °C annealing. For spray coated PEDOT:PSS, the coating was applied using air spray gun while substrate being heated at 100 °C. For both methods, SEM were performed first to examine the thickness and the coverage of the PEDOT:PSS layer.

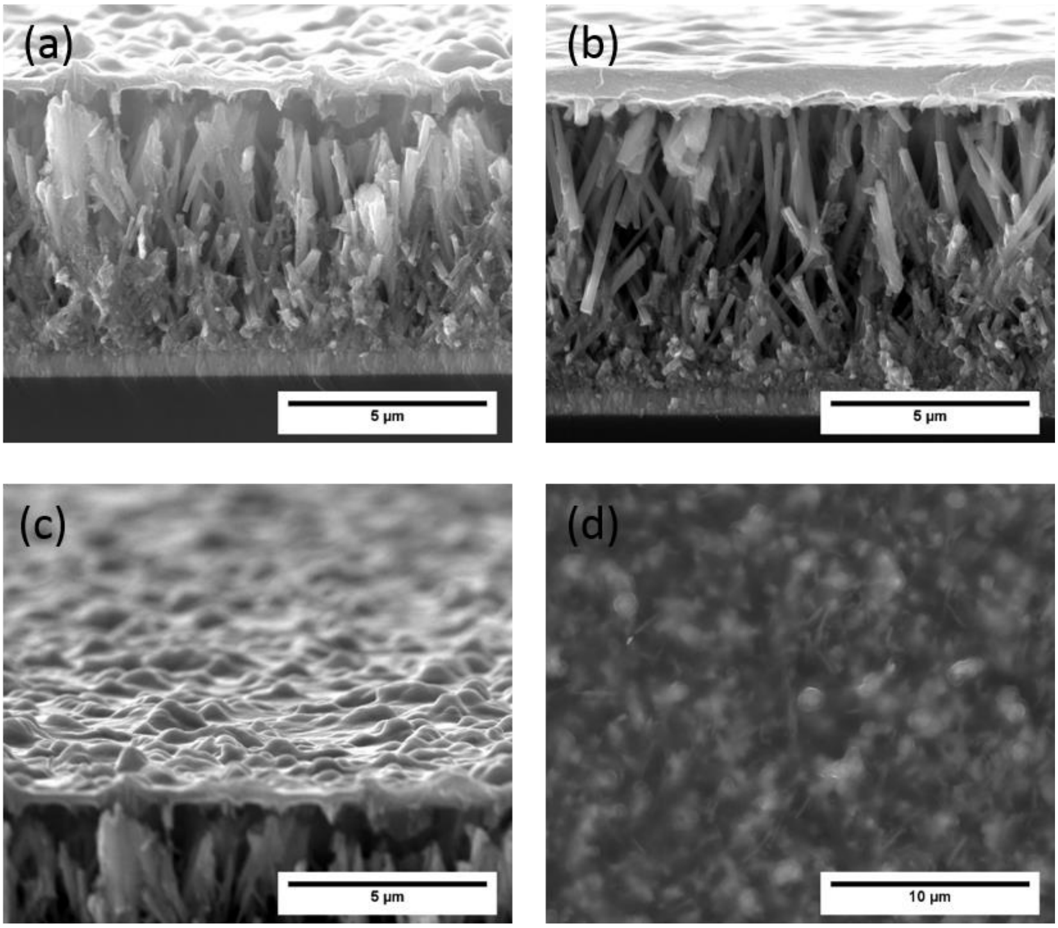

Figure 5-19: SEM images of spin coated PEDOT layer on ZnO based on CW substrate: (a) Edge of the substrate, (b) Central area of the substrate, (c) Close up of the edge of the substrate, (d) Top view of edge of the substrate.

From Figure 5-19, it can be seen that, spin coating would lead to non-uniform coated film on ZnO grown on CW substrates. This is due to the long aspect ratio of the substrate (10×1 cm^2). The non-uniform coverage of PEDOT:PSS layer would potentially leave nanorods exposed. In this way, the rods would make physical contact with the gold electrode, causing short-circuiting. During spin coating, the centrifugal force around the edges of the substrate pulled on the PEDOT:PSS outward, and the attractive forces within the PEDOT:PSS pulled on the PEDOT:PSS near the centre of the substrate, where the centrifugal forces is smaller[153]. This effect is enhanced on long aspect ratio substrate, leaving central area of the CW significantly darker then the two ends of the CW after PEDOT:PSS spin coating. Due to the poor wetting, an interference pattern is also shown on the surface, indicating the non-uniform coating of the substrate. It can also be seen in Figure 5-19c that, the thickness of the film is 400 nm, while the height of the pointed top on the film is approximately another 400 nm. This indicates, to fully cover the rods and leading to a flat top surface, at least 800 nm thick PEDOT:PSS is required, which is the thickness shown in Figure 5-19b. However, the top surface of the PEDOT:PSS layer in Figure 5-19b is still not completely flat. Thus, it is suggested that at least 1 μm film is required to fully embed the nanorods.

As for spray coating, various amount of PEDOT:PSS was spray coated and examined under SEM, shown in Figure 5-20 below.

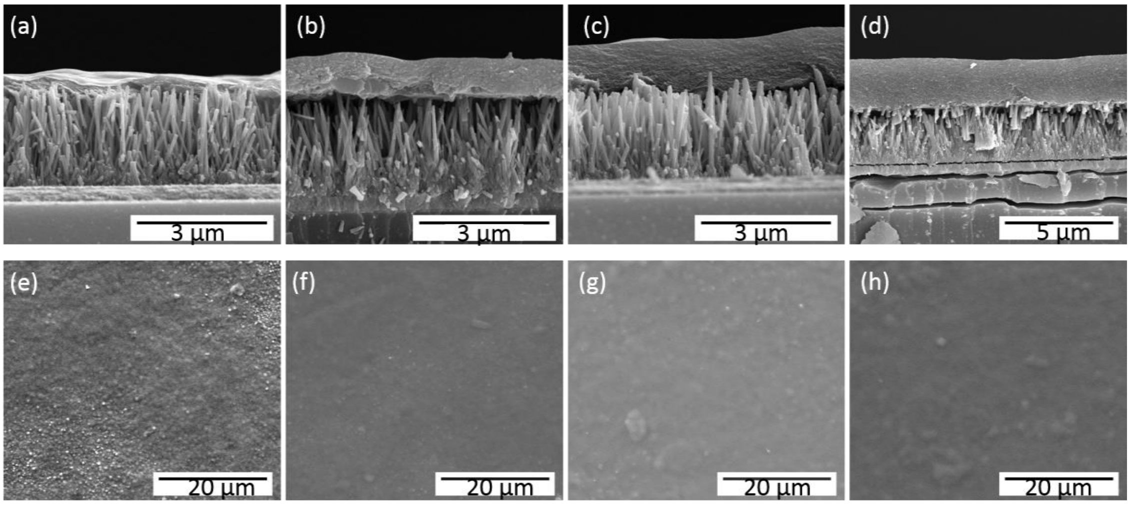

Figure 5-20: Cross section and top view of various amount of PEDOT:PSS layer via spray coating. (a) and (e) 0.5 ml/substrate, (b) and (f) 1 ml/substrate, (c) and (g) 1.5 ml/substrate, (d) and (h) 2 ml/substrate.

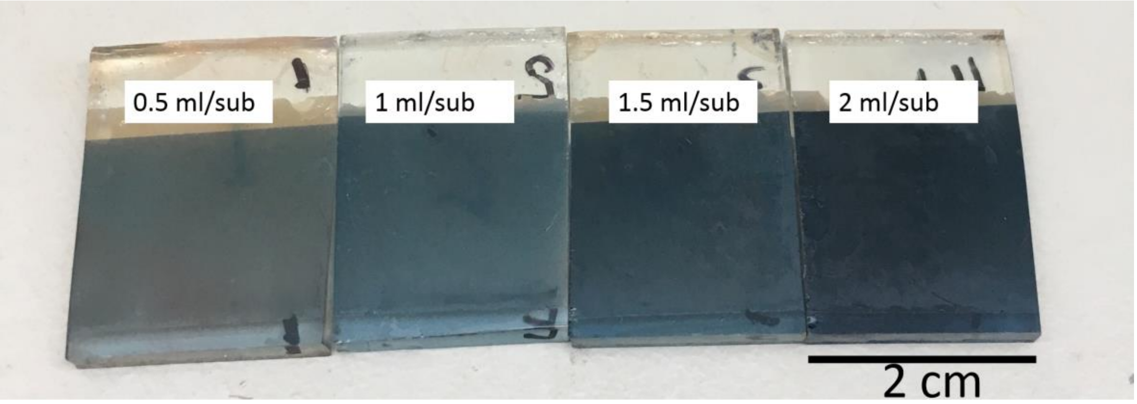

Figure 5-21: Images of the top view with corresponding amount of spray coated PEDOT:PSS.

From Figure 5-20, the thickness of the PEDOT:PSS films are: (a) 380 nm, (b) 810 nm; (c) 1200 nm and (d) 2000 nm. As expected, 380 nm thickness is not enough to cover the tips of the nanorods as shown in Figure 5-20a. From image (b) to image (c), the rods are fully covered. This is consistent with the spin coated results which suggests a PEDOT:PSS film of 1 μm is required to fully cover the rods.

Results shown in the Figure 5-22 below are obtained from devices made on CW substrate/ZnO nanorods (pH=6 method, 4 μm)/CuSCN/PEDOT:PSS (spin or spray coated as marked)/gold. For one device, ZnO was not annealed and PEDOT:PSS was spray coated. The other two devices: both ZnO were annealed while one device utilized spray coated PEDOT:PSS and the other utilized spin coated PEDOT:PSS.

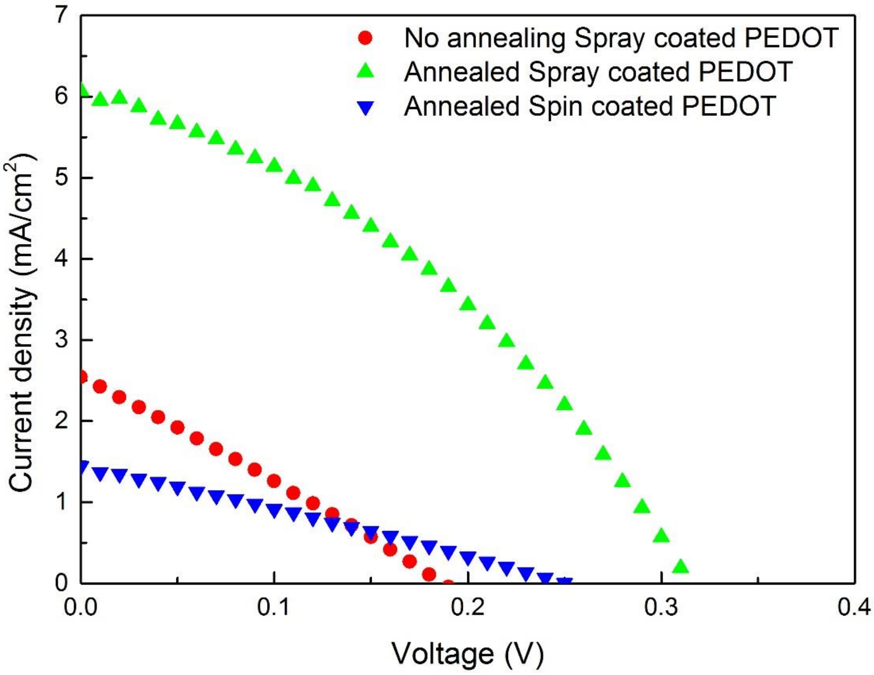

Figure 5-22: *J-V* plots of PV performance of HEH based on CW.

Table 5-7: Solar cell parameters of HEH based on CW.

Device	J_{sc} (mA/cm^2)	V_{oc} (V)	P_{max} (mW/cm^2)	*FF*	PCE (%)
No annealing Spray	2.54	0.18	0.13	0.28	0.13
Annealed Spray	6.07	0.31	0.70	0.37	0.70
Annealed Spin	1.44	0.25	0.10	0.27	0.10

From Figure 5-22 and Table 5-7, it can be seen that the performance of the solar cell is significantly improved after thermal annealing on ZnO nanorods. Short-circuit current, open-circuit voltage and *FF* all increase, leading to a 0.7% efficiency with post annealing comparing to 0.13% without. This is as expected which is due to improved crystallinity of ZnO which leads to less recombination. Comparing results from spray coating to spin coating, devices fabricated via spray coating showed a better performance, which is attributed to a better coverage of the rods. Thus, even though spin coating is considered to result in a uniform coating, this advantage is restricted on small scale samples. For large scale, long aspect ratio samples, spin coating would result non-uniform coatings and interference patterns which lead to short-circuiting in the device. As a conclusion, spray coating of PEDOT:PSS is selected for future fabrication process for CW-based HEH.

Another discovery during SEM imaging was how the tip of the rods interact with spray-coated PEDOT:PSS layer, which further demonstrates the importance of optimized CuSCN coating thickness.

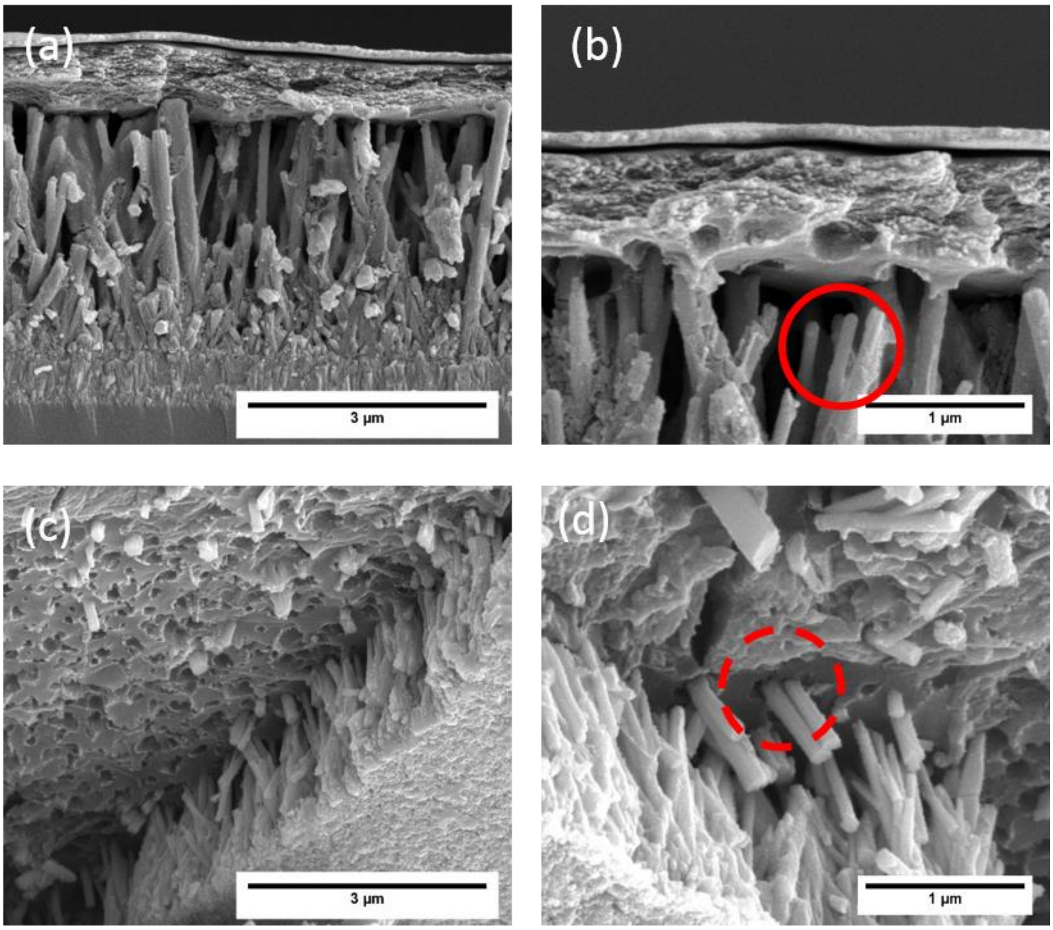

Figure 5-23: SEM images showing isolated rods (circled in red) and contacted rods (circled in dashed red).

From Figure 5-23, it can be seen that the PEDOT:PSS film shows poor contact with the tips of ZnO nanorods. Considering the structure design of the device, the FTO/ZnO nanorod/N719/CuSCN/PEDOT:PSS/gold heterojunction indicates the components of p-a-n structure are connected in series. In this way, the individual resistance from FTO, ZnO and PEDOT:PSS are arranged in series. Thus, the film thickness of the PEDOT and the contact area between the rods and PEDOT:PSS would affect the overall resistance of the device as $R = \rho \frac{L}{A}$ where ρ is the resistivity of the material, L and A are the length and cross section area of the material. Due to the poor wetting, the majority of the area at the bottom of the PEDOT:PSS film is not in contact with the rods, as shown in Figure 5-23c. The limited electron pathway would significantly increase the resistance due to reduced A. However, the contact area could be improved by CuSCN coating, as shown in Figure 5-16. The diameter of the photo anode would increase with increased CuSCN coating comparing to bare rods. In this way, the charge transfer resistance would be reduced as shown from impedance analysis in Figure 5-18, which leads to improved PV performance as shown in Figure 5-17.

5.3.2 Combined photovoltaic and nanogenerator performances

Based on the optimization results, a number of CW-based HEH devices were fabricated. In order to show the effect of optimized CuSCN coating. Both sets of results prior and after the CuSCN optimization are shown below, results achieved on HEH005-007 were based on devices prior to CuSCN optimization process, and are suggested to have low pore filling of CuSCN, shown in Figure 5-24b. Results achieved on HEH008-010 were based on devices after CuSCN optimization process, and are suggested to have completely filled CuSCN, shown in Figure 5-24c.

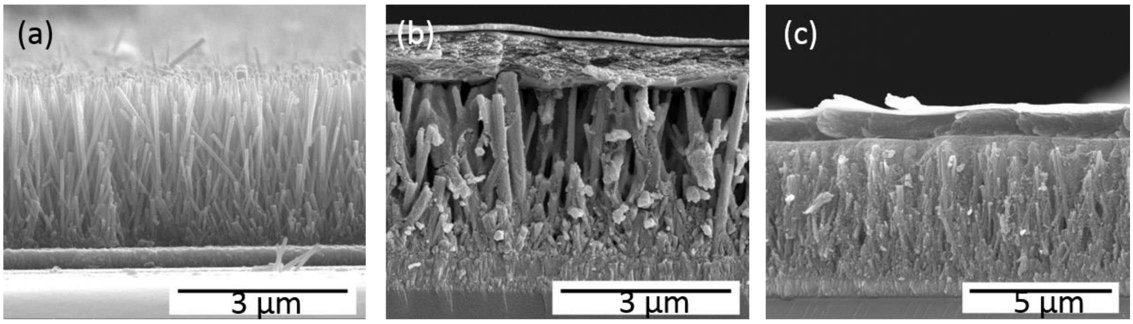

Figure 5-24: SEM images of cross section of (a) As grown nanorods; (b) Low pore filling CuSCN coated rods; (c) Completely filled CuSCN coated rods.

Table 5-8: Devices fabrication details for CW-based HEHs.

CW-HEH	Seeding method	ZnO	Post annealing	N719	CuSCN	PEDOT	Gold
HEH005	Sol-gel Spin	24 h pH=6 synthesis	500 °C 1 h	4 h Dye loading	Low pore filling Shown in Figure 5-24b	Spray coating	100 nm via evaporation
HEH006	Sputter						
HEH007	Sputter						
HEH008	Sol-gel Spin				Completely filled Shown in Figure 5-24c		
HEH009	Sol-gel Spin						
HEH010	Sol-gel Spin						

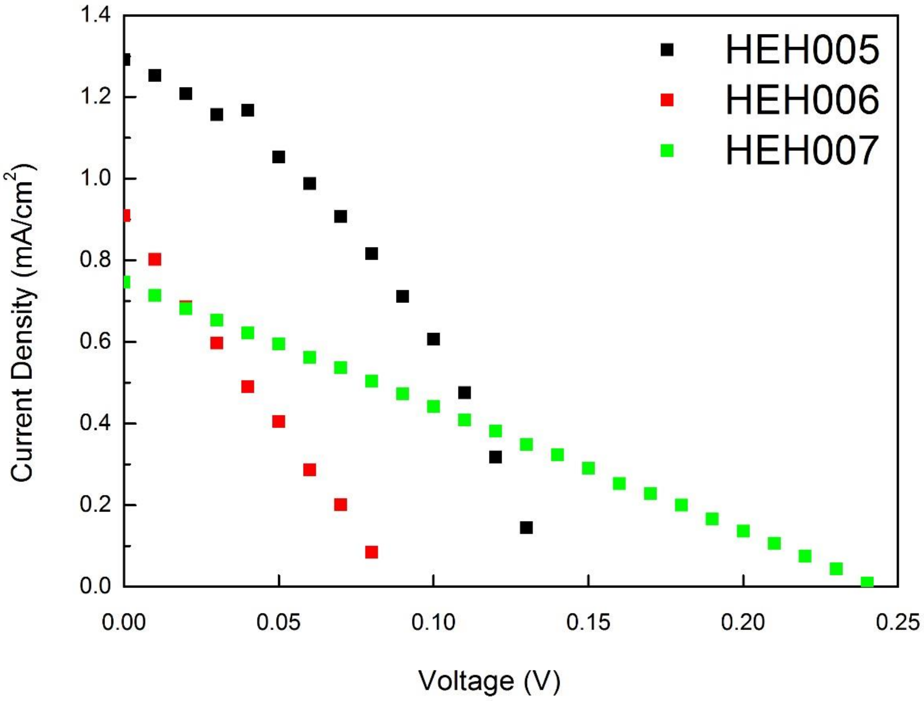

Figure 5-25: *J-V* plot of CW-based HEHs, HEH005-HEH007.

Table 5-9: Solar cell parameters of CW-based HEHs, HEH005-HEH007.

Device	J_{sc} (mA/cm^2)	V_{oc} (V)	P_{max} (mW/cm^2)	*FF*	PCE (%)
HEH005	1.29	0.13	0.07	0.39	0.07
HEH006	0.91	0.08	0.02	0.28	0.02
HEH007	0.75	0.24	0.05	0.26	0.05

From Figure 5-25 and Table 5-9, it can be seen that the PV performances of the devices with low CuSCN pore filling are poor. Current density shows the average value of 0.98 mA/cm^2 which is higher than those obtained from HEH based on PET (HEH001-004, average 0.42 mA/cm^2), average open-circuit voltage shows 0.15 V which is significantly lower than those obtained from HEH based on PET (HEH001-004, average 0.45 V). The average *FF* of 0.31 is in the similar range with PET-based

HEH (HEH001-004, average 0.33). As a result, the average PCE shows 0.047% comparable to PET-based HEH (HEH001-004, average 0.058%). The poor performance is mainly attributed to the insufficiently coated CuSCN which confirmed to have high charge transfer resistance from impedance analysis shown in Figure 5-18. The cross section of the CuSCN coating is shown in Figure 5-24, which confirms the low pore filling of CuSCN.

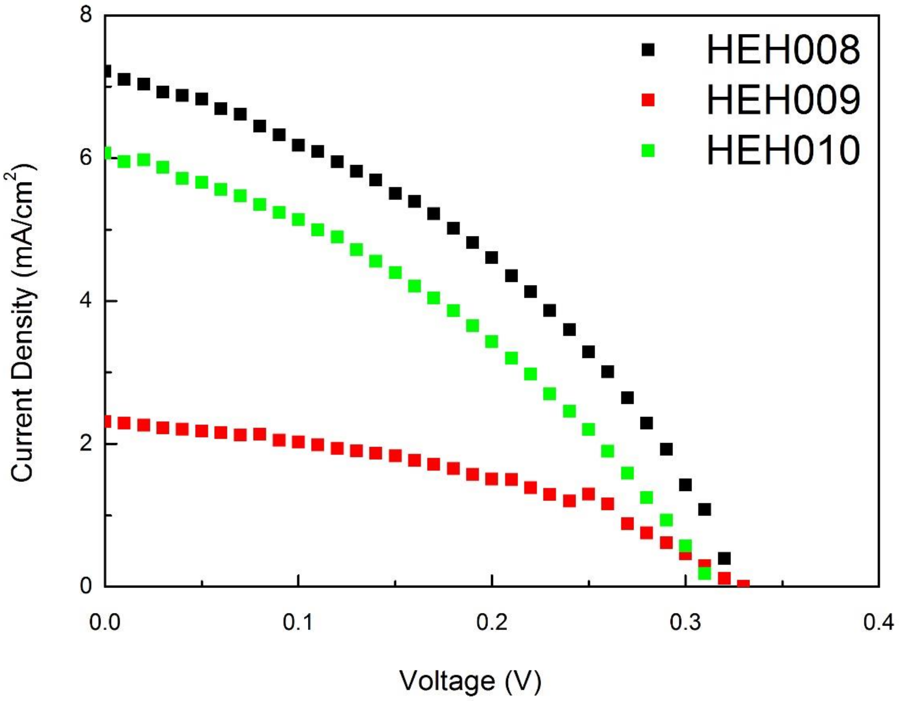

Figure 5-26: *J-V* plot of HEHs with completely filled CuSCN coating, HEH008-HEH010.

Table 5-10: Solar cell parameters of HEHs, HEH008-HEH010.

Device	J_{sc} (mA/cm^2)	V_{oc} (V)	P_{max} (mW/cm^2)	*FF*	PCE (%)
HEH008	7.22	0.32	0.92	0.40	0.92
HEH009	2.31	0.33	0.32	0.43	0.32
HEH010	6.07	0.31	0.70	0.37	0.70

From Figure 5-26 and Table 5-10, it can be seen that the optimized CuSCN coating significantly improved the PV performance of HEHs. HEH008 and HEH010 exhibit efficiency above 0.7%, which is comparable to the champion value achieved from FTO-based devices during optimization trials (0.63% from 3ml CuSCN deposited per sub). This demonstrates the successful transfer of the device fabrication from FTO to CW. Comparing to results achieved on devices with low CuSCN pore filling, current density increased from an average of 0.98 mA/cm^2 up to an average of 5.2 mA/cm^2; open-circuit voltage increased from average 0.15 V up to average 0.32 V; *FF* increased from average 0.31 up to 0.40. As a result, average PCE of HEH008-009-010 is 0.65%, significantly higher than those of HEH005-006-007 which is 0.047%. These results indicate the importance of optimization for the CuSCN coating. Optimal CuSCN coating would reduce the internal resistance and lead to a higher short-circuit current and open-circuit voltage. The average PCE of optimized HEH (0.65%) is higher than that of PET-based HEH (0.058%). This is attributed to the low resistance from CW-based devices. Impedance analysis was performed to compare the devices based on PET and CW.

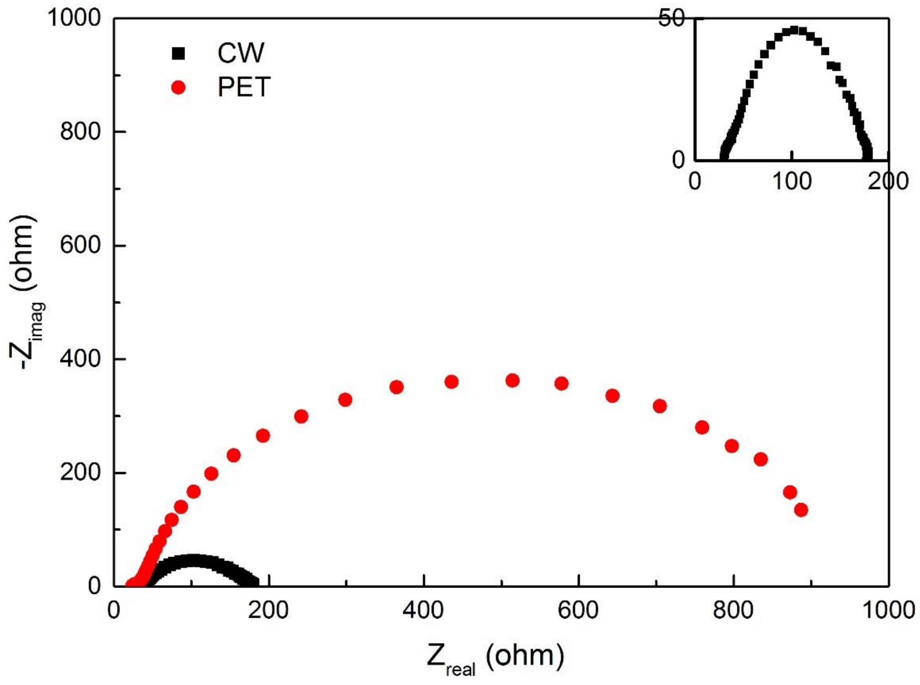

Figure 5-27: Impedance analysis of CW-based HEH008 and PET-based HEH003. Both tests were carried under AM1.5 illumination.

Table 5-11: Solar cell parameters and impedance results of CW-based HEH008 and PET-based HEH003.

	PV parameters					EIS results	
Device	J_{sc} (mA/cm^2)	V_{oc} (V)	P_{max} (mW/cm^2)	*FF*	PCE (%)	R_s (Ω)	R_{ct} (Ω)
CW-HEH008	7.22	0.32	0.92	0.40	0.92	29.85	141.5
PET-HEH003	0.25	0.39	0.05	0.49	0.05	34.14	930

From Figure 5-27 and Table 5-11, it can be seen that the improved PV performance from CW-based HEH can be attributed to reduced charge transfer resistance. High temperature post annealing is suggested to remove the surface defects and enhance the near band edge emission as shown in PL results (see Section 4.2.5). The optimized CuSCN coating would also passivate the surface defects and reduce the number of recombination sites. As a result, CW-based HEH show higher PV performances than PET-based HEH.

For the NG performance, the CW-based HEH was initially tested in the same way as PET-based HEH. However, due to the long aspect ratio and brittle nature of the glass, the resonance frequency was found to be in the range of 20-40 Hz comparing to 200 Hz for PET-based HEH. Also, the amplitude of the magnetic shaker had to be set at half the value used for PET substrate to avoid cracks occurring on the brittle CW-based devices. Cracks would potentially occur when the substrate is undergoing high amplitude (>4 cm) oscillation. As a result, the voltage output signal was not able to be captured on the oscilloscope. Thus, time-dependent current output characteristics were measured using a Keithley 2400 SMU combined with NI LabVIEW. The test was carried out at 0 V bias (short-circuit). The sample was fixed on the stage (no spring steel cantilever) of the magnetic shaker under the solar simulator. During 5-15 s, the shaker was turned on at the pre-set resonance frequency for the device. The current output from the NG effect of the HEH was recorded. During 20-30 s, sample was kept steady while the solar simulator was turned on. The current output from the PV effect of the HEH was recorded. During 35-50 s, both shaker and solar simulator were turned on. The sample was oscillating under illumination. The current output of the hybrid energy harvesting effect of the HEH was recorded.

For the NG performance and hybrid energy harvesting performance of HEH005-010, time-dependent current density scans were performed and results shown in Figure 5-28 and Figure 5-29 below. In Figure 5-28 below, responses from devices with low pore filling CuSCN were recorded and plotted.

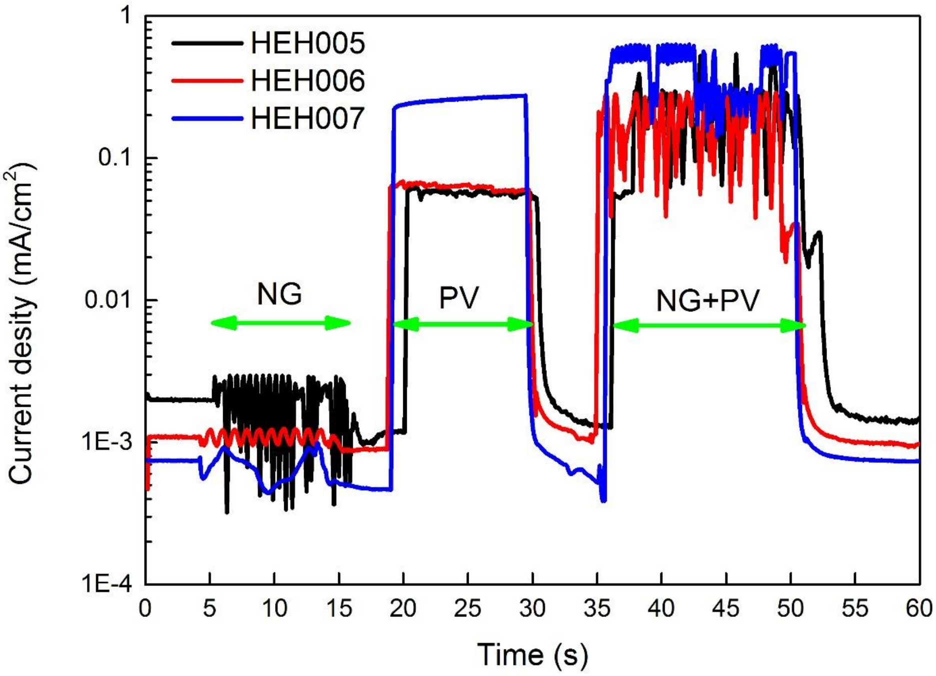

Figure 5-28: Time-dependent peak-current density (log scale) of CW-based HEH005, HEH006 and HEH007. Details regarding the fabrication parameters are shown in Table 5-8.

Table 5-12: Current density (mA/cm^2) values of HEHs tested under solely oscillation (NG), solely illumination (PV) and oscillation under illumination (NG+PV).

	HEH005		HEH006		HEH007	
	Peak	Average	Peak	Average	Peak	Average
NG	0.0030	0.0021	0.0012	0.0011	0.0010	0.0007
PV	0.0644	0.0564	0.0674	0.0615	0.2761	0.2502
NG+PV	0.5682	0.1915	0.2882	0.2016	0.6304	0.3851

From Figure 5-28 and Table 5-12, it can be seen that: the current density generated while the device was oscillating is on the range of 0.001 to 0.003 mA/cm^2 (averaging 0.00172 mA/cm^2). As a comparison, the current density generated under illumination is in the range of 0.06 to 0.27 mA/cm^2 (averaging 0.14 mA/cm^2). This (together with results achieved on PET-HEHs shown in 5.2) further supports the conclusion that the main power of the HEH would be coming from the PV effect. As for the current output generated under NG+PV condition, the current density significantly increased comparing to the value at PV condition. The resulted value is not a simple summation of the current density generated by the NG and PV alone. This is further evidence corresponding to the resistive load matching plot shown in Figure 5-11. It suggests the current output from NG+PV condition is not only a summation of the current output from the NG and PV individually. Thus, it is suggested that, under oscillating and illumination, the HEH is not only performing as NG and PV separately. The current output can be further improved. These results are further evidence to support the theory proposed in Figure 5-14. The average value of the alternating current generated by NG effect is lower than the constant direct current generated by the PV effect. Under NG+PV condition, the piezoelectric ZnO would develop an alternating polarization which affects the carrier transport dynamics in the devices. According to the oscillating mode shown in Figure 5-14, the alternating polarization would further separate the electrons and holes after charge separation process. This is suggested to reduce recombination and further increase the electron density extracted which leads to increased current output. The results achieved here confirm that PV efficiency can be enhanced by piezoelectric effect in this system, and it is not just an additive effect.

In Figure 5-29 below, responses from devices with completely filled CuSCN were recorded and plotted.

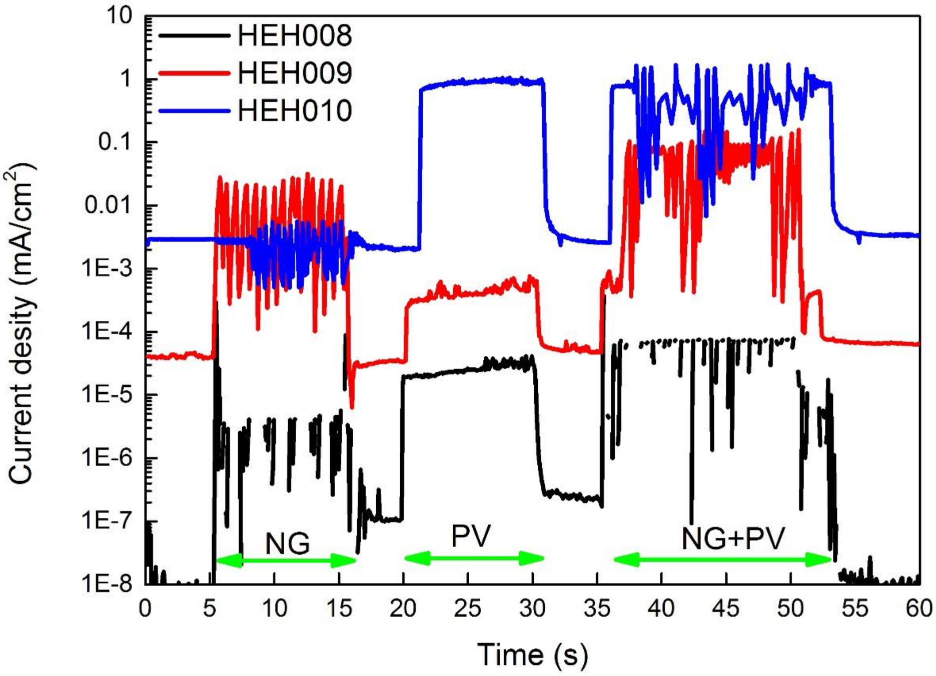

Figure 5-29: Time-dependent peak-current density (log scale) of CW-based HEH008, HEH009 and HEH010. Details regarding the fabrication parameters are shown in Table 5-8.

Table 5-13: Peak-current density (mA/cm²) values of HEHs tested under solely oscillation (NG), solely illumination (PV) and oscillation under illumination (NG+PV).

	HEH008		HEH009		HEH010	
	Peak	Average	Peak	Average	Peak	Average
NG	0.0003	3.6656E-06	0.0316	0.0091	0.0056	0.0026
PV	4.1172E-05	2.54074E-05	0.0008	0.0004	1.0560	0.7768
NG+PV	3.6983E-04	2.57577E-05	0.1577	0.0400	1.7058	0.7223

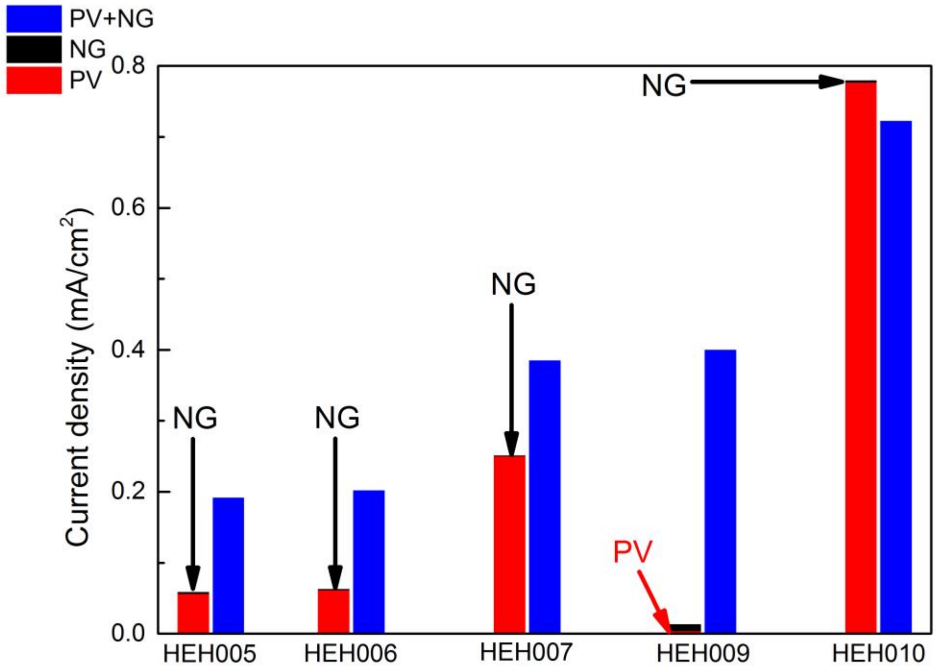

Figure 5-30: Average current density (mA/cm^2) comparison of N719-HEHs achieved under NG, PV and NG+PV conditions.

From Figure 5-29 and Table 5-13, the result shows consistency on HEHs with completely filled CuSCN. HEH008 broke during the test which was caused by high amplitude oscillation (>4 cm). Thus, HEH008 showed the lowest current density even it has the highest PV performance obtained from *J-V* scans (PCE=0.92%, see Table 5-10). The empty points on the curve also indicates discontinued contacts. For HEH009, the PV performance was the lowest among HEH008-HEH010, hence the current density measured here is low. For the average value, NG generated current density is higher than PV generated current density. Current density tested under NG+PV condition is significantly higher than NG and PV alone or combined. This further suggests the improvement is not a simple additive effect. For HEH010, the peak current density under NG+PV condition shows 1.706 mA/cm^2 comparing to 0.006 mA/cm^2 under NG and 1.056 mA/cm^2 under PV. However the average value from NG+PV is slightly lower than PV, which is attributed to unstable contact possibly due to crack formed within the device. It is suggested that the unstable contact may originate from the completely filled CuSCN film. It has been demonstrated that complete filling of CuSCN would reduce the charge transfer resistance and improve the PV performances of the devices. However, the rigid, ceramic-like CuSCN structure could lead to cracks under mechanical bending, which reduces the stability of the devices.

Figure 5-30 shows the comparison for CW-based N719-HEHs. HEH008 is not included due to the sample was broken. Other than HEH010 shows slight lower current density output under NG+PV, HEH005, HEH006, HEH007 and HEH009 all show further enhancement under NG+PV compared to the summation of results achieved under NG and PV alone.

5.4 Summary

In summary, a N719-based hybrid energy harvester was designed and fabricated. The addition of light absorber layer into the p-n junction based kinetic-to-electric nanogenerator is found to enable the device to harvest both solar and kinetic energy. The substrate plays an important role for the power output of the device due to the different resistance, thermal stability and flexibility. P-type HTM is found to have a great impact on the performance of the PV effect from the HEHs. For PET-based HEHs, higher flexibility leads to higher kinetic-to-electric output, however the PV output is poor due to the high charge transfer resistance revealed by impedance analysis. For CW-based HEH, PV performance is greatly improved which is attributed to the post annealing process on the ZnO nanorods. Post annealing was found to reduce the recombination and improve the photo current output. Due to fact that CW is brittle and shows low flexibility, NG performance of the device is limited. For HEHs based on both substrates, resistive load matching tests and time-dependent current output measurement revealed the power tested under NG+PV condition is higher than power tested under NG and PV condition separately or even the simple summation of the two. This suggests when tested under oscillation and illumination condition, the charge carrier dynamics can be affected by oscillation. It is suggested that oscillation leads to polarization formed due to the piezoelectric nature of ZnO nanorods. The direction of the dipole alternates as the ZnO nanorod oscillates. Thus the electric field associated with the polarization is expected to further drive the separated electrons and holes away from each other at the interface. This effect would lead to reduced recombination within the device, hence improve the current density. This finding confirms that the previously reported enhancement of PV device efficiency in ZnO nanorod/P3HT system[87] can be observed in a very different PV device based on the solid-state DSSC concept.

Chapter 6 Hybrid energy harvester based on perovskite light absorber layer

From chapter 5, a hybrid energy harvester based on N719 dye was successfully designed and fabricated. The addition of N719 dye molecules enabled energy harvesting of both kinetic and solar energy within one device. Solid-state solar cells utilizing perovskite-structured methylammonium lead iodide (MAPI) as light absorber layer have been reported to exhibit higher power conversion efficiency as discussed in Section 2.3. It is then within our great interest to design and fabricate perovskite-based hybrid energy harvesters (PSC-HEHs) which have the potential to improve the power output compared to N719-based HEHs.

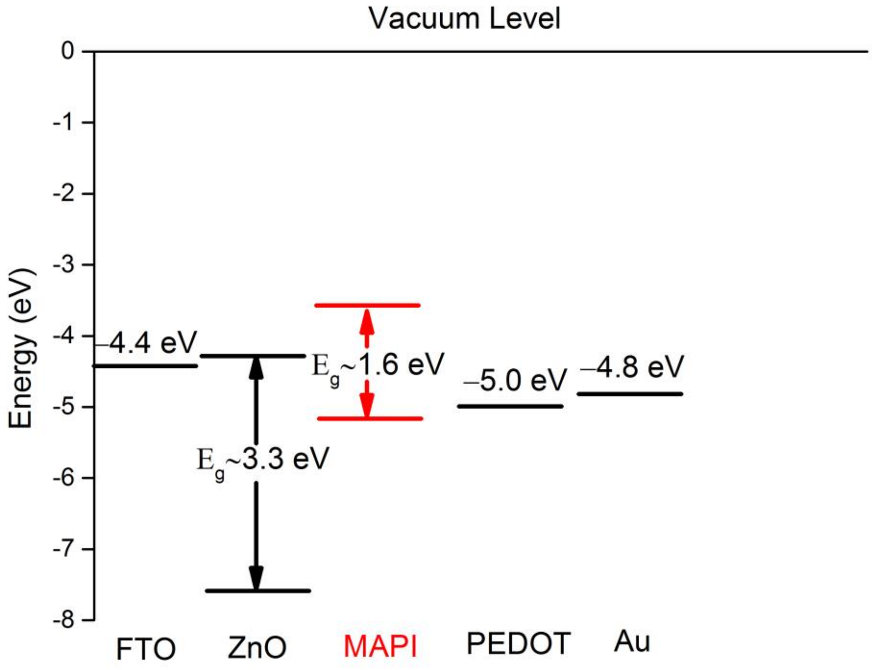

Figure 6-1: Band diagram of the materials used to fabricate PSC-HEH.

The proposed band alignment is shown in Figure 6-1 above. The substrate utilized is Corning® Willow™ glass. The n-type material is ZnO nanorod. As discussed in

Section 2.4, shorter nanorods (<1 μm) are typically used in ZnO-based perovskite solar cells (PSC). Methylammonium lead iodide is used as light absorber layer. PEDOT:PSS is used as hole transport material (HTM). Unlike conventional aqueous PEDOT:PSS solution, perovskite-compatible, commercial toluene-based PEDOT:PSS solution (Clevios™) was purchased from Heraeus, Germany and used as received. Finally, 100 nm gold is evaporated on top of PEDOT:PSS. The device is then sealed using a laminator (details in Chapter 3).

6.1 Morphology optimization of perovskite on ZnO nanorods

Regarding to the design of PSC-HEH, the morphologies of ZnO nanorods and the perovskite layer were considered as important variables which could significantly affect the performance of ZnO-based perovskite solar cells[61,63,154]. Similar to the design methodology utilized in Chapter 5 regarding N719-HEH, photovoltaic (PV) performance of the PSC-HEH was optimized on FTO-glass substrates first. The optimized fabrication processes were then transferred onto Corning© Willow™ glass to probe the performances of kinetic and solar energy harvesting.

As reported in literature[61,62], pH=6 synthesis method (Sol-gel spin seeding, equimolar 0.025 M Zinc Nitrate and HMT, 90 °C, details in Section 3.2) was utilized for the growth of ZnO nanorods included in this chapter. ZnO nanorods were annealed at 500 °C for one hour prior to the perovskite layer deposition. The deposition methods for perovskite layer were two-step sequential method (noted as 2) and two-step with additive method (noted as 2-A), as shown in details in Section 3.3. For the precursor deposition step (first step), recipe 2 utilizes 0.46 g PbI_2 (Sigma Aldrich, 99%) dissolved in 1 ml of solvent containing 70% dimethylformamide (DMF, Sigma Aldrich, 99.8%) and 30% dimethyl sulfoxide (DMSO, Alfa Aesar, 99+%); recipe 2-A utilizes 0.46 g PbI_2, 0.1 g methylammonium iodide (MAI, Sigma, 98%) and 0.04 g additive dissolved in 1 ml DMF. The additive is 2-(Dibutylamino)ethanol. It has been reported to reduce precipitation of insoluble solid and stabilize the precursor solution[155]. Similar interfacial modifiers have also been reported to improve the stability, suppress hysteresis and induce smoother and larger grain sized perovskites[156]. For the MAI deposition step (second step), 0.1 g methylammonium iodide (Solaronix) is dissolved in 10 ml in anhydrous isopropanol (Sigma Aldrich, 99.5%), which is same for both recipes.

Substrate preheating[157] and anti-solvent treatment[158–160] have been reported to modify the morphologies of the perovskite structures on TiO_2 mesoporous layer. However the effect on ZnO nanorods remain unclear. Thus, in this section, effect of preheating and anti-solvent treatment will be discussed. Both first step precursor deposition and second step MAI deposition utilize 3000 RPM (30 s) for spin coating and 100 °C for post annealing.

6.1.1 Effect of preheating

The substrate was preheated on a hotplate set at 100 °C. It was then quickly transferred onto the sample stage of spin coater. The first-step precursor solution was then deposited onto the surface of the substrate immediately. The substrate was spin coated at 3000 RPM for 30 s, followed by thermal annealing at 100 °C. The resulted perovskite films were examined under SEM, results shown in Figure 6-2 below.

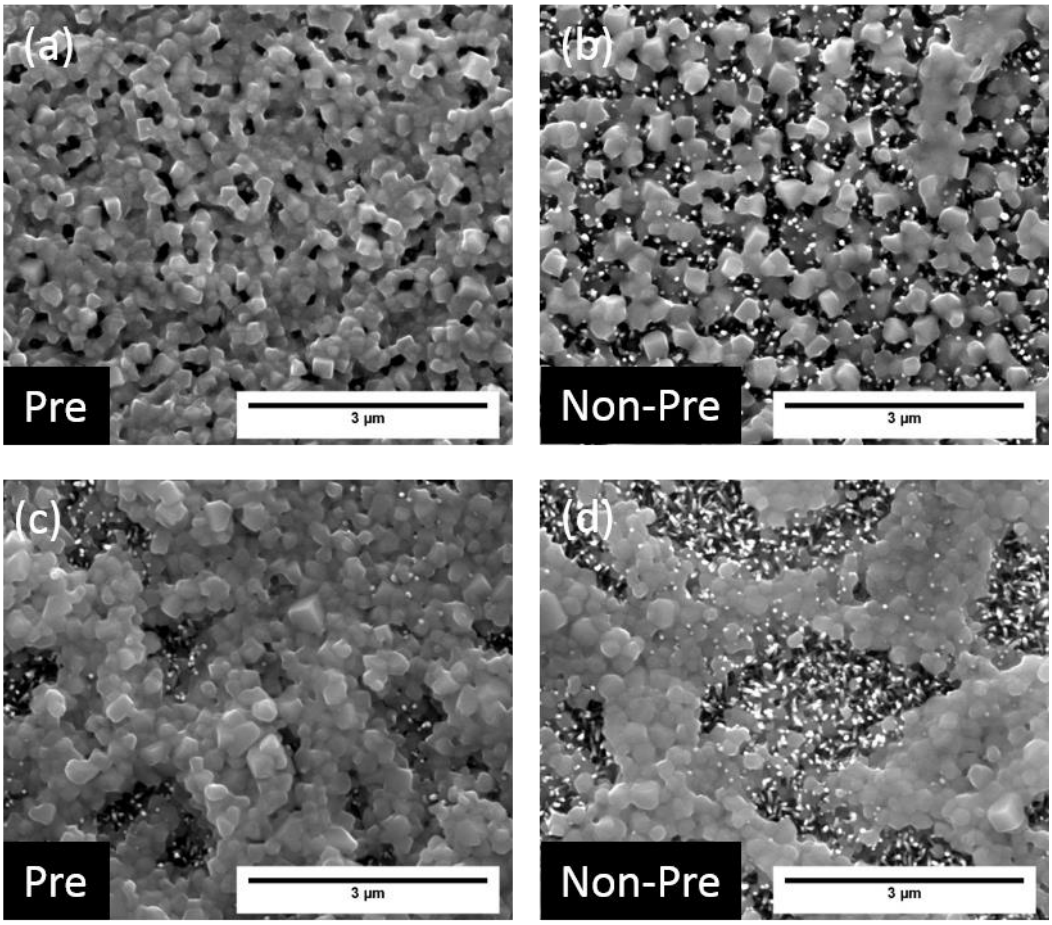

Figure 6-2: Preheating effect on the morphology of perovskite on ZnO nanorods. (a) and (b) Perovskite deposited using 2-A recipe. (c) and (d) Perovskite deposited using 2 step recipe.

The nanorods of samples shown in Figure 6-2 were grown using pH=6 method for 4 h (900 nm). From Figure 6-2, it can be seen that preheating treatment improves the continuity of the film. Non-preheated substrates lead to isolated crystals shown in image (b). For both recipes, areas with exposed ZnO tips are discovered which could lead to contact between ZnO and p-type hole transport material (HTM). This could cause short-circuiting within the device and deteriorate the performance of the solar cell. It would be beneficial for the rods to be fully covered with a perovskite capping layer.

From results shown in Figure 6-2, preheating is found to improve the uniformity and continuity of the perovskite film from both recipes. The reason is attributed to the crystallization rate of PbI_2 becoming higher than the solvent evaporation rate as the preheating substrate temperature increases. Therefore, preheating treatment is beneficial to promoting the crystallization rate of PbI_2 and obtaining a more uniform and denser film morphology[161,162]. It is suggested that the preheating affects the surface-induced nucleation: as the temperature increases, so does the number of nucleation events, resulting a larger number of smaller crystals and better surface coverage. The nucleation process requires a higher activation energy and therefore slower rate than the following growth process. Temperature increase leads to faster nucleation and hence higher number of crystals, resulting in denser films[162].

6.1.2 Effect of anti-solvent treatment

Effect of anti-solvent treatment was investigated. Toluene (Anhydrous, 99.8% Sigma Aldrich) was used as the anti-solvent. The deposition of toluene takes place in the second step of perovskite recipe 2 and 2-A, which is the MAI deposition step. During the MAI deposition, once the substrate is wet with MAI solution, it is accelerated to 3000 RPM for 30 s. It then decelerates down to 500 RPM and maintains for two seconds. During the two-second window, a consistent flow of toluene (0.5 ml) is injected onto the centre of the substrate from a syringe. The substrate then accelerates again to 3000 RPM for another 30 s. The resulted perovskite film is then annealed on a hot plate at 100 °C.

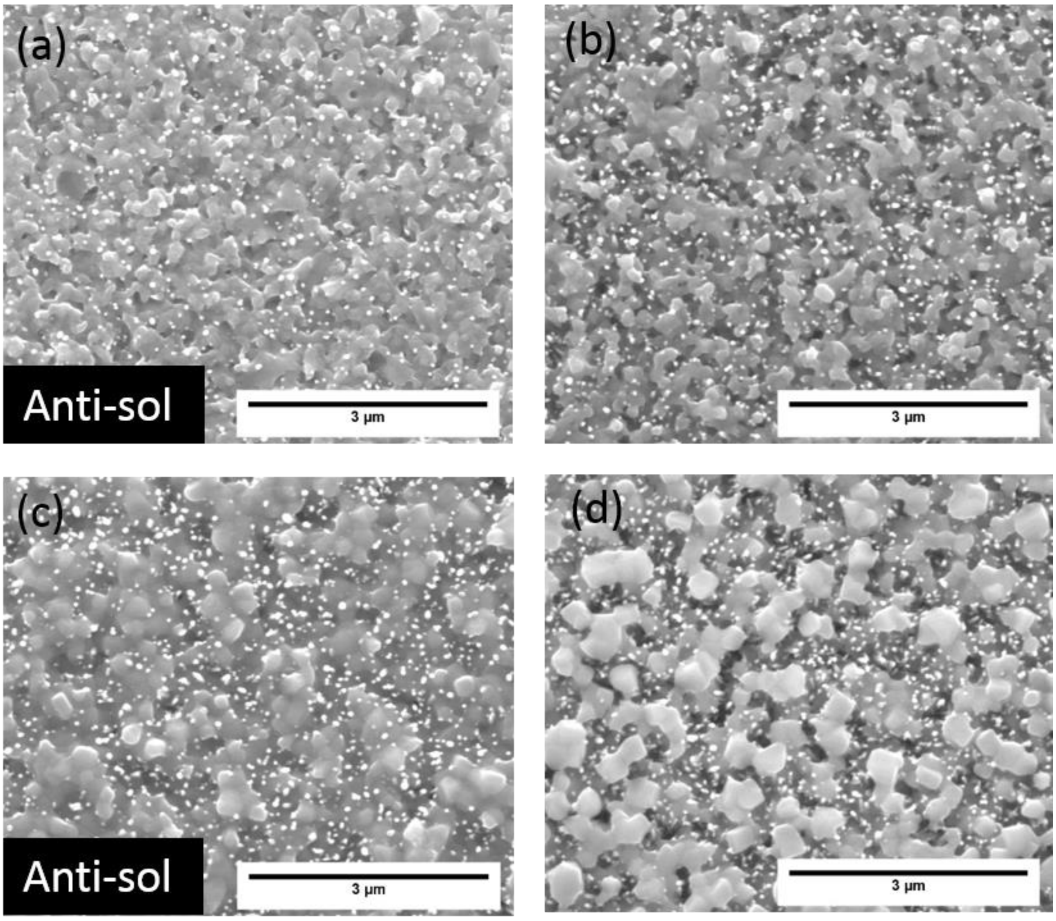

Figure 6-3: Effect of anti-solvent treatment on the morphology of perovskite on ZnO nanorods. (a) and (b) Perovskite deposited using 2 step recipe. (c) and (d) Perovskite deposited using 2-A recipe.

From Figure 6-3a and b, it can be seen that anti-solvent treatment does not have any significant effect on the morphology of perovskite deposited using 2 step recipe. Comparing image (c) and (d), it can been seen that anti-solvent treatment clearly improves the film uniformity and continuity of perovskite deposited using 2-A recipe. Image (d) shows isolated crystals; image (c) shows higher degree of connection between the crystals.

For two-step with additive recipe (2-A), the initial precursor contains PbI_2, MAI and additive in DMF, which indicates perovskite structure would form after the first step. After the first step, it is suggested that a mixture of PbI_2-MAI-Perovskite was achieved as the film turns to light brown color[160]. Due to the presence of perovskite structure, the post annealing time after the first step was limited at 45 s as longer time was found to severely degrade the perovskite with yellow areas (PbI_2) beginning to appear. Prolonged exposure time to high temperature (100 °C) has been reported to accelerate thermal decomposition for perovskite deposited on ZnO[163]. The decomposition process is a result of the surface properties of ZnO: the alkaline nature causes deprotonation of methylammonium ions and hence degradation of the perovskite[164]. Thus, DMF solvent was not fully evaporated before the second step of MAI deposition. After the anti-solvent treatment, toluene is less polar than DMF and decrease the solubility of the precursors in DMF. This leads to fast crystallization within the film, the perovskite precursor rapidly precipitates and uniform crystals are formed[158].

On the other hand, two-step recipe has pure PbI_2 dissolved in DMF/DMSO as precursor. Without MAI, the film deposited after the first step contains only PbI_2 and DMF/DMSO. Thus, prolonged annealing time was applied (5 min). As a result, only small amount of DMF would be left after the first annealing. When the anti-solvent treatment was applied during the second step, majority of the DMF solvent had likely already evaporated. Hence the PbI_2 would be converted to perovskite upon MAI addition prior to the anti-solvent treatment. Also, the presence of DMSO which strongly coordinates with lead halides by forming intermediate phases, has been reported to prevent the immediate crystallization upon application of toluene droplets[165]. Hence, no significant effect was observed from anti-solvent treatment by toluene in 2-step recipe.

6.1.3 Effect of length of nanorods

The length of the nanorods greatly affect the deposited perovskite structure. For kinetic-to-electric application, high aspect ratio rods lead to higher power output[72]. Thus, it would be ideal to design a HEH based on longer rods. However, as discussed in Section 2.4, nanorod with shorter length (<1 μm) is typically utilized in ZnO nanorod-based PSC. For ZnO grown using pH=6 method, length of the rods reaches 350 nm, 600 nm and 900 nm with growth time being 2.5, 3 and 4 h (see Table 4-1). The perovskite structures on ZnO with various lengths are shown in Figure 6-4 below. Preheating temperature was 100 °C and no anti-solvent treatment was applied.

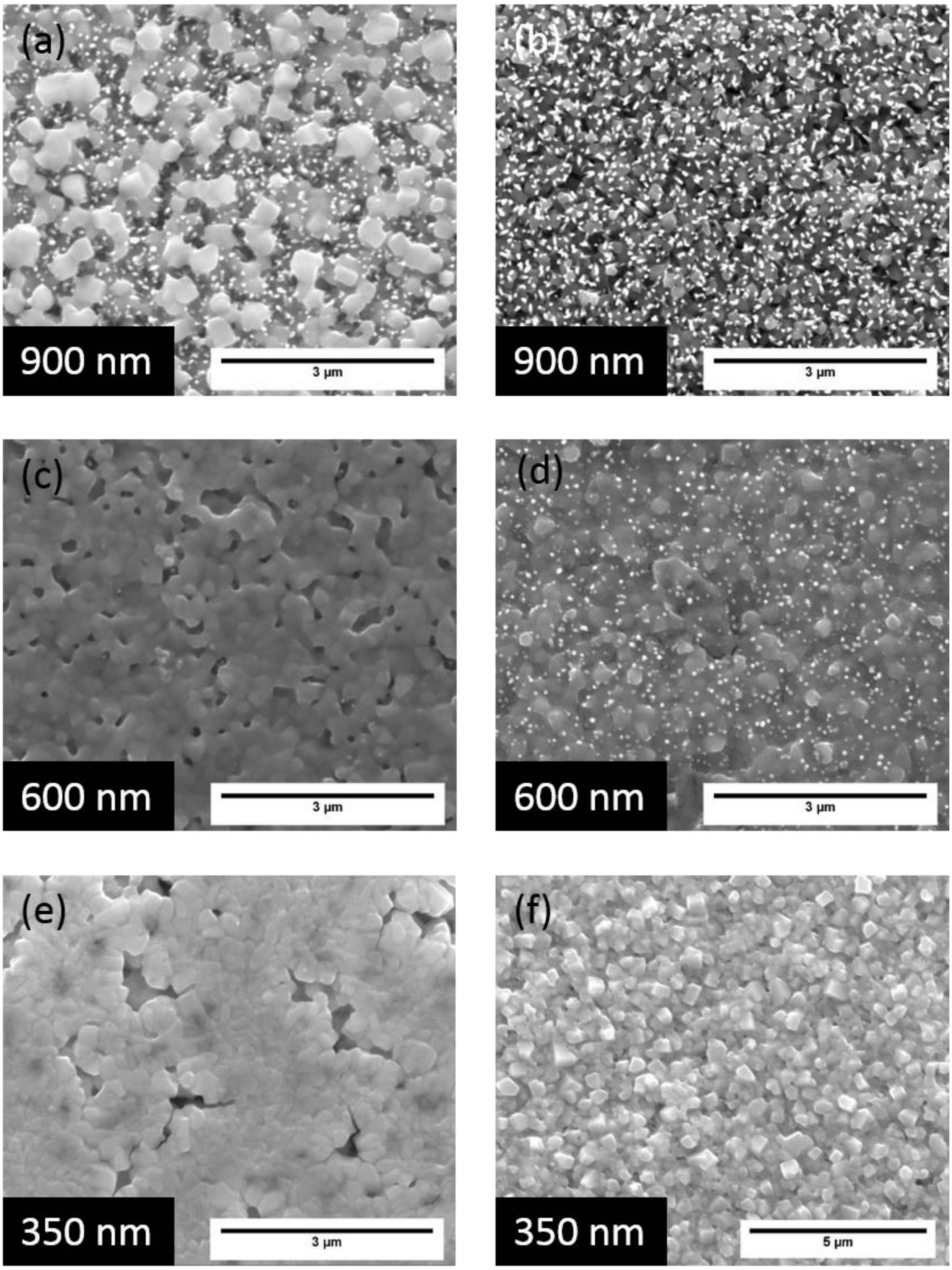

Figure 6-4: Effect of the nanorod length on the morphologies of perovskite on ZnO nanorods. (a), (c) and (e) Perovskite deposited using 2-A recipe. (b), (d) and (f) Perovskite deposited using 2 step recipe.

From Figure 6-4, it can be seen that on 900 nm rods, the coverages of perovskite from both recipes are incomplete. 2-A recipe result shows isolated crystals as seen in image (a). 2 step recipe result shows exposed nanorod tips as seen in image (b). When the length of nanorods is reduced down to 600 nm, the coverage of perovskites from both recipes show great improvement. 2-A recipe result shows less pin holes and only a small amount of nanorod tips can be discovered on the surface of the film as seen in image (c). 2 step recipe result shows significantly improved coverage as seen in image (d). When the length is further reduced down to 350 nm, it can be seen that a complete coverage can be achieved for perovskites using both recipes. No tips of ZnO nanorods can be discovered. This indicates a capping layer of perovskite is achieved, which could screen the contact between ZnO and HTM and reduce recombination. Thus, lower ZnO length facilitates the infiltration of perovskite due to reduced depth of the pores. Even though longer rods would benefit the kinetic energy harvesting aspect, shorter rods appear to be needed for the achievement of a functioning perovskite solar cell.

6.1.4 PV performances of PSC

From the results shown in Figure 6-4e and Figure 6-4f above, the PV performance of the PSCs based on both 2 step and 2-A recipes were tested. The ZnO nanorods were grown using 2.5 h pH=6 method (350 nm) and annealed at 500 °C for 1 hour.

Table 6-1: Parameters of perovskite selected to fabricate devices on FTO.

Recipe	Preheat (°C)	Precursor (kRPM)	First annealing (°C)	MAI spin coating (kRPM)	Final annealing (°C)
2	100	3	100	3	100
2+A	70	3	100	3	100

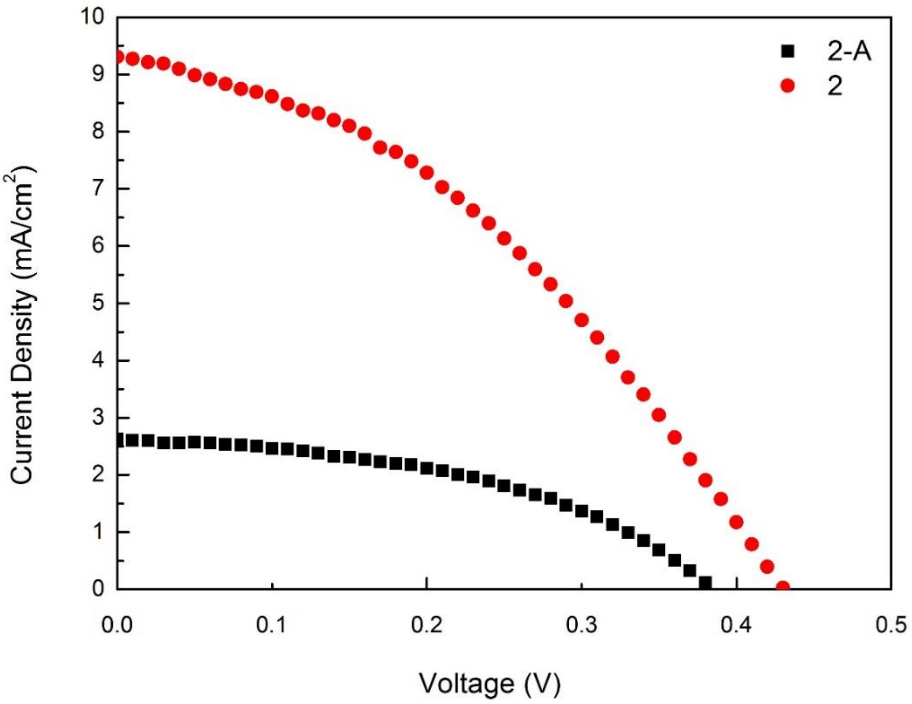

Figure 6-5: *J-V* plot of PSCs based on different perovskite recipes.

Table 6-2: Solar cell parameters of PSC based on different perovskite recipes.

PSC recipe	J_{sc} (mA/cm^2)	V_{oc} (V)	P_{max} (mW/cm^2)	*FF*	PCE (%)
2-A	2.62±0.15	0.38±0.02	0.46±0.07	0.46±0.06	0.46±0.07
2	9.31±0.70	0.43±0.02	1.54±0.14	0.38±0.02	1.54±0.14

From Figure 6-5 and Table 6-2, the device made using the 2 step method without additive shows higher J_{sc}, V_{oc} and efficiency. The only drawback was the low *FF*. The tripled efficiency is mainly attributed to tripled J_{sc} (Table 6-2). The differences of the morphologies of perovskite layer and cross section of the devices were revealed in SEM images shown in Figure 6-6.

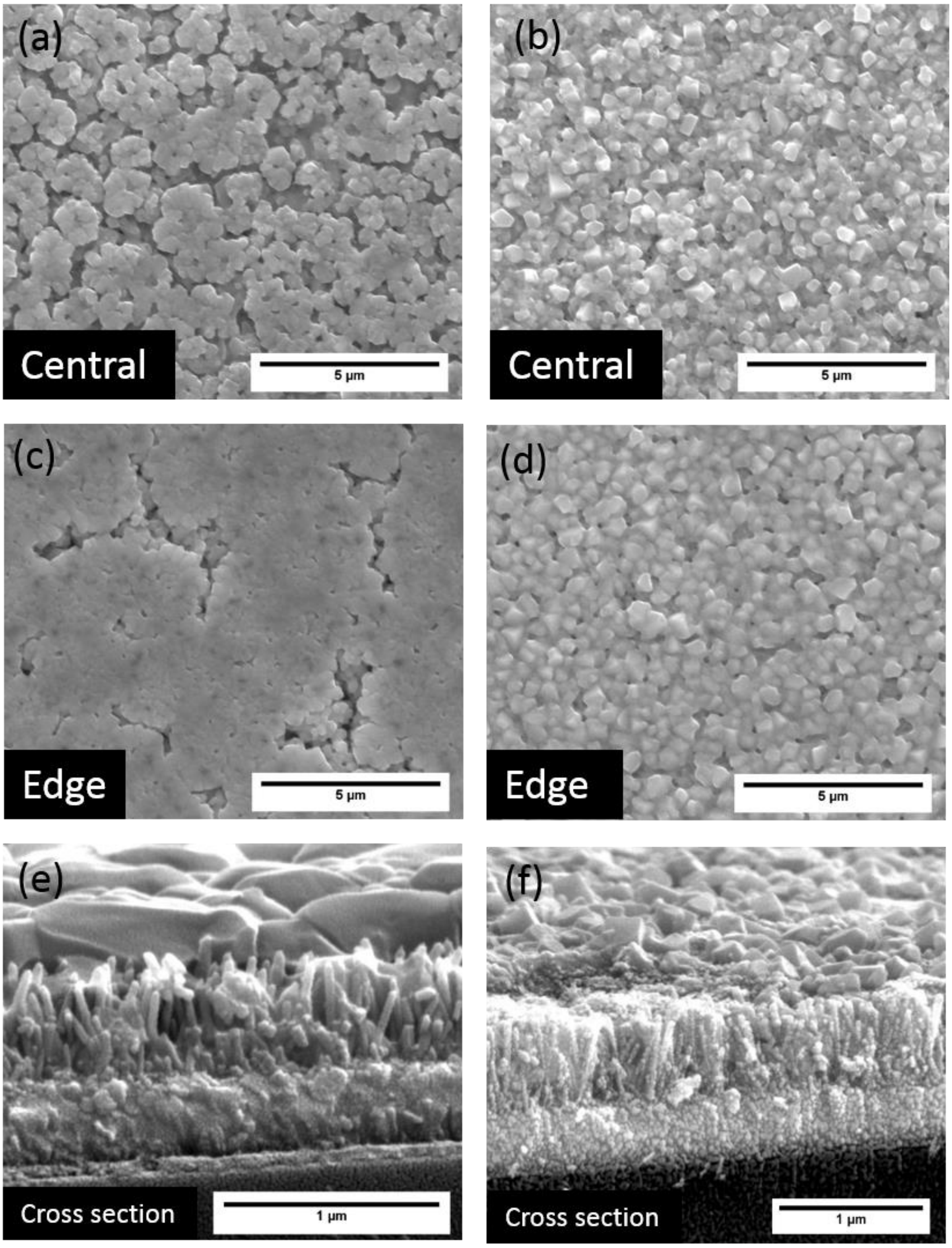

Figure 6-6: SEM images of device cross section and perovskite top view from 2+A recipe: (a) Central area of substrate, (c) Edge area of substrate and (e) Cross section. 2 step recipe: (b) Central area of substrate, (d) Edge area of substrate and (f) Cross section.

It can be seen from Figure 6-6 that, the edge areas of the substrates show a denser film with high continuity as shown in image (c) and image (d). Central areas show low uniformity as shown in image (a) and image (b). Comparing image (a) and (b) alone, the two different recipes result in two different morphologies. The perovskite deposited using 2-A method has small amount of pinholes on the top surface in image (a). Cross section images revealed the differences of thickness of the perovskite capping layers. The thickness of the capping layer for 2-A perovskite is ~280 nm. For 2 step without additive recipe, the thickness of capping layer is ~100 nm. Gaps between the rods can also be noted from image (e), indicating the infiltration of the perovskite between the rods is poor. This could reduce the contact area between the rods and perovskite. Furthermore, if the perovskite layer is thinner, the probability of physical contacts between ZnO and HTM could be increased. However, benefiting from the thick layer (280 nm) and the low-infiltration nature of spin coated PEDOT:PSS, it is unlikely for the PEDOT:PSS to make contact with ZnO. Thus, the low short-circuit current from the devices made using 2-A recipe is mainly attributed to the poor contact between ZnO/perovskite and the high recombination rate due to the poor electron transport paths. The thick capping layer (280 nm) is also suggested to increase the probability of charge recombination. Impedance analysis was performed on devices made using 2 step recipe and 2-A recipe, results shown in Figure 6-7.

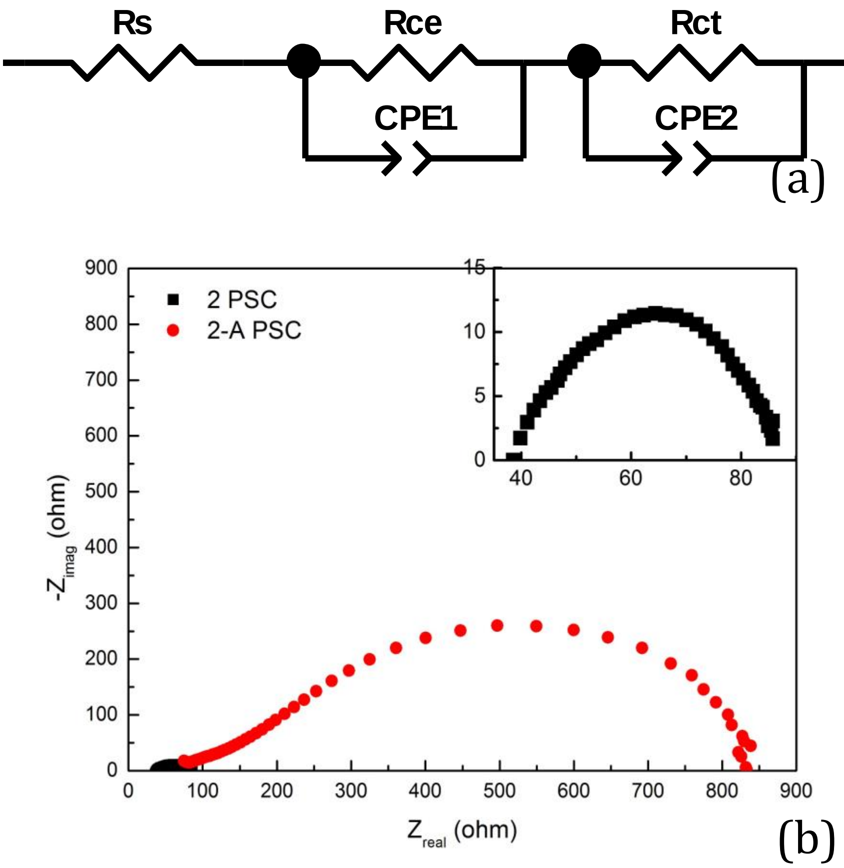

Figure 6-7: (a) Equivalent circuit, (b) Impedance plot of the PSCs based on different perovskite recipes.

Table 6-3: Impedance analysis fitting results of the PSCs based on different perovskite recipes.

Sample	R_s (Ω)	R_{ct} (Ω)
2	40	44.61
2-A	41.12	289.5

From impedance shown in Figure 6-7 and Table 6-3, the series resistance of both devices are within the similar range. The main difference is the charge transfer resistance which is related to recombination process. Perovskite made using 2-A recipe shows 289.5 Ω compared to 44.61 Ω achieved using 2-step recipe. This further supports the explanation that the high resistance caused by the poor contact between ZnO and perovskite as shown in Figure 6-6e, which leads to lowered current density of 2.62 mA/cm^2 for 2-A recipe compared to 9.31 mA/cm^2 for 2 step recipe. Thus, 2 step recipe was selected to fabricate HEH devices.

6.1.5 Structure transfer from FTO glass to Corning© Willow™ glass

From results achieved in Section 6.1.4, the perovskite recipe suitable for ZnO nanorods (350 nm) on FTO is selected to be 2 step without additive. The next step would be to transfer the structure onto Corning© Willow glass™ (CW) then test the combined energy harvesting performances. However, after the first step of PbI_2 precursor deposition on CW substrates, highly reflective PbI_2 crystals (1 mm^2 dimension, visible by eye) formed on the surface (mainly around the edge). The similar PbI_2 structure was discovered in early trials in this project which led to poor perovskite structure as shown in Figure 6-8. Thus, no MAI was further deposited. The cause of the quick crystallization of PbI_2 is attributed to the evaporation of the solvent. First, edge bead effect is a common issue during spin coating process. At the periphery of the substrate, fluid dries first due to increased friction with air. This leads to quick solvent evaporation which explains the fact that majority of the crystals form near the edge. This also explains the differences of film morphologies of perovskite in the central and at the edge as shown in Figure 6-6. Secondly, the surface induced nucleation is sensitive to temperature, it is restricted to the initial deposition time (from the moment of solution casting until the substrate cools down)[162]. It was found during initial trials that, for 2 step deposition method (no additive), the loading time (from the moment of solution casting until the start of spin coating) of PbI_2 on preheated substrate affects the resulted PbI_2 film morphology. Prolonged loading time (>10 s) would result large-sized branched structures shown in Figure 6-8 below.

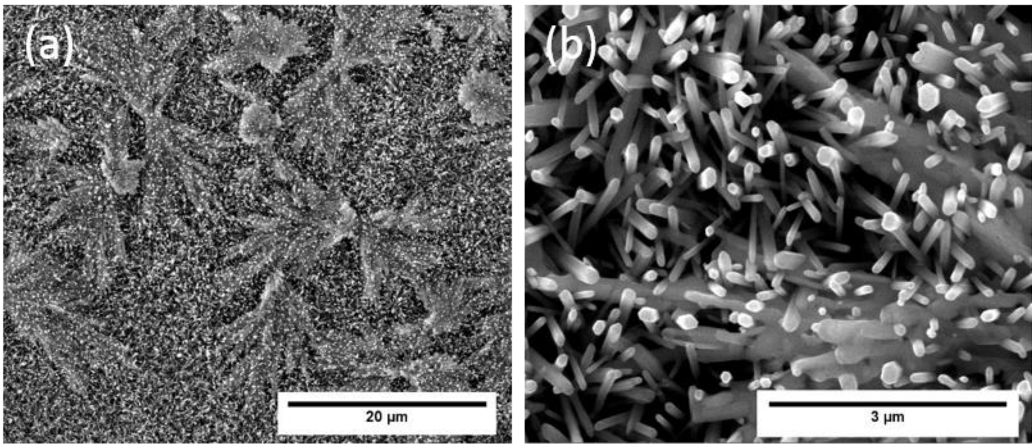

Figure 6-8: Large-sized branched perovskite structure.

As shown in Figure 6-8, the preferential growth is parallel to the surface. During the loading time on a preheated substrate, more nucleation sites are formed resulting in a large number of crystallites with different orientation. The origin of this effect is attributed to the lower symmetry (tetragonal I4/ mcm) of the perovskite crystals[166], which allows for a preferred growth facet.

As a result, preheating process is not suitable for the CW substrates. According to Newton's cooling law of heat transfer, $\frac{dQ}{dt} = h \cdot A \Delta T(\mathrm{t})$, where Q is the thermal energy, h is the heat transfer coefficient, A is the heat transfer surface area and T is the temperature of the objects' surface and interior. Larger surface area would lead to faster cooling of the object. As a result, the long and thin CW substrate dissipates heat at a higher speed than FTO glass, which is attributed to the high surface-to-volume ratio of CW (102.2 cm^{-1} compared to 12.3 cm^{-1} for FTO). By the time when CW substrate is transferred from hot plate to the spin coater, the temperature of the surface is already way below the preheating temperature. Due to the brittleness of the substrate, the handling process of transferring the substrate from hot plate to spin coater also require extra time. Furthermore, due to the long aspect ratio of the substrate, anti-solvent treatment is also not suitable as the droplet of the anti-solvent could not fully cover both ends of the long substrate, leading to non-uniform coverage of the perovskite layer. As a result, the perovskite deposition method for CW needs to be further adjusted. It would therefore be ideal to deposit the perovskite layer without preheating or anti-solvent treatment. Without preheating, the quick crystallization rate of the perovskite structure results poor coverage film shown in Figure 6-2. As reported, $PbCl_2$ can be used as an additive to assist the formation of perovskite in two-step deposition[167]. It is suggested that $PbCl_2$ could inhibit PbI_2 crystallization and contribute to the full conversion of PbI_2, which leads to enhanced perovskite film morphology control[167]. The resulted $CH_3NH_3PbI_{3-x}Cl_x$ shows slowed crystal growth rate due to Cl^- induced lattice distortion during perovskite crystallization[57]. Thus, an adjusted 2 step recipe was proposed with $PbCl_2$ added into the precursor solution. The molar ratio for PbI_2 and $PbCl_2$ is 9:1 in the 7:3 volume ratio of DMF/DMSO precursor solution. The deposition method (noted as 2+Cl) details are shown in Table 6-4:

Table 6-4: Parameters of 2-Cl method selected to deposit perovskite on CW substrate.

Recipe	Preheat (°C)	Precursor (kRPM)	First annealing (°C)	MAI spin coating (kRPM)	Final annealing (°C)
2+Cl	No	3	100	3, No anti-solvent	100

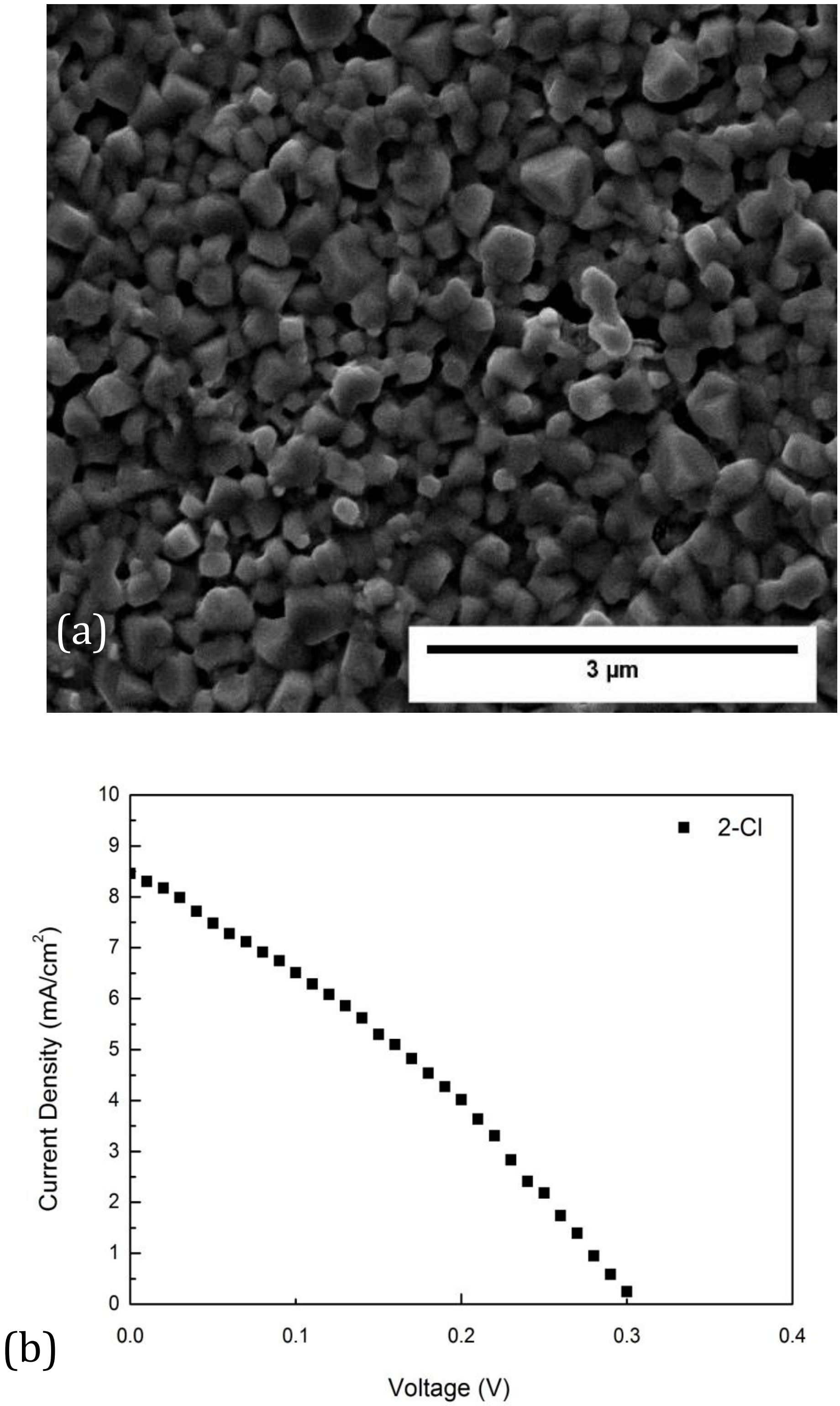

Figure 6-9: (a) Top view of perovskite deposited using 2-Cl recipe. (b) *J*-*V* plot of the device made from 2-Cl recipe.

Table 6-5: Solar cell parameters of PSC based on 2-Cl recipe.

PSC recipe	J_{sc} (mA/cm^2)	V_{oc} (V)	P_{max} (mW/cm^2)	*FF*	PCE (%)
2-Cl	8.46±0.24	0.30±0.03	0.82±0.11	0.32±0.01	0.82±0.11

Although the efficiency is lower than devices based on 2-step perovskite (1.54% PCE), 2-Cl recipe demonstrates good and uniform coverage on CW glass without preheating or anti-solvent treatment. The speed of crystallization was greatly reduced as the colour change (from yellow to black) took 45 s upon post annealing after MAI deposition. For 2 step recipe without $PbCl_2$, the colour change normally took 15 s.

6.2 Perovskite-based HEH using Corning© Willow™ glass

From section 6.1, it was concluded that for CW substrates, 2-Cl recipe (details shown in Table 6-5) was suitable for depositing perovskite. In this section, results of PSC-HEHs made using 2-Cl method are presented. The structure is comprised of CW substrate/ZnO seed layer (spin-coated or sputtered similarly to Chapter 5)/ZnO nanorods using pH=6 method (350 nm)/ $CH_3NH_3PbI_{3-x}Cl_x$ (deposited via 2-Cl recipe)/toluene-based PEDOT:PSS (spin-coated)/gold contact (100 nm via evaporation). The devices were then laminated to test combined PV and NG performances. The structure of the device is shown in the cross section SEM image in Figure 6-10 below:

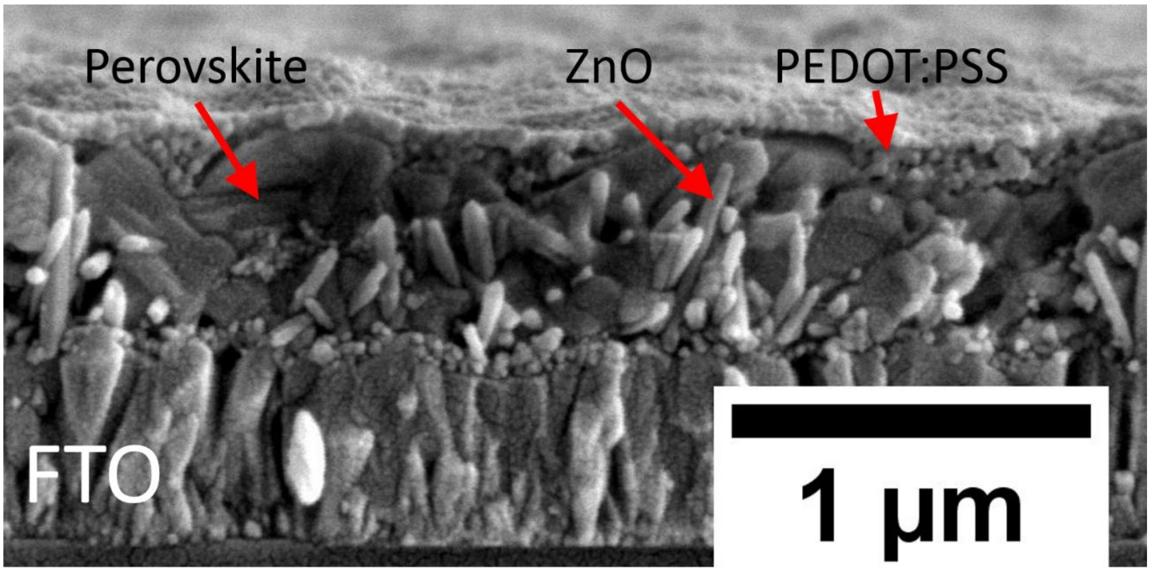

Figure 6-10: Cross section SEM image of PSC-HEH based on ZnO nanorods grown using pH=6 method.

It can be seen from Figure 6-10 that, ZnO nanorods are fully embedded in perovskite with a thin capping layer of 150 nm. The perovskite structure infiltrates down to the bottom of the rods. The spin-coated ZnO seed layer acts as barrier to screen the contact between perovskite and FTO.

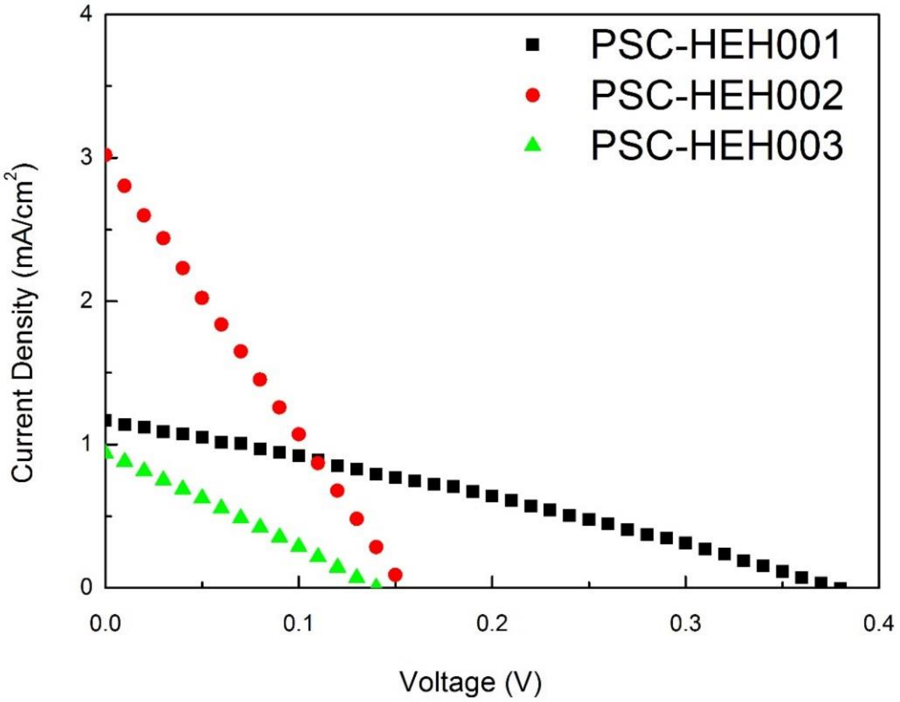

Figure 6-11: *J-V* plot of PSC-HEH001-003.

Table 6-6: Solar cell parameters of PSC-HEH001-003.

Device	Seeding	J_{sc} (mA/cm^2)	V_{oc} (V)	P_{max} (mW/cm^2)	*FF*	PCE (%)
PSC-HEH001	Spin-coat	1.17	0.37	0.13	0.30	0.13
PSC-HEH002	Spin-coat	3.02	0.15	0.12	0.26	0.12
PSC-HEH003	Sputter	0.94	0.14	0.03	0.26	0.03

From Figure 6-11 and Table 6-6, it can be seen that the performances of PSC-HEHs are not consistent. PSC-HEH001 showed the highest open-circuit voltage of 0.37 V which is close to the values achieved on devices based on FTO. PSC-HEH003 shows the lowest short-circuit current and open-circuit voltage, possibly due to high resistance from the sputtered ZnO film. The PV performance is lower than N719-based HEH (average PCE: 0.65%). For N719-based HEH, the light absorber layer of N719 was deposited via soaking, which leads to a uniform coating. The p-type HTM of CuSCN and PEDOT:PSS were deposited via spray coating, which lead to relatively uniform coating even including manual errors. For PSC-HEHS, the light absorber layer of perovskite and p-type HTM of PEDOT:PSS were all deposited via spin coating. The spin coating method leads to uniform film on small FTO substrates. However on long aspect ratio CW substrates, the uniformity of the perovskite film was not ideal. The large gold electrode area (2-3 cm^2) also increased the potential amount of surface defects, which commonly leads to reduced current and *FF* on large scale solar cells[168]. The devices were all made in ambient environment with relatively high humidity which could accelerate degradation. It has been reported that the stability of perovskite on ZnO is lower than it on TiO_2 [163,164,169]. The lamination process includes hot pressing at temperatures from 100-150 °C. It was found that degradation process was accelerated during the lamination process, which lead to degraded perovskite (yellow area) shown after lamination. Thus, in order to further improve the PV performance of PSC-HEHs, a better perovskite deposition method is still to be identified. It would be ideal to fabricate the device inside of a glovebox and using cold lamination methods to avoid degradation of the device. However, as a proof-of-concept, these HEH devices were tested for combined solar and kinetic energy harvesting performances.

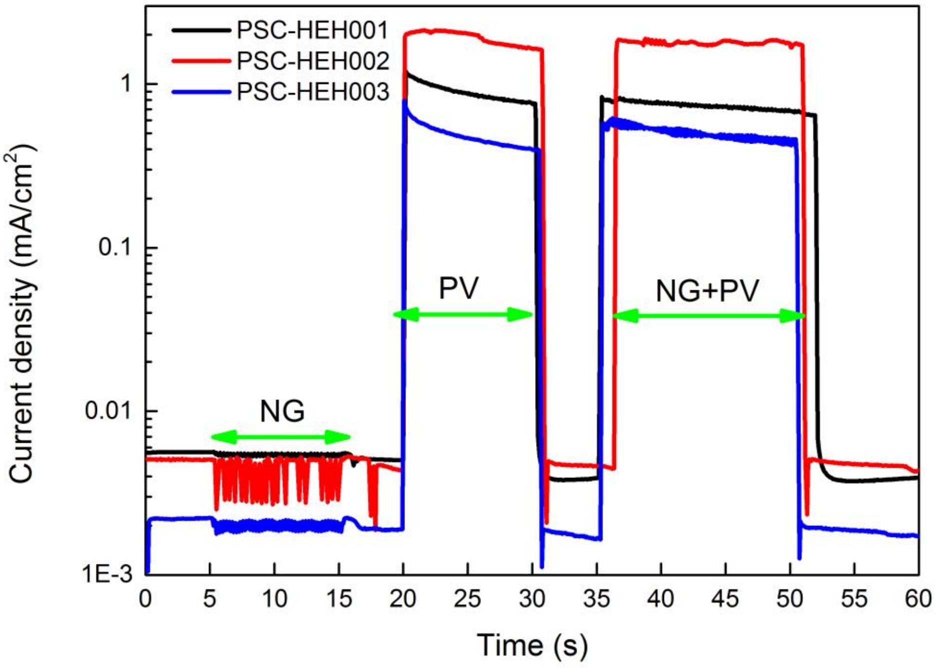

Figure 6-12: Time-dependent current density (log scale) scans of PSC-HEH001, 002 and 003.

Table 6-7: Peak/average current density (mA/cm^2) values of HEHs tested under solely oscillation (NG), solely illumination (PV) and oscillation under illumination (NG+PV).

	PSC-HEH001		PSC-HEH002		PSC-HEH003	
	Peak	Average	Peak	Average	Peak	Average
NG	0.0057	0.0054	0.0053	0.0046	0.0022	0.0020
PV	1.1941	0.8856	2.1259	1.9143	0.7930	0.4832
NG+PV	0.8320	0.7324	1.8891	1.7876	0.6169	0.5008

Figure 6-12 and Table 6-7 show the devices perform as HEHs. For the NG part, all device show response to oscillation. The average current density (mA/cm^2) generated from NG part is ~0.005 from PSC-HEH001-002 which are based on spin-coated seed layer, and 0.002 for PSC-HEH003 which is based on sputtered seed layer.

It is worth noted that, in order to avoid breaking the brittle CW substrate, the amplitude setting from signal generator was only 100 mV (compared to the 400 mV setting for PET-substrates). Higher amplitude setting would lead to higher degree of oscillation displacement (See Figure 5.5), which would give higher current density output. However, this would also cause higher risk of breaking the substrate.

For the PV part, the PSC-HEH002 shows the highest current density while the PSC-HEH003 shows the lowest (average values in Table 6-7), corresponding to the results achieved from *J*-*V* scans shown in Table 6-6. All current responses show a strong overshoot when turned on then slowly start to decay. At time t = 20 s, illumination is switched on and photo current rises to the maximum value. Due to the slow charge extraction, overshoots emerge. The diffusion gradient is then established with charge recombination increases due to high charge carrier density, leading to the decrease of photo current[170]. The overshoot is also seen when switching off for HEH-002 and HEH003 (t = 30 s and t = 50 s in Figure 6-12). This is attributed to injected charges that are delivered from the electrodes and cancel the charge carrier density, which made up the diffusion gradient[170].

It can be seen that 10 s (PV, illumination time length) and 15 s (NG+PV, illumination with oscillation time length) are not long enough for the current to reach a steady state. It has been reported that structural deformation can be induced by absorption of photon on perovskite[171]. Distortions[171], migration[172] of iodide ions and freely reorienting organic dipole ($CH_3NH_3^+$) alignment[173] have been reported. The activation energy for $CH_3NH_3^+$ migration has been reported to be 0.84 eV, which makes it unfavourable compared to low activation energy (0.58 eV) iodide ion migration[172]. A decrease in the binding energy of $CH_3NH_3^+$ ion to the inorganic cage is suggested to allow the cations to freely rotate upon light excitation, leading to dipole alignment[173]. This dipole alignment would return to relaxed state in the dark. However, the amount of dark time it takes for the perovskite to reach a relaxed state is suggested to be on the order of tens of seconds[174] (~30 s[173]). Thus for the 5 s of dark time (t = 30-35 s shown in Figure 6-12), the material is re-illuminated before full relaxation, and a small amount of dipoles are still aligned. As a result, the starting point (t = 35 s in Figure 6-12) of NG+PV output is slightly lower than the start of PV output (t = 20 s in Figure 6-12). This is the reason why both peak and average current outputs are lower for results achieved under NG+PV condition compared to results achieved under PV condition. Except HEH003, which shows improved average current output under NG+PV condition (0.50 mA/cm^2) compared to results under PV condition (0.48 mA/cm^2). This suggests that, for HEH003 (based on sputtered seed layer), effect of kinetic energy harvesting may be stronger which compensates and even overcomes the relaxation process.

Thus, in order to further evaluate the effect of oscillation upon illumination, a second round of time-dependent current output scan was performed. In this 60 s scan, illumination was kept on during 5-55 s. The oscillation was turned on intermittently during 5-55 s. The focused plots are shown below in Figure 6-13.

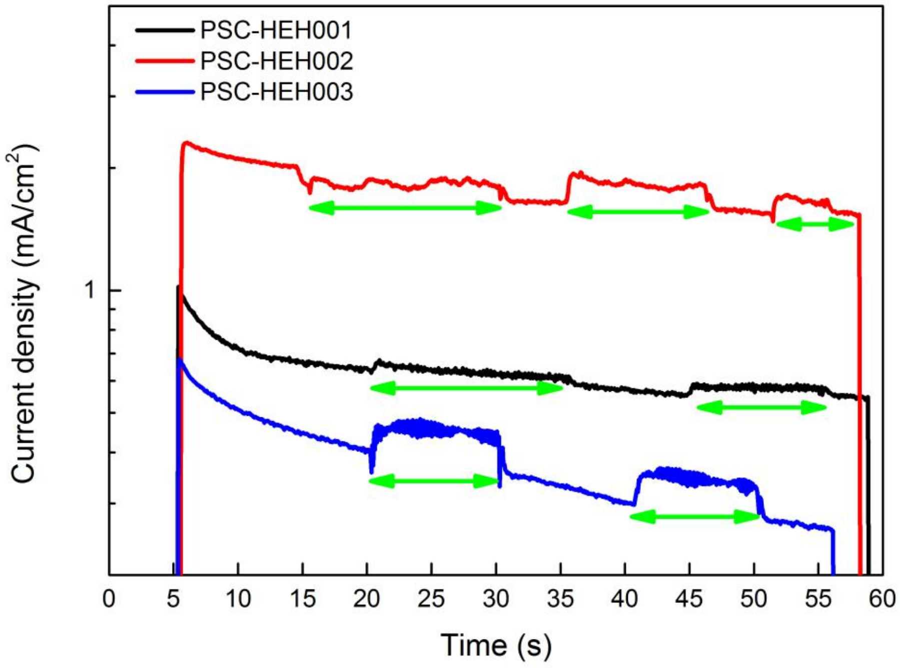

Figure 6-13: Time-dependent current density (log scale) scans focused on NG+PV effect. The green arrow relates to the results of oscillation turned on.

Table 6-8: Average current density (mA/cm^2) values of HEHs tested under solely illumination (PV) and oscillation under illumination (NG+PV).

	PSC-HEH001	PSC-HEH002	PSC-HEH003
PV (average)	0.5687	1.6201	0.3074
NG+PV (average)	0.6076	1.7808	0.3981

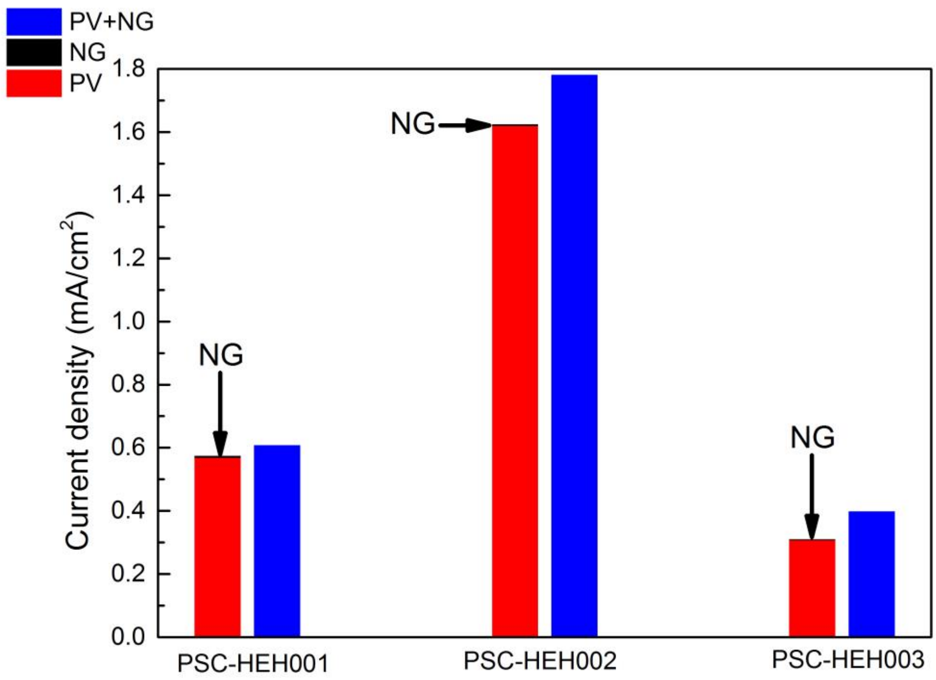

Figure 6-14: Average current density (mA/cm^2) comparison of PSC-HEHs achieved under NG, PV and NG+PV conditions.

Figure 6-13 , Figure 6-14 and Table 6-8 show the improved performance under NG+PV compared to PV. The general trend of the current density under illumination is still decreasing as shown in Figure 6-13. But it is clear to see that oscillation improves the photo current output, which slows the current relaxation process. PSC-HEH003 still shows the lowest current density, but the average value shows the greatest improvement of 29.5% compared to 6.8% from PSC-HEH001 and 9.9% from PSC-HEH002. As the average current generated from NG performance (see Table 6-7) is on the range of 0.002 to 0.005 mA/cm^2, the improvement is not simply an additive effect. In general, due to the piezoelectric property of ZnO nanorods, oscillation induced strain is suggested to generate a piezoelectric potential which would affect the charge dynamics within the system. First, the alternating piezoelectric potential is suggested to improve the spatial charge separation within the perovskite layer, similar to the mechanism of N719-based HEH discussed in Section 5.3.2, leading to reduced radiative recombination between free electrons and free holes. Secondly, within the perovskite structure, vacancy-mediated diffusion is the most common process, which is further supported by the ease of formation of Schottky disorder[175]. Three ion migration mechanisms (mediated by vacancy defects) are commonly considered, including I^- migration, Pb^{2+} migration and $CH_3NH_3^+$ migration. The activation energies have been calculated to be 0.58 eV, 2.31 eV and 0.84 eV for I^-, $Pb^{2+}$and $CH_3NH_3^+$, respectively[172]. This indicates that diffusion of iodide ions is favourable[172]. When the cell is short-circuited externally, a built-in electric field is present in the perovskite layer due to the difference in the work functions of the contacts[172]. This could drive iodide ion migration towards the contacts, where they accumulate instead and generate a space charge region. This region could counteract the built-in field by partially screening it. Thus the magnitude of the short-circuit photo current is controlled by the extent to which the electric field is screened[170,172]. A reduced internal field within the device (due to ionic screening) could lead to less efficient charge collection of photo induced charge carriers. Upon oscillation, the piezoelectric potential generated from piezoelectric ZnO nanorods is suggested to reduce the built-in field. This would allow a dissipation of ionic charge from the contacts by diffusion, thus improve the charge collection efficiency leading to improved photocurrent. Thirdly, trap-assisted recombination sites are suggested to reside at grain boundaries and predominantly at interfaces between ZnO/perovskite and PEDOT:PSS/perovskite[176]. For perovskite at ZnO/perovskite interface, positively charged iodide vacancies (corresponding to iodide ion migration) would cause recombination between trapped electron and free holes in the valence band. It is suggested that, piezoelectric potential affects the ion migration dynamics via dissipating ionic charge from the contacts by diffusion. As a result, trap-assisted nonradiative recombination is suppressed, leading to improved current output.

6.3 Summary

In summary, morphology optimization of perovskite films deposited on ZnO nanorods was conducted. For FTO substrates, 350 nm nanorods were able to achieve the most uniform and complete coverage. Different perovskite deposition methods were investigated. The addition of 2-(Dibutylamino)ethanol was found to improve the perovskite stability and lead to large-sized crystals. However the PCE was limited by large charge transfer resistance, potentially due to poor penetration of the perovskite between the nanorods. In comparison, 2-step without additive recipe shows higher PCE which is attributed to low charge transfer resistance. In order to achieve a more uniform perovskite film on long aspect ratio CW substrate, no preheating or anti-solvent treatment was applied. Instead, $PbCl_2$ was added into the 2-step recipe which decelerates the crystallization of perovskite crystals. Finally, CW-based PSC-HEHs were fabricated and tested. Due to the nature of spin coating procedure and long aspect ratio, the resulted perovskite film was not homogeneous. The resulted PCEs from large working area showed inconsistency. However, the PSC-HEHs were demonstrated to work as NG and PV individually. Furthermore, the current density under NG+PV condition showed further improvement compared to result achieved under PV condition instead of a simple summation. This result corresponds well with the further improvement achieved on N719-based HEHs. It is suggested that, the piezoelectric potential generated by piezoelectric ZnO nanorods affects the ion migration dynamics within the perovskite system. Reduced recombination leads to higher charge collection efficiency, which leads to higher current output. Therefore, a perovskite-based hybrid energy harvester scavenging kinetic and solar energy was successfully designed and developed.

Chapter 7 Conclusions and Future works

7.1 Conclusions

7.1.1 Background and aims

Benefiting from the fact that solar and kinetic energy are commonly existing simultaneously in the environment, it is within great interest to design a hybrid energy harvesting device that could harvest both kinetic and solar energy. A number of designs have been proposed and demonstrated (Section 2.5.5). However these designs mainly comprise of a single solar cell and a single nanogenerator connected in series or parallel. The output generated from the hybrid device is the summation of the output generated from solar cell and nanogenerator individually. Thus, the fabrication and assembly of the device remain complicated. It would be beneficial to fabricate a hybrid energy harvester with integrated design and can simultaneously harvest multiple forms of energies.

The aim of the research reported in this thesis was to fabricate a solar cell based on piezoelectric ZnO nanorod, and probe the piezoelectric effect on the performance of the solar cell. The piezoelectric effect could be induced via acoustic waves as reported by Shoaee[87]. Alternatively, it can also be induced via bending the device which is based on a flexible substrate. Liquid-state and solid-state DSSCs based on ZnO nanorods could be fabricated and tested using a loud speaker as the acoustic source. Furthermore, in order to induce a higher degree of strain onto the nanorods, flexible substrates such as ITO coated PET and FTO coated Corning® Willow™ (CW) glass were considered. Based on the nanogenerator structure reported by Briscoe[72] and Jalali[82], which is ZnO/CuSCN/PEDOT:PSS, the design of hybrid energy harvesters (HEHs) were proposed to be based on flexible substrate/ZnO nanorod/light absorber layer/CuSCN/PEDOT:PSS (Chapter 5 and Chapter 6). The different light absorber materials such as N719 and methylammonium lead iodide (MAPI) were investigated, which requires different device designs.

The summarized aims and objectives are shown below.

1) Fabricate ZnO-based solar cells and probe the acoustic effect on the efficiencies of the devices.
2) Design, fabricate a dye-based HEH (N719-HEH) and investigate the NG and PV performances of the devices.
3) Design, fabricate a perovskite-based HEH (PSC-HEH) and investigate the NG and PV performances of the devices.

7.1.2 Completion of objectives

The extent to which the objectives of the project were met are discussed below.

1) Acoustic enhancement investigation for ZnO-based solar cells.

During the early stage of the project, the acoustic effect was investigated on ZnO nanorod-based solar cells. For liquid-state solar cell, different parameters were tested to achieve a relatively high and stable (compared to the literature: 1.5%) efficiency. Longer aspect ratio rods were found to improve the efficiency which is attributed to higher surface area. Higher surface area could enhance the dye loading and light scattering effect of the photo anode and increase the charge injection and collection efficiencies. Optimal dye loading time was found to be within the range of 2-3 h for ZnO nanorods compared to 6-12 h for TiO_2 nanoparticles reported in literature. The acidic nature of dye molecules would dissolve the ZnO and cause complex aggregations on the surface of the rods and reduce the short-circuit current. Different spacers and Pt-counter electrodes were also tested. Comparing the two spacers, Surlyn spacer leads to higher short-circuit current while Sellotape spacer leads to higher *FF,* which is attributed to the amount of electrolyte contained. For the Pt-counter electrodes, lab-sputtered Pt leads to higher short-circuit current and *FF*, which is attributed to the better surface quality and higher thickness of the Pt layer. Finally, a stabilized performance was achieved via proper sealing of the device using epoxy. However, no significant acoustic enhancement effect was discovered. Then, solid-state DSSCs based on ZnO/N719/CuSCN were fabricated and tested. Acoustic enhancement of the efficiency was discovered in a number of devices. Although the effect was neither significant nor consistent, it shows a promising design approach which is based on a solid-state structure. It may also be beneficial to utilize a flexible substrate such as Corning© Willow™ glass, which could potentially induce a higher degree of strain onto the rods.

2) Performance characterization of N719-HEH

A HEH based on N719 light absorber layer was designed and fabricated (Section 5.1). For HEH fabricated on PET substrates, the power output was found to be further improved when the device was oscillating under illumination as comparing to solely oscillating or solely under illumination. The output value (NG+PV) was higher than a simple summation of the outputs from NG and PV individually, indicating the charge dynamics may be affected by the piezoelectric potential from the piezoelectric nanorods similarly to the report by Shoaee[87] *et al*. It is suggested that the piezoelectric potential would enhance the charge separation within the device and reduce the recombination, leading to a higher charge collection efficiency and current output. This was further supported by results achieved on HEHs based on CW substrates. The time-dependent current density plots revealed that under illumination condition, further application of oscillation would further improve the current output. The thickness of CuSCN coating was also found to affect the PV performances of the devices. Increasing CuSCN coating led to improved PCE, which was attributed to improved photo current from reduced charge transfer resistance. Thus, a N719-based hybrid energy harvester was successfully designed and fabricated. The device works as both NG and PV. Furthermore, the power output of device working under NG+PV condition is higher than the summation of power achieved on NG and PV individually.

3) Performance characterization of PSC-HEH

In order to further improve the power output of the device, perovskite-based HEHs (PSC-HEHs) were designed using methylammonium lead iodide as light absorber layer. Preheating and anti-solvent treatment were found to improve the coverage and continuity of the perovskite film. Short rods (350 nm) were found to result a better coverage of the perovskite layer. The PV performance (PCE < 1%) was not as expected compared to literature values (PCE > 10%). This was attributed to the long aspect ratio substrate which has a large contact area (> 2 cm^2), as well as the non-optimized deposition processes. Large area contains higher amount of defects which commonly leads to low performances. Once the deposition processes are fully optimized, higher efficiency should be achieved. However, the goal in current stage was to demonstrate the HEH working principle. Time-dependent current density plot successfully proved the devices were able to harvest both kinetic (as NG) and solar energy (as PV). Despite a decreasing trend in the photocurrent over time, the oscillation clearly improved the current output.

The success of hybrid energy harvester based on perovskite solar cell further supports the theory that the piezoelectric potential originating from the ZnO nanorods could affect the charge dynamics within the solar cell and further improve the performance of the device. The integrated structure requires simpler fabrication process compared to the hybrid energy harvesters reported in literature.

7.2 Future works

In the following section, a number of suggestions for future areas of investigation that continue the work described in this thesis are given. As with the other parts of the thesis, these are divided in the sequence from bottom to top components of the HEH device in additions to variations that can be made to the complete devices.

7.2.1 Substrate

In this project, commonly reported PET substrate was used for the HEH device fabrication. PET substrate has the advantage of high flexibility. However it suffers from high resistance and low temperature annealing limitation. Alternatively, CW substrate can be annealed up to 800 °C and remain relatively flexible. However the substrate is brittle and requires extra care during handling. It would be ideal to utilize a transparent substrate which has both high flexibility and high thermal stability. Polyethersulfone (PES) is an alternative substrate, which remain thermally stable up to 220 °C. Flexible perovskite solar cells based on PES[177] have been reported. Furthermore, alternative flexible glass such as D263-T™ (fabricated by PGO, Germany) can be utilized instead of CW substrate. Commercially available titanium foil combined with transparent, conductive adhesive coated laminate have also been reported to fabricate flexible, FTO-free perovskite solar cell[178].

7.2.2 ZnO nanorods

In this project, different morphologies of nanorods were achieved using different synthesis methods. For N719-based HEH, longer aspect ratio or doping are the potential ways to further improve the charge transfer property of the photo anode and PV performance of the devices. As for PSC-based HEH, although 350 nm rods were proven in our experiment to achieve the best coverage. It would still be ideal to utilize longer rods, as the longest ZnO nanorods reported for PSC in literature is ~1 µm[62]. This would require different perovskite deposition method to be optimized for such long rods.

7.2.3 Light absorber layer

The deposition process for light absorber layer is considered to be the most important step during the fabrication processes because it directly determines the

PV performance of the device. As the results shown in this report, photo current output of PV performance is orders of magnitude higher than that of NG performance. Thus, the main design target of the HEH is to achieve the highest PV performance possible, while testing the oscillation effect on the PV performance to see if it can further improve the efficiency or produce a small amount of additional power during dark periods. For N719-based HEH, the dye loading time greatly affects the performance of the device. Alternatively, TiO_2 shell structure can be applied to enhance the dye loading and charge injecting as suggested in Section 4.1. For PSC-based HEH, the deposition of perovskite could be carried out in a glove box which would slow down the degradation process and improve efficiency. Also, adjusted deposition recipe is required to deposit a perovskite layer with better coverage on longer rods (1 μm). With an optimized perovskite device, recombination and ion migration will be suppressed. It would be interesting to see if any further improvement can be achieved upon oscillation.

7.2.4 P-type hole transporting material

For N719-HEH, double p-type layers are essential as CuSCN would improve the surface passivation and facilitate the charge transfer, while PEDOT:PSS acts as stress/strain buffer and provide a flat surface for gold deposition. The coverage of CuSCN and PEDOT:PSS could be controlled via automatic spray coating to reduce manual errors. For PSC-HEH, toluene-based PEDOT:PSS exhibits good coverage via spin coating benefiting from the excellent wetting property from toluene solution. The thickness of the PEDOT:PSS could be further optimized. Too thick of a coating would increase the series resistance while too thin of a coating would cause potential gaps within the film.

7.2.5 Device sealing and finish

Currently, the hot pressing sealing via lamination shows less effect on N719-HEH. On the other hand, PSC-HEH is more sensitive towards high temperature and shows accelerated degradation after lamination. The lamination process is beneficial for the device in principle. It fully seals the device and screens the external humidity or air. It also improves the flexibility of the device by acting as a protection layer. Thus, an alternative cold lamination is potentially beneficial for PSC-HEH devices. It would also be beneficial for the lamination process to take place in the glove box right after the assembly of the device.

For the testing, it would be beneficial to investigate the dependency of the current output with the oscillation frequency. Thus, using root-mean-square (RMS) value would provide a clear comparison with the DC output of solar energy harvesting.

The further investigation suggested above should lead to improved power output and understanding of ZnO-based hybrid energy harvesters, building on that developed in this thesis. It is hoped that with this understanding this new type of device could be developed and improved so that it may operate at efficiencies that are competitive with other energy harvesters and at various environmental conditions.

References

1. WEC. World Energy Resources. *World Energy Counc. Rep.* **1,** 4 (2016).
2. REN21. *Renewables 2017: global status report*. *Renewable and Sustainable Energy Reviews* **72,** (2017).
3. Energy, R. & Act, S. Act on Granting Priority to Renewable Energy Sources (Renewable Energy Sources Act, Germany, 2000). *Sol. Energy* **70,** 489–504 (2001).
4. COP 21. Report of the Conference of the Parties on its twenty-first session, held in Paris from 30 November to 13 December 2015. *Unfccc* **1192,** Al-Homoud, M. S. (2015).
5. Green, M. A. Third generation photovoltaics: Ultra-high conversion efficiency at low cost. *Prog. Photovoltaics Res. Appl.* **9,** 123–135 (2001).
6. Safarian, J., Tranell, G. & Tangstad, M. Processes for upgrading metallurgical grade silicon to solar grade silicon. *Energy Procedia* **20,** 88–97 (2012).
7. Irvine, S. J. C. & Candelise, C. Introduction and Techno-economic Background. *Mater. Challenges Inorg. Photovolt. Sol. Energy* 1–26 (2015). doi:10.1039/9781849733465-00001
8. Shockley, W. & Queisser, H. J. Detailed balance limit of efficiency of p-n junction solar cells. *J. Appl. Phys.* **32,** 510–519 (1961).
9. Soitec, CEA-Leti, Fraunhofer ISE. French-German partnership achieve 46% PV conversion efficiency in the lab. 2014. *ICEF2015.*
10. Grätzel, M. Dye-sensitized solar cells. *J. Photochem. Photobiol. C Photochem. Rev.* **4,** 145–153 (2003).
11. Mathew, S. *et al.* Dye-sensitized solar cells with 13% efficiency achieved through the molecular engineering of porphyrin sensitizers. *Nat. Chem.* **6,** 242–247 (2014).
12. Tennakone, K., Kumara, G., Kumarasinghe, A. R., Wijayantha, K. G. U. &

Sirimanne, P. M. A dye-sensitized nano-porous solid-state photovoltaic cell. *Semicond. Sci. Technol.* **10,** 1689 (1995).

13. O'Regan, B. & Schwartz, D. T. Efficient dye-sensitized charge separation in a wide-band-gap *p* - *n* heterojunction. *J. Appl. Phys.* **80,** 4749–4754 (1996).
14. Law, M. *et al.* ZnO-Al2O3 and ZnO-TiO2 core-shell nanowire dye-sensitized solar cells. *J. Phys. Chem. B* **110,** 22652–22663 (2006).
15. Kojima, A., Teshima, K., Shirai, Y. & Miyasaka, T. Organometal halide perovskites as visible-light sensitizers for photovoltaic cells. *J. Am. Chem. Soc.* **131,** 6050–6051 (2009).
16. Saliba, M. *et al.* Cesium-containing triple cation perovskite solar cells: improved stability, reproducibility and high efficiency. *Energy Environ. Sci.* **9,** 1989–1997 (2016).
17. Jeon, N. J. *et al.* Efficient inorganic-organic hybrid perovskite solar cells based on pyrene arylamine derivatives as hole-transporting materials. *J. Am. Chem. Soc.* **135,** 19087–19090 (2013).
18. Wang, Z. *Nanogenerators for self-powered devices and systems*. *Georgia Institute of Technology, SMARTech digital repository (http://hdl.handle.net/1853/39262)* (2011).
19. Beeby, S. P., Tudor, M. J. & White, N. M. Energy harvesting vibration sources for microsystems applications. *Meas. Sci. Technol.* **17,** R175 (2006).
20. Sirohi, J. & Chopra, I. Fundamental Understanding of Piezoelectric Strain Sensors. *J. Intell. Mater. Syst. Struct.* **11,** 246–257 (2000).
21. Chopra, I., Sirohi, J., Society, A. H. & Corporation, S. A. Smart structures theory. (1997).
22. Min-Hua Zhao,, Zhong-Lin Wang,. Scott X. Mao,. Piezoelectric Characterization of Individual Zinc Oxide Nanobelt Probed by Piezoresponse Force Microscope. (2004). doi:10.1021/NL035198A
23. Schmidt-Mende, L. & MacManus-Driscoll, J. L. ZnO - nanostructures, defects, and devices. *Mater. Today* **10,** 40–48 (2007).

24. Özgür, Ü. *et al.* A comprehensive review of ZnO materials and devices. *J. Appl. Phys.* **98,** 1–103 (2005).

25. Wang, Z. L. Nanostructures of zinc oxide. *Mater. Today* **7,** 26–33 (2004).

26. Song, Z. L. W. and J. Piezoelectric Nanogenerators Based on Zinc Oxide Nanowire Arrays. *Science.* **312,** 242–246 (2006).

27. Briscoe, J. & Dunn, S. Piezoelectric nanogenerators - A review of nanostructured piezoelectric energy harvesters. *Nano Energy* **14,** 15–29 (2014).

28. Hagfeldt, A., Boschloo, G., Sun, L., Kloo, L. & Pettersson, H. Dye-Sensitized Solar Cells. *Chem. Rev.* **110,** 6595–6663 (2010).

29. Nelson, J. *The physics of solar cells.* (Imperial College Press, 2003).

30. O'Regan, B. & Grätzel, M. A low-cost, high-efficiency solar cell based on dye-sensitized colloidal TiO2 films. *Nature* **353,** 737–740 (1991).

31. Hardin, B. E., Snaith, J., Mcgehee, M. D., Snaith, H. J. & Mcgehee, M. D. The renaissance of dye-sensitized solar cells. *Nat. Photonics* **6,** 162–169 (2012).

32. Tennakone, K., Kumara, G., Kottegoda, I. R. M., Perera, V. P. S. & Aponsu, G. Nanoporous n-TiO_2/selenium/p-CuCNS photovoltaic cell. *J. Phys. D-APPLIED Phys.* **31,** 2326–2330 (1998).

33. Kalyanasundaram, K. *Dye-sensitized solar cells.* (CRC Press, 2010).

34. Hsu, C.-Y., Chen, Y.-C., Lin, R. Y.-Y., Ho, K.-C. & Lin, J. T. Solid-state dye-sensitized solar cells based on spirofluorene (spiro-OMeTAD) and arylamines as hole transporting materials. *Phys. Chem. Chem. Phys.* **14,** 14099–109 (2012).

35. Kron, G., Egerter, T., Werner, J. H. & Rau, U. Electronic transport in dye-sensitized nanoporous TiO_2 solar cells - Comparison of electrolyte and solid-state devices. *J. Phys. Chem. B* **107,** 3556–3564 (2003).

36. Qin, P. *et al.* Inorganic hole conductor-based lead halide perovskite solar cells with 12.4% conversion efficiency. *Nat. Commun.* **5,** 1–6 (2014).

37. Burschka, J. *et al.* Sequential deposition as a route to high-performance perovskite-sensitized solar cells. *Nature* **499,** 316–320 (2013).

38. Liu, D. & Kelly, T. L. Perovskite solar cells with a planar heterojunction structure prepared using room-temperature solution processing techniques. *Nat. Photonics* **8,** 133–138 (2014).

39. Heo, J. H. *et al.* Efficient inorganic-organic hybrid heterojunction solar cells containing perovskite compound and polymeric hole conductors. *Nat Phot.* **7,** 486–491 (2013).

40. Christians, J. A., Fung, R. C. M. & Kamat, P. V. An inorganic hole conductor for Organo-lead halide perovskite solar cells. improved hole conductivity with copper iodide. *J. Am. Chem. Soc.* **136,** 758–764 (2014).

41. Pattanasattayavong, P. *et al.* Electric field-induced hole transport in copper(I) thiocyanate (CuSCN) thin-films processed from solution at room temperature. *Chem. Commun. (Camb).* **49,** 4154–6 (2013).

42. O'Regan, B., Schwartz, D. T., Zakeeruddin, S. M. & Grätzel, M. Electrodeposited nanocomposite n-p heterojunctions for solid-state dye-sensitized photovoltaics. *Adv. Mater.* **12,** 1263–1267 (2000).

43. Kieven, D. *et al.* Effect of internal surface area on the performance of ZnO In2 S3 CuSCN solar cells with extremely thin absorber. *Appl. Phys. Lett.* **92,** 3–6 (2008).

44. Tena-Zaera, R., Elias, J. & Lévy-Clément, C. ZnO nanowire arrays: Optical scattering and sensitization to solar light. *Appl. Phys. Lett.* **93,** 233119 (2008).

45. Keis, K., Lindgren, J., Lindquist, S. & Hagfeldt, A. Studies of the Adsorption Process of Ru Complexes in Nanoporous ZnO Electrodes Studies of the Adsorption Process of Ru Complexes in Nanoporous ZnO Electrodes. *Langmuir* **16,** 4688–4694 (2000).

46. Lee, K. E., Gomez, M. A., Elouatik, S. & Demopoulos, G. P. Further understanding of the adsorption mechanism of N719 sensitizer on anatase TiO 2 films for DSSC applications using vibrational spectroscopy and confocal raman imaging. *Langmuir* **26,** 9575–9583 (2010).

47. Law, M., Greene, L. E., Johnson, J. C., Saykally, R. & Yang, P. Nanowire dye-

sensitized solar cells. *Nat. Mater.* **4,** 455–459 (2005).

48. Baxter, J. B. & Aydil, E. S. Nanowire-based dye-sensitized solar cells. *Appl. Phys. Lett.* **86,** 1–3 (2005).

49. Jiang, C. Y., Sun, X. W., Lo, G. Q., Kwong, D. L. & Wang, J. X. Improved dye-sensitized solar cells with a ZnO-nanoflower photoanode. *Appl. Phys. Lett.* **90,** 263501 (2007).

50. Dwivedi, C. & Dutta, V. Vertically aligned ZnO nanorods via self-assembled spray pyrolyzed nanoparticles for dye-sensitized solar cells. *Adv. Nat. Sci. Nanosci. Nanotechnol.* **3,** 15011 (2012).

51. Hongsith, K. *et al. Efficiency Enhancement of ZnO Dye-sensitized Solar Cells by Modifying Photoelectrode and Counterelectrode*. *Energy Procedia* **79,** (Elsevier B.V., 2015).

52. Zhao, Y. & Zhu, K. Charge Transport and Recombination in Perovskite $(CH_3NH_3)PbI_3$ Sensitized TiO_2 Solar Cells. *J. Phys. Chem. Lett.* **4,** 2880–2884 (2013).

53. Zhu, K., Neale, N. R., Miedaner, A. & Frank, A. J. Enhanced charge-collection efficiencies and light scattering in dye-sensitized solar cells using oriented TiO_2 nanotubes arrays. *Nano Lett.* **7,** 69–74 (2007).

54. Peter, L. M. Characterization and Modeling of Dye-Sensitized Solar Cells. *J. Phys. Chem. C*, 2007, 111 (18), 6601–6612.

55. Zhu, K., Jang, S. R. & Frank, A. J. Impact of high charge-collection efficiencies and dark energy-loss processes on transport, recombination, and photovoltaic properties of dye-sensitized solar cells. *J. Phys. Chem. Lett.* **2,** 1070–1076 (2011).

56. Leijtens, T., Lauber, B., Eperon, G. E., Stranks, S. D. & Snaith, H. J. The Importance of Perovskite Pore Filling in Organometal Mixed Halide Sensitized TiO_2-Based Solar Cells. *J. Phys. Chem. Lett.* **5,** 1096–1102 (2014).

57. Alcocer, M. J. P., Leijtens, T., Herz, L. M., Petrozza, A. & Snaith, H. J. Electron-Hole Diffusion Lengths Exceeding 1 Micrometer in an Organometal Trihalide

Perovskite Absorber. *Science.* **342,** 341–344 (2014).

58. Ball, J. M. *et al.* Low-temperature processed meso-superstructured to thin-film perovskite solar cells. *Energy Environ. Sci.* **6,** 1739 (2013).

59. Lee, M. M., Teuscher, J., Miyasaka, T., Murakami, T. N. & Snaith, H. J. Efficient hybrid solar cells based on meso-superstructured organometal halide perovskites. *Science.* **338,** 643–647 (2012).

60. Kavan, L., O'Regan, B., Kay, A. & Grätzel, M. Preparation of TiO_2 (anatase) films on electrodes by anodic oxidative hydrolysis of $TiCl_3$. *J. Electroanal. Chem.* **346,** 291–307 (1993).

61. Bi, D. *et al.* Efficient and stable $CH_3NH_3PbI_3$-sensitized ZnO nanorod array solid-state solar cells. *Nanoscale* **5,** 11686–91 (2013).

62. Son, D., Im, J., Kim, H. & Park, N. 11% Efficient Perovskite Solar Cell Based on ZnO Nanorods: An Effective Charge Collection System. *J. Phys. Chem. C,* 2014, 118 (30), 16567-16573.

63. Mahmood, K., Swain, B. S. & Amassian, A. 16.1% Efficient Hysteresis-Free Mesostructured Perovskite Solar Cells Based on Synergistically Improved ZnO Nanorod Arrays. *Adv. Energy Mater.* **5,** 1–11 (2015).

64. KATZIR, S. The Discovery of the Piezoelectric Effect. *Arch. Hist. Exact Sci.* **57,** 61–91 (2003).

65. Ii, E. C. *et al. Piezoelectric and Acoustic Materials for Transducer Applications (ハードカバー ハードカバー) ハードカバー 内容説明*. (2010). doi:10.1007/978-0-387-76540-2

66. Arnau, A. & Soares, D. Fundamentals of piezoelectricity. *Piezoelectric Transducers Appl.* 1–38 (2008). doi:10.1007/978-3-540-77508-9_1

67. Lippmann, G. Principe de la conservation de l' electricité , ou second principe de la théorie des phénomene electriques. *J . Phys . Theor . Appl* 381–394 (1881). doi:10.1051/jphystap:0188100100038100>

68. John Peifer. Structure - What is Zinc Oxide? Available at: https://whatiszincoxide.weebly.com/structure.html. (Accessed: 29th March

2018)

69. Hoffmann, S. *et al.* Fracture strength and Young's modulus of ZnO nanowires. *Nanotechnology* **18,** 205503 (2007).

70. Xu, F., Qin, Q., Mishra, A., Gu, Y. & Zhu, Y. Mechanical properties of ZnO nanowires under different loading modes. *Nano Res.* **280,** 1–10 (2010).

71. Wang, X., Song, J., Liu, J. & Wang, Z. L. Direct-current nanogenerator driven by ultrasonic waves. *Science.* **316,** 102–5 (2007).

72. Briscoe, J. *et al.* Nanostructured p-n junctions for kinetic-to-electrical energy conversion. *Adv. Energy Mater.* **2,** 1261–1268 (2012).

73. Wang, X. *et al.* Matrix-assisted energy conversion in nanostructured piezoelectric arrays. *Nano Lett.* **10,** 4901–4907 (2010).

74. Choi, M. Y. *et al.* Mechanically powered transparent flexible charge-generating nanodevices with piezoelectric ZnO nanorods. *Adv. Mater.* **21,** 2185–2189 (2009).

75. Lee, M. *et al.* Self-powered environmental sensor system driven by nanogenerators. *Energy Environ. Sci.* **4,** 3359–3363 (2011).

76. Lee, S. *et al.* Super-flexible nanogenerator for energy harvesting from gentle wind and as an active deformation sensor. *Adv. Funct. Mater.* **23,** 2445–2449 (2013).

77. Wurfel, P. & Batra, I. P. Depolarization-Field-Induced Instability in Thin Ferroelectric Film-Experiment and Theory. *Phys. Rev. B* **8,** 5126 (1973).

78. Sze, S. M. & Ng, K. K. *Physics of Semiconductor Devices*. *Physics of semiconductor device* (2007). doi:10.1049/ep.1970.0039

79. Anderson, J. & Chris, G. V. de W. Fundamentals of zinc oxide as a semiconductor. *Reports Prog. Phys.* **72,** 126501 (2009).

80. Kim, G. H., Hwang, D. H. & Woo, S. I. Thermoelectric properties of nanocomposite thin films prepared with poly(3,4-ethylenedioxythiophene) poly(styrenesulfonate) and graphene. *Phys. Chem. Chem. Phys.* **14,** 3530 (2012).

81. Jalali, N. *et al.* Passivation of Zinc Oxide Nanowires for Improved Piezoelectric Energy Harvesting Devices. *J. Phys. Conf. Ser.* **476,** 12131 (2013).

82. Jalali, N. *et al.* Improved performance of p–n junction-based ZnO nanogenerators through CuSCN-passivation of ZnO nanorods. *J. Mater. Chem. A* **2,** 10945 (2014).

83. Xu, C., Wang, X. & Wang, Z. L. Nanowire structured hybrid cell for concurrently scavenging solar and mechanical energies. *J. Am. Chem. Soc.* **131,** 5866–5872 (2009).

84. Xu, C. & Wang, Z. L. Compact hybrid cell based on a convoluted nanowire structure for harvesting solar and mechanical energy. *Adv. Mater.* **23,** 873–877 (2011).

85. Choi, D. *et al.* Piezoelectric touch-sensitive flexible hybrid energy harvesting nanoarchitectures. *Nanotechnology* **21,** 405503 (2010).

86. Choi, D. *et al.* Control of naturally coupled piezoelectric and photovoltaic properties for multi-type energy scavengers. *Energy Environ. Sci. Energy Environ. Sci* **4,** 4607–4613 (2011).

87. Shoaee, S., Briscoe, J., Durrant, J. R. & Dunn, S. Acoustic enhancement of polymer/ZnO nanorod photovoltaic device performance. *Adv. Mater.* **26,** 263–268 (2014).

88. Kumar, B. & Kim, S. W. Energy harvesting based on semiconducting piezoelectric ZnO nanostructures. *Nano Energy* **1,** 342–355 (2012).

89. Mang, A., Reimann, K. & Rübenacke, S. Band gaps, crystal-field splitting, spin-orbit coupling, and exciton binding energies in ZnO under hydrostatic pressure. *Solid State Commun.* **94,** 251–254 (1995).

90. Look, D. C. *et al.* Electrical properties of bulk ZnO. *Solid State Commun.* **105,** 399–401 (1998).

91. H. Nanto, H. Sokooshi and T. Usuda, Smell sensor using zinc oxide thin films prepared by magnetron sputtering, *Solid-State Sensors and Actuators, 1991. Digest of Technical Papers, TRANSDUCERS '91., 1991 International Conference*

on, San Francisco, CA, USA, 1991, pp. 596-599.

92. Rahman, M., Alam, M. M., Asiri, A. M. & Islam, M. A. Ethanol sensor development based on ternary-doped metal oxides (CdO/ZnO/Yb_2O_3) nanosheets for environmental safety. *RSC Adv.* **7,** 22627–22639 (2017).
93. Eda, K. Zinc Oxide Varistors. *IEEE Electr. Insul. Mag.* **5,** 28–30 (1989).
94. Larciprete, M. C. *et al.* Characterization of second and third order optical nonlinearities of ZnO sputtered films. *Appl. Phys. B Lasers Opt.* **82,** 431–437 (2006).
95. Hanada, T. Basic Properties of ZnO, GaN, and Related Materials. *Oxide Nitride Semicond. SE* **12,** 1–19 (2009).
96. Vayssieres, L., Keis, K., Hagfeldt, A. & Lindquist, S. E. Three-dimensional array of highly oriented crystalline ZnO microtubes. *Chem. Mater.* **13,** 4395–4398 (2001).
97. Vayssieres, L. Growth of arrayed nanorods and nanowires of ZnO from aqueous solutions. *Adv. Mater.* **15,** 464–466 (2003).
98. Kashiwaba, Y., Katahira, F., Haga, K., Sekiguchi, T. & Watanabe, H. Hetero-epitaxial growth of ZnO thin films by atmospheric pressure CVD method. *J. Cryst. Growth* **221,** 431–434 (2000).
99. Chiou, W.-T., Wu, W.-Y. & Ting, J.-M. Growth of single crystal ZnO nanowires using sputter deposition. *Diam. Relat. Mater.* **12,** 1841–1844 (2003).
100. Zhang, Y. *et al.* Synthesis of nano/micro zinc oxide rods and arrays by thermal evaporation approach on cylindrical shape substrate. *J. Phys. Chem. B* **109,** 13091–13093 (2005).
101. Nagata, T. *et al.* Schottky metal library for ZNO-based UV photodiode fabricated by the combinatorial ion beam-assisted deposition. *Appl. Surf. Sci.* **252,** 2503–2506 (2006).
102. Fan, H. J. *et al.* Template-assisted large-scale ordered arrays of ZnO pillars for optical and piezoelectric applications. *Small* **2,** 561–568 (2006).
103. Tian, Z. R., Voigt, J. A., Liu, J., Mckenzie, B. & Mcdermott, M. J. Biomimetic arrays

of oriented helical ZnO nanorods and columns. *J. Am. Chem. Soc.* **124,** 12954–12955 (2002).

104. Greene, L. E. *et al.* Low-temperature wafer-scale production of ZnO nanowire arrays. *Angew. Chemie - Int. Ed.* **42,** 3031–3034 (2003).

105. Govender, K., Boyle, D. S., Kenway, P. B. & O'Brien, P. Understanding the factors that govern the deposition and morphology of thin films of ZnO from aqueous solution. *J. Mater. Chem.* **14,** 2575–2591 (2004).

106. Song, J. & Lim, S. Effect of Seed Layer on the Growth of ZnO Nanorods. *J. Phys. Chem. C* **111,** 596–600 (2007).

107. Guo, M., Diao, P., Wang, X. & Cai, S. The effect of hydrothermal growth temperature on preparation and photoelectrochemical performance of ZnO nanorod array films. *J. Solid State Chem.* **178,** 3210–3215 (2005).

108. Guo, M., Diao, P. & Cai, S. Hydrothermal growth of well-aligned ZnO nanorod arrays: Dependence of morphology and alignment ordering upon preparing conditions. *J. Solid State Chem.* **178,** 1864–1873 (2005).

109. Jennings, J. R., Ghicov, A., Peter, L. M., Schmuki, P. & Walker, A. B. Dye-Sensitized Solar Cells Based on Oriented TiO_2 Nanotube Arrays: Transport, Trapping, and Transfer of Electrons. *J. Am. Chem. Soc.* **130,** 13364–13372 (2008).

110. O'Regan, B. C., Scully, S., Mayer, a C., Palomares, E. & Durrant, J. The effect of Al_2O_3 barrier layers in TiO_2/dye/CuSCN photovoltaic cells explored by recombination and DOS characterization using transient photovoltage measurements. *J. Phys. Chem. B* **109,** 4616–4623 (2005).

111. Greene, L. E., Law, M., Yuhas, B. D. & Yang, P. ZnO-TiO_2 Core-Shell Nanorod/P3HT Solar Cells. *J. Phys. Chem. C* **111,** 18451–18456 (2007).

112. Qiu, J. *et al.* A facile route to aligned TiO_2 nanotube arrays on transparent conducting oxide substrates for dye-sensitized solar cells. *J. Mater. Chem.* **21,** 5062 (2011).

113. Tredici, I. G. *et al.* A simple two-step solution chemistry method for synthesis of micropatterned ZnO nanorods based on metal-loaded hydrogels. *Thin Solid*

Films **526,** 22–27 (2012).

114. Downing, J. M., Ryan, M. P. & McLachlan, M. A. Hydrothermal growth of ZnO nanorods: The role of KCl in controlling rod morphology. *Thin Solid Films* **539,** 18–22 (2013).
115. Effect of incorporation of ethylene glycol into PEDOT:PSS on electron phonon coupling and conductivity. *J. Appl. Phys.* **117,** 215501 (2015).
116. Xu, C. & Gao, D. Two-stage Hydrothermal Growth of Long ZnO Nanowires for Efficient TiO_2 Nanotube-based Dye-sensitized Solar Cells. *J. Phys. Chem. C* **116,** (12), 7236-7241 (2012).
117. Han, Z., Li, S., Chu, J. & Chen, Y. Controlled growth of well-aligned ZnO nanowire arrays using the improved hydrothermal method. *J. Semicond.* **34,** 1–6 (2013).
118. Choi, H.-S., Vaseem, M., Kim, S. G., Im, Y.-H. & Hahn, Y.-B. Growth of high aspect ratio ZnO nanorods by solution process: Effect of polyethyleneimine. *J. Solid State Chem.* **189,** 25–31 (2012).
119. Hsu, J. W. P., Tallant, D. R., Simpson, R. L., Missert, N. A. & Copeland, R. G. Luminescent properties of solution-grown ZnO nanorods. *Appl. Phys. Lett.* **88,** 252103 (2006).
120. McCluskey, M. D. & Jokela, S. J. Defects in ZnO. *J. Appl. Phys.* **106,** 71101 (2009).
121. Shalish, I., Temkin, H. & Narayanamurti, V. Size-dependent surface luminescence in ZnO nanowires. *Phys. Rev. B* **69**, 245401, (2004)
122. Richters, J.-P., Voss, T., Kim, D. S., Scholz, R. & Zacharias, M. Enhanced surface-excitonic emission in ZnO/Al_2O_3 core–shell nanowires. *Nanotechnology* **19,** 305202 (2008).
123. Vanheusden, K., Seager, C. H., Warren, W. L., Tallant, D. R. & Voigt, J. A. Correlation between photoluminescence and oxygen vacancies in ZnO phosphors. *Appl. Phys. Lett.* **68**, 403 (1996)
124. Weber, D. H. *et al.* Determination of the specific resistance of individual freestanding ZnO nanowires with the low energy electron point source microscope. *Appl. Phys. Lett.* **91,** 253126 (2007).

125. Sun, W. C., Yeh, Y. C., Ko, C.T., He, H. & Chen, M.J. Improved characteristics of near-band-edge and deep-level emissions from ZnO nanorod arrays by atomic-layer-deposited Al_2O_3 and ZnO shell layers. *Nanoscale Res. Lett.* **6,** 556 (2011).

126. Lin, B., Fu, Z. & Jia, Y. Green luminescent center in undoped zinc oxide films deposited on silicon substrates. *Appl. Phys. Lett.* **79**, 943 (2001).

127. Zhou, H. *et al.* Behind the weak excitonic emission of ZnO quantum dots: ZnO/Zn $(OH)_2$ core-shell structure. *Appl. Phys. Lett.* **80**, 210 (2002).

128. Wu, X. L., Siu, G. G., Fu, C. L. & Ong, H. C. Photoluminescence and cathodoluminescence studies of stoichiometric and oxygen-deficient ZnO films. *Appl. Phys. Lett.* **78,** 2285–2287 (2001).

129. Leung, Y. H. *et al.* Defect photoluminescence of ZnO nanorods synthesized by chemical methods. *J. Phys. Chem. Solids* **69,** 353–357 (2008).

130. Hang, D.-R. *et al.* Annealing effects on the optical and morphological properties of ZnO nanorods on AZO substrate by using aqueous solution method at low temperature. *Nanoscale Res. Lett.* **9,** 632 (2014).

131. Hatch, S. M. *et al.* Influence of anneal atmosphere on ZnO-nanorod photoluminescent and morphological properties with self-powered photodetector performance. *J. Appl. Phys.* **113,** (2013).

132. Shi, G. A. *et al.* Hydrogen local modes and shallow donors in ZnO. *Phys. Rev. B* **72,** 195211 (2005).

133. Studenikin, S. a., Golego, N. & Cocivera, M. Fabrication of green and orange photoluminescent, undoped ZnO films using spray pyrolysis. *J. Appl. Phys.* **83,** 2104 (1998).

134. J. Frank, A., Kopidakis, N. & Lagemaat, J. van de. Electrons in nanostructured TiO_2 solar cells: transport, recombination and photovoltaic properties. *Coord. Chem. Rev.* **248,** 1165–1179 (2004).

135. Chen, L., Tsai, S., Chen, J. & Wang, G. Preparation of Vertically Aligned ZnO / TiO_2 Core-Shell Composites for Dye-Sensitized Solar Cells. *International*

Journal of Photoenergy, 417964, **2013,** (2013).

136. Zhao, R. *et al.* ZnO/TiO_2 core-shell nanowire arrays for enhanced dye-sensitized solar cell efficiency. *Appl. Phys. A Mater. Sci. Process.* **113,** 67–73 (2013).
137. Von Roos, O. A simple theory of back surface field (BSF) solar cells. *J. Appl. Phys.* **49,** 3503–3511 (1978).
138. Horiuchi, H. *et al.* Electron Injection Efficiency from Excited N3 into Nanocrystalline ZnO Films: Effect of (N_3–Zn^{2+}) Aggregate Formation. *J. Phys. Chem. B* **107,** 2570–2574 (2003).
139. Fang, X. *et al.* Effect of the thickness of the Pt film coated on a counter electrode on the performance of a dye-sensitized solar cell. *J. Electroanal. Chem.* **570,** 257–263 (2004).
140. Yoon, C. H., R. Vittal, Lee, J., Chae, W.-S. & Kim, K.J. Enhanced performance of a dye-sensitized solar cell with an electrodeposited-platinum counter electrode. *Electrochim. Acta* **53,** 2890–2896 (2008).
141. El-Shater, R. E., Abdel-Galeil, M. M., Kawamura, G. & Matsuda, A. Spacer thickness-dependent electron transport performance of titanium dioxide thick film for dye-sensitized solar cells. *J. Nanomater.* **2015,** (2015).
142. Lai, H., Wang, Y., Du, G., Li, W. & Han, W. Dual functional YVO_4:Eu^{3+},Bi^{3+}@SiO_2 submicron-sized core-shell particles for dye-sensitized solar cells: Light scattering and downconversion. *Ceram. Int.* **40,** 6103–6108 (2014).
143. Boushehri, A., Tao, F., Mason, E., Common bulk modulus point for compressed liquids. *The Journal of Physical Chemistry*. **97** (11), 2711-2714 (1993).
144. Kumara, G. R. R. A. *et al.* Dye-sensitized solar cell with the hole collector p-CuSCN deposited from a solution in n-propyl sulphide. *Sol. Energy Mater. Sol. Cells* **69,** 195–199 (2001).
145. Desai, U. V, Xu, C., Wu, J. & Gao, D. Solid-state dye-sensitized solar cells based on ordered ZnO nanowire arrays. *Nanotechnology* **23,** 205401 (2012).
146. Briscoe, J. *et al.* Measurement techniques for piezoelectric nanogenerators.

Energy Environ. Sci. **6,** 3035 (2013).

147. Sarker, S., Ahammad, A. J. S., Seo, H. W. & Kim, D. M. Electrochemical impedance spectra of dye-sensitized solar cells: Fundamentals and spreadsheet calculation. *International Journal of Photoenergy* **2014,** (2014).
148. Adachi, M. *et al.* Comparison of Electrochemical Impedance Spectroscopy between Illumination and Dark Conditions. *Chem. Lett.* **40,** 890–892 (2011).
149. Kong, C. S. A general maximum power transfer theorem. *IEEE Trans. Educ.* **38,** 296–298 (1995).
150. Chung, J., Lee, J. & Lim, S. Annealing effects of ZnO nanorods on dye-sensitized solar cell efficiency. *Phys. B Condens. Matter* **405,** 2593–2598 (2010).
151. Elliott, P. R. *et al.* Combined Hydrophobicity and Mechanical Durability through Surface Nanoengineering. *Sci. Rep.* **5,** 9260 (2015).
152. Park, Y., Park, C. H. & Kim, J. A quantitative analysis on the surface roughness and the level of hydrophobicity for superhydrophobic ZnO nanorods grown textiles. *Text. Res. J.* **84,** 1776–1788 (2014).
153. Levinson, H. J. & Society of Photo-optical Instrumentation Engineers. *Principles of lithography*. (SPIE, 2005).
154. Dong, J. *et al.* Impressive enhancement in the cell performance of ZnO nanorod-based perovskite solar cells with Al-doped ZnO interfacial modification. *Chem. Commun. (Camb).* **50,** 13381–4 (2014).
155. Hirano, Shin *et al.* Synthesis of Highly Oriented Lead Zirconate-Lead Titanate Film Using Metallo-organics. *J. Am. Ceram. Soc.* **75,** 2785–2789 (1992).
156. Zhang, Y. *et al.* Enhanced performance and light soaking stability of planar perovskite solar cells using an amine-based fullerene interfacial modifier. *J. Mater. Chem. A* **4,** 18509–18515 (2016).
157. Ito, S., Tanaka, S. & Nishino, H. Substrate-Preheating Effects on PbI_2 Spin Coating for Perovskite Solar Cells via Sequential Deposition. *Chem. Lett.* **44,** 849–851 (2015).
158. Kara, K. *et al.* Solvent washing with toluene enhances efficiency and increases

reproducibility in perovskite solar cells. *RSC Adv.* **6,** 26606–26611 (2016).

159. Li, W. *et al.* High Performance of Perovskite Solar Cells via Catalytic Treatment in Two-Step Process: The Case of Solvent Engineering. *ACS Appl. Mater. Interfaces* **8,** 30107–30115 (2016).

160. Jeon, N. J. *et al.* Solvent engineering for high-performance inorganic–organic hybrid perovskite solar cells. *Nat Mater* **13,** 897–903 (2014).

161. Pei, Y. *et al.* Effect of perovskite film preparation on performance of solar cells. *Journal of Chemistry* **2016,** (2016).

162. Tidhar, Y. *et al.* Crystallization of Methyl Ammonium Lead Halide Perovskites : Implications for Photovoltaic Applications Crystallization of Methyl Ammonium Lead Halide Perovskites : Implications for Photovoltaic Applications. 1–18 (2014). doi:10.1021/ja505556s

163. Dong, Q. *et al.* Encapsulation of Perovskite Solar Cells for High Humidity Conditions. *ChemSusChem* **9,** 2518 (2016).

164. Yang, J., Siempelkamp, B. D., Mosconi, E., De Angelis, F. & Kelly, T. L. Origin of the Thermal Instability in $CH_3NH_3PbI_3$ Thin Films Deposited on ZnO. *Chem. Mater.* **27,** 4229–4236 (2015).

165. Zhang, F. *et al.* Film-through large perovskite grains formation via a combination of sequential thermal and solvent treatment. *J. Mater. Chem. A* **4,** 8554–8561 (2016).

166. Stoumpos, C. C., Malliakas, C. D. & Kanatzidis, M. G. Organic Tin and Lead Iodide Perovskites with Organic Cations : Unique Semiconductors , with Phase Transitions and Near-infrared Photoluminescent Properties. *Inorg. Chem.* **52,** 9019–9038 (2013).

167. Chen, S. *et al.* $PbCl_2$ -assisted film formation for high-efficiency heterojunction perovskite solar cells. *RSC Adv.* **6,** 648–655 (2016).

168. Chen, W. *et al.* Efficient and stable large-area perovskite solar cells with inorganic charge extraction layers. *Science.* (2015).

169. Kim, H. S., Seo, J. Y. & Park, N. G. Material and Device Stability in Perovskite

Solar Cells. *ChemSusChem* **9,** 2528–2540 (2016).

170. Tress, W. *et al.* Understanding the rate-dependent J–V hysteresis, slow time component, and aging in $CH_3NH_3PbI_3$ perovskite solar cells: the role of a compensated electric field. *Energy Environ. Sci.* **8,** 995–1004 (2015).

171. Wu, X. *et al.* Light-induced picosecond rotational disordering of the inorganic sublattice in hybrid perovskites. *Sci. Adv.* **3,** (2017).

172. Eames, C. *et al.* Ionic transport in hybrid lead iodide perovskite solar cells. *Nat. Commun.* **6,** 7497 (2015).

173. Gottesman, R. *et al.* Extremely Slow Photoconductivity Response of CH_3NH_3 PbI_3 Perovskites Suggesting Structural Changes under Working Conditions. *J. Phys. Chem. Lett.* **5,** 2662–2669 (2014).

174. Snaith, H. J. *et al.* Anomalous hysteresis in perovskite solar cells. *J. Phys. Chem. Lett.* **5,** 1511–1515 (2014).

175. Walsh, A., Scanlon, D. O., Chen, S., Gong, X. G. & Wei, S. H. Self-regulation mechanism for charged point defects in hybrid halide perovskites. *Angew. Chemie - Int. Ed.* **54,** 1791–1794 (2015).

176. Sherkar, T. S. *et al.* Recombination in Perovskite Solar Cells: Significance of Grain Boundaries, Interface Traps, and Defect Ions. *ACS Energy Lett.* **2,** 1214–1222 (2017).

177. Qin, F. *et al.* Indium tin oxide (ITO)-free, top-illuminated, flexible perovskite solar cells. *J. Mater. Chem. A* **4,** 14017–14024 (2016).

178. Troughton, J. *et al.* Highly efficient, flexible, indium-free perovskite solar cells employing metallic substrates. *J. Mater. Chem. A* **3,** 9141–9145 (2015).